

HOMOGENEOUS NUCLEATION AND GROWTH OF SILICON POWDER

FROM

LASER HEATED GAS PHASE REACTANTS

by

ROBERT A. MARRA

B.S., B.A. Alfred University
(1978)

SUBMITTED IN PARTIAL FULFILLMENT OF THE
REQUIREMENTS FOR THE DEGREE OF
DOCTOR OF PHILOSOPHY

at the

MASSACHUSETTS INSTITUTE OF TECHNOLOGY

February, 1983

© Massachusetts Institute of Technology 1982

Signature of Author

Department of Materials Science and Engineering
January 7, 1983

Certified by

John S. Haggerty
Thesis Supervisor

Certified by

H. Kent Bowen
Co-Thesis Supervisor

Accepted by

Robert W. Balluffi
Chairman, Departmental Committee

Archives
MASSACHUSETTS INSTITUTE
OF TECHNOLOGY

MAY 12 1983

LIBRARIES

HOMOGENEOUS NUCLEATION AND GROWTH OF SILICON POWDER

FROM

LASER HEATED GAS PHASE REACTANTS

by

ROBERT A. MARRA

Submitted to the Department of Materials Science and Engineering
on January 7, 1983 in partial fulfillment of the requirements
for the Degree of Doctor of Philosophy in Ceramics.

ABSTRACT

Nucleation and growth behavior of fine silicon powders synthesized from the thermal decomposition of laser heated silane gas was examined. At sufficiently high temperatures, gas phase decomposition occurs. Due to the high degree of supersaturation, the critical size of the nucleus is extremely small, resulting in a nucleation rate which is not thermodynamically limited but dependent on the concentration of vapor phase silicon atoms and the collision frequency between atoms.

HeNe light scattering/extinction measurements showed that nucleation occurred at the beginning of the reaction zone then ceased. The observed nucleation rate ($> 10^{14}$ nuclei/cm³·sec) is in good agreement with the rate calculated from the classical theory of Volmer and Weber. After nucleation, particle growth occurred by the accretion of silicon bearing vapor species with the growth limited by the rate at which the gaseous molecules arrive at the particle surface. The nature of the growth process resulted in a narrow distribution of particle sizes. The final particle size was limited by the depletion of the reactant gas and not the elapsed growth time at elevated temperatures. Particle agglomeration did not occur within the reaction zone but occurred as the particles travelled to the microfibrinous collection filter or as they were collected.

The particle characteristics fulfill many of the requirements for an ideal sinterable powder. The particles are fine (< 150 nm), nearly monodispersed, of high purity, and loosely agglomerated. The agglomerates can be broken up by the proper dispersion techniques.

The final particle characteristics are dependent upon the process variables. The reactant gas flow rate, laser intensity, reactant pressure, and reaction zone dilution were varied systematically. The reaction zone temperature and partial pressure of the reacting gas species were determined by these variables. In general, an increased reaction temperature resulted in a decreased density of particles and a larger particle size. An increased reactant gas pressure had little effect on the particle number density but resulted in a larger individual particle size. With very low reaction zone temperatures, the particles were amorphous. At higher temperatures, the particles were polycrystalline or comprised of amorphous and polycrystalline silicon. The fraction of amorphous silicon decreased as the reaction zone temperature increased; at sufficiently high temperatures, the particles were fully crystalline. The crystal structure was confirmed by annealing studies in an inert argon atmosphere and scanning transmission electron microscopy (STEM).

Thesis Supervisor: Dr. John S. Haggerty
Title: Senior Research Scientist

Co-Thesis Supervisor: Professor H. Kent Bowen
Title: Professor of Ceramics and Electrical Engineering

TABLE OF CONTENTS

Chapter	Page
Title Page	1
Abstract	2
Table of Contents	4
List of Figures	7
List of Tables	11
Acknowledgements	12
I INTRODUCTION	13
II BACKGROUND	18
A. Homogeneous Nucleation Theory	18
1. The Critical Nucleus and the Nucleation Barrier	18
2. Mechanism for Nucleation	24
3. Modifications to the Homogeneous Nucleation Theory	27
B. Growth Mechanisms	30
1. Transport Controlled Growth	32
a. General Theory	32
b. Effect of Plurality of Particles	37
c. Effect of a Moving Boundary	39
2. Surface Controlled Growth	40
C. Laser Chemistry	41
D. Particulate Synthesis from Vapor Phase Reactions	58
1. General	58
2. Pyrolysis of Silane	62
3. Particulate Crystallinity	66

TABLE OF CONTENTS

Chapter	Page
III EXPERIMENTAL PROCEDURE	71
A. Powder Synthesis	71
B. Analysis of the Reaction Zone	75
1. Reaction Temperature	75
a. Possible Measurement Techniques	75
b. Experimental Procedure	78
2. In Situ Nucleation and Growth Measurements	82
C. Powder Characterization	86
IV RESULTS AND DISCUSSION	87
A. Temperature Measurement	87
1. Temperature Distribution	87
2. The Effect of Process Parameters on the Maximum Temperature	91
3. Heat Balance Analysis	95
B. In Situ Particle Nucleation and Growth Measurements	106
1. Particle Radius as a Function of Position	106
2. Particle Number Density	110
3. Gas Depletion and Possible Growth Mechanisms	115
C. Effect of Process Variables on the Powder Characteristics	119
1. General Characteristics	119
2. Effect of Process Variables	126
a. Gas Velocity	126
b. Laser Intensity	130
c. Argon Dilution	133
d. Cell Pressure	136
e. Boron Doping and Powder Synthesis Reproducibility	137

TABLE OF CONTENTS

Chapter	Page
D. Discussion of Particle Nucleation and Growth	139
1. Nucleation	139
2. Cessation of Nucleation	157
3. Growth of the Particles	162
a. Transport Limited Growth	163
b. Surface Controlled Growth	168
4. Control of Particle Size and Size Distribution	171
E. Particle Agglomeration	177
1. General	177
2. Experimental Results	183
F. Particle Crystallinity	185
1. General	185
2. Annealing Results	186
3. STEM Analysis	190
4. Temperature Dependence	196
5. Mechanisms for Particle Formation	200
V CONCLUSIONS	207
VI SUGGESTIONS FOR FUTURE WORK	209
Appendix 1: Summary of Run Conditions for Silicon Powder Synthesis	213
Appendix 2: Summary of Silicon Powder Characteristics	216
Appendix 3: Particle Size Analysis Techniques - BET Surface Area, X-Ray Line Broadening	219
Appendix 4: Gas Flow Characteristics	226
References	230
Biographical Note	239

LIST OF FIGURES

Figure		Page
II.1	Free energy change for the formation of a nucleus versus the cluster size.	20
II.2	The potential energy curve for a diatomic molecule.	47
II.3	The absorption coefficient of silane as a function of pressure for the P(20) CO ₂ laser line.	56
II.4	Structural phase diagram for a solid phase deposited from the vapor.	68
II.5	Microstructural development as a function of vapor deposition conditions.	68
III.1	Powder synthesis cell.	72
III.2	Schematic of optical layout for measuring scattering and extinction in the reaction zone.	79
III.3	Ratio of scattered to extinction cross sections versus the measured scattered to extinction ratio for various refractive indices.	83
III.4	Measured scattered to extinction ratio as a function of particle radius for various values of the particle refractive index.	85
III.5	Extinction efficiency as a function of particle radius for various values of the particle refractive index.	85
IV.1	Measured scattered and transmitted intensities and scattered to extinction ratio as a function of distance above the inlet nozzle. (Run 631S.)	88
IV.2	True temperature, brightness temperature, and emissivity as a function of distance above the inlet nozzle. (Run 631S.)	88
IV.3	True temperature as a function of distance above the inlet nozzle for various synthesis runs.	90
IV.4	Maximum reaction zone temperature versus silane flow rate. (Pressure = 2×10^4 Pa.)	92
IV.5	Maximum reaction zone temperature versus SiH ₄ flow rate. (Pressure = 3.5×10^4 Pa.)	92

Figure		Page
IV.6	Maximum reaction zone temperature versus SiH ₄ flow rate. (Pressure = 6×10^4 Pa.)	93
IV.7	Maximum reaction zone temperature versus laser intensity.	93
IV.8	Maximum reaction zone temperature as a function of dilution of reactant gas with argon.	94
IV.9	Calculated gas heating rate for various flow rates. (SiH ₄ absorption coefficient = 5×10^{-3} Pa ⁻¹ m ⁻¹ .)	99
IV.10	Calculated gas heating rate for various flow rates. (SiH ₄ absorption coefficient = 2×10^{-3} Pa ⁻¹ m ⁻¹ .)	99
IV.11	Effect of dilution of the reaction zone with argon on the calculated gas heating rate.	102
IV.12	Effect of laser intensity on the calculated gas heating rate.	102
IV.13	Particle size calculated from the scattering/ extinction results as a function of distance above the inlet nozzle. (Run 631S.)	108
IV.14	Particle size calculated from the scattering/ extinction results as a function of distance above the inlet nozzle for various synthesis runs.	108
IV.15	Product of particle density and optical pathlength as a function of distance above the inlet nozzle for Run 654S.	113
IV.16	Product of particle density and optical pathlength as a function of distance above the inlet nozzle for various synthesis runs.	113
IV.17	Calculated silicon concentration in the reaction zone as a function of distance above the inlet nozzle. (Run 654S.)	116
IV.18	The logarithm of the growth rate calculated from the scattering/extinction measurements versus the logarithm of the silicon concentration in the reaction zone.	118
IV.19	The logarithm of the growth rate calculated from the scattering/extinction results versus the logarithm of the quotient of the gas concentration and particle radius.	118

Figure	9 Page	
IV.20	Bright field TEM micrograph of a typical laser synthesized silicon powder. (Run 634S.)	122
IV.21	Dark field micrograph of powder shown in Figure IV.20.	122
IV.22	X-ray diffraction pattern of a typical laser synthesized silicon powder. ($\text{Cu}_{K\alpha}$ radiation.).	123
IV.23	Comparison of particle diameter measured by TEM and BET surface area.	125
IV.24	Effect of flow rate on the particle diameter calculated from BET surface area measurements. (Pressure = 2×10^4 Pa.)	127
IV.25	Effect of flow rate on the particle diameter calculated from BET surface area measurements. (Pressure = 3.5×10^4 Pa.)	127
IV.26	Effect of flow rate on the particle diameter calculated from BET surface area measurements. (Pressure = 6×10^4 Pa.)	128
IV.27	Effect of flow rate on the ratio of particle to crystallite size. (Pressure = 2×10^4 Pa.)	128
IV.28	Effect of flow rate on the ratio of particle to crystallite size. (Pressure = 3.5×10^4 Pa.)	129
IV.29	Effect of flow rate on the ratio of particle to crystallite size. (Pressure = 6×10^4 Pa.)	129
IV.30	Effect of laser intensity on particle diameter calculated from the BET surface area measurements.	132
IV.31	Effect of laser intensity on the ratio of particle to crystallite size.	132
IV.32	Effect of argon dilution on the particle diameter calculated from the BET surface area measurements.	135
IV.33	Effect of argon dilution on the ratio of particle to crystallite size.	135
IV.34	Effect of temperature and percent reaction on the supersaturation ratio for silane pyrolysis.	149
IV.35	The logarithm of the calculated particle number density versus the reciprocal of the maximum reaction zone temperature for various synthesis runs.	175

Figure		Page
IV.36	The particle collision correction factor l/W versus A/kT for van der Waals attraction.	182
IV.37	The effect of a 550°C, 3 hour anneal on powder crystallinity for Run 640S.	188
IV.38	The effect of a 550°C, 3 hour anneal on the powder crystallinity of Run 646S.	188
IV.39	The effect of a 550°C, 3 hour anneal on the ratio of the particle to crystallite size for powders synthesized at different laser intensities.	189
IV.40	STEM analysis of as synthesized powder from Run 658S.	191
IV.41	STEM analysis of as synthesized powder from Run 640S.	191
IV.42	STEM analysis of as synthesized powder from Run 635S.	192
IV.43	STEM analysis of annealed powder from Run 658S.	192
IV.44	STEM analysis of annealed powder from Run 640S.	193
IV.45	STEM analysis of annealed powder from Run 635S.	193
IV.46	Effect of reaction zone temperature on the fraction of crystalline silicon in the final particles (varied laser intensity).	199
A3.1	Plot of $P/V(P_0 - P)$ versus P/P_0 from BET multipoint surface area measurement.	221
A3.2	Diffraction line broadening from typical laser synthesized silicon	224
A4.1	Average velocity of gas stream as a function of distance from inlet nozzle.	
A4.2	The computed width of the gas stream as a function of distance from inlet nozzle.	227
A4.3	The computed velocity profile of reactant gases at several distances from the inlet nozzle.	228

LIST OF TABLES

Table		Page
I.1	Vapor Phase Powder Synthesis Techniques	15
II.1	Absorption Coefficients for the 10.6 μm ($00^{\circ}1-10^{\circ}0$) Band of the CO_2 Laser	54
IV.1	Chemical Analyses of Silicon Powders	121
IV.2	Density of Silicon Powder Measured by He Pycnometry	125
IV.3	Comparison of $\text{B}_2\text{H}_6/\text{SiH}_4$ and Undoped SiH_4 Runs	138
IV.4a	Extent of Gas Phase Decomposition and Equilibrium Pressures of Gaseous Species ($P_{\text{SiH}_4(\text{initial})} = 0.2 \text{ atm}$)	144
IV.4b	Nucleation Calculation for Reaction Zone Initially Comprised of 0.2 atm of Pure Silane	145
IV.5	Extent of Gas Phase Decomposition and Equilibrium Pressures of Gaseous Species ($P_{\text{SiH}_4(\text{initial})} = 0.6 \text{ atm}$)	147
IV.6	Percent of Silane Converted to Solid Silicon at Position Particles were First Observed by Light Scattering	158
IV.7	Comparison of Experimental Growth Rate and Calculated Growth Rate (Transport Limited)	166
IV.8	Calculated Collision Frequency Resulting from Brownian Motion	182
IV.9	Summary of Powder Annealing Results	189
A3.1	Comparison of Multipoint and Single Point BET Surface Area Measurements	221
A3.2	Diffraction Line Broadening from Typical Laser Synthesized Silicon (Run 631S)	224

ACKNOWLEDGEMENTS

I would like to express my deepest gratitude to Dr. John S. Haggerty for his insights and guidance throughout this research project. I would also like to thank Professor H. Kent Bowen for serving as co-thesis advisor and Professor Kenneth C. Russell and Professor Robert L. Coble for reading and serving on my thesis committee.

Pat Kearney, John Centorino, Paul McGrath, Granpa and the rest of the 13-4078 gang are acknowledged for their technical assistance as well as congenial coffee breaks. Thanks go to Tom Kelly for his assistance with the STEM. The author acknowledges the members of the "ceramics laser group" - Roger Cannon, Steve Danforth, Todd Gattuso, Yoko Suyama, and especially John Flint for his assistance in performing the light scattering extinction measurements. I thank Cindy Cali for her help in typing and preparing the final manuscript.

It would take an entire thesis to recognize all the friendships I have developed at M.I.T. Therefore a general collective list must suffice. Thanks go to my 12-096 officemates, the ceramics group-past and present, the rugby team and the many people with whom I've had a beer or two at the Muddy.

Last and not least I wish to thank my family for their support and encouragement during my many years as a student.

This research was sponsored by ARPA under contract number N00014-77-C-0581.

I. INTRODUCTION

Many ceramic materials have certain properties that make them ideal for applications in energy related systems. Because of its' high temperature strength, chemical inertness, refractoriness, creep resistance, and corrosion resistance, silicon nitride is a leading candidate for high temperature structural applications such as gas turbine engines.¹ To achieve the full potential of this material, it is necessary to produce reliable and reproducible components with a controlled microstructure.

The densification of fine powders to produce crystalline components with little or no porosity is one of the most important ceramic fabrication techniques.² High density reaction bonded Si_3N_4 can be produced by predensifying a silicon compact prior to nitridation. For uniform and controlled densification, the characteristics of the starting powder is of great importance.

Strength limiting defects are usually attributable to some specific event in the component's processing history extending from powder synthesis through all handling steps to the final consolidation into a densified part. Achieving the desired level of property reliability requires that starting powders fulfill both physical and chemical requirements. The physical requirements include fineness, homogeneity (single phase), narrow size distribution, non-agglomerated, and equiaxed shapes. Chemically, a powder must have proper stoichiometry and contain no impurities. The powder should be able to

pack to high green density without significant density gradients. The final microstructure of a ceramic component is particularly dependent on the characteristics of the powder and the powder packing.

Because of the importance of the powder characteristics on the sinterability, there has been increasingly more interest in the study of powder synthesis. Many synthesis techniques involve reactions and thermal decomposition in the solid state which often result in powders that must be calcined and purified. The particles must be separated by grinding which leads to a wide particle size distribution and extensive agglomeration. The direct synthesis of particles from dilute systems such as liquids or vapors offer many advantages over solid state synthesis. Powders are formed with their final composition and size (submicron) ideal for sintering; high purity can be maintained by controlling the purity of the starting liquids or vapors. Since dilute systems are utilized, agglomeration can normally be controlled during the synthesis. With a high degree of supersaturation, the particles tend to grow isotropically resulting in equiaxed shapes.³

Numerous techniques have been utilized to synthesize powders from vapor phase reactants. These include flow through tube furnaces, arc plasmas, flash thermolysis, and shock tubes. Table I.1 lists the general characteristics associated with each type of process.⁴ The presence of hot walls is undesirable since they act as heterogeneous nucleation sites and sources of contamination. With these processes, the thermal profiles within the reaction zones are often complex and nonideal resulting in nonuniform nucleation and growth times thereby

Table I.1. Vapor Phase Powder Synthesis Techniques

Technique	Max. Temp. (°C)	dT/dt (°Cs ⁻¹)	Hot Walls	Equipment Required	Volatility Required
Flow Reactor	<900	100	yes	Simple	Low
Flash Thermolysis	<900	10 ⁴	yes	Simple	Low
Shock Tube	>5000	10 ¹¹	no	Complex	High
Laser Driven	900-2000	10 ⁶ -10 ⁹	no	Simple	Low

reducing the controllability of the process and producing nonuniform particle characteristics.

The laser driven gas phase reaction process⁵ offers many advantages over other vapor phase processes. In this process, an optical energy source, specifically a CO₂ laser, is used to transfer energy to initiate and sustain a chemical reaction in the vapor phase. This thesis describes a detailed study of silicon powder synthesized from the pyrolysis of silane. Silicon nitride and silicon carbide powders have been synthesized from silane-ammonia⁶ and silane-ethylene⁷ gas mixtures respectively. Recently, work has been initiated to study the pyrolysis of more complex silicon bearing precursors⁸ and the synthesis of aluminum oxide from a variety of reactions.⁹

In the laser synthesis process, the reactant gases are self heated since the gaseous molecules absorb the laser radiation and a thermal reaction results through molecular collisions. During the reaction, the container walls remain cold; therefore, there is freedom from contamination and the absence of heterogeneous nucleation sites. The

purity levels are controlled by the purity of the reactant and inert gases and post production handling. The reaction zone is well defined by the intersection of the laser beam and reactant gas stream. The amount of energy supplied to the system can be precisely calculated from the laser energy output and the absorptivity of the gaseous products. If the wavelength of the emitted light and the absorption lines of the gaseous molecules are in near coincidence, the optical to thermal efficiency is very high. Uniform and precise process control can be achieved by varying the gas mixture, laser intensity, pressure, and reactant flow rates.

It should be noted that at the laser intensities and pressures typically utilized there is insufficient energy to permit dissociation of a molecule prior to collisions with other molecules. Thus, the process is not a photochemical reaction but rather the laser is simply used to initiate a thermal reaction. Since the reaction is thermal in nature, only one of the gas species needs to absorb the laser radiation and the other reactants will be heated by thermal collisions. With an inert gas absorber any conventional vapor phase reactants could be heated by laser radiation.

In order to control the formation of the fine particulates from the vapor phase, it is necessary to develop an understanding of the nucleation and growth behavior. This understanding requires the determination of the driving forces and rate limiting steps for the formation and growth of fine powders. This understanding will enable more precise control of the particle size, shape, and size distribution. The causes of agglomeration and the probability that

agglomeration will be accompanied by neck growth between particles need to be studied both theoretically and experimentally. Also, the conditions which result in the formation of amorphous, polycrystalline, and single crystal particles need to be elucidated.

There has been little work reported on the nucleation and growth of ceramic materials from vapor phase reactions and the fundamentals are not well understood. The inability to precisely define the reaction zone and the thermal-time histories of the gas phase molecules and the resulting particulates in conventional vapor phase synthesis techniques has limited the analyses required to establish a basic understanding of the formation mechanisms. The advantages of the laser synthesis process enables analysis in terms of nucleation and growth kinetics. Hence, this thesis research has involved a systematic study of the effect of the laser synthesis process variables on the reaction zone and powder characteristics. The results are discussed in terms of nucleation and growth mechanisms and a basic understanding of the particulate formation, agglomeration, and crystallinity is developed. The pyrolysis of silane to form silicon was chosen as a model system because of the simple reaction as well as the technical importance in the production of high purity, high density reaction bonded silicon nitride.

II. BACKGROUND

A. Homogeneous Nucleation Theory

The statistical theory of nucleation, also referred to as homogeneous nucleation theory, was developed by Volmer and Weber¹⁰ and Becker and Doring¹¹ for the formation of liquid droplets from a supersaturated vapor. Homogeneous nucleation results when the phase change occurs in the bulk of the original phase and is independent of surfaces and foreign particles. The theory is based on the assumption that through random thermal fluctuations, a sufficient number of molecules of the vapor phase become arranged in such a way as to have the structure and composition which is characteristic of the new phase. In the following discussion, this theory is applied to the nucleation of solid silicon embryos or nuclei from pure SiH_4 gas or SiH_4/Ar gas mixtures.

1. The Critical Nucleus and The Nucleation Barrier

The formation of a solid state silicon embryo will result in a change in free energy,

$$\Delta F_{\text{Si Embryo}} = \Delta F_{\text{Surface}} + \Delta \dot{F}_{\text{Transformation}}. \quad \text{IIA.1}$$

The first term on the right hand side of equation IIA.1 is the free energy change associated with the formation of a surface between the solid silicon embryo and the vapor phase. The surface free energy is always positive. The second term on the right hand side of equation

IIA.1 is the change in volume free energy for the transformation. When the vapor is supersaturated, that is, a metastable situation exists, the volume free energy change is negative. For spherical particles with radius r , equation IIA.1 can be rewritten as:

$$\Delta F_{\text{Si, Embryo}} = 4\pi r^2 \sigma + 4/3\pi r^3 \Delta F_{\text{Transformation}} \quad \text{IIA.2}$$

where σ is the specific surface energy of the interface separating the silicon embryo and the vapor phase and $\Delta F_{\text{Transformation}}$ is the free energy change per unit volume of the product associated with the formation of solid silicon from the silane gas.

The free energy change is plotted as a function of embryo size in Figure II.1. Whenever the volume free energy change $\Delta F_{\text{Transformation}}$ is negative, there exists a maximum in the total free energy change. It is the maximum in the free energy that acts as a potential barrier to nucleation. Differentiation of equation IIA.2 yields the critical size,

$$r^* = -2\sigma / \Delta F_{\text{Transformation}} \quad \text{IIA.3}$$

and the free energy change for the formation of a critical nucleus,

$$\Delta F^* = 16\pi\sigma^3 / 3(\Delta F_{\text{Transformation}})^2. \quad \text{IIA.4}$$

Embryos having a radius less than r^* are unstable, while those with a radius greater than r^* are stable, supercritical nuclei.

This free energy change can be explicitly described in terms the state of the system by examining the work required to form the critical size nucleus. This work can be determined from the difference in Helmholtz free energy of a thermodynamic system with and without a critical size nucleus. The Helmholtz free energy is defined as:

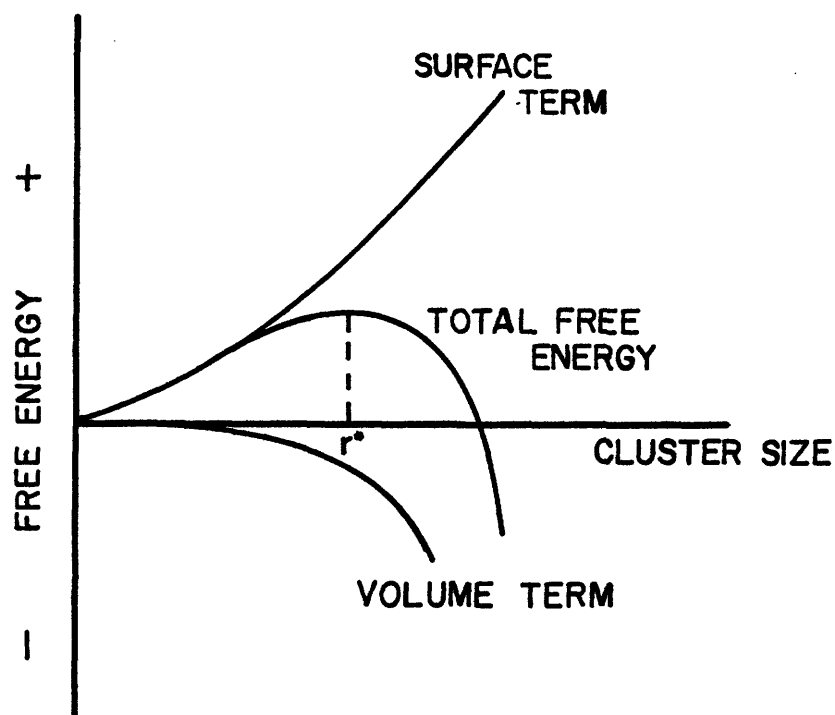


Figure II.1. Free energy change for the formation of a nucleus versus the cluster size.

$$F \equiv U - TS \quad \text{IIA.5}$$

where F is the Helmholtz free energy, U is the internal energy, T is the absolute temperature and S is the entropy. Since,

$$H = U + PV \quad \text{IIA.6}$$

and

$$m\mu = H - TS \quad \text{IIA.7}$$

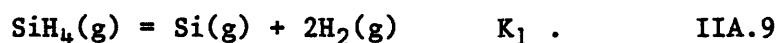
the Helmholtz free energy can be expressed in terms of chemical potential,

$$F = m\mu - PV. \quad \text{IIA.8}$$

In the above relations, H is enthalpy, P is pressure, V is volume, m is mass and μ is specific chemical potential.

Consider a volume of silane gas initially at a pressure $P_{\text{SiH}_4}(\text{g})$ and a temperature T . There will exist an equilibrium pressure of

silicon vapor, $P_{\text{Si}}(\text{g})$, in accordance with the reaction



It will be assumed that reaction IIA.9 is the only significant vapor phase reaction occurring. This assumption is discussed more fully in Section II.D. Therefore, the only vapor species present are $\text{SiH}_4(\text{g})$, $\text{Si}(\text{g})$, $\text{H}_2(\text{g})$ and any $\text{Ar}(\text{g})$ added to the reaction zone. The thermodynamic system will be defined to consist of only the silicon vapor and any solid silicon embryos. The other vapor species, $\text{SiH}_4(\text{g})$, $\text{H}_2(\text{g})$ and $\text{Ar}(\text{g})$ will be considered as part of the environment. This is not actually valid since as a $\text{Si}(\text{s})$ embryo grows and some of the $\text{Si}(\text{g})$ is transformed to solid, the $\text{SiH}_4(\text{g})$ and $\text{H}_2(\text{g})$ concentrations will change in accordance to the equilibrium reaction of Equation IIA.9. If the critical size nucleus is small, this assumption will introduce negligible error.

Consider the system at State I consisting of silicon vapor, at a pressure $P_{\text{Si}(\text{g})}$ and temperature T , occupying a volume V_v . Also consider the system at State II consisting of a critical size nucleus of solid silicon having a volume V_s at a temperature T and internal pressure $P_{\text{Si}(\text{g})}$ coexisting with a vapor phase which was initially at a state identical to State I. The total Helmholtz free energies for the system at States I and II are:

$$F_{\text{SI}} = m_{\text{Si}(\text{g})} \mu_{\text{Si}(\text{g})} - m_{\text{Si}(\text{g})} P_{\text{Si}(\text{g})} V_v \quad \text{II.A.10}$$

$$F_{\text{SII}} = (m_{\text{Si}(\text{g})} - m_{\text{Si}(\text{s})}) \mu_{\text{Si}(\text{g})} - (m_{\text{Si}(\text{g})} - m_{\text{Si}(\text{s})}) P_{\text{Si}(\text{g})} V_v \quad \text{II.A.11}$$

$$+ m_{\text{Si}(\text{s})} \mu_{\text{Si}(\text{s})} - m_{\text{Si}(\text{s})} P_{\text{Si}(\text{s})} V_s + \sigma A_s$$

where m_i is the mass of species i , μ_i is the chemical potential of

species i , P_i is the pressure of species i , v is the specific volume, σ is the interfacial energy and A_S is the surface area of the solid silicon.

The Helmholtz free energies for the environment at the two states are given by equations IIA.15 and IIA.16. Note that the change in volume of the environment is the same as the change in volume of the system.

$$V_{SI} = m_{Si(g)} v_g \quad \text{IIA.12}$$

$$V_{SII} = (m_{Si(g)} - m_{Si(s)}) v_g + m_{Si(s)} v_s \quad \text{IIA.13}$$

$$\Delta V = V_{SII} - V_{SI} = m_{Si(s)} (v_s - v_g) \quad \text{IIA.14}$$

$$F_{EI} = m_E \mu_E - P_{Si(g)} V_E \quad \text{IIA.15}$$

$$F_{EII} = m_E \mu_E - P_{Si(g)} (V_E - \Delta V) \quad \text{IIA.16}$$

$$= m_E \mu_E - P_{Si(g)} V_E - P_{Si(g)} m_{Si(s)} u_s - P_{Si(g)} m_{Si(s)} u_g$$

The work required to form the nucleus is given by the difference in the total Helmholtz free energy for states I and II,

$$\Delta F = F_{SII} - F_{SI} + F_{EII} - F_{EI} \quad \text{IIA.17}$$

$$\begin{aligned} \Delta F = & \sigma A_S + m_{Si(s)} (\mu_{Si(s)} - \mu_{Si(g)}) \\ & - m_{Si(g)} v_s (P_{Si(s)} - P_{Si(g)}). \end{aligned} \quad \text{IIA.18}$$

The critical size nucleus is actually in a state of unstable equilibrium, that is the temperature and chemical potential of the silicon nucleus and the Si(g) in the surrounding vapor are equal. Therefore the free energy change for the formation of the critical

nucleus can be simplified as:

$$\Delta F^* = 4\pi r^{*2} \sigma - 4/3\pi r^{*3} (P_{Si(g)}^* - P_{Si(g)}). \quad \text{IIA.19}$$

The equality of the chemical potential of the silicon nucleus and the Si(g) in the surrounding vapor determines the pressure P^* within the critical size nucleus. A force balance on the nucleus gives the relation between the pressure difference across the interface and the radius,

$$P_{Si(s)}^* - P_{Si(g)} = 2\sigma/r^*. \quad \text{IIA.20}$$

Therefore,

$$\Delta F^* = \frac{16\pi\sigma^3}{3 (P_{Si(s)}^* - P_{Si(g)})^2}. \quad \text{IIA.21}$$

The dependence of the nucleation barrier on the extent of supersaturation can be easily seen. For an ideal vapor phase, r^* is given by the Gibbs-Kelvin equation,

$$r^* = \frac{2\sigma v}{kT \ln \frac{P_{Si(g)}}{P_\infty}} \quad \text{IIA.22}$$

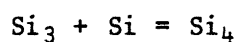
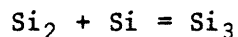
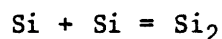
where v is the molecular volume of the condensed phase, k is Boltzman's constant, $P_{Si(g)}$ is the pressure of silicon vapor in gas phase, and P_∞ is the equilibrium vapor pressure of solid silicon. Substitution of Equations IIA.20 and IIA.22 into Equation IIA.21 gives the free energy of formation of the critical nuclei,

$$\Delta F^* = \frac{16\pi\sigma^3 v^2}{3(kT \ln \frac{P_{Si(g)}}{P_\infty})^2}. \quad \text{IIA.23}$$

Therefore as the supersaturation ratio increases, the number of molecules necessary to form a critical size nucleus becomes smaller and the nucleation barrier decreases. The critical radius and the energy barrier are now defined explicitly in terms of the state of the system. The state of the system is established by the pressure of silicon vapor $P_{\text{Si}(g)}$ and temperature T with P_{∞} being the saturation vapor pressure corresponding to the system temperature.

2. Mechanism for Nucleation

Regardless of the saturation of the vapor phase, atomic clusters will exist due to the attractive forces between the atoms. Statistical fluctuations in the distribution of vapor phase atoms give rise to small groups of silicon atoms which are characteristic of the solid silicon phase. Once these clusters form, van der Waals forces will keep them loosely bound. Fisher¹³ proposed a mechanism to describe the growth of these small embryos to larger sizes and finally to critical size. Larger embryos are formed by a series of bimolecular reactions between the clusters and single silicon atoms. Since the clusters are present initially in very small numbers, it is a good approximation to ignore reactions between clusters and consider only the reactions consisting of a cluster and a single molecule. The nucleation mechanism is then described by the following series of bimolecular reactions:



IIA.24

⋮

In the equilibrium situation, both the forward and reverse reaction rates are equal. From Figure II.1, it is clear that any Si embryo, Si_k , of sizes less than critical nucleus, Si_n^* , will attempt to decrease the free energy of the system by collapsing to a smaller size. Therefore for these reactions to be in equilibrium, the concentration of embryos of size r_k must be larger than the concentration of the next larger size embryo r_{k+1} . The equilibrium number density of embryos of size r_k is proportional to $\exp[-\Delta F_{r_k}/kT]$. Thus the critical size nucleus r_n^* is the least probable species in the system.

When an embryo reaches the critical size, it may continue to grow and leave the system as a macroscopic particle. In order to restore the equilibrium concentration of nuclei of size n^* , all the reactions involving smaller size clusters will undergo a net forward reaction. Since these net forward reactions will cause a decrease in the concentration of Si(g) atoms, the homogeneous nucleation theory assumes that any silicon atom leaving the system as a macroscopic particle will be replaced by a silicon vapor atom. Pesthy¹⁴ discusses this assumption and it will be looked at in more detail in Section IV.D.

The ratio of the probability of an embryo of size Si_k to grow to size Si_{k+1} by gaining a Si atom to the probability of an embryo of size Si_{k+1} to collapse to size Si_k by losing a Si atom can be expressed in terms of the equilibrium concentrations of Si_k and Si_{k+1} ,

$$\frac{W(Si_k \rightarrow Si_{k+1})}{W(Si_{k+1} \rightarrow Si_k)} = \frac{N_{Si_{k+1}}}{N_{Si_k}} \quad \text{IIA.25}$$

where $W(\text{Si}_k \rightarrow \text{Si}_{k+1})$ is the probability per unit time and concentration of Si_k of a transition from Si_k to Si_{k+1} and N_{Si_k} is the concentration of embryos of size r_k . The probability of embryo growth is given by the molecular impingement rate¹⁵ times the surface area of the embryo times the condensation coefficient,

$$W(\text{Si}_k \rightarrow \text{Si}_{k+1}) = \alpha_c \frac{P}{(2\pi mkT)^{1/2}} \cdot 4\pi r_k^2 \quad \text{IIA.26}$$

where P is the vapor pressure, m is silicon molecular mass and α_c is the condensation coefficient. Volmer and Weber¹⁰ determined the rate of homogeneous nucleation to be equal to the probability of a critical size nucleus r_n^* growing to a nucleus of size r_{n+1}^* times the concentration of critical size nuclei. They assumed that the actual concentration of critical size nuclei was the metastable equilibrium concentration given by Equation IIA.25. Therefore, the homogeneous nucleation rate, the nuclei formed per unit volume per unit time, is

$$J = W(\text{Si}_n^* \rightarrow \text{Si}_{n+1}^*) \cdot N_{\text{Si}_n^*} \quad \text{IIA.27}$$

As stated above, the concentration of critical size nuclei is proportional to the work required to create the nuclei. The concentration of single silicon atoms will be much greater than the concentration of all other embryos. Thus, the concentration of critical size nuclei is

$$N_{\text{Si}_n^*} = n_1 \exp \left[\frac{-\Delta F^*}{kT} \right] = \frac{P_{\text{Si}(g)}}{kT} \exp \left[\frac{-\Delta F^*}{kT} \right] \quad \text{IIA.28}$$

Substitution of Equations IIA.28 and IIA.26 into Equation IIA.27 yields the Volmer-Weber Equation for the homogeneous nucleation rate,

$$J = \alpha_c \cdot 4\pi r^*{}^2 \frac{P_{\text{Si(g)}}}{(2\pi mkT)^{1/2}} \cdot \frac{2P_{\text{Si(g)}}}{kT} \exp(-\Delta F^*/kT) \quad \text{IIA.29}$$

3. Modifications to the Homogeneous Nucleation Theory

The Volmer-Weber formulation of the nucleation rate treats the concentration of embryos as an equilibrium case. The actual steady-state nucleation rate should be lower than the equilibrium rate approximation. First, both the loss of a critical size nuclei by growth to supercritical size and finite probability that a critical nuclei will lose an atom and collapse to subcritical size must be considered. Secondly, any finite nucleation rate will disturb the equilibrium distribution of embryos by depleting the most reactive species. These arguments were addressed by Becker and Doering¹¹ and Zeldovich¹⁶ by considering the actual steady-state concentration of critical nuclei. The steady-state solution to the series of reactions in Equation IIA.24 yields the non-equilibrium or Zeldovich factor,

$$Z = \left(\frac{\Delta F^*}{3\pi kT k^*} \right)^{1/2} \quad \text{IIA.30}$$

or

$$Z = \frac{v(kT \ln SS)^2}{8\pi\sigma(\sigma kT)^{1/2}} \quad \text{IIA.31}$$

where SS is the super-saturation ratio, $P_{\text{Si(g)}}/P_\infty$.

Thus, the Becker-Doering-Zeldovich expression for the homogeneous nucleation rate is

$$J = \alpha_c Z \cdot 4\pi r^{*2} \cdot \frac{P_{\text{Si(g)}}}{(2\pi mkT)^{1/2}} \cdot \frac{P_{\text{Si(g)}}}{kT} \exp\left(\frac{-\Delta F^*}{kT}\right) \quad \text{IIA.32}$$

The fundamental uncertainty of the classical homogeneous nucleation theory lies in the assumption that clusters containing a few atoms can be described in terms of macroscopic thermodynamic quantities. As the cluster size becomes large, the condensation coefficient α_c becomes equal to the coefficient for a bulk condensed phase and the radius of a cluster of k molecules can be determined from:

$$r_k = \left(\frac{k\nu}{4/3\pi}\right)^{1/3} \quad \text{IIA.33}$$

It is probable that Equation IIA.33 will underestimate the effective collision radius for small clusters.¹⁷ Also the condensation coefficient for a small cluster is expected to be less than the bulk coefficient since due to thermal nonaccommodation the smallest clusters are unable to absorb the heat of condensation to the extent that larger clusters can.

If the radius of a cluster is much larger than the intermolecular spacing, Kirkwood and Buff¹⁸ have shown that the surface free energy of the cluster can be assumed equal to the surface free energy of a planar surface. If clusters have high surface curvatures, the surface of tension will be located below the surface of density discontinuity and a decrease in surface tension at high curvatures is expected. Kirkwood and Buff¹⁸ and Buff¹⁹ derived an expression for the surface free energy of a cluster with radius of r

$$\sigma_r = \frac{\sigma_0}{\left(1 + \frac{2d'}{r}\right)} \quad \text{IIA.34}$$

where σ_s is the surface free energy of a planar surface and d' is a positive distance approximately equal to the molecular diameter.

Lothe and Pound²⁰ suggested that statistical mechanical contributions to the free energy of formation of embryos may be significant. They assumed that a stationary cluster vibrates about a set of equilibrium coordinates that are fixed in space. The atoms in the cluster are constrained to volume elements of the order of the free volume of the bulk condensed phase. The free energy for the formation of a critical nucleus should therefore include the translational and rotational components necessary to energize the nuclei to the vapor temperature T . A less important contribution arising from the free energy necessary to separate a group of k molecules from a larger cluster should also be considered. These additional terms are relatively insensitive to size and supersaturation and can therefore be included in the pre-exponential of Equation IIA.32 as the Lothe-Pound correction factor Γ . This results in the Lothe-Pound expression for the homogeneous nucleation rate,

$$J = \alpha_c Z \Gamma \cdot 4\pi r^{*2} \cdot \frac{P_{\text{Si(g)}}}{(2\pi mkT)^{1/2}} \cdot \frac{P_{\text{Si(g)}}}{kT} \exp\left(\frac{-\Delta F^*}{kT}\right) \quad \text{IIA.35}$$

where Γ is approximately equivalent to $\exp\left(\frac{2\Delta H_{\text{vap}}}{RT}\right)$, where ΔH_{vap} is the molar enthalpy of vaporization.

For a given initial distribution of clusters, there will always be a finite induction time τ_n before a steady-state condition is achieved. Only if $\tau_n \cdot J$ is much larger than n , will the system exhibit a steady-state nucleation rate. This is equivalent to $\Delta F^*/kT \gg 1.0$ for the steady-state approximation to be valid. Various investigators²¹⁻²⁴

determined the induction time by approximating the set of reactions in Equation IIA.24 by a differential equation having time dependent $N_k(t)$. The induction time was determined to be approximately

$$\tau_n \cong \frac{kr^{*2} (2\pi mkT)^{1/2}}{\alpha_c (4\pi r^{*2}) P_{Si(g)}} \quad \text{IIA.36}$$

If thermal non-accomodation is considered, the induction time would be increased since the condensation coefficient is less than 1.0.

In summary, the kinetic model of Volmer and Weber has proved to be qualitatively correct, although there is still some doubt concerning its quantitative validity. In general, the kinetic and non-equilibrium corrections appear to be relatively unimportant. Recent attempts to refine the theory have not resolved the uncertainties.²⁵ There is substantial controversy as to which model is best, although the Becker-Doering-Zeldovich theory has been found to be in quite good agreement with some experimental results.

B. Growth Mechanisms

Once the silicon particles are nucleated, they will grow to their final dimensions. The growth process is expected to be dominant over further homogeneous nucleation for two reasons. First, the existing nuclei act as heterogeneous sites for further condensation. Second, any growth will deplete the silicon vapor atoms, thereby reducing the supersaturation and effectively ceasing the homogeneous nucleation. This will be discussed more thoroughly in Section IV.D.

The vapor growth process involves the transport of the vapor to the silicon nuclei surface and the condensation or deposition at the surface. If the reaction shown in Equation IIA.9 occurs, the Si(g) atoms will diffuse to the nuclei surface and growth will occur by simple condensation. This is generally referred to as homogeneous deposition. The growth process may also involve the adsorption of silane gas molecules or other vapor phase silicon hydrides or radicals on the silicon surface. A chemical reaction occurs to form solid silicon and hydrogen gas. The hydrogen must then be desorbed into the vapor phase. This is referred to as heterogeneous deposition.

The maximum growth rate can be predicted from equilibrium thermodynamics. In the actual growth process, kinetic factors will generally prevent the system from achieving the equilibrium growth rates. This is especially true for solid silicon growth from silane gas. The free energy change for the reaction,



is negative at all temperature above 0°K,²⁶ but due to kinetic limitations the reaction will not proceed at any measurable extent until approximately 700°C.

The kinetic factors required for growth can be visualized by considering the steps involved in a typical vapor growth process.

1. Transport of the reactive species to the particle surface.
2. Adsorption of the reactants on the particle surface.
3. Formation of the solid product either by simple condensation or a chemical reaction.
4. Desorption of any gaseous reaction products.

5. Transport of the gaseous reaction products from the particle surfaces.

The overall growth rate will be determined by the slowest step. Steps 1 and 5 involve the transport of material in the vapor and generally occur by gaseous diffusion. Step 2 through 4 occur at or on the particle surface. Growth limited by one of these steps is called chemical or surface controlled. The rate limiting step may change as the process parameters are altered. In the following discussion, each rate limiting step is considered. The effect of reaction parameters such as concentration of the vapor species, temperature, and surface morphology is discussed in Section IV.D.

1. Transport Controlled Growth

- a. General Theory

Consider the growth of a single particle with radius r_p much larger than the mean free path λ within the gas stream. If the growth is limited by the transport of vapor to the particle surface, the rate can be determined from diffusion theory. For a single sphere in an infinite diffusion field, the equation of diffusion in spherical coordinates is given by Fick's second law in the form,

$$\frac{\partial c}{\partial t} = D \left[\frac{\partial^2 c}{\partial r^2} + \frac{2}{r} \frac{\partial c}{\partial r} \right] \quad \text{IIB.2}$$

where c is the vapor concentration, D is the diffusion coefficient, r is the distance from the particle center, and t is time.

Smoluchowski²⁷ proposed a boundary condition: the concentration of vapor species at the particle surface is always zero. This is not valid since it requires that all atoms colliding with the surface are adsorbed, when in fact there is always a finite vapor pressure. A more realistic boundary condition was proposed by Collins and Kimball:²⁸

$$\left(\frac{\partial c}{\partial r}\right)_{r_p} = \frac{\alpha}{\rho} c(r_p, t) \quad \text{IIB.3}$$

where α is the probability that impinging molecules are absorbed and ρ is

$$\rho = \frac{\int_0^{\infty} S^2 \psi(S) ds}{\int_0^{\infty} S \psi(S) ds} = \frac{\langle S^2 \rangle}{\langle S \rangle} \quad \text{IIB.4}$$

where S is the diffusion jump distance (which is approximately equal to the path of an atom between collisions λ) and $\psi(S)$ is the jump density function. Assuming the initial concentration is constant,

$$c(r, 0) = c_0 \quad r > r_p \quad \text{IIB.5}$$

and far from the particle:

$$c(r, t) \rightarrow c_0 \quad r \rightarrow \infty \quad t > 0, \quad \text{IIB.6}$$

solution of Equation III.2 subject to the initial and boundary conditions gives,

$$\frac{c}{c_0} = 1 - \frac{r_p - \beta}{r} \left\{ \operatorname{erfc} \left[\frac{r - r_p}{2(Dt)^{1/2}} \right] - \exp \left[\frac{Dt}{\beta^2} + \frac{r - r_p}{\beta} \right] \operatorname{erfc} \left[\frac{(Dt)^{1/2}}{\beta} + \frac{r - r_p}{2(Dt)^{1/2}} \right] \right\} \quad \text{IIB.7}$$

where $\beta = \frac{r_p \gamma}{r_p \gamma}$ with $\gamma = \frac{\rho}{\alpha}$.

The total flux of molecules impinging on the surface is

$$F(t) = 4\pi r_p^2 D \left(\frac{\partial c}{\partial r} \right)_{r_p} . \quad \text{IIB.8}$$

Thus the total flux is given by

$$F(t) = 4\pi D c_0 \left\{ r_p - \beta + \frac{(r_p + \beta)^2}{\beta} \exp \frac{Dt}{\beta^2} \operatorname{erfc} \frac{(Dt)^{1/2}}{\beta} \right\} . \quad \text{IIB.9}$$

For the controlled growth process the time dependent term is small and may be neglected.²⁷ So the flux of molecules to the particle surface becomes

$$F(t) = 4\pi D c_0 (r_p - \beta) = 4\pi D c_0 \left(\frac{\alpha r_p^2}{\alpha r_p - \rho} \right) \quad \text{IIB.10}$$

For sufficiently large r_p , that is for particles with diameters much larger than the mean free path,

$$F(t) = 4\pi D r_p c_0 . \quad \text{IIB.11}$$

Assuming the gas behaves ideally, $c_0 = \frac{P_0}{kT}$, and the molecular volume of silicon is v_{Si} , the growth law for a large particle becomes,

$$\frac{dv}{dt} = \frac{4\pi D r_p v_{Si} P_0}{kT} \quad \text{IIB.12}$$

or since $\frac{dr}{dt} = \frac{1}{4\pi r_p^2} \frac{dv}{dt}$,

$$\frac{dr}{dt} = \frac{D v_{Si} P_0}{r_p kT} \quad \text{IIB.13}$$

Note the growth law given by Equation IIB.13 is independent of the accommodation coefficient. If the equilibrium vapor pressure of the solid P_∞ is significant in comparison with the vapor pressure in the

gas phase $P_{\text{Si(g)}}$, then Equation IIB.13 must be adjusted to include the vapor pressure difference ($P_{\text{Si(g)}} - P_{\infty}$). For small particles the Kelvin effect may be significant²⁹ and Equation IIB.13 becomes

$$\frac{dr}{dt} = \frac{Dv_{\text{Si}} \left[P_{\text{Si(g)}} - P_{\infty} \exp\left(\frac{2\sigma v_{\text{Si}}}{r kT}\right) \right]}{r_p kT} \quad \text{IIB.14}$$

Since it was determined²⁷ that for colloid growth the transient period is not important, Equation IIB.14 can be derived³⁰ by considering the steady-state solution to Equation IIB.2,

$$\frac{dc}{dt} = D \left[\frac{\partial^2 c}{\partial r^2} + \frac{2}{r} \frac{\partial c}{\partial r} \right] = 0 \quad \text{IIB.15}$$

with the boundary condition $c = c_{\infty}$ at $r = r_p$ and $c = c_0$ at $r = \infty$. The solution to Equation IIB.15 which satisfies the boundary conditions is

$$\frac{c - c_{\infty}}{c_0 - c_{\infty}} = 1 - \frac{r_p}{r} \quad \text{IIB.16}$$

Differentiation of Equation IIB.16 and substitution into Equation IIB.8 gives

$$F(t) = 4\pi r_p D(c_0 - c_{\infty}) \quad \text{IIB.17}$$

If the gas behaves ideally, the molecular volume is v_{Si} , and the Kelvin effect is important, Equation IIB.17 becomes identical to Equation IIB.14.

There are numerous ways to derive a growth expression for vapor transport limited growth with the mean free path in the vapor much larger than the particle diameter. Based on the kinetic theory of gases¹⁵, the net flow of molecules to a surface of area $4\pi r_p^2$ is

$$F(t) = \frac{4\alpha(P_0 - P_\infty)\pi r_p^2}{(2\pi mkT)^{1/2}} \quad \text{IIB.18}$$

where the accommodation coefficient α for the condensation and evaporation fluxes are assumed to be equal. Thus the resulting growth law is

$$\frac{dv}{dt} = \frac{4\alpha\pi r_p^2 v_{Si} \left[P_{Si(g)} - P_\infty \exp\left(\frac{2\sigma v_{Si}}{r_p kT}\right) \right]}{(2\pi mkT)^{1/2}} \quad \text{IIB.19}$$

or

$$\frac{dr}{dt} = \frac{\alpha v_{Si} \left[P_{Si(g)} - P_\infty \exp\left(\frac{2\sigma v_{Si}}{r_p kT}\right) \right]}{(2\pi mkT)^{1/2}} \quad \text{IIB.20}$$

Frisch and Collins³¹ have shown that Fick's second law given by Equation IIB.2 can be applied to the growth of an aerosol with the particle size much smaller than the mean free path if an appropriate boundary condition is applied. They found that at the particle surface $r = r_p$, the concentration $c(r,t)$ must satisfy

$$\gamma \left(\frac{dc}{dr} \right) = \int_{r_p}^{\infty} c(r_0, t) \phi(r_0 - r_p) dr_0 \quad \text{IIB.21}$$

where $\gamma = \frac{2}{3} \frac{\langle s^2 \rangle}{\langle s \rangle} = \frac{2}{3} \frac{\rho}{\alpha}$ and $\phi(r_0 - r_p) = \frac{1}{\langle S \rangle} \int_{r_0 - r_p}^{\infty} \psi(s) ds$ with S ,

$\psi(s)$, ρ and α as defined previously. Solution of Fick's second law (Equation III.2) subject to the boundary conditions IIB.6 and IIB.21 and the initial condition IIB.5 yields

$$\frac{c}{c_0} = 1 - \frac{r_p - \beta}{r I(\sigma)} \left\{ \operatorname{erfc} \frac{r - r_p}{2(Dt)^{1/2}} - \exp \frac{Dt}{\beta^2} + \frac{r - r_p}{\beta} \right.$$

$$\operatorname{erfc} \frac{(Dt)^{1/2}}{\beta} - \frac{r - r_p}{2(Dt)^{1/2}} \left\{ \right. \quad \text{IIB.22}$$

where

$$\beta = \frac{\gamma r_p}{r + r_p} I(\delta) \quad \text{and} \quad I(\delta) = \int_0^\delta \phi(z) z \quad \text{where } \delta \text{ is given such that}$$

$r_p \leq r_p + \delta \leq \infty$. Frisch and Collins³¹ showed that $I(\delta)$ is approximately equal to 1.0 and thus Equation IIB.22 is equivalent to Equation IIB.7 and the growth for long mean free path is given by Equation IIB.9.

Fuchs and Sutigin³² and Fuchs³³ have formulated an approximate relation for vapor transport limited growth for the entire range of particle sizes. Their derived relation is

$$\frac{dr}{dt} = \frac{v_{Si} D (r_p - \alpha \lambda)}{kT (r_p^2 + b \lambda r_p + a \lambda^2)} \left[P_{Si(g)} - P_\infty \exp \left(-\frac{2\sigma v_{Si}}{r_p kT} \right) \right] \quad \text{IIB.23}$$

where λ is the mean free path in the vapor and a , b , and α are given by Fuchs³³ as

$$a = \frac{\alpha D}{\lambda} \left(\frac{2\pi m}{kT} \right)^{1/2} \cong \frac{4}{3} \quad b = \frac{a}{\alpha} \cong \frac{4}{3} \quad \alpha \cong 1.0 \quad \text{IIB.24}$$

and by Fuchs and Sutigin³² as

$$a = 1.33 \quad b = 1.71 \quad \alpha = 1.0.$$

Equation IIB.23 reduces to Equation IIB.14 for continuum range when $r_p \gg \lambda$ and to approximately 1.2 times Equation IIB.20 when $\lambda \gg r_p$.

b. Effect of Plurality of Particles

All of the growth laws derived so far have considered only the

growth of a single particle. For diffusion controlled aerosol growth, the flow of vapor atoms is not directed towards a single particle but towards a large number of them. Thus the effective flux is smaller than that calculated for a single particle in an infinite medium. This competition leads to the depletion and final disappearance of the supersaturation of vapor species and therefore a limit to the final particle dimensions.

The effect of competing condensation sinks was first treated by Reiss and LaMer.³⁴ They accounted for the plurality by considering a single particle confined to grow in an impermeable shell of volume $1/N$ where N is the number density of particles. A much simpler formulation was presented by Collins and Frisch³¹, who considered N particles randomly distributed in volume V all having the same radius. It was also assumed that the sinks act independently of each other and the adsorption probability of each sink is the same. A modified form of Fick's law is obtained by considering the rate of change of vapor atoms in a volume δV containing δM randomly distributed sinks,

$$\frac{\partial c}{\partial t} = D\nabla^2 c - \frac{mF(t)c}{c_0 - m \int_0^t F(\tau) d\tau} \quad \text{IIB.26}$$

where c_0 is the initial vapor concentration, and $m = \frac{\delta M}{\delta V} = \frac{M}{V}$ since the particles are randomly distributed. Solution of Equation IIB.26 yields the flux of vapor atoms to a given particle in the presence of a concentration m of other sinks,

$$F(t) = F_0(t) \exp \left[-\frac{m}{c_0} \int_0^t F_0(\tau) d\tau \right] \quad \text{IIB.27}$$

where $F_0(t)$ is the flux of vapor atom to the particles in the absence

of other sinks. Equation IIB.27 possesses the properties of $\lim_{t \rightarrow 0} F(t) = F_0(t)$ indicating that at early times the competition between competing sinks is unimportant and $\lim_{t \rightarrow \infty} F(t) = 0$ corresponding to the disappearance of the supersaturation and the cessation of growth.

c. Effect of a Moving Boundary

All the growth law solutions presented so far have ignored the effect of the moving boundary of the spherically growing particle on the flux of vapor atoms to the particle surface and the consequent growth rate. Reiss and LaMer³⁴ described the effect of the three-dimensional moving boundary for the steady-state growth described by Equation IIB.15 with the Smoluchowski boundary condition which assumes that every molecules arriving at the particle surface is absorbed.

Frisch and Collins³⁵ solved the general form of Fick's second law given by Equation IIB.2 with the boundary condition IIB.3 using a perturbation method,³⁶ they obtained the differential equation for the moving boundary,

$$\frac{dr}{dt} = \frac{v_{Si} D(c_0 - c_\infty) \beta}{\gamma r_p} \left\{ 1 - \exp \frac{Dt}{\beta^2} \operatorname{erfc} \frac{(Dt)^{1/2}}{\beta} \right\} \quad \text{IIB.28}$$

where $\beta = \frac{\gamma r_p}{r_p + \gamma}$ with $\gamma = \frac{\rho}{\alpha}$ with ρ defined by Equation IIB.4. If the mean free path in the vapor is much larger than the particle radius and the short transient time is ignored, the rate of advance of the boundary can be approximated by the leading term of Equation IIB.28,

$$\frac{dr}{dt} = \frac{v_{Si} D (c_o - c_\infty)}{r + \gamma} \quad \text{IIB.29}$$

Integration by separation of variables with initial condition of radius $r = r_o$ at time $t = 0$ yields,

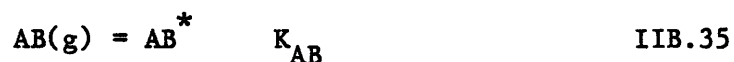
$$\gamma [r(t) - r_o] + 1/2 [r^2(t) - r_o^2] = (c_o - c_\infty) v_{Si} Dt \quad \text{IIB.30}$$

Equation IIB.34 predicts that the radius of the growing aerosol particle will initially show a linear time dependence before r becomes sufficiently large for Equation IIB.30 to exhibit the limiting form of the parabolic growth law. Again we should consider the effect of a concentration of M competing monodispersed particles homogeneously¹⁴ and randomly distributed in a volume V . These solutions are described by Frisch and Collins.³⁶

2. Surface Controlled Growth

If the rate at which molecules are delivered to the particle surface is rapid, the overall particle growth will be limited by processes that occur at the surface. The growth rate will be determined by the slowest of the following processes: 1) adsorption of reactants, 2) reaction on the surface, or 3) desorption of reaction products. The following section hypothetically discusses the kinetics of the growth process in which the rate limiting process occurs at the particle surface.

Consider the adsorption of gaseous AB onto the surface of solid A,



where K_{AB} is the adsorption rate constant and AB^* signifies an adsorbed AB molecule. The rate of adsorption is

$$R_{AB} = K_{AB} \phi [AB] \quad \text{IIB.36}$$

where ϕ is the fraction of vacant surface site and $[AB]$ is the concentration of $AB(g)$ in the vapor phase. The adsorbed AB molecule may be desorbed without undergoing decomposition,



where K_{-AB} is the desorption rate constant. The rate of desorption is

$$R_{-AB} = K_{-AB} \phi_{AB} \quad \text{IIB.38}$$

with ϕ_{AB} equal to the fraction surface sites containing adsorbed AB.

The adsorbed AB may also decompose to form solid A and adsorbed B,



at a rate,

$$R_{\text{REACTION}} = K_R \phi_{AB} \quad \text{IIB.40}$$

where K_R is the reaction rate constant. The adsorbed B will have to be desorbed into the surrounding vapor:



with a corresponding rate,

$$R_B = K_{-B} \phi_B \quad \text{IIB.42}$$

where ϕ_B is the fraction of surface sites occupied by adsorbed B.

At steady state, the concentrations of AB^* and B^* on the surface are constant so the rates of adsorption of AB is equal to the reaction rate plus the rate of AB desorption,

$$R_{AB} = R_{-AB} + R_{REACTION} \quad IIB.43$$

and the rate of desorption must equal the rate of reaction,

$$R_{-B} = R_{REACTION} \quad IIB.44$$

Since $\phi = 1 - \phi_{AB} - \phi_B$, the rate of growth, which is equivalent to $R_{REACTION}$, can be determined by algebraic manipulation of Equations IIB.36 to IIB.44,

$$R_{REACTION} = \frac{K_R K_{AB} [AB]}{K_{-AB} + K_R + \left(1 + \frac{K_B}{K_{-B}}\right) K_{AB} [AB]} \quad IIB.45$$

$R_{REACTION}$ signifies the rate at which silicon atoms are incorporated into the solid; the volumetric growth rate is equal to the product $R_{REACTION}$ and the molecular volume of silicon v_{Si} .

It is useful to examine the various rate-limiting conditions. If the rate constant for adsorption K_{AB} is much smaller than K_R , K_{-AB} or K_{-B} , the rate of growth given by Equation IIB.45 reduces to

$$R_G = \frac{K_R K_{AB} [AB]}{K_{-AB} + K_R} \quad IIB.46$$

Therefore, the growth rate is directly proportional to the partial pressure of AB in the vapor phase. Since chemisorption is an activated process, the growth rate should exhibit an exponential temperature dependence. The rate is also expected to be dependent on the nature of the surface, i.e., whether the particle is amorphous or crystalline and

if crystalline, the crystallographic orientations of the growth surfaces. Therefore if the particle is a single crystal possessing highly anisotropic growth surfaces, the final shape may be fibrous or platelike.

The second rate limiting case occurs if the surface chemical reaction is slow compared to the adsorption and desorption of the reactants and products. Therefore $K_R \ll K_{AB}, K_{-AB}, K_{-B}$ and Equation IIB.45 reduces to

$$R_G = \frac{K_R K_{AB} [AB]}{K_{-AB} + K_{AB} [AB]} \quad \text{IIB.47}$$

or

$$R_G = \frac{K_R \beta_{AB} [AB]}{1 + \beta_{AB} [AB]} \quad \text{IIB.48}$$

where β_{AB} is the Langmuir adsorption coefficient, $\beta_{AB} = K_{AB}/K_{-AB}$. The dependence on the partial pressure can be seen by examining limiting cases: 1) at low partial pressure $\beta_{AB} [AB] < 1$, the growth rate is linearly dependent on $[AB]$, and 2) at high partial pressure $\beta_{AB} [AB] \gg 1$, Equation IIB.48 reduces to $R_G = K_R$ and is thus independent of the partial pressure of $AB(g)$. Again the rate will have an exponential temperature dependence and will be effected by the nature of the particle surface in the same manner as with adsorption controlled growth.

If the desorption of the reaction product is rate-limiting, $K_{-B} \ll K_R, K_{AB}, K_{-AB}$, Equation IIB.45 reduces to

$$R_G = K_{-B}$$

The growth rate is independent of the partial pressure of the reactant

gas. The rate is expected to have an exponential temperature dependence since desorption is also an activated process, and it may depend on the crystallographic orientation at the particle surface.

Since the processes which occur at the particle surface are all thermally activated, surface controlled growth tends to be dominant at low reaction temperatures. At higher temperature, the transport of vapor to the surface becomes rate limiting. This was evidenced by the work of Bloem⁷⁸ who determined that the chemical vapor deposition of silicon from silane was controlled by vapor transport at deposition temperatures above 900°C; at lower temperatures, the surface reaction was rate limiting.

The different theoretical growth rates are dependent on such parameters as temperature, particle size, reactant gas concentration, and the crystallographic nature of the particle surfaces. The functional relationships vary depending upon the rate limiting process. Therefore by comparing the measured particle growth with those predicted by the different rate limiting process and investigating the growth behavior as the process parameters change, it is possible to determine the most probable growth mechanism.

C. Laser Chemistry

As described in Section II.A, in a supersaturated system there exists a nucleation barrier or activation energy related to the work required to form a nucleus of critical size; this activation barrier must be overcome if a particular reaction is to proceed at a significant rate. To achieve nucleation, energy in excess of the free

energy required to form a critical size cluster must be supplied to the system. For a bimolecular reaction, both reactants must be raised to the top of the activation barrier. Each reactant may be raised independently or one may acquire the energy for both and the excess energy is transferred through molecular collisions. Certain reactions proceed on their own without the need of additional energy once the activation energy is overcome; others must be driven by heat, pressure, or catalysts.

Conventional heat sources deposit energy indiscriminately in all vibrational levels. Since any chemical reaction requires the breaking of chemical bonds and/or the creation of new ones, any energy which is not introduced at the particular energy levels (frequencies) which effect these bonds is essentially wasted. Therefore, the efficiency at which the individual reaction modes are excited is directly proportional to the efficiency at which the driving force is coupled to the reactants. One of the principal attributes of laser excitation is the ability to produce a large population of highly excited states with a low overall thermal temperature.

It is well known that electromagnetic radiation can alter the chemical properties of many substances. In 1970, Basov et al.³⁷ and Mayer et al.³⁸ discovered that chemical reactions can be selectively activated with laser radiation. Pratt³⁹ patented a method of altering the biological and chemical activity of molecular species with laser radiation. Because of the monochromatic nature of laser radiation, energy levels in the molecules which are resonance with the radiation can be selectively excited with little effect on the other levels. The high energy fluxes at a particular frequency obtainable with laser

radiation are many times more intense than the fluxes that can be obtained from conventional heat and light sources by filtering. This high intensity makes it possible to excite a large number of molecules within a brief excitation period.

Molecules absorb and emit energy only in discrete quanta. The potential energy curve for a diatomic molecule is shown in Figure II.2. The largest separation is between the electronic levels which correspond to the excitation of electrons. Within each electronic level, there are many vibrational energy states and many rotational states within each vibrational state. The absorption of a visible or ultraviolet photon results in the transition between electronic states in the molecule and may lead to dissociation.⁴⁰ Since the energy of an infrared photon is considerably less, the absorption of an infrared photon is insufficient to create a transition between electronic states. Molecules irradiated with a powerful CO₂ laser remain in the electronic ground state but their vibrational modes may become highly excited often resulting in large increases in the chemical reaction rates. Dissociation can be induced directly in the ground state by the absorption of multiple infrared photons.

It may not be necessary to excite a molecule to the energy level comparable to the activation energy to have a significant effect on the reaction rates. The rate of reaction W is generally related to the temperature and activation energy by the Arrhenius equation,

$$W = K_{\text{exp}} \exp(-E_a/kT) . \quad \text{IIC.1}$$

The absorption of a single quantum $h\nu$ will increase the reaction rate by $\exp(h\nu/kT)$ times. This can have a significant effect if

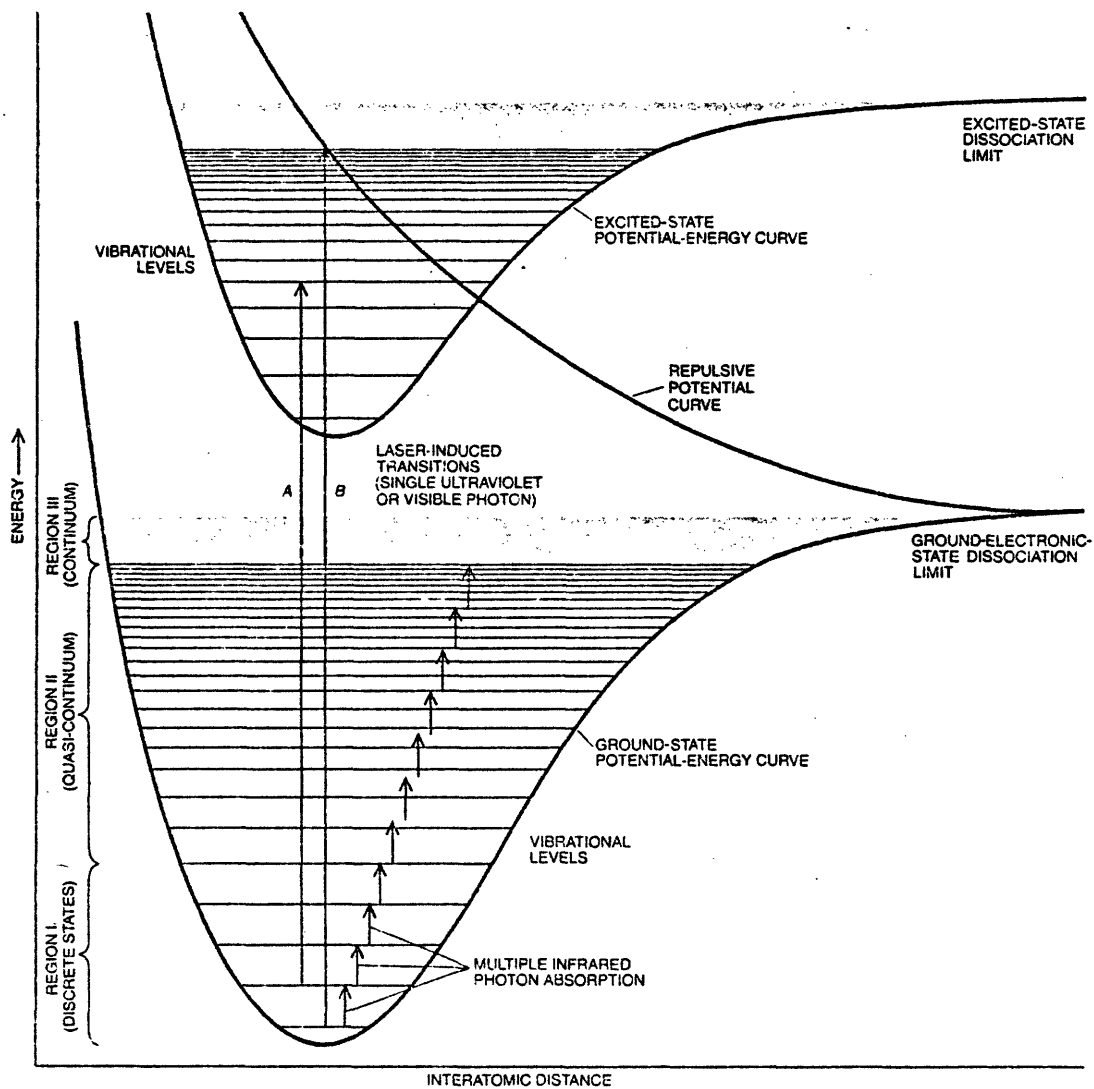


Figure II.2. Potential energy curve for a diatomic molecule.
(From Ref. 42c)

$h\nu/kT > 1$. For a $10.6 \mu\text{m}$ photon at 300K , $h\nu/kT \approx 5$; thus, the reaction rate is expected to increase by approximately two orders of magnitude if each silane molecule has absorbed only a single photon. If the increase in the reaction rate is sufficient to cause the reaction to proceed faster than the relaxation processes, the laser energy will have a direct effect on the chemical reaction. Normally, the relaxation processes within the reaction system are rapid in comparison to the rate of absorption of photons. Even in collisionless multiphoton processes, there will exist an equilibrium, Boltzmann type distribution of molecular energies in the vibrational states. Those molecules with energies in the upper tail of the Boltzmann distribution will be most active and may dissociate. Upon dissociation, equilibrium is restored by the excitation of more molecules to the high vibrational energies.

The infrared spectra of many of the vapor species of interest in the forming of ceramic powders, including SiH_4 and other silanes, have absorption bands in the range from 330 cm^{-1} ($\lambda = 30 \mu\text{m}$) to 3330 cm^{-1} ($\lambda = 3 \mu\text{m}$).⁴¹ An intense electromagnetic radiation source is required to induce vibrations and rotations with sufficient amplitudes to create either reversible or irreversible breakage of molecular bonds. Because of the availability of high powered CO_2 and CO lasers, infrared excitation of chemical reactants has received extensive study in the past ten years.⁴² If the frequencies of the vibrational and rotational absorption are in near coincidence with the frequency of the laser output, the efficiency can be extremely high. The selectivity can be improved by tuning the frequency output of the laser either by use of diffraction gratings, frequency doubling techniques and spin-flip Raman scattering.⁴³

Typically the activation energy of reactions which require stimulation are on the order of 100-380 kJ/mol (1 to 4 eV/molecule). For example the energy required for the dissociation of SiH_4 into an SiH_3 radical and a hydrogen atom has been calculated to be 318 kJ/mol (3.3 eV/molecule).⁴⁴ The allowable transition between the vibrational levels of a molecule lie in the infrared region of the spectrum with corresponding energy of the quanta less than 40 kJ/mol (0.42 eV/molecule). Hydrogen vibrations have the largest vibrational quanta. Bonds between heavier atoms yield vibrational quanta which are considerably less than 40 kJ/mol (0.42 eV/molecule). A $10.6 \mu\text{m}$ photon has an energy of $1.9 \times 10^{-20} \text{J}$ (0.12 eV). Thus for a molecule to accumulate energy comparable to the activation energy of the reaction, it must absorb multiple infrared photons. For instance, the dissociation of a single SiH_4 molecule into an SiH_3 radical and a hydrogen atom requires the absorption of approximately thirty $10.6 \mu\text{m}$ photons.

It would seem possible that the molecule could absorb a photon, the frequency of which is the same as the transition from the vibrational level $\nu = 0$ to $\nu = 1$, and then a second photon drives the molecule from level $\nu = 1$ to $\nu = 2$, and so on, until the molecule reaches energy equivalent to activation energy of the reaction. But, as shown in Figure II.2, the vibrational levels of a molecule are not precisely equidistant. The first three or four vibrational levels are discrete states and the restriction on the wavelength of photons must be strictly satisfied if absorption is to occur. The radiation which permits the transition from $\nu = 0$ to $\nu = 1$ is not exactly in resonance

with the transition from $v = 1$ to $v = 2$. Above the first few vibrational levels, the number of available states becomes increasingly larger (quasi-continuum region) and thus the restriction on the wavelength of radiation is greatly reduced.

One of the most important questions that needs to be addressed is whether a molecule while in an excited state can undergo a chemical change before the energy accumulated in the excited vibrational modes is dissipated by relaxation processes such as molecular collisions. This requires that the transition time, that is, the time required for a molecule to obtain vibrational energy in excess to the activation energy, is shorter than the time between molecular collisions. Collisionless multiphoton dissociation has been observed in such molecules as SF_6 and BCl_3 .⁴⁵ The heavy polyatomic molecules have extremely dense rotational structures providing channels to compensate for the anharmonicity between the lowest energy states.⁴⁰ The fine rotational structure within each vibrational level act to broaden the vibration band and lessen the strictness of the requirement for exact coincidence between the frequency of the incident photons and the transition between vibrational states. The light hydrogen atoms in SiH_4 molecules result in a much sparser rotational structure making it difficult to absorb multiple photons of a single wavelength; that is, the photon frequency resulting in the transition from the ground state to the higher energy level is not likely to be able to cause a resonant transition out of the excited state.

At very low pressure (< 1 torr), where relaxation by molecular collisions is relatively unimportant, the absorption line width is determined by Doppler broadening. The absorptivity will be very small

if the absorption and emission lines are more than a few Doppler widths apart. For SiH_4 , the absorption line nearest to the P(20) CO_2 laser line ($\nu = 944.19 \text{ cm}^{-1}$) is at 944.213 cm^{-1} .⁴⁶ The calculated Doppler width of this line are $2.1 \times 10^{-3} \text{ cm}^{-1}$ at 300K and $4.6 \times 10^{-3} \text{ cm}^{-1}$ at 1500K.⁴⁷ Therefore, at low pressures the absorption of a P(20) photon will be highly improbable. As the pressure increases, the width of the absorption band will broaden due to the collisions between the gas molecules. It is doubtful that unimolecular multiphoton dissociation can occur in silane with a single wavelength infrared source since broadening of the absorption band through molecular collisions is required to enable significant absorption.

Once a molecule has absorbed one or more infrared photons, there are various mechanisms through which the molecule may lose a portion or all of its excess energy:⁴⁸ 1) it may reemit a photon of the same energy as the photon absorbed, 2) it may dispose energy through collision with neighboring molecules, or 3) it may dissociate if the absorbed energy is high enough.

Deutsch⁴⁹ postulated that the relaxation process involving nearly resonant vibrational-vibrational transfer was predominant in laser irradiated silane. In vibrational-vibrational transfer, energy is transferred from an excited vibrational state in one molecule to one or more vibrational states in the less excited molecule through a molecular collision. This process continues until all energy is transferred into the rotational and translational levels of the ground vibrational state. If the time required to accumulate sufficient energy to initiate reaction is in the same time frame as the relaxation from excited states to the lower translational and rotational levels,

the reaction will be basically thermal; that is there will be a Boltzmann type distribution of vibrational, rotational, and translational energies. There will be an equilibrium concentration of molecules having energy in the high end tail of the potential distribution. These molecules are highly active and may readily dissociate. In the thermal regime, the infrared energy acts mainly as a heat source. The thermal energy supplied to the gas is then simply related to the energy output of the laser, the absorption coefficient's at the particular output line, and the heat capacity of the reactant gas mixture.

The selectivity of the monochromatic laser light will only be fully utilized if the reaction can occur fast enough so that the relaxation processes are unimportant. Even if collisions and other relaxation processes occur, the resulting thermal reaction induced by laser radiation may be quite different from a conventional reaction. The major difference is the time required to achieve total excitation. For a laser induced reaction, excitation times are on the order of a microsecond, several thousand times more rapid than those typically encountered by conventional means. These extremely short reaction times and large heating rates may result in different and unique intermediate states in the reaction pathway.

To accurately model the energy absorption process the optical absorption coefficient of SiH_4 had to be determined since the reported absorption spectra⁴⁶ were not sufficient to calculate the fraction of incident laser power absorbed by the gas stream. The absorptivity influences the gas heating rates and the overall efficiency of the synthesis process. The absorption characteristics of silane were

studied by Dr. John Haggerty's group at M.I.T., and the results are presented in Reference 5. The following discussion summarizes the key results.

All absorptivity measurements were performed in a manner which permitted analysis in terms of the Beer-Lambert equation,

$$\frac{I}{I_0} = \exp(-\alpha Px)$$

where I and I_0 are the transmitted and initial laser intensities passing through a column of absorbing gas of thickness x and at a pressure p and α is the absorption coefficient having units $(\text{cm-Pa})^{-1}$. The absorption coefficient is a sensitive function of the wavelength of the emitted light and temperature and pressure broadening effects. If a reaction is initiated during the absorption experiment, the measured absorptivity will not be representative of that of pure silane since reaction intermediates and products will have different absorptivities than silane.

A series of runs were performed with a tunable CO_2 laser to determine the absorption coefficient at a large number of emission frequencies. The laser intensity was maintained at low levels so that no significant heating of the gas occurred; therefore, the measured absorptivity was indicative of the room temperature (approximately 300K) silane absorptivity. The results⁵ are presented in Table II.1. For strong attenuation, it was necessary to decrease the sample pressure. The absorptivities inside parentheses indicate uncertainties of up to 25% in the measurement of I/I_0 . The highest silane absorption occurs for the P(20) emission from the CO_2 laser. Since the P(20) emission has the highest gain and is the predominant emission line for

Table II.1.1. Absorption Coefficients for the 10.6 μm ($00^{\circ}1-10^{\circ}0$)
Band of the CO_2 Laser

Spectral Line	Wave Length (μm)	Absorption Coefficients ($\text{atm}^{-1}\text{cm}^{-1}$)		Spectral Line	Wave Length (μm)	Absorption Coefficients ($\text{atm}^{-1}\text{cm}^{-1}$)	
		NH_3	SiH_4			NH_3	SiH_4
R(38)	10.137	.044 A	1.68 C	P(8)	10.476	.35 A	2.70 C
R(36)	10.148	not measured	.27 C	P(10)	10.494	.16 A	.50 C
R(34)	10.159	.0072A	(small) C	P(12)	10.513	.65 A	3.95 C
R(32)	10.171	.0065A	.19 C	P(14)	10.532	.83 A	1.94 C
R(30)	10.182	.047 A	.96 C	P(16)	10.551	.41 A	.96 C
R(28)	10.195	.057 A	2.68 C	P(18)	10.571	.18 A	11.8 C
R(26)	10.207	.059 A	.70 C	P(20)	10.591	.30 A	(43.0) C
R(24)	10.220	.056 A	.31 C				12.9 D
R(22)	10.233	.071 A	1.36 C	P(22)	10.611	.13 A	(28.9) C
R(20)	10.247	.12 A	1.61 C				8.17 D
R(18)	10.260	.22 B		P(24)	10.632	.16 A	(34.5) C
R(16)	10.275	7.25 B	.87 C				10.7 D
R(14)	10.289	.24 A	1.14 C	P(26)	10.653	.42 A	7.42 C
		.47 E	.79 C	P(28)	10.675	.35 A	(29.4) C
		.50 A					8.94 D
R(12)	10.304	21.5 E	.23 C	P(30)	10.696	.87 A	6.46 C
R(10)	10.319		.34 C	P(32)	10.719	13.6 E	3.79 C
R(8)	10.333		.007C	P(34)	10.741	3.5 A	5.01 C
				P(36)	10.765	1.8 E	18.1 C
				P(38)	10.788	1.02 E	1.05 C
				P(40)	10.812	1.0 A	

Conditions: A: 136 + 2 torr 10 cm cell
 B: 130 \pm 2 torr 1.7 cm cell
 C: 53 + 1 torr 1.7 cm cell

D: 11 + 1 torr 1.7 cm cell
 E: 25 \pm 1 torr 1.7 cm cell
 () denote uncertainty in precision of results

most high power, commercial CO₂ lasers, the high absorptivity at this line results in high optical to thermal efficiency.

These results correlate well with the results of Deutsch⁴⁹ who qualitatively determined the absorption characteristics of silane by measuring the infrared spectra and optoacoustic signal at different laser emissions. When the silane gas was exposed to laser radiation at a specific frequency, the vibrational energy was transferred into rotational and translational energy, thus heating the gas and creating a pressure pulse that was detected by a microphone. The energy absorbed by the gas is directly proportional to the acoustic signal produced by the gas heating.

Since the laser used for powder synthesis (Coherent Model 150 Everlase) emits almost exclusively at the P(20) line ($\lambda = 10.591 \mu\text{m}$), the absorption characteristics at this wavelength are most important. Figure II.3 shows the results of the absorption experiment measuring the effect of SiH₄ pressure on the absorptivity for a variety of energy fluences. It is evident that the silane absorptivity exhibits a strong pressure and intensity dependence; the intensity dependence is probably related to a temperature effect. The ascending then descending pressure dependence is characteristic of the pressure broadening effects for near coincident absorption and emission lines. The dashed curve represents the calculated effect of pressure broadening.⁴⁷ The deviation at higher pressures may result from a small amount of non-P(20) emission that is not strongly absorbed by the silane.

The experiments performed with the 10 mW cw (continuous wave) laser beam should result in very little heating of the SiH₄ gas. The absorption of the pulsed 90 W average and 220 W average beam is

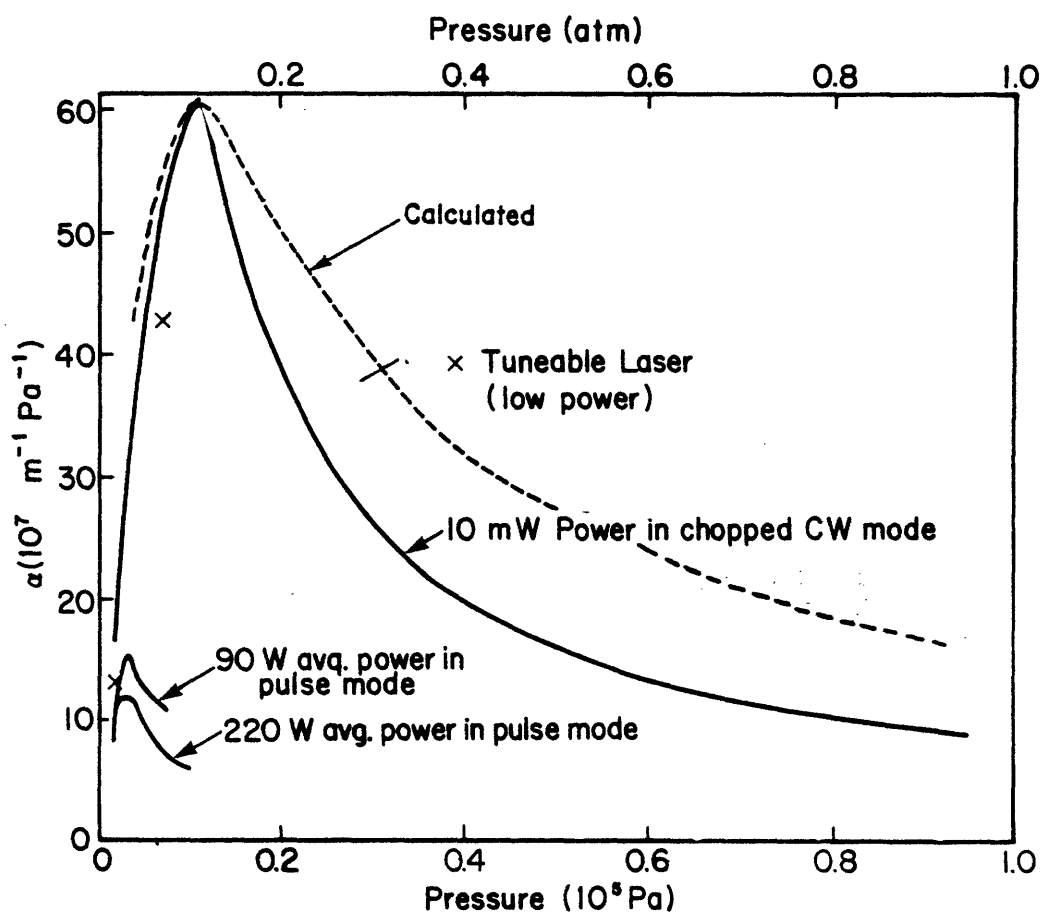


Figure II.3. Absorption coefficient of SiH_4 as a function of pressure for the P(20) CO_2 laser line.

expected to result in significant heating of the gas. The much lower absorptivity for the higher energy pulses may result from several factors. Irradiation with high laser intensities will result in the excitation of a significant number of molecules to the high energy upper tail of Boltzmann energy distribution. These molecules are highly active and may dissociate; if the reaction products have a low absorptivity, the overall absorption coefficient of the gas steam will decrease. Since only one rotational level of the ground vibrational level absorbs the laser radiation, any changes in the gas temperature will effect the number of molecules having that particular rotational energy, and therefore the absorptivity will be altered even if the silane molecules do not dissociate. Finally, whenever an infrared photon is absorbed, the molecule makes a transition into an excited vibrational level. Through molecular collisions, the molecule will soon return to the ground vibrational state. During the time which the molecule is excited, absorption will not occur unless the transition between the first and second vibrational levels is in resonance with the frequency of the infrared photon. Since the rotational structure of a SiH_4 molecule is sparsely spaced, it is not anticipated that the anharmonicity of the vibrational levels will be compensated; therefore, a decrease in absorptivity is expected.

Further experiments are necessary to determine the actual temperature effects. A careful series of experiments should be performed to determine the effect of varying the laser intensity. Also, thermally heating the silane gas and measuring the absorptivity with low energy laser irradiation should enable the separation of the pure thermal effects and the effects of vibrational excitation.

D. Particulate Synthesis from Vapor Phase Reactions

1. General

The nucleation and growth of condensed phases from supersaturated vapors has been studied extensively both theoretically and experimentally although very little of this work has involved the synthesis of ceramic particulates. Vapor synthesis processes are widely used in the pigment and particle reinforcing industries to produce fine particulates such as TiO_2 , SiO_2 , and C.⁵⁰ These processes generally involve the reaction of metal chlorides with oxygen. Recently numerous studies have shown that small equiaxed Si_3N_4 and SiC particles can be produced from the vapor phase reaction of SiH_4 and nitrogen or carbon containing gases.⁵¹ Many of the fundamentals of the nucleation and growth processes which govern the particle size, shape, and distribution are not well understood.

Much of the research involving the nucleation and growth of fine particulates in the vapor phase has been confined to metal smokes formed by evaporation in inert atmospheres. Uyeda⁵² reviews the results of approximately twenty metal and semimetal powders produced by this technique. Grangvist and Burhman⁵³ examined the nucleation and growth behavior for the condensation of Al, Mg, and Zn in argon. They concluded that the metal atoms which effused from the evaporation source are cooled through collisions with the inert gas atoms resulting in a high degree of supersaturation which leads to homogeneous nucleation. Once nucleation occurs, the growth begins initially by the

accretion of single metal vapor atoms; later stages of growth involve the coalescence of the particles. In general, it is agreed upon that nucleation occurs early in the growth process and is rapidly quenched by the reduction in the supersaturation.

Numerous investigators have reported that an increase in the evaporation temperature results in an increased particle size.⁵⁴ Yokozeki and Stein⁵⁵ have shown that the number density of nuclei decreases as the evaporation temperature is increased. The following explanation was presented. The higher temperature results in a higher metal vapor pressure and density in the vicinity of the evaporation source causing the nucleation zone to move closer to the source. The higher density of metal vapor causes the clusters just nucleated to grow faster, thereby decreasing the nucleation. This results in a lower density of nuclei and since there is a higher concentration of vapor available, the nuclei grow to larger sizes.

The most extensive investigations of the nucleation and growth of ceramic materials via vapor phase reactions have been carried out by Kato and co-workers. They have studied the formation of oxide powders such as Al_2O_3 from $\text{AlCl}_3\text{-O}_2$ ⁵⁶ and $\text{AlBr}_3\text{-O}_2$ gas mixtures,⁵⁷ SiO_2 from $\text{SiCl}_4\text{-O}_2$ ⁵⁸ and TiO_2 from $\text{TiCl}_4\text{-O}_2$ ⁵⁹ as well as a multitude of carbide and nitride powders.³

Suyama and Kato⁵⁹ described the thermodynamic factors involved in TiO_2 (anatase) formation from the reaction of TiCl_4 with O_2 . The effects of reaction temperature and gas composition on the particle size and particle size distribution were interpreted in terms of nucleation and growth mechanisms. They observed a decrease in the average particle size with increased reaction temperature and $\text{O}_2(\text{g})$

concentration but an increase as the $\text{TiCl}_4(\text{g})$ concentration increased. The average particle size was related to the relative nucleation and growth rates by

$$d \propto R_G/R_N \quad \text{IID.1}$$

with

$$R_N = K_N \exp(-E_N/RT) P_{\text{TiCl}_4}^n P_{\text{O}_2}^m \quad \text{IID.2}$$

and

$$R_G = K_G \exp(-E_G/RT) P_{\text{TiCl}_4}^p P_{\text{O}_2}^q \quad \text{IID.3}$$

where R_G is the growth rate, R_N the nucleation rate, K_N and K_G are constants, E_N and E_G are the activation energies for nucleation and growth, and P_{TiCl_4} and P_{O_2} are the partial pressures of $\text{TiCl}_4(\text{g})$ and $\text{O}_2(\text{g})$. The decrease in particle size with increasing temperature was attributed to the activation energy for nucleation being greater than that for growth. It should be noted that Suyama and Kato's analysis is only valid if the nucleation and growth processes are occurring simultaneously. If nucleation ceases early in the process and growth continues by the depletion of available vapor, the particle size is determined by the number of nuclei formed and the vapor concentration and is essentially independent of the rate at which the particles grow.

Kato, Hojo, and Okabe³ have recently reported results for the formation of various powders of refractory nitrides and carbides (TiN , ZrN , VN , Si_3N_4 , SiC , TiC , WC , and Mo_2C) from vapor phase reactions. Their results indicate that the production of fine powder requires a

high degree of supersaturation and therefore a large equilibrium constant for the vapor phase reaction. Three types of particulate formation processes were observed: 1) formation of adduct particles of the reactants which thermally decompose to form the nitride or carbide, 2) formation of nuclei of the nitride or carbide which grow by accretion of vapor phase molecules, and 3) formation of metal particles which subsequently nitride or carburize. The predominate formation process is dependent on the reaction conditions, in particular the reaction temperature; for instance, in TiN powder formation from TiCl_4 - NH_3 gas mixtures, TiCl_4 - NH_3 adduct formation was predominate at low temperatures whereas higher temperatures resulted in TiN nucleation and growth by accretion.

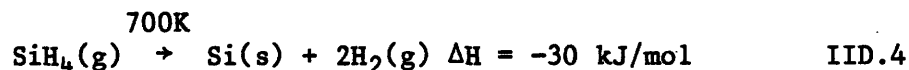
Murthy, et al.⁶⁰ studied the gas phase nucleation of silicon particles during the thermal decomposition of silane in a resistance heated tube reactor. Fine particles of silicon were observed to form during the low temperature epitaxial growth of silicon films when the silane concentration was increased. Powder formation was not observed in the epitaxial growth from the chlorosilanes. Thermodynamic calculations⁶¹ show that above 800°C monatomic silicon is formed in the gas phase during silane decomposition, whereas in the case of the chlorosilanes, free silicon cannot exist in an appreciable quantity because of the presence of chlorine.

Murthy, et al. observed that most of the silicon particles are formed at the beginning of the reactor hot zone. After nucleation, the particles grow very rapidly to macroscopic size. It was deduced that once nucleation begins, the silicon in the gas phase is rapidly depleted thereby reducing the supersaturation to a level insufficient

to support further nucleation. The particle growth was found to be limited by vapor diffusion. The average particle size increased with temperature and silane concentration although an increased reaction temperature resulted in a decreased particle number density. The particle size and number density results were not analyzed in terms of nucleation and growth theory.

2. Pyrolysis of Silane

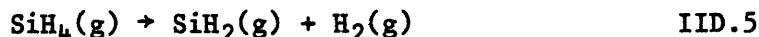
The pyrolysis of silane has been studied extensively and there is still no total agreement on the reaction mechanism. At about 700K, the pyrolysis reaction goes almost to completion. The overall reaction is



$|\Delta H|$ decreases slightly with increasing temperature. The activation energy of reaction is 234 kJ/mol and increases with increasing silane purity.⁶²

Unimolecular decomposition, i.e. the formation of only silicon and hydrogen, has been suggested by various investigators.^{62, 63} The reaction sequence may also include intermediate radicals such as silyl (SiH_2) and silylene (SiH_3). Other investigators favor a multistage chain-mechanism⁶⁴⁻⁶⁶ with intermediate products including hydrogen atoms and molecules, radicals SiH_2 and SiH_3 , disilane (Si_2H_6), trisilane (Si_3H_8) and a solid polymeric hydride $(-\text{SiH}_x-)_n$ where x varies from 0-2. A mechanism proposed by Dudorov and Zorin⁶⁷ describes a multistage process of pyrolysis which includes both homogeneous and heterogeneous reactions.

Newman et al.⁶⁸ studied the kinetics of silane decomposition in the temperature regime from 1035 to 1184K. They determined that the rate limiting step for decomposition was the silylene reaction,



with a reaction rate given by

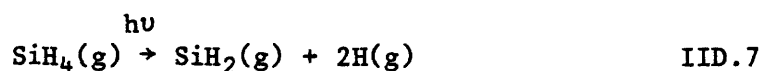
$$\log K = 13.33 - \frac{221(\text{kJ})}{2.303 RT} \quad \text{IID.6}$$

Simple bond rupture, $\text{SiH}_4(\text{g}) \rightarrow \text{SiH}_3(\text{g}) + \text{H}(\text{g})$, was considered an unlikely initial step because of its higher activation energy (390 kJ/mol). Scott et al.⁶⁹ also determined that the formation of SiH_2 in the gas phase was the rate limiting step in the homogeneous chemical vapor deposition of amorphous silicon films at gas temperatures below 650°C. They calculated an activation energy for reaction IID.5 of 226 kJ/mol.

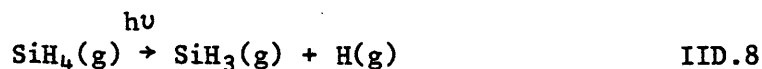
Hirose also concluded that the homogeneous reaction given by Equation IID.5 was the initial decomposition step, although he determined the adsorption of the SiH_2 radical onto the solid surface was the rate limiting step in the chemical vapor deposition of amorphous silicon in the temperature range from 500–650°C. Seto⁷¹ postulated a different mechanism for the growth of polycrystalline silicon from the chemical vapor deposition of silane in argon at temperatures between 650–800°C. He concluded that rather than a homogeneous reaction occurring in the vapor phase, deposition occurred through the adsorption and decomposition of silane and the desorption of hydrogen from the surface. This postulate was verified experimentally. Jones and Shaw⁷² argued that the adsorption of a

nonlinear SiH_2 radical is energetically favorable to the adsorption of an SiH_4 molecule. If the silane is adsorbed, it must do so with hydrogen atoms in contact with the surface. The decomposition on the surface must then involve the removal of the peripheral hydrogen atoms to bring the silicon atom into direct contact with the surface. At elevated temperatures, hydrogen atoms are highly mobile so this does not present a major barrier to deposition. In contrast, the SiH_2 radical can be incorporated directly into the solid during adsorption since the silicon atom is not sterically blocked.

There have been numerous studies involving the interaction of electromagnetic radiation with silane. In general, the mechanism for decomposition is dependent upon the reaction conditions and the type of radiation. Numerous investigations have involved the mercury sensitized decomposition of silane.⁷³ Since silane is transparent to ultra-violet up to 185 nm, mercury is added to the system to allow the absorption of the 254 nm mercury lamp radiation. Niki and Mains⁶⁴ observed both Si_2H_6 and Si_3H_8 as well as atomic hydrogen. It is believed that the decomposition occurred predominately through the formation and subsequent reaction of the monovalent silyl radical, SiH_3 . Perkins et al.⁷⁴ studied the direct photolysis of silane with 147 nm radiation. The reaction products included H_2 , Si_2H_6 , Si_3H_8 and a solid polymeric film. It was postulated that both



and



were involved in the initial decomposition process.

The infrared photochemistry of silane has also been examined. The absorption of a single infrared photon is insufficient to result in unimolecular decomposition. At the pressures and intensities required to initiate pyrolysis, there are many collisions between the gaseous molecules; therefore, a thermal reaction results. (See Section II.C.) It is expected the reaction path in this thermal reaction will be significantly different from that in the UV photolysis in which the absorption of a high energy UV photon can result in a photochemical reaction.

When silane was irradiated with a focused CO₂ P(20) laser beam (40 ns pulse length, fluences of 0.2 to 150 J/cm², average power density 5 x 10⁶ to 4 x 10⁹ W/cm²), Deutsch⁴⁹ observed a pale red luminescence. Examination of the spectral content of the luminous zone showed lines corresponding to molecular hydrogen, atomic hydrogen, possibly SiH, and a number of lines which were not identified. Mass spectrometric analysis showed the presence of SiH₂ but gave no evidence of Si₂H₆ or higher silanes suggesting the silylene reaction (Equation IID.7) is initially dominant.

Oraevskii et al.⁷⁵ examined the laser decomposition of monosilane at pressures (5 to 760 torr) and intensities (15-387 W/cm²) similar to that used in the present study. The maximum yield was 0.08%; that is, on average, the absorption of approximately 13 photons were required for the decomposition of one silane molecule. Quantitative mass spectrometric analysis revealed that molecular hydrogen was the main gaseous product. The absence of the higher silane molecules suggested that decomposition occurred via a unimolecular process.

Bilenchi and Musci⁷⁶ reported on the CO₂ laser enhanced chemical vapor decomposition of amorphous silicon onto heated substrates (220 to 400°C). From mass spectrometric analysis, in which SiH₂, SiH₃ and molecular hydrogen were observed, it was concluded that the dissociation occurred predominately in the vapor phase. There was no evidence of Si₂H₆ or higher silanes. When the pressure of silane was increased above 10 torr, nucleation and growth of powder resulted within the vapor.

In summary, the mechanism for the pyrolysis of SiH₄ is not conclusively known. Different reaction paths have been observed and postulated for different reaction conditions. In all the studies involving the infrared laser induced pyrolysis of silane, there was no evidence of higher silanes. Therefore when particulates are produced within the vapor phase, they do not form by the polymerization of chain-like adducts of the type $(-\text{SiH}_x-)_n$; rather, their formation occurs via nucleation and growth processes. It is not known which chemical species participate in the nucleation process. Bilenchi and Musci⁷⁶ concluded that when the concentration of free radicals becomes large they condense in the vapor phase to form powder. In the study by Oraevskii et al.,⁷⁵ quantitative mass spectrometric analysis showed no evidence of radical formation suggesting unimolecular decomposition was predominate and that powder was produced through classical nucleation involving the clustering of silicon vapor atoms.

3. Particulate Crystallinity

Most of the work regarding the crystallinity of solids synthesized from vapor phase reactions appears in the chemical vapor deposition

literature. Depending upon the reaction conditions the resulting product can be amorphous, polycrystalline, or single crystalline. Kirkorian and Sneed⁷⁷ performed an extensive study of the nucleation, growth, and transformation of amorphous and crystalline germanium condensing from the vapor phase. In general, it was observed the structure of the deposited film was related to the deposition conditions, i.e. the deposition temperature and growth rate, by a simple structural phase diagram illustrated in Figure II.4. The polycrystalline to single crystal transition is both temperature and rate dependent. The transition from the amorphous to the polycrystalline state was found to be independent of the growth rate. This is in contradiction to work of Bloem⁷⁸ who found the growth rate had a large effect on the formation of amorphous silicon deposited from silane. Amorphous formation was favored at high deposition rates since the rate at which atoms arrived at the surface was much faster than the rate of atom diffusion to surface sites favorable for crystalline formation.

Depending upon the reaction temperature, the formation of the solid phase can involve amorphous, crystalline, or both amorphous and crystalline nucleation. The structure of the final deposit is dependent on the type of nucleation and the time in which growth occurs after the film is nucleated. At very low temperatures, deposition and subsequent growth will result exclusively in an amorphous film. Amorphous growth occurs by the adsorption of individual atoms or molecules onto the surface. At somewhat higher temperatures both crystalline and amorphous nucleation can occur. If the temperature is

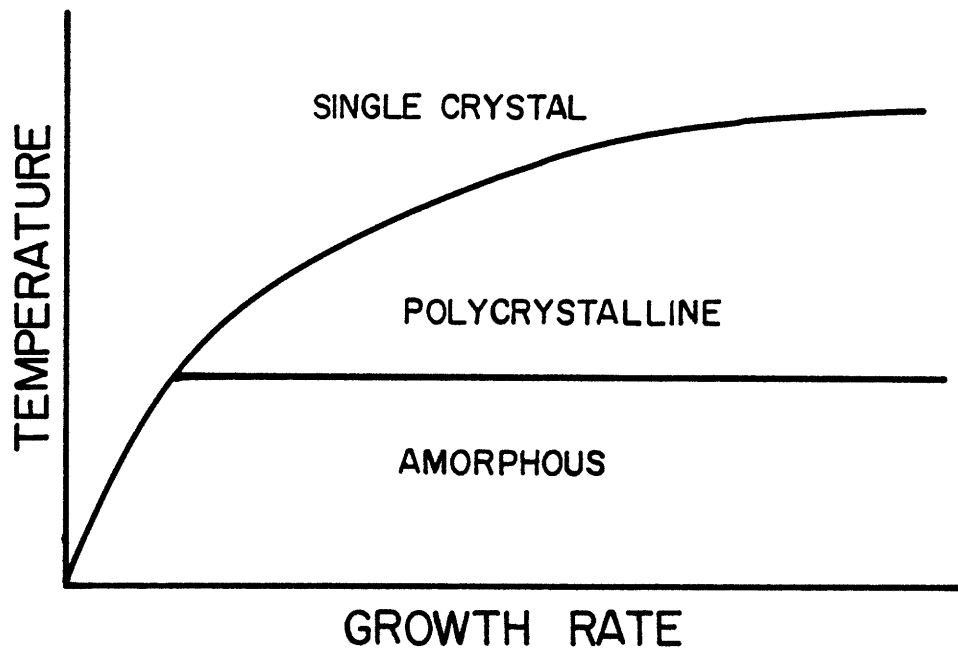


Figure II.4. Structural phase diagram for a solid deposited from the vapor phase.

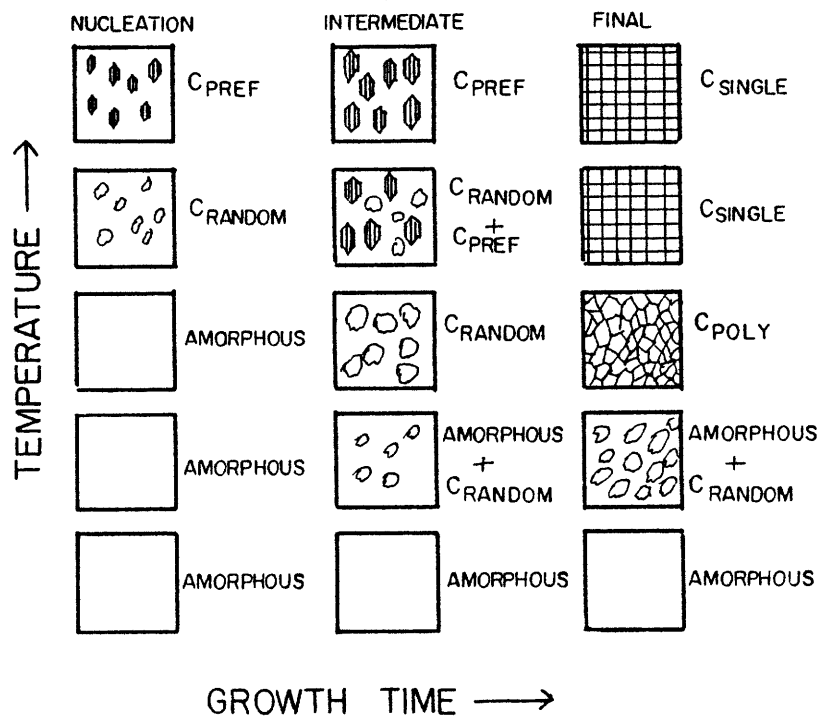


Figure II.5. Microstructural development as a function of vapor deposition conditions. C_{SINGLE} = Single crystalline, C_{POLY} = Polycrystalline, C_{PREF} = Preferentially oriented crystallites, C_{RANDOM} = Randomly oriented crystallites.

initially low and only amorphous nucleation occurs, the solid can crystallize during further growth. If the growth time is insufficient to produce a fully crystalline material, the final film will consist of both amorphous and crystalline regions. As shown in Figure II.4, if the temperature is very high the film will consist of a single crystal. Figure II.5 summarizes the types of structures that can evolve with different conditions.

The crystallinity of CVD silicon films has been studied extensively from two standpoints: 1) the conditions that determine whether the as-deposited film will be amorphous or crystalline and 2) the annealing conditions required to crystallize an amorphous as-deposited film. Bloem and Clausen⁷⁹ determined that the structure of a silicon deposit grown on a single crystalline silicon substrate was polycrystalline for deposition temperatures below approximately 1000°C and single crystalline at higher temperatures. The grain size of the polycrystalline deposit decreased as the deposition temperature decreased. At temperatures below 700°C, amorphous silicon was produced. The transition temperatures between single crystalline to polycrystalline and polycrystalline to amorphous growth was dependent on the growth rate and pressure; the crystal perfection improved with both decreased growth rate and pressure. At deposition temperatures of 700°C, Popova et al.⁸⁰ found that all films chemically deposited from silane were polycrystalline; the type of substrate used (Si, SiO₂ or Si₃N₄) had no effect on the nature of the crystal structure. Bustarret et al.⁸¹ used Raman spectroscopy to examine the structure of films deposited from silane on substrates heated from 550 to 750°C.

Only in films grown at temperatures above 650–680°C was any crystallinity observed by this technique.

The crystallization of amorphous silicon has been reported to occur in the 450 to 700°C temperature range. Koster and Weiss⁸² showed that the crystallization occurs by nucleation and growth processes. From an in situ electron microscopy study, Drosd and Washburn⁸³ concluded that nucleation of the crystalline phase is a difficult process; once a crystalline region is formed, further crystallization will occur entirely by the migration of the amorphous-crystalline interface rather than the nucleation of new crystallites. The deposition conditions, particularly the substrate temperature, were found to effect the post synthesis crystallization characteristics. The crystalline nucleation temperature was generally lower for films deposited at higher temperatures, since these films were already partially crystalline.

III. EXPERIMENTAL

A. Powder Synthesis

The powder synthesis cell is shown in Figure III.1. A cross-flow configuration is used in which a laser beam having a Gaussian shaped intensity profile orthogonally intersects the reactant gas stream possessing a parabolic velocity profile. The laser beam enters and leaves the cell through KCl windows. The unfocused beam diameter is approximately 6 mm. For one synthesis run, the intensity was increased by focusing the beam to a diameter of 2 mm using a 13 cm focal length lens. The silane reactant gas, under some conditions diluted with argon, enters through a 1.5 mm ID stainless steel nozzle located 6 mm from the beam center. A coaxial stream of argon is used to keep the particles entrained in the gas stream. The argon annular flow is introduced through an inlet tube with a diameter much smaller than the annular sleeve. To improve the uniformity of the argon flow, an aluminum insert, approximately 4 cm long, comprised of hexagonal cross section tubes was positioned inside the annular sleeve. Argon is also passed across the inlet KCl window to prevent powder buildup and possible window breakage. Synthesis cell pressures are maintained between 2×10^4 to 1×10^5 Pa (0.2 to 1.0 atm) with a pressure controller[#] located between a mechanical pump and the reaction cell.

The reactant gas is electronic grade SiH_4 . Prepurified argon (10-15 ppm O_2) is used as the carrier gas and optical dilutant.

[#]MKS Model 250A

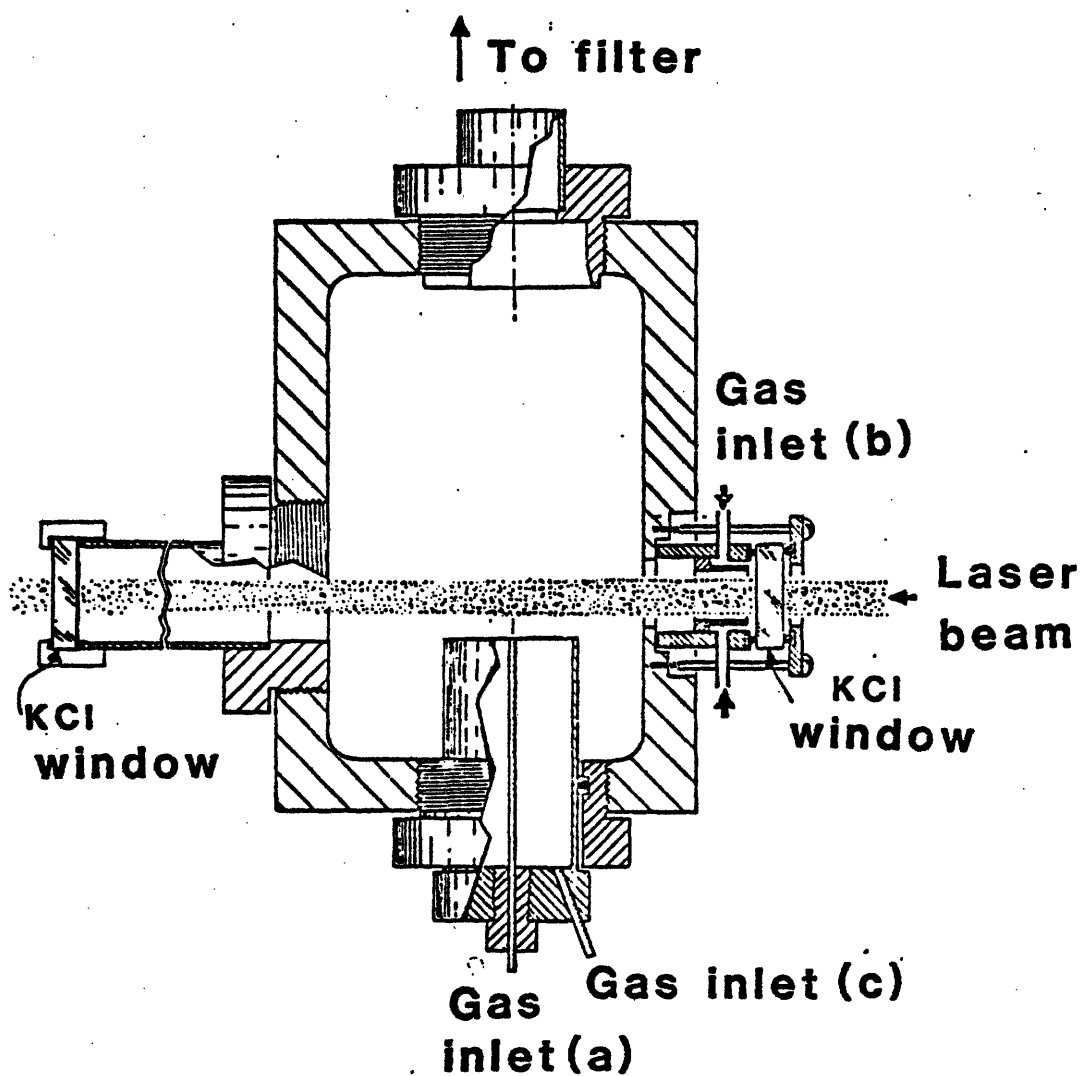


Figure III.1. Schematic of powder synthesis cell.

The exit KCl window allows measurement of the exiting beam power during a synthesis run. Under normal process conditions only about 10-15% of the laser energy is absorbed during the SiH_4 decomposition reaction. In this experimental configuration, the reactant gas stream was purposely made optically thin to insure uniform thermal histories and simplify analyses. A production scale-up would require different optics to avoid wasting 85-90% of the light energy.

Depending on the process conditions, powder is synthesized at a rate of 1 to 10 grams per hour. The powders produced in the reaction zone are carried to a microfiber filter by the product and argon gases. To facilitate collection, a 9 cm long, 2 cm ID glass tube was inserted into the cell outlet tube, forming a confined path from a position directly above the laser beam to the filter. Virtually all of the powder is collected in the filter. Up to 10 grams of powder can be collected before the filter fills and it is no longer possible to maintain a constant cell pressure.

The reaction variables will effect the nucleation and growth kinetics and thus the resulting powder characteristics. With this in mind, the process variables were manipulated to determine the effect on the reaction zone and particle characteristics. The synthesis runs and their respective process conditions are listed in Appendix 1. Three series of runs at total cell pressure of 2×10^4 , 3.5×10^4 , and 6×10^4 Pa (0.2, 0.35, and 0.6 atm) were performed to determined the effect of the reactant gas velocity.

In investigating the effect of reaction cell pressure it is difficult to make a run-to-run comparison since constant flow conditions are not easily maintained while changing the total cell

pressure. Therefore the effect of cell pressure was examined by comparing the series of runs produced at 2×10^4 Pa (0.2 atm) and 6×10^4 Pa (0.6 atm). The runs performed at 3.5×10^4 Pa (0.35 atm) utilized an unfocused 170 W laser beam while an unfocused 150 W beam was used for the runs synthesized at 2×10^4 and 6×10^4 Pa (0.2 and 0.6 atm). It will be shown that the reaction zone and powder characteristics are highly dependent on the beam power. Therefore, it is inaccurate to compare the series of runs produced at 3.5×10^4 Pa (0.35 atm) with the other runs.

The effect of laser intensity on the reaction zone and particle characteristics was studied. All runs were performed with identical conditions except the laser intensity was varied from 134 W/cm^2 to 601 W/cm^2 . In run 645S, a 170 W laser beam was focused to a diameter of 0.2 cm giving an average intensity of 5410 W/cm^2 .

In one series of runs, the reactant gas stream was diluted with argon. The argon was introduced to the silane before the gases entered the cell. The Ar/SiH₄ molar ratio was varied from 0/1 to 5/1.

It has been reported that the addition of small amounts of boron increases the sinterability of silicon.⁸⁴ It is difficult to add amounts typically less than 0.5 wt.% in the solid state and achieve a uniform dopant distribution. The laser synthesis process offers a unique method to add the dopant. A gas species containing the dopant is added directly to the reactant gas stream. Since this process is in the thermal domain, it is not necessary for the dopant gas to absorb the laser energy. The dopant can be uniformly distributed throughout the powder and can be incorporated directly into the silicon particles.

Diborane, B_2H_6 , was used as the boron source. Because of the toxicity of this gas, a 1.0% B_2H_6 + 99.0% Ar mixture was used. The run conditions are shown in Appendix 1. To determine if the diborane had any effect on the reaction or powder characteristics, runs were made with identical run conditions except pure Ar was used instead of the 1.0% B_2H_6 + 99.0% Ar mixture. If the dopant is fully incorporated, a 2/1 SiH_4 to (1.0% B_2H_6 + 99.0% Ar) mixture will result in a silicon powder containing a 0.38 wt.% boron. The powders synthesized by these runs were used for sintering and nitriding experiments.⁵ Numerous doped and undoped runs were performed. The results of these runs were used to determine the reproducibility of this process.

B. Analysis of the Reaction Zone

1. Reaction Temperature

a. Possible Measurement Techniques

In contrast to most synthesis techniques, the reaction temperature in the laser powder process is not an extrinsically manipulable parameter but is dependent on process variables such as laser intensity, flow velocity, reactant gas composition and pressure. The temperature within the reaction zone determines the thermodynamic driving forces and vapor phase reaction kinetics, nucleation and growth rates, and particle crystallinity. Therefore, it is important to accurately measure the reaction temperature.

Various methods have been used to measure the temperature of flames containing hot particles. These include the use of a thermocouple, measurement of the relative emittance as a function of wavelength, and optical pyrometry.

It was found⁸⁵ that placing a thermocouple into the laser synthesis flame gave an inaccurate measure of the reaction temperature since solid particles collected on the thermocouple bead. Also since the thermocouple will absorb the CO₂ laser radiation, it is not possible to measure the reaction temperature within the beam path.

The temperature of a radiating body is related to the intensity of emitted radiation at a particular wavelength and can be described by Wein's approximation to Plank's law⁸⁶

$$I_{\lambda} = \frac{C_1 \epsilon_{\lambda} \exp(-C_2/\lambda T)}{\lambda^5} d\lambda d\Omega \quad \text{IIIB.1}$$

where I_{λ} and ϵ_{λ} are the intensity and emissivity at wavelength λ , C_1 and C_2 are radiation constants, and $d\lambda$ and $d\Omega$ are the wavelength and solid angle intervals of the detector. If the emissivity is independent of wavelength, the temperature can be calculated from the slope of the plot $\ln I_{\lambda} \lambda^5$ versus $1/\lambda$. If the emissivity is dependent on wavelength, it is not necessary to know the absolute emissivity, but the functional dependence must be determined before temperature can be calculated.

The emissivity is expected to vary with temperature, and particle density, size, and chemistry.⁸⁷ The silicon emissivity results reported in the literature are not sufficient to establish a reliable functional dependence. Therefore, before this technique can be

utilized to provide accurate temperature measurements, a study of the emissivity of the reaction zone is required.

Optical pyrometry measures the radiance at a single wavelength by superimposing the field of view on a heated filament. The brightness temperature S , which assumes an emissivity of 1.0, is determined when the radiating body and filament have the same intensity. The true temperature T is related to the brightness temperature by the relation⁸⁶

$$\frac{1}{T} = \frac{1}{S} + \frac{\lambda \ln \epsilon_{\lambda}}{C_2} \quad \text{IIIB.2}$$

A micropyrometer images a small area of the radiating body on the filament. The absolute emissivity of the same area must be determined before the true temperature can be calculated.

The emissivity of a cloud of particles can be represented by⁸⁸

$$\epsilon = (1 - \tau) \left(\frac{C_{\text{ABS}}}{C_{\text{EXT}}} \right) \quad \text{IIIB.3}$$

where τ is transmittance and C_{ABS} and C_{EXT} are the absorption and scattering cross sections respectively. The transmittance is the fraction of light which having entered the cloud of particles reaches the further boundary and is related to the extinction cross section by the Beer-Lambert relation:

$$\tau = I/I_0 = \exp(-NC_{\text{EXT}}\ell) \quad \text{IIIB.4}$$

where I is the transmitted intensity, I_0 is the incident intensity, N is the particle density, and ℓ is the width of the particle cloud. The extinction cross section is related to the scattering cross section and the absorption cross section by

$$C_{EXT} = C_{ABS} + C_{SCA} \quad \text{IIIB.5}$$

The emissivity is related to the transmission of light through the flame and the scattering to extinction ratio:

$$\epsilon = (1 - I/I_0) (1 - C_{SCA}/C_{EXT}) \quad \text{IIIB.6}$$

Therefore, the temperature of a particular region in the flame can be accurately calculated from the brightness temperature measured by micropyrometry if the emissivity of the same region is determined from transmission and scattering measurements.

b. Experimental Procedure

A technique described by Flint⁸⁹ was used to measure the reaction zone temperature. It involved the measurement of a particular region of the reaction zone with a micro optical pyrometer. The extinction and scattering of the same region were measured simultaneously.

The experimental apparatus used for the scatter/extinction measurement is shown schematically in Figure III.2. A 5 milliwatt, vertically polarized HeNe laser ($\lambda = 632.8 \text{ nm}$) was mounted on an x-y micrometer stand. This enabled the temperature distribution within the reaction zone to be measured. The transmitted HeNe laser light was measured with a silicon photodiode. The intensity of the scattered HeNe light was detected with a photomultiplier.

A vertically polarizing filter, aperture, and a neutral density (optical density = 2) filter were placed between the reaction cell and the photomultiplier. The aperture defined the solid angle (2.2×10^{-4} steradians) viewed by the photomultiplier. The neutral density filter

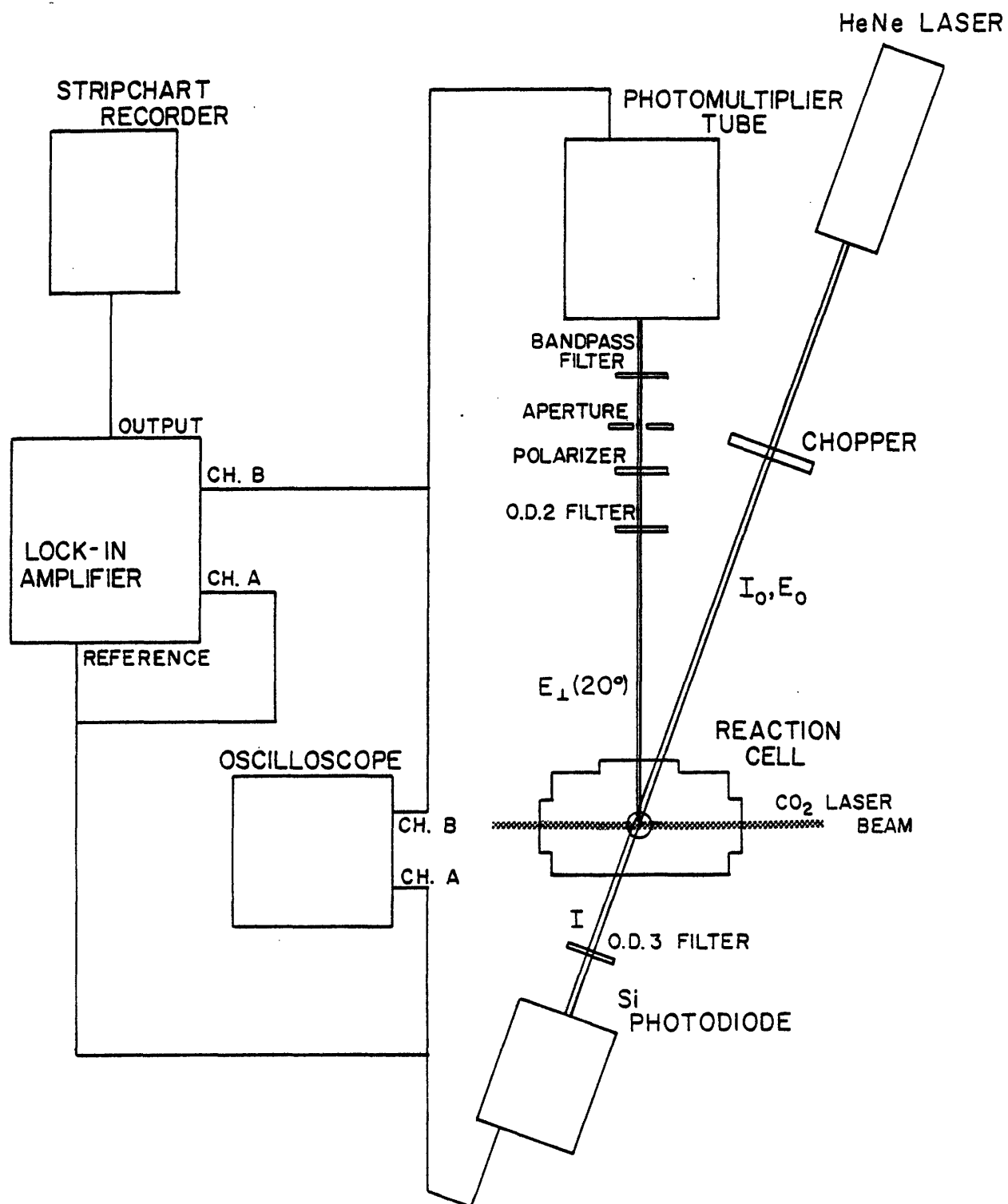


Figure III.2. Schematic of optical layout for measuring scattering and extinction in the reaction zone.

insured the photomultiplier was operating in the linear range. The angle between the incident light and the photomultiplier was 20° .

A 632.8 nm bandpass filter located in front of the photomultiplier eliminated most of the thermal emission from the flame. To further eliminate the effect of the thermal emission, the HeNe laser beam was chopped at approximately 200 hz before it entered the reaction cell. The output from the silicon photodiode was connected to the non-inverting and reference inputs of a lock-in amplifier. The photomultiplier signal was connected to the inverting input of the lock-in amplifier. Therefore only the transmitted and scattered light in synchronism with the chopped HeNe light was measured.

The temperature distribution directly above the reactant inlet nozzle was measured by the following procedure. The HeNe laser light was adjusted to the appropriate position in the flame. The photodiode was translated to give the maximum signal. The RMS transmitted and scattered intensities were measured. The micro optical pyrometer was focused on the scattered HeNe light. The HeNe beam was blocked and the brightness temperature of the region was determined.

The true temperature was then calculated from Equations IIIB.2 and IIIB.6. This required that the determination of the ratio of scatter to extinction cross sections from the experimental results. The Lorenz-Mie scattering theory⁹⁰ can be applied to the scattering from a particulate cloud if the following conditions are satisfied: 1) each particle scatters independently, 2) the particles are randomly distributed, and 3) there is no multiple scattering.

Condition 1 requires the particles be separated by at least three radii and are not agglomerated. The results shown in Section IV.B

indicate this restriction was satisfied. Condition 2 is valid for most systems. Condition 3 requires the turbidity (NC_{EXT}^{λ}) of the particulate cloud to be less than 0.1. For most silicon synthesis reaction zones this was not fulfilled. The major effect of a turbid flame is to decrease the scattered signal since both the incident beam and scattered light from the interior of the flame are attenuated. Following Flint,⁸⁹ the measured power scattered was multiplied by $\frac{1 - (I/I_0)^2}{2 \ln (I/I_0)}$ to account for this effect.

A computer program⁹¹ was used to calculate the ratio of the scatter to extinction cross sections from Lorenze-Mie scattering theory.⁹⁰ The cross sections are dependent on the particle radius, index of refraction, and wavelength of light. In the vicinity of the wavelength of HeNe laser light, the optical properties of silicon are strongly dependent on wavelength, temperature, and degree of crystallinity. Therefore various reported⁹² values for the real and complex indices of refraction were used in the calculations. An index of $m = 4.1 - 0.113i$ is appropriate for polycrystalline silicon at 500°C and $m = 4.38 - 0.99i$ for amorphous silicon at 500°C. An extrapolated value of $m = 4.38 - 0.26i$ should be valid for polycrystalline silicon around 1100°C or for a mixture of polycrystalline and amorphous material at a lower temperature.⁸⁹

Figure III.3 shows a plot of the ratio of the scatter to extinction cross sections as a function of the measured scatter to extinction ratio. If the particles are small, that is approaching the Rayleigh scattering regime, the scatter to extinction ratio is independent of the refractive index.⁹⁰ This is an important property,

since it enables accurate calculation of the scatter to extinction ratio and thus the particulate cloud emissivity and temperature regardless of the powder chemistry or crystallinity.

The temperature distribution in the reaction zone was measured for a wide range of process conditions. The results are presented and discussed in Section IV.A. In all cases, it was determined that the scatter to extinction ratio of the hottest region in the reaction zone was less than 0.3. Therefore, it was concluded that the temperature could be determined to within at least 50°C by measuring only the transmission through this portion of the reaction zone. The brightness temperature of the hottest portion of the "flame" and the transmission at that position was measured for runs listed in Appendix 1.

2. In Situ Nucleation and Growth Measurements

The inception of the nucleation events and the growth process can be monitored directly with respect to the position in the reaction zone. These observations were made using the scatter extinction method described in the previous section.

The experimental scatter to extinction ratio was determined at a particular position in the reaction "flame". Using Lorenz-Mie theory,⁹⁰ the experimental scatter to extinction ratio can be related to the various cross sections, ratio of the cross sections, and particle radius. It is assumed the particles are spherical and monodispersed.

The Mie scattering function and cross sections are dependent on the index of refraction and size of the particles, the wavelength and

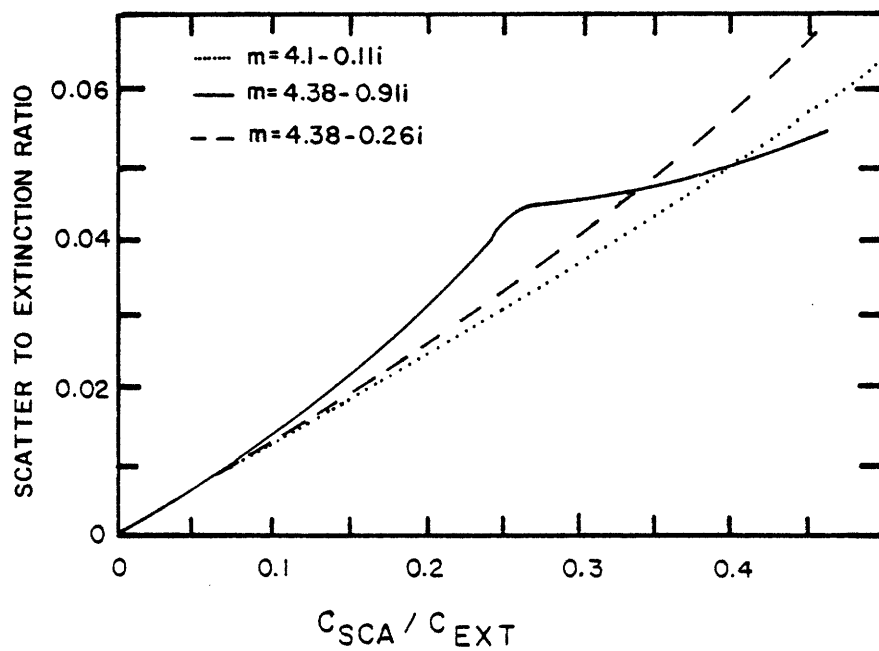


Figure III.3. Ratio of the scattered to extinction cross sections versus the measured scattered to extinction ratio for various refractive indices.

polarization of the incident light, and the polarization and direction of the scattered radiation. In this experimental setup, both the incident and scattered radiation are polarized orthogonal to the scattering plane with a scattering angle of 20°. The computer program⁹¹ calculates the scattering and extinction cross sections and the ratio of the scattering to extinction cross sections as a function of particle size and refractive index, and wavelength of incident light.

A plot of the ratio of the scattering to extinction cross sections as a function of the measured scatter to extinction ratio was presented in Figure III.3 of the previous section. In Figure III.4, the measured scatter to extinction ratio is plotted as a function of particle radius for three different silicon refractive indices. At a particular particle radius, the scatter to extinction ratio is largely dependent upon the value of the refractive index used.

The particle number density was calculated from the Beer-Lambert relation:

$$N = \frac{\ln I/I_0}{\lambda C_{EXT}} \quad \text{IIIB.7}$$

The calculated extinction cross section is plotted in Figure III.5 as a function of the measured scatter to extinction ratio for the three values of the silicon refractive index. To actually calculate the number density the path length through the reaction zone must be known. Since the path length is difficult to measure, the product of the number density and the reactant path length was calculated. If the

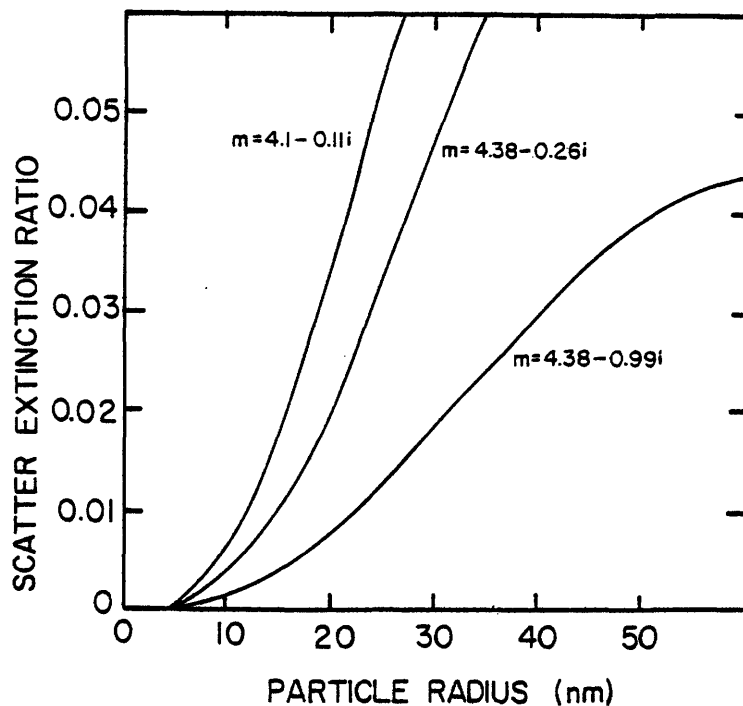


Figure III.4. Measured scattered to extinction ratio as a function of particle radius for various values of the particle refractive index.

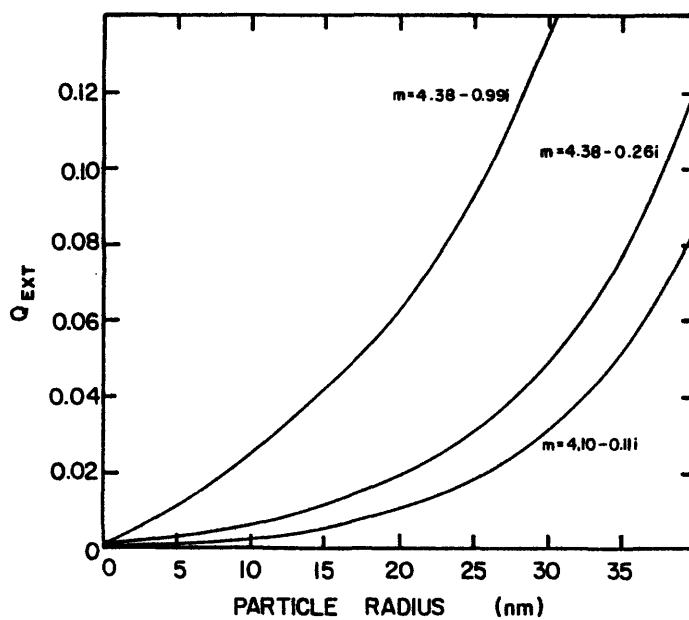


Figure III.5. Extinction efficiency as a function of particle radius for various values of the particle refractive index.

path length is assumed constant, the number density as a function of position could be inferred.

C. Powder Characterization

A number of powder characterization techniques have been employed to determine the physical, chemical, and crystalline character of the powders. A mass balance was performed to determine the process efficiency.

The particle and crystallite size has been measured using TEM, STEM, and X-ray line broadening. The surface area of selected powders was measured by the multipoint BET method. Since it was found that the value of the BET constant C was sufficiently large, a single point BET analysis could be used to better than 95% accuracy. The techniques used by X-ray line broadening and BET surface area measurements are discussed in more detail in Appendix C. The powder density was measured by He pycnometry.

Chemical analyses were performed on the powders using neutron activation for O, wet chemical analysis for Si, H, and O, and emission spectrographic analysis for other elements. The crystalline characteristics, both crystal structure and crystal size, of the powders were evaluated using powder diffractometry, electron diffraction, and dark field microscopy. The degree of agglomeration was examined by TEM.

IV. RESULTS AND DISCUSSION

A. Temperature Measurements

1. Temperature Distribution

The temperature distribution within the flame was measured by the technique described in Section IIIB for a variety of process conditions. The process conditions are listed in Appendix 1. Figure IV.1 shows the measured scattered and transmitted intensities for Run 631S as a function of position above the reactant gas nozzle. Also shown in this figure is the calculated ratio of the scatter to extinction cross-sections. As a spatial reference, the position of the laser beam is indicated.

In general, the results illustrated in Figure IV.1 are representative of all temperature distribution runs. Both the scattered power and the ratio of the scatter to extinction cross sections increased with distance above the nozzle and approached a constant value. The transmission decreased steadily until a constant value was achieved. There were no abrupt changes in any of the measured and calculated values.

Figure IV.2 shows the emissivity, brightness temperature, and true temperature for Run 631S. It is evident that the reaction was well underway before the reactants reached the CO₂ laser beam. The temperature increased rapidly and achieved a maximum before the reactants and products reached the beam center. The temperature decreased as the particles travelled further from the nozzle. The

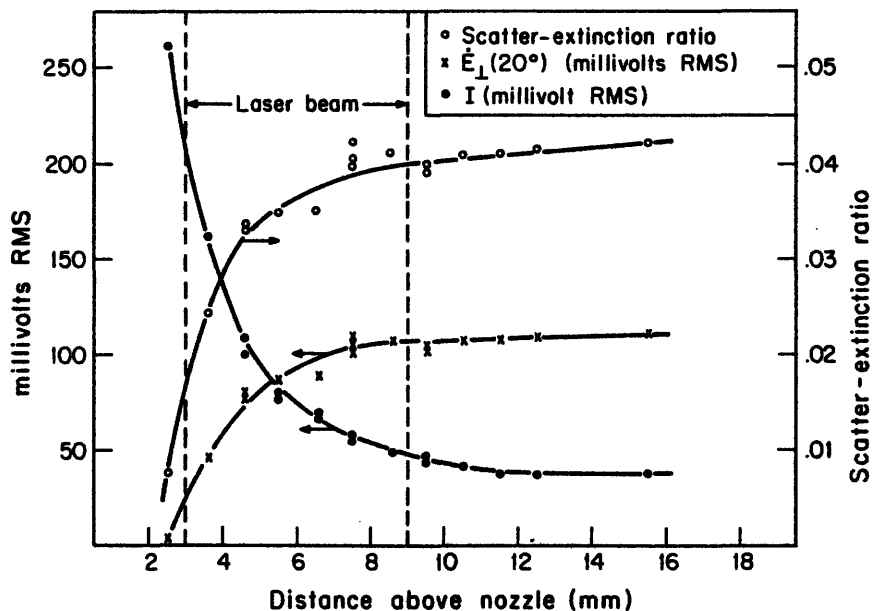


Figure IV.1. Measured scattered and transmitted intensities and scatter to extinction ratio as a function of distance above the inlet nozzle. (Run 631S)

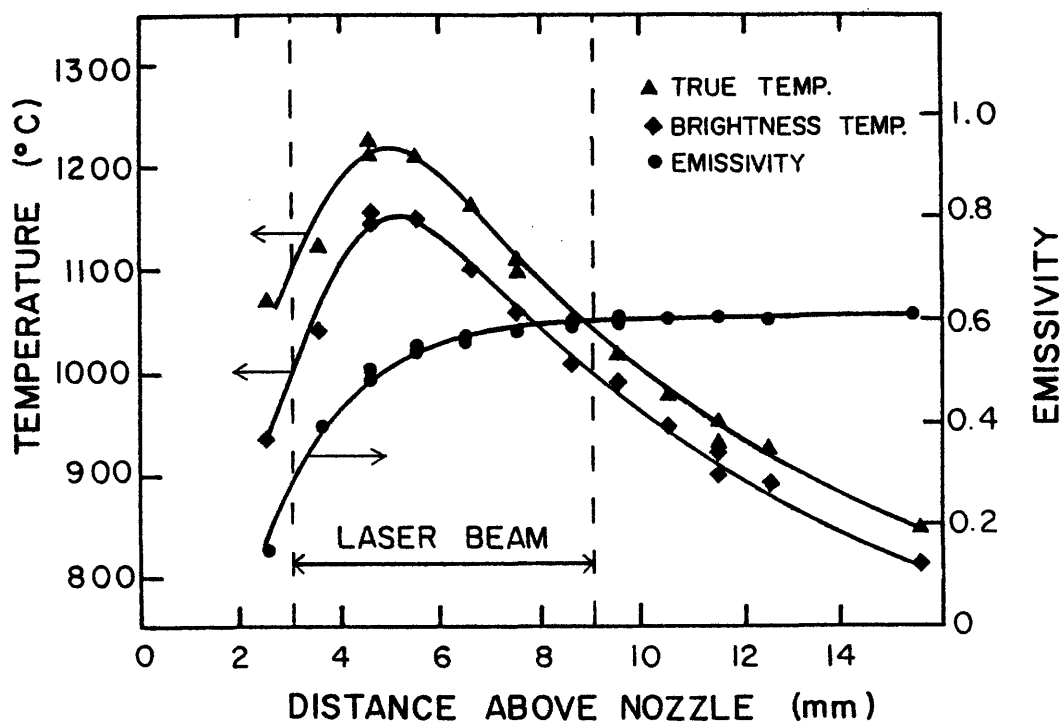


Figure IV.2. True temperature, brightness temperature, and emissivity as a function of distance above the inlet nozzle. (Run 631S)

measured temperature of the particles in the upper region of the "flame" may be somewhat higher than the actual temperature since some of the light emitted from the hottest region of the reaction zone is scattered by these particles.

Figures IV.3 shows the temperature profiles for other runs listed in Appendix 1. Diluting the reactant stream with argon (Run 631S, Ar/SiH₄ = 0/1; Run 654S, Ar/SiH₄ = 2/1; Run 634S, Ar/SiH₄ = 5/1) decreased the reactant temperature and shifted the peak temperature toward the laser beam center. An increase in total cell pressure (Run 631S, 0.2 atm; Run 650S, 0.6 atm) resulted in an increased peak temperature, a faster initial heating rate, and a broader temperature profile. The effect of the scattering of the light emitted from the particles in the hottest region of the "flame" may partially account for the broad temperature profile. An increase in the reactant gas flow rate (Run 631S, 38 cm³/min SiH₄; 630S, 104 cm³/min SiH₄) resulted in a decreased reaction temperature, and the reaction was initiated further into the laser beam.

From the results shown in Figures IV.2 and IV.3, it is evident that under certain conditions the reaction was initiated before the gases reach the laser beam. Two mechanisms by which the reactant gases may be heated prior to direct interaction with the laser radiation are thermal conduction and radiation from the hot region of the reaction zone. If the reactant gas velocity is greater than the velocity of heat transfer back to the reactant gas nozzle, the effect of thermal conduction will not be important. For slower SiH₄ flow velocities, it is possible for the reactant gas to be heated below the laser beam. It was determined that the scattering of the CO₂ laser light by the

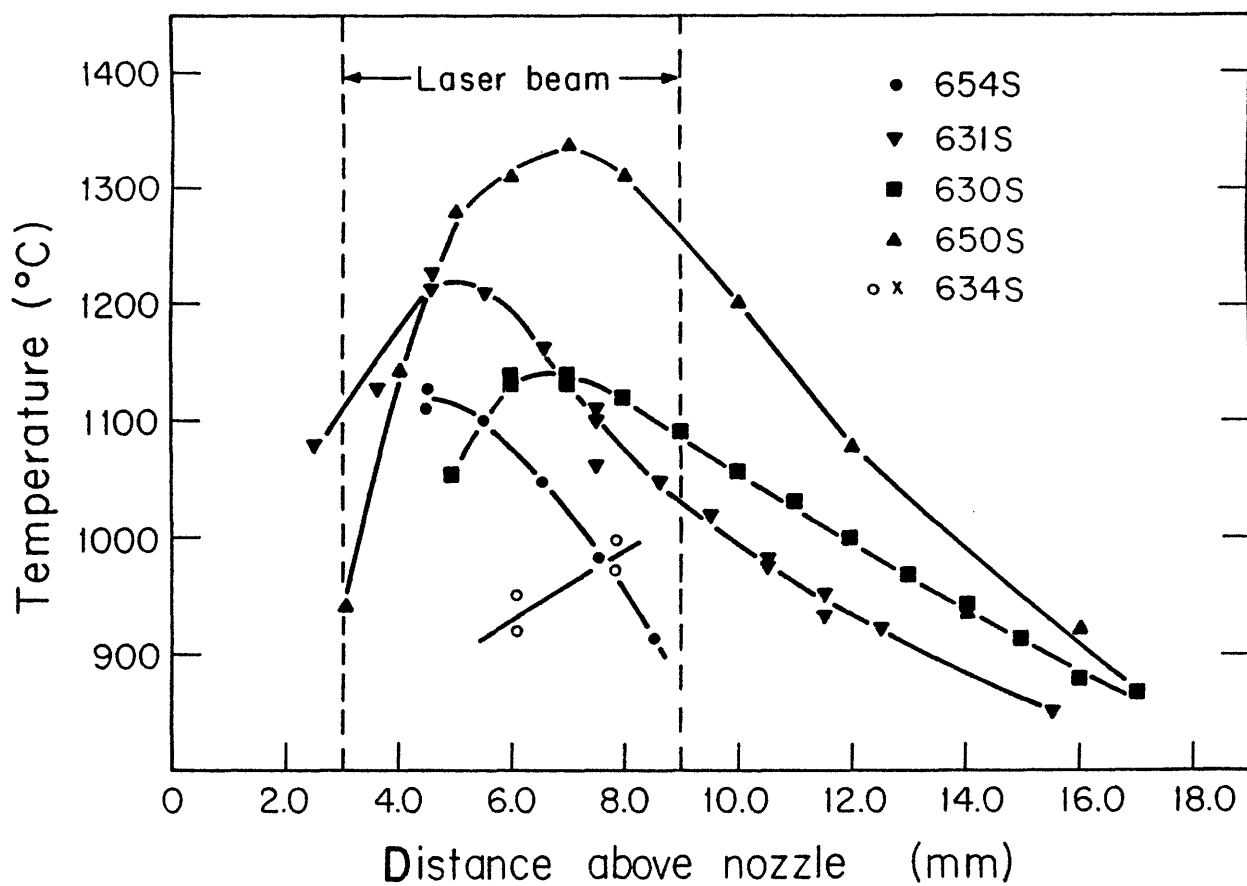


Figure IV.3. True temperature as a function of distance above the inlet nozzle for various synthesis runs.

particles within the beam path and the absorption of this light by the SiH_4 molecules below the beam contributed little to the heating of the gas.⁸⁹

The particle temperature begins to decrease while the particles are still in the laser beam. There is no apparent correlation between the particle temperature and the laser intensity distribution. This suggests the silicon particles are not strongly heated by the CO_2 laser beam; this is expected since the $10.6 \mu\text{m}$ absorption efficiency for a silicon particle with a diameter of about 50 nm is quite low.

2. The Effect of Process Parameters on the Maximum Temperature

For the entire range of synthesis conditions examined by the scatter/extinction method, it was found that in the hottest portion of the reaction zone the ratio of the scatter to extinction cross sections was never greater than 0.3. Therefore, it was decided that the reaction temperature of the hottest region in the flame could be calculated with sufficient accuracy by only measuring the brightness temperature and transmittance of that volume. Bounds on the true temperature were determined by assuming the ratio of scatter to extinction cross sections was either 0.0 or 0.3.

A series of temperature measurements was performed to determine the maximum temperature for each set of the synthesis conditions shown in Appendix 1. The results are summarized in Appendix 1 and Figures IV.4 to IV.8.

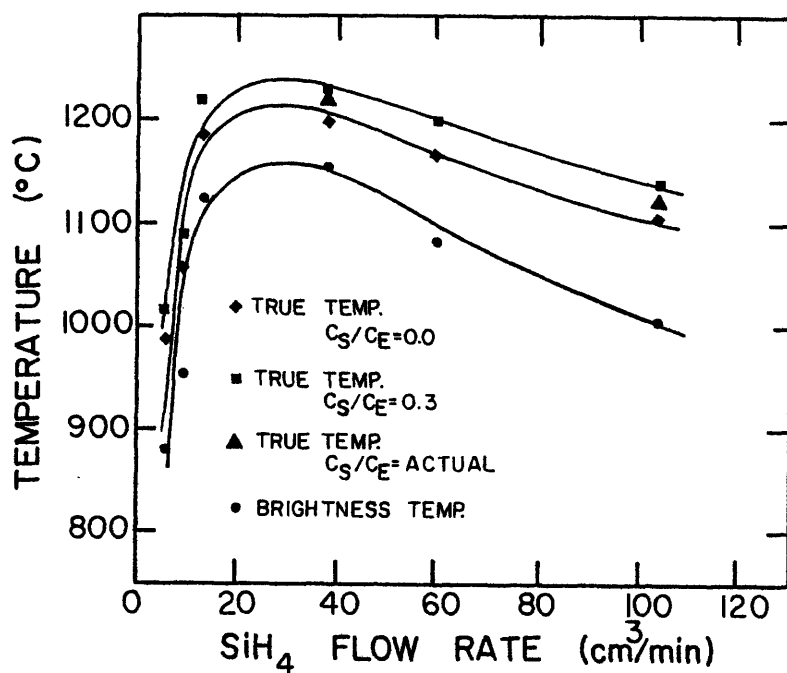


Figure IV.4. Maximum reaction zone temperature versus silane flow rate. (Pressure = 2×10^4 Pa, Laser intensity = 531 W/cm^2)

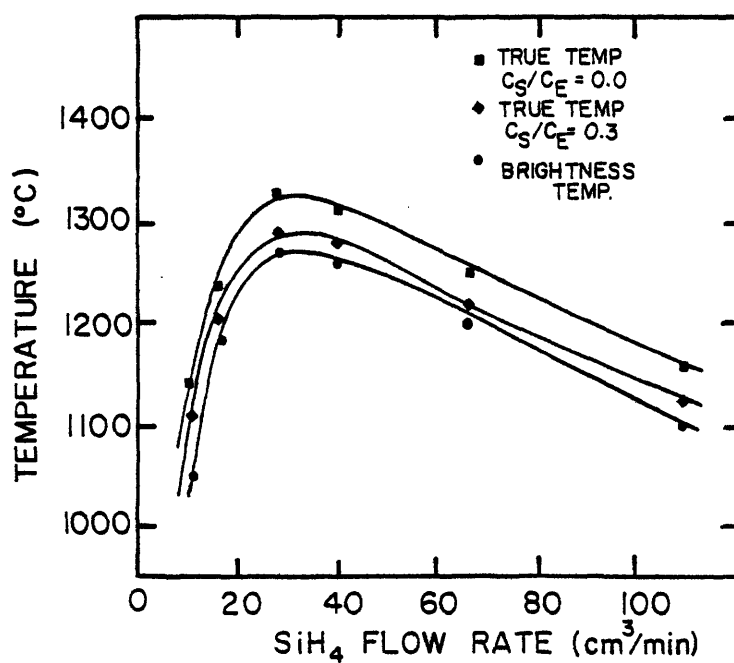


Figure IV.5. Maximum reaction zone temperature versus silane flow rate. (Pressure = 3.5×10^4 Pa, Laser intensity = 601 W/cm^2)

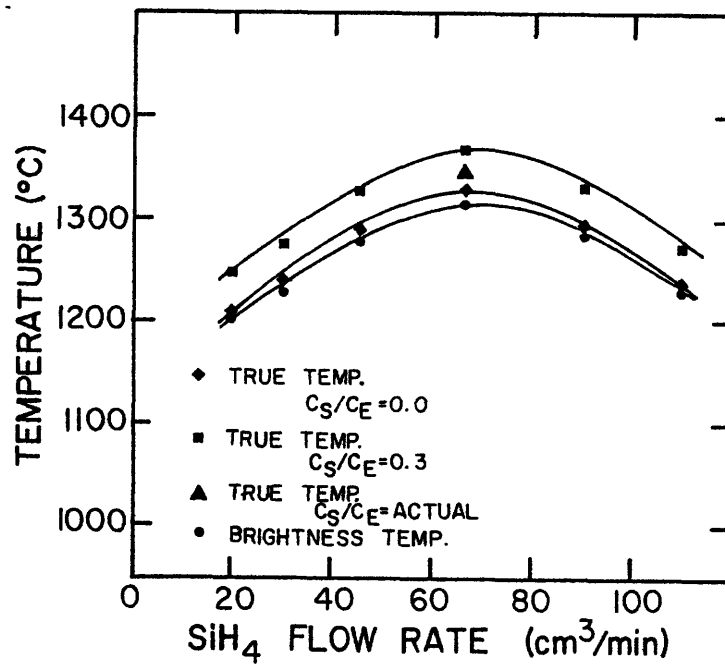


Figure IV.6. Maximum reaction zone temperature versus silane flow rate. (Pressure = 6×10^4 Pa, Laser intensity = 531 W/cm^2)

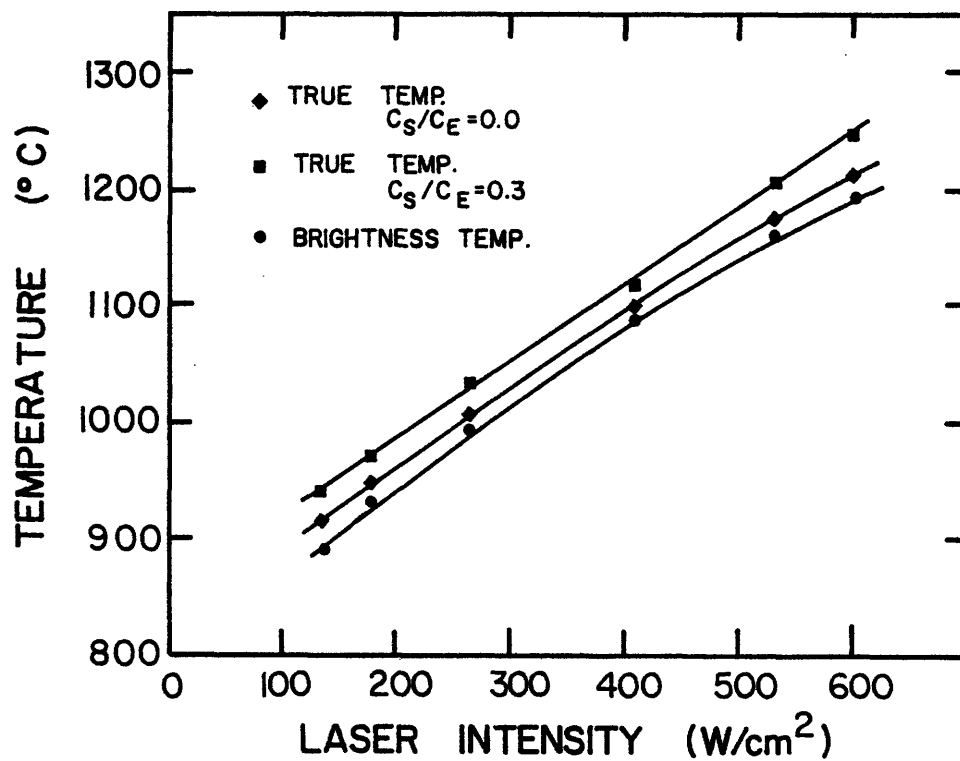


Figure IV.7. Maximum reaction zone temperature versus laser intensity. (Pressure = 3.5×10^4 Pa, SiH₄ flow rate = $66 \text{ cm}^3/\text{min}$)

Figure IV.4 shows the brightness temperature and the bounds on the true temperature assuming the ratio of the scatter to extinction cross sections was 0.0 or 0.3. The run conditions were identical except the SiH_4 flow rate was varied. The reaction cell pressure was 2×10^4 Pa (0.2 atm). Figures IV.5 and IV.6 show similar plots for other synthesis runs in which the flow rate was varied at 3.5×10^4 Pa (0.35 atm) or 6×10^4 Pa (0.6 atm). In Figure IV.7, the maximum reaction temperature is plotted as a function of laser intensity. All other process parameters were held constant. Figure IV.8 shows the effect of diluting the reactant gas stream with argon. In each of these plots, a triangular symbol represents a synthesis run in which the actual scatter/extinction ratio was measured.

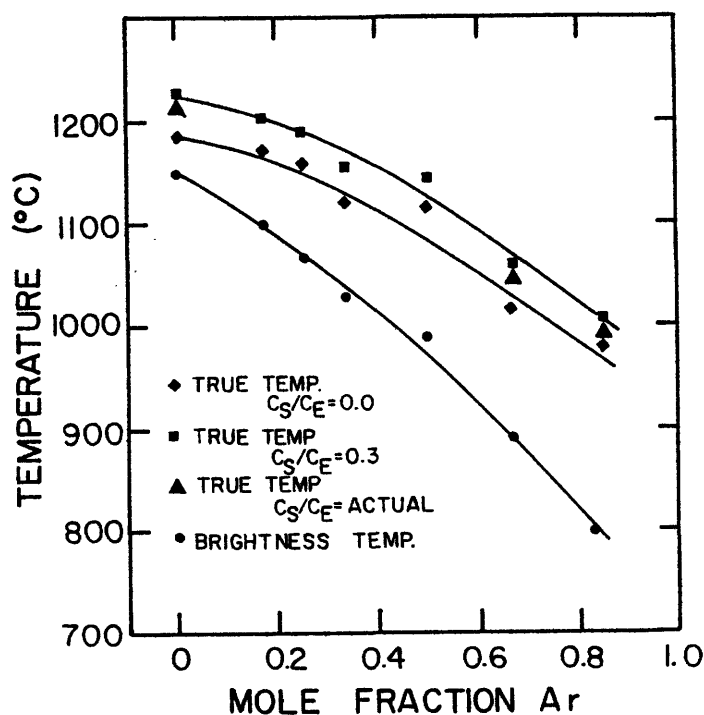


Figure IV.8. Maximum reaction zone temperature as a function of dilution of reactant gas with argon. (Pressure = 2×10^4 Pa, Laser Intensity = 531 W/cm^2 , Total Flow Rate = $38 \text{ cm}^3/\text{min}$.)

3. Heat Balance Analysis

In investigating the effect of the process variables on the reaction and particle temperature, it is informative to examine the heat power balance. The following situations are considered: 1) the heat power balance in any volume element of absorbing gas prior to the initiation of the reaction, 2) the importance of conduction and radiation of heat from the hot reaction zone, and 3) the effect of the reaction and the exothermic heat release on the gas and particle temperature.

As described in Section IIC at the gas pressures and laser intensities used during the synthesis process, the resulting chemical reaction is thermal in nature. The amount of energy supplied to the system can be calculated from the power output of the laser and the absorptivity and heat capacity of the gases. The heat balance in any volume element of partially absorbing gas is:

$$I_0 \Delta x \ell [1 - \exp(-\sum \alpha_i p_i \Delta x)] = C_p \frac{n}{V} \Delta V \frac{dT}{dt} + \Delta H_v \Delta V \frac{dn}{dt} + \text{heat transfer losses} \quad \text{IVA.1}$$

where I_0 is the laser intensity, Δx is the thickness of the gas element, $(\Delta x \ell)$ is the cross-section of the element, α_i is the absorption coefficient of the i^{th} chemical species, p_i is the partial pressure of the i^{th} species, C_p is the heat capacity of the gas, n/V is the molar density in the volume element ΔV , dT/dt is the rate of change of temperature, ΔH_v is the heat of reaction per unit volume, and dn/dt is the moles of gas reacting per unit time.

The first limiting solution involves only the heating of the absorbing gas by the incident laser light. It is assumed that the heat

losses are negligible and no reaction occurs. Therefore, all the absorbed energy is converted to the sensible heat required to raise the gas temperature. To accurately determine the absorption character and thermal history of the reacting gas, it is necessary to consider the spatially variant gas velocity distribution and laser intensity profile. The actual problem involving a gas stream having a parabolic velocity distribution intersecting a laser beam possessing a Gaussian shaped intensity distribution can be simplified by considering a small gas volume element at some particular position in the gas stream. A stepwise calculation is performed to determine the temperature-time history of the volume element as it passes through the laser beam.

The path of a gas element through the laser beam is divided into a finite number of intervals. In each interval, the gas element is assumed to have a constant velocity and is subjected to a constant laser beam intensity. The laser beam intensity in each interval is calculated assuming a Gaussian shaped profile. The gas velocity at any point is determined from a computer model (see Appendix 4, References 93 and 94). The volume element is assumed to have a square cross-section of width Δx and length ℓ determined by the number of intervals in the path. It is assumed that there is no dilution by the annular argon stream. Thus the gas volume consists of only silane and argon added directly to the gas stream.

The power absorbed (P_{AB}) by a particular gas element is

$$P_{AB} = I_0(\Delta x \ell) [1 - \exp(-\sum_i \alpha_i P_i \Delta x)] \quad \text{IVA.2}$$

Using the substitution $x_i P_{tot} = P_i$ where x_i is the mole fraction of species i , $\sum_i \alpha_i P_i \Delta x = \Delta x P_{tot} \sum_i x_i \alpha_i = \alpha_{AVE} P_{tot} \Delta x$ where α_{AVE} is the average absorption coefficient. Assuming the volume element is optically thin,

i.e. $\alpha_{\text{AVE}} P_{\text{tot}} \Delta x \ll 1$, $1 - \exp(-\alpha_{\text{AVE}} P_{\text{tot}} \Delta x) = \alpha_{\text{AVE}} P_{\text{tot}} \Delta x$ and a correction for a freely expanding gas stream $\alpha_{\text{AVE}} P(T) = \alpha_{\text{AVE}} P_0 T/T_0$ where T_0 and P_0 are the initial temperature and pressure, the total power absorbed P_{AB} becomes

$$P_{\text{AB}} = I_0 \Delta x^2 \lambda \alpha_{\text{AVE}} P_0 T_0 / T \quad \text{IVA.3}$$

If all the absorbed power is converted to sensible heat, the temperature increase $T_{\text{R}} - T_0$ in the volume element is

$$T_{\text{R}} - T_0 = \frac{\Delta t P_{\text{AB}}}{C_p (n/V) \Delta V} \quad \text{IVA.4}$$

Substitution of Equation IVA.3 into Equation IVA.4 and using $n/V = P/RT$ and $\Delta t = \lambda/\bar{v}$ where \bar{v} is the calculated gas velocity within the volume element, the gas temperature when it leaves the volume is

$$T_{\text{R}} = T_0 + \frac{\lambda I_0 \alpha_{\text{AVE}} T_0 R}{C_p \bar{v}} \quad \text{IVA.5}$$

Figure IV.9 shows the effect of velocity on the calculated heating rate for a gas volume element travelling along the central axis of the gas stream through the maximum laser intensity. The four curves correspond to Runs 629S (silane flow rate = 5.5 cm³/min), 625S (11 cm³/min), 631S (38 cm³/min) and 630S (104 cm³/min). An average value of 5 (atm-cm)⁻¹ taken from an extrapolation of the 90 W and 220 W average power absorptivity results shown in Figure II.3 was used for the silane absorption coefficient and it was assumed to be independent of temperature. There is evidence that this assumption is not valid⁵ but there is insufficient data to determine the actual temperature dependence of the absorptivity.

For all these velocities, the heating rate analysis predicts that the gases should reach temperatures in excess of 1000K before travelling through the maximum laser intensity at the center of the beam. For Run 625S (SiH_4 flow rate = $5.5 \text{ cm}^3/\text{min}$), the reactant gas is heated to 1200K after it has travelled only 0.04 cm into the 0.6 cm diameter beam.

Figure IV.10 predicts that both the average heating rate and instantaneous heating rate at the temperature levels where silane pyrolyzes rapidly, approximately 1000K, increase with increasing reactant gas flow rate. It is anticipated that the higher heating rate will force the reaction temperature to higher levels, so that faster SiH_4 flow rate should produce a higher reaction temperature. This is not in agreement with the ascending-descending maximum reaction zone temperature dependence on gas flow rate shown in Figure IV.4.

There are numerous uncertainties and assumptions that may account for this inconsistency. The reactant gas flow rates and absorptivities are not accurately known. The effect of temperature increase on the flow characteristics is not considered by the computer model. Absorptivity measurements suggest that the silane absorption coefficient is highly temperature dependent. By choosing a smaller average absorption coefficient, it is possible to force the calculated heating into qualitative agreement with the measured results.

This is illustrated by Figure IV.10 in which an absorption coefficient of 2 (atm-cm)^{-1} was used to calculate the temperature history for runs having conditions identical to Run 625S, 631S, and 630S. In this case, for the highest reactant gas velocity (630S), a temperature of 1200K is not achieved until the reactant gas has

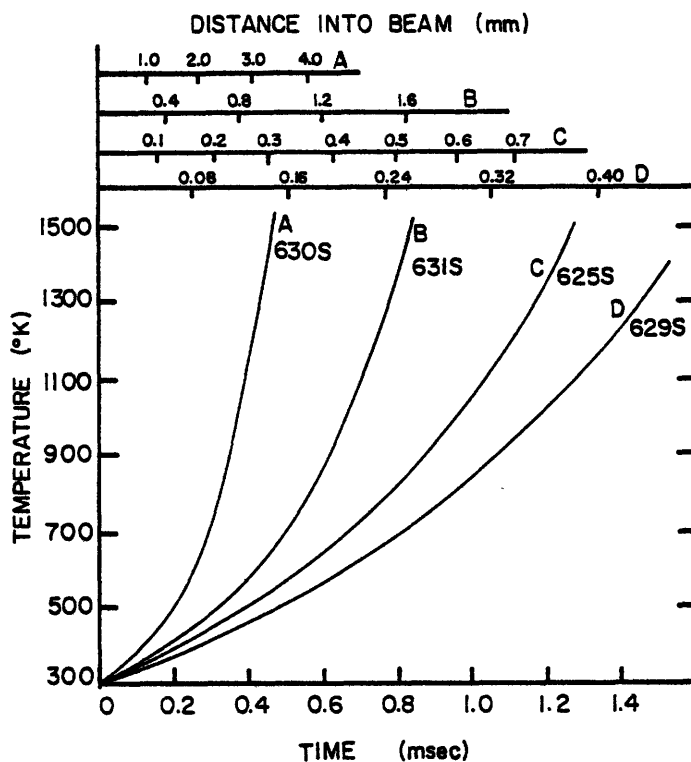


Figure IV.9. Calculated gas heating rate for various flow rates. Top scale represents the distance gas travelled into the laser beam. (SiH_4 absorption coefficient = $5 \times 10^{-3} \text{ Pa}^{-1} \text{ m}^{-1}$)

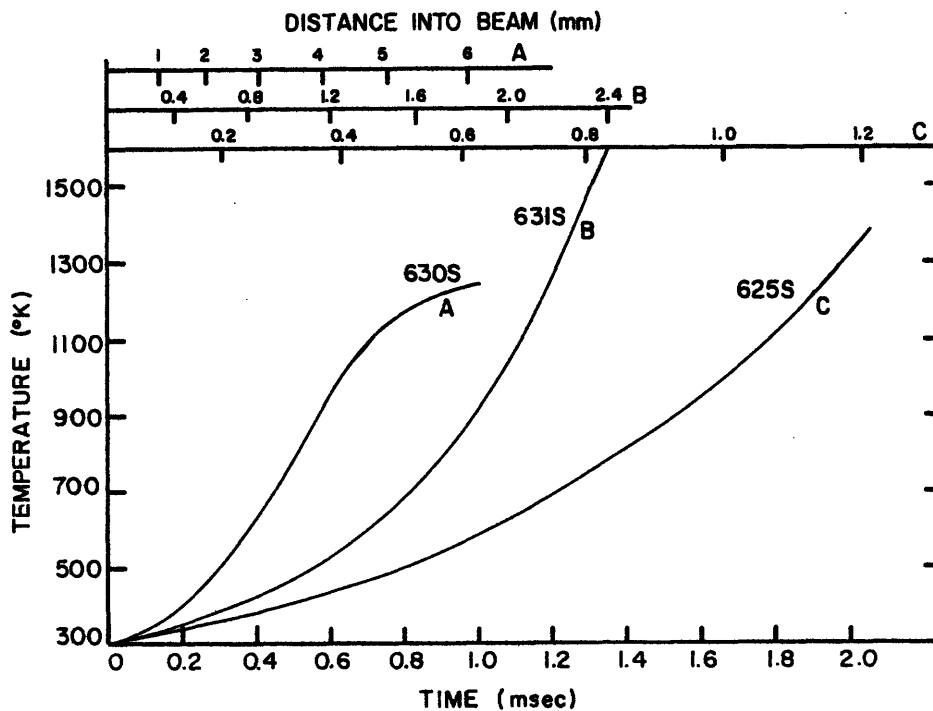


Figure IV.10. Calculated gas heating rate for various flow rates. Top scale represents the distance gas travelled into the laser beam. (SiH_4 absorption coefficient = $2 \times 10^{-3} \text{ Pa}^{-1} \text{ m}^{-1}$)

travelled past the center of the beam. For Run 625S, the heating rate is much lower than the other runs and the reactant gas is heated to pyrolysis temperatures soon after it enters the beam; therefore a low reaction temperature is expected. Thus, with this choice of the absorption coefficient, the ascending-descending temperature dependence can be explained by the following: 1) at low flow rates, the reaction is initiated and goes to completion before the gases and products reach the maximum intensity; therefore, a low reaction temperature is expected, 2) at intermediate flow rates, the reaction is initiated soon after the gases enter the beam but to a large extent occurs near the beam center resulting in a high temperature, and 3) with high flow rates, a large extent of the reaction occurs past the maximum intensity region resulting in a decreased temperature. These generalizations are consistent with the observations of the particle growth from light scattering extinction measurements (see Section IVB).

Figure IV.11 shows the effect of diluting the reactant gas stream on the temperature-time history. An absorption coefficient of $2(\text{cm-atm})^{-1}$ was used. Diluting the reactant gas stream with Ar effects two critical parameters which determine the gas heating rate. First, the overall absorption coefficient is decreased since Ar is essentially nonabsorbing at a wavelength of $10.6 \mu\text{m}$. Second, the gas heat capacity is altered since the heat capacity of SiH_4 is 3 to 4 times that of Ar. These two effects act in opposite directions. Combined, they produce a less pronounced effect than if the reactant gas stream was diluted with a nonabsorbing species having a heat capacity similar to that of SiH_4 . Figure IV.11 shows that the average heating decreases and the reaction is forced further into the reaction zone as the reactant gas stream is

diluted. This is consistent with the measured temperature and particle growth behavior determined from the scattering/extinction measurements. Figure IV.8 showed the maximum reaction zone temperature decreased as the reaction zone was increasingly diluted indicating the effect of reducing the absorptivity of the gas stream outweighs the effect of a lower heat capacity.

Figure IV.12 shows the effect of changing the laser intensity on the reactant gas heating rate. The heating rate increases significantly with increased laser intensity. This results in a higher reaction zone temperature as was shown in Figure IV.7. For a nearly optically dilute gas stream, to a first approximation, the temperature increase is directly proportional to the laser intensity as was observed. Run 645S was synthesized with a 170 W laser beam focused to a 0.2 cm diameter giving a power intensity of approximately 5400 W/cm^2 . The brightness temperature was measured to be 1245°C suggesting that there is a limit to the temperature achieved by the laser synthesis reaction. It should be noted that in all cases the maximum corrected temperature was less than the melting point of silicon.

The above analysis predicts the gas heating rate will be independent of pressure for gas streams which are optically thin. This follows from the assumption that $1 - \exp(-\alpha p \Delta x) = \alpha p \Delta x$. At high pressure, it can no longer be assumed that the gas is optically thin. In a highly absorbing gas stream, the laser beam will be progressively absorbed as it passes through the gas stream causing differences in the thermal histories of the volume elements on the entering and exiting side of the gas stream. The heating rate analysis also assumed

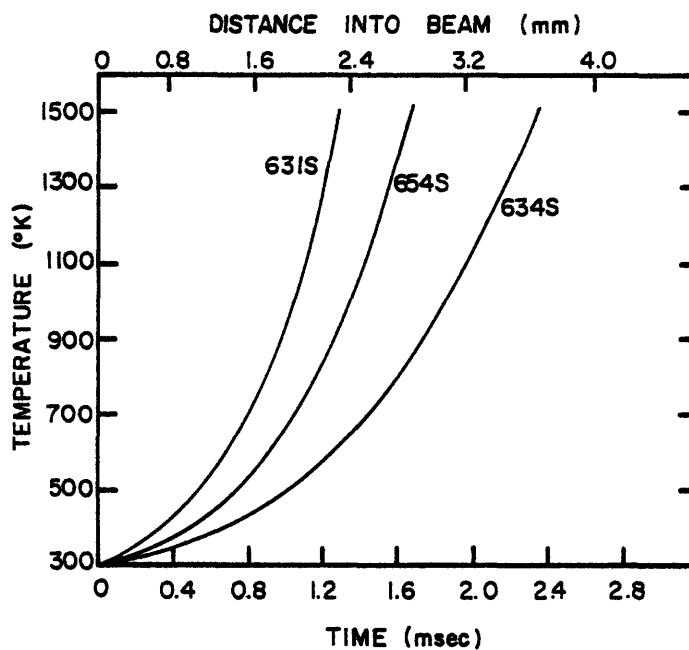


Figure IV.11. Effect of dilution of the reaction zone with argon on the calculated gas heating rate.

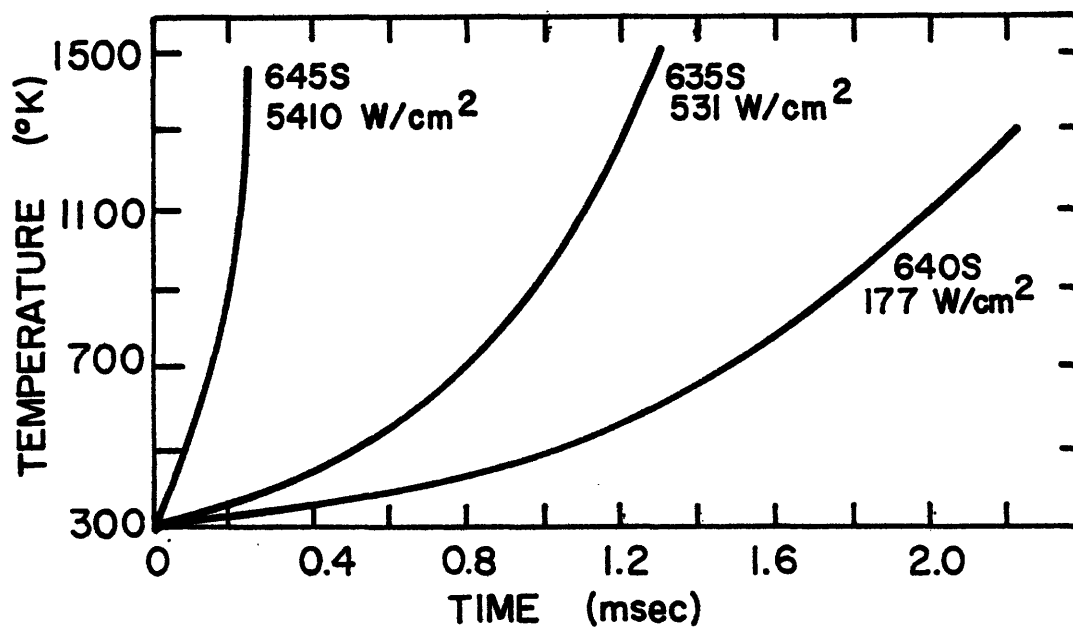


Figure IV.12. Effect of laser intensity on the calculated gas heating rate.

that the optical absorptivities are independent of pressure. As shown in Section IIC, this is not precisely valid.

The analysis described above did not include the effect of latent heat associated with pyrolysis of SiH_4 . In fact, it is a thermal analysis of the process up to the point that the reaction begins. Also, the effect of any preheating of the reactant gas prior to the intersection with the laser beam has been ignored. The temperature profile measurements have shown that under certain conditions the gases are heated and the reaction is initiated before the reactants intersect the laser beam. The following analysis considers the effect of thermal conduction from the hottest region of the reaction zone back to the inlet nozzle.

To a first approximation, under steady state conditions, the rate at which the thermal interface propagates back into a stagnant gas is

$$\text{RATE} = x/\tau \quad \text{IVA.6}$$

where τ is a time constant given by $x^2/4\kappa$ with κ representing the thermal diffusivity and x is the thermal diffusion distance. The thermal diffusivity is related to the thermal conductivity k , the density ρ , and the specific heat capacity C_p :

$$\kappa = k/\rho C_p .$$

At 1000K and 0.2 atm, $k = 2.4 \times 10^{-3} \text{ W/cm}^\circ\text{C}$,^{*} $\rho = 6.8 \times 10^{-5} \text{ g/cm}^3$ and $C_p = 2.3 \text{ J/}^\circ\text{K} \cdot \text{g}$, thus the thermal diffusivity $\kappa = 15 \text{ cm}^2/\text{sec}$.

Assuming a 3 mm diffusion distance, the rate of thermal conduction back to the nozzle is approximately 200 cm/sec. A shorter diffusion distance will result in a higher average rate.

*Taken from Reference 95 and assuming a temperature dependence given by Reference 96.

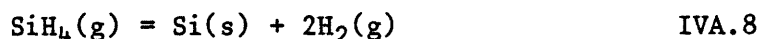
If the velocity of the reactant gas is less than this rate, the effect of conduction will be important. The average gas velocity at the nozzle inlet can be calculated from the initial volumetric flow rate, the nozzle cross sectional area, and the pressure within the cell. At a pressure of 0.2 atm, a volumetric flow rate of approximately $40 \text{ cm}^3/\text{min}$ produces an average velocity at the nozzle at 200 cm/sec. As described in Appendix 4, the gas velocity will decrease with distance from the nozzle. Therefore, the conduction of heat from the hottest region of the reaction may be significant for flow rates less than $40 \text{ cm}^3/\text{min}$. Radiation from the hot zone will also contribute to the increase in gas temperature in the vicinity of the reaction zone.

This simplified analysis shows that the effect of conduction is important in determining the temperature of the reactant gas prior to the interaction with the laser beam. If the flow velocity is less than the rate of propagation of thermal interface, the gas can be heated to significantly high temperatures and a reaction is initiated before the gases reach the beam. The reaction may be complete before the gases travel significantly into the laser beam and result in a low reaction zone temperature [as was observed by the sharp decrease in temperature at low flow rates (Figure IV.4)].

The effect of pressure on the thermal diffusivity can be determined by examining the pressure dependence of each term in Equation IVA.7. The thermal conductivity is independent of pressure up to approximately 10^6 Pa (10 atm). By definition, the specific heat capacity is pressure independent. Therefore, the thermal diffusivity decreases with increased pressure since the density increases. Thus,

the effect of thermal conduction is expected to be less significant at higher pressures. This explains why the increase in the maximum temperature at low flow rates for runs at 6×10^4 Pa (Figure IV.6) is not as steep as at 2×10^4 Pa (Figure IV.4).

The final thermal consideration involves the latent heat associated with the pyrolysis of SiH_4 to form solid Si. The reaction:



is slightly exothermic with a heat of reaction ranging from -24.8 kJ/mole at 600K to -22.1 kJ/mole at 1500K. The amount of power supplied to the reaction zone by the pyrolysis is

$$P_R = \Delta H \, dn/dt \quad \text{IVA.9}$$

If it is assumed the reaction goes to completion, under steady state conditions, the number of moles reacting per unit time dn/dt is equal to the molar flow rate into the reaction zone. With a typical silane flow rate of $40 \text{ cm}^3/\text{min}$ (8.8×10^{-4} mole silane/sec) approximately 2 W are liberated by the reaction. If we assume that all this energy is converted to sensible heat to raise the temperature of the reaction products, a temperature increase of 240°K is predicted. The low exothermicity of the silane pyrolysis makes spontaneous decomposition impossible, i.e. the energy released by the pyrolysis of one silane molecule is insufficient to raise the temperature of another silane molecule from room temperature to the temperature where pyrolysis occurs rapidly. This was confirmed experimentally by closing the laser shutter during synthesis and noting the extinguishing of the reaction "flame".

B. In Situ Particle Nucleation and Growth Experiments

1. Particle Radius as a Function of Position

It was discussed in Section IIIB.2 that the scatter and extinction measurements could be applied to determine various characteristics of the nucleation and growth behavior. The particle radius at a particular position in the flame was determined from Figure III.4 which plots the particle size as a function of the scatter to extinction ratio for various refractive indices. The calculated particle size is highly dependent on the complex refractive index. Therefore, the particle radius was calculated assuming various reported values of refractive index. The results were compared with the diameter measured from BET surface area and TEM measurements to determine the value of the refractive index which gave the best agreement.

Figure IV.13 shows the calculated particle size for Run 631S performed with 0.2 atm, 150 W unfocused laser beam, and 38 cm³/min SiH₄ flow rate. It is apparent that the reaction begins below the laser beam. The particles grow rapidly and the growth is essentially complete while the particles and gases are still in the laser beam. The closest agreement with the BET measurements was obtained when a refractive index of $m = 4.38 - 26i$, suitable for polycrystalline Si at approximately 1000°C, was utilized.

To be completely accurate, the refractive index used for the particle size calculations should reflect the temperature changes within the flame. The temperature profile shown in Figure IV.2 suggests the calculated diameter should initially follow that predicted

with a low temperature index, a higher temperature index in the intermediate region of the flame, and a low temperature index in the upper regions of the flame. This would result in a predicted particle size which increased very rapidly and then decreased in the upper regions of the flame. This decrease is obviously not expected and suggests that the refractive index is not significantly effected by the observed temperature changes. In any event the particle growth predicted using a constant refractive index provides a valid understanding of the basic growth processes.

Figure IV.14 shows the calculated particle diameter as a function of position for other run conditions listed in Appendix 1. The general shape of these curves is similar to that previously discussed. Comparison of these results with the temperature profiles shown in the previous section shows that most of the growth occurs in the hottest regions of the flame. In all cases, the growth is essentially complete when the gases and particles are still in the beam.

For the diluted runs, Run 654S with a 2/1 Ar/SiH₄ gas mixture and Run 634S with a 5/1 Ar/SiH₄ mixture, the best agreement with BET equivalent diameters was obtained by using refractive index suitable for polycrystalline particles at 500°C or particles consisting of an amorphous-crystalline mix at a somewhat higher temperature. This is consistent with the temperature measurements reported in the previous section and the crystal structure of the particles as will be discussed in Section IVF. The dilution of the gas stream resulted in a decrease in the final particle size.

Since Runs 631S (0/1 Ar/SiH₄), 654S (2/1 Ar/SiH₄) and 634S (5/1 Ar/SiH₄) were all performed with the same flow conditions,

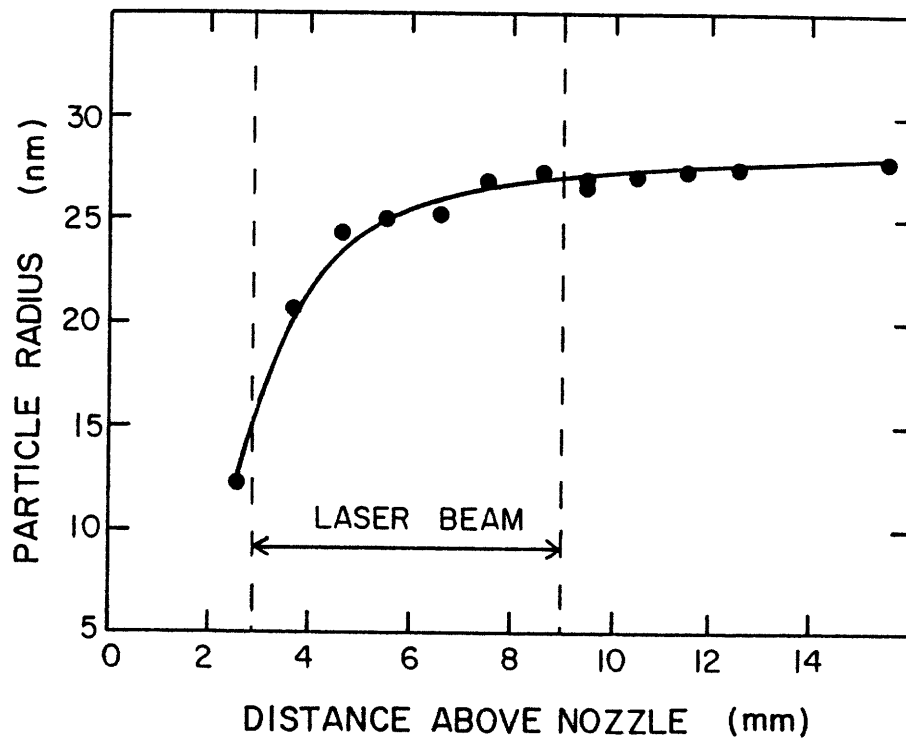


Figure IV.13. Particle size calculated from the scattering/extinction results as a function of distance above the inlet nozzle. (Run 631S)

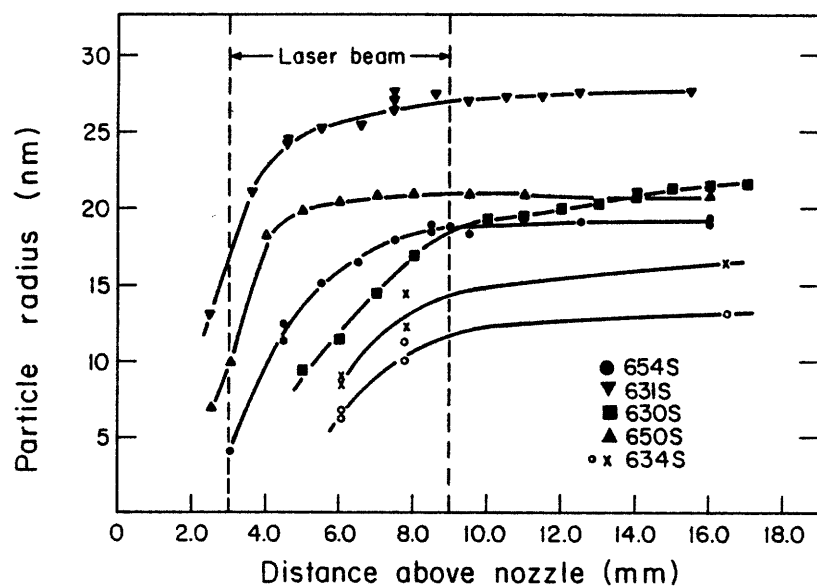


Figure IV.14. Particle size calculated from the scattering/extinction results as a function of distance above the inlet nozzle for various synthesis runs.

comparison of Figures IV.13 and IV.14 can provide some insight into the effect of dilution on the growth rate. Figure IV.14 shows that the average growth rate decreased with increasing Ar dilution. This was expected for two reasons. Since, the growing particles are always smaller than the mean free path in the vapor phase, the growth is expected to be dependent on the rate of molecular bombardment (see Section IVD). That is, the growth rate is directly proportional to the rate at which vapor molecules arrive at the particle surfaces. From the kinetic theory of gases, the growth rate is expected to decrease with decreasing reaction temperature. Since the growth rate is directly proportional to the concentration of silicon bearing vapor species, dilution of the gas stream will reduce the particle growth rate. It is difficult to separate the temperature and concentration effects because they are not independently variable.

At the highest gas flow rate (Run 630S at $104 \text{ cm}^3/\text{min SiH}_4$), the particle growth behavior was significantly different from Run 631S performed at the same pressure and laser intensity but with a much slower reactant gas flow rate ($38 \text{ cm}^3/\text{min}$). With the high flow rate, a reaction was not observed until the gases had travelled approximately 2 mm into the 6 mm unfocused beam. The final particle size decreased with the increased flow rate. Although most of the growth occurred in the hottest region of the reaction zone, it is apparent that the growth continued after the particles had travelled through the laser beam.

For the run performed at 0.6 atm (Run 650S), the calculated particle size was much smaller than the measured BET equivalent diameter regardless of the refractive index used. The turbidity, $\text{NC}_{\text{EXT}}^\lambda$, of this run is on the order of 6. Under these conditions, 90%

of the incident HeNe laser light will be attenuated in the first millimeter of the particulate cloud assuming that the particulate cloud has a uniform optical density throughout its entire diameter.

Regardless of this assumption, it is evident that the majority of the measured scattering originates from the outer edge of the flame. This region will have the highest dilution by the annular argon flow; so, it is likely that the gas stream temperature and resulting particle diameter will be significantly smaller than the average values.

Therefore, it was concluded that this method cannot be used to accurately calculate the particle growth behavior unless the overall flame turbidity is less than about 3.

2. Particle Number Density

Using the Beer-Lambert Law:

$$\frac{I}{I_0} = \tau = \exp(-N\ell C_{EXT}) , \quad \text{IBV.2}$$

the particle number density was calculated from the results of the scatter/extinction measurements. Since it is difficult to measure the path length ℓ through the reaction zone, the product of the number density and the path length was calculated. For most runs, the path length was relatively constant and approximately equal to 1 cm; thus, it was assumed that the number density was well represented by this product. The calculated number density is very dependent on the refractive index used. Therefore, the quantitative validity of these results is uncertain, but the qualitative results provide valuable insight into the particle nucleation and growth behavior.

Figure IV.15 shows the calculated number density as a function of position above the gas inlet nozzle for Run 654S synthesized with a 150 W unfocused laser beam, at a pressure of 0.2 atm, and with a 2/1 Ar/SiH₄ gas mixture. The particle number density was calculated using refractive indices suitable for both amorphous and polycrystalline silicon.

There are numerous interesting features of the nucleation and growth processes that can be gleaned from Figure IV.15. If the refractive index is taken to be constant, either polycrystalline or amorphous, the product $N\ell$ decreases from a maximum value at the base of the "flame" to a constant value further into the reaction zone. The reactant gas stream expands slightly as the gases travel further from the nozzle and are heated (see Appendix 4). The decreased value of $N\ell$ at the base of the flame may be related to this expansion, but since the temperature increase is small, a 7x decrease in the number density is unlikely. The decrease in $N\ell$ may indicate the particles are coagulating as they travel further into the reaction zone. This is unlikely since it is expected the number density within the flame would continue to decrease if agglomeration was occurring. If the particles are assumed to have a refractive index appropriate for amorphous silicon when they first form and a polycrystalline index in the higher regions of the reaction zone, the number density remains essentially constant. This suggests the particles form as amorphous silicon and crystallize in the hotter regions of the flame. The particle crystal structure and possible crystallization mechanisms are discussed further in Section IV.F.

The number density remained essentially constant from the center of the laser beam to the highest position measured. This suggests the particles did not agglomerate in the region of reaction zone observed. Thus, chain-like agglomeration typically observed in the laser synthesized powders results from either agglomeration in the upper regions of the particulate cloud where it was not possible to measure the scattering and extinction or is a consequence of the powder collection technique. Particle agglomeration and surface force interactions are discussed more fully in Section IV.E.

Figure IV.15 suggests the nucleation occurred at the very base of the reaction zone and rapidly ceased before much particle growth occurred. The nuclei formed then grew to their final dimensions. Possible mechanisms for this type of nucleation and growth behavior as well as the effects on the resulting particle size and particle size distributions is discussed in Section IV.D.

Figure IV.16 shows numerous runs in which the nuclei density, or more specifically the product $N\lambda$, was calculated. The run conditions are listed in Appendix 1. In all cases, the nuclei density remained essentially constant in the upper regions of the reaction zone. This supports the inference that the particles did not agglomerate within the region measured. Using an index of refraction suitable for polycrystalline silicon, there is additional evidence that the number density decreases rapidly from a maximum value at the base of the "flame" to a constant level further into the reaction zone. Within the regions analyzed, there was no evidence of nucleation. It is therefore postulated that nucleation occurred rapidly and then ceased. The number of nuclei formed was determined by the product of the nucleation

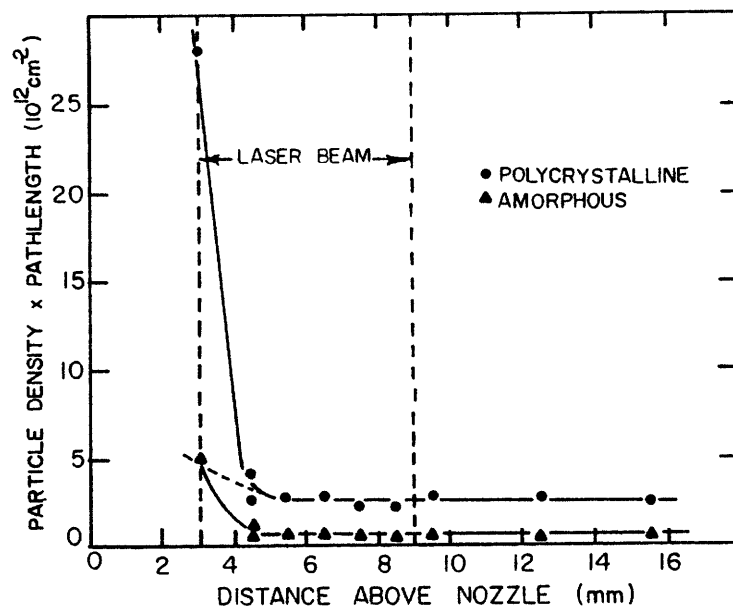


Figure IV.15. Product of the particle number density and optical pathlength as a function of distance above the inlet nozzle. Calculated from the scattering/extinction results assuming both amorphous and polycrystalline particle refractive indices. (Run 654S)

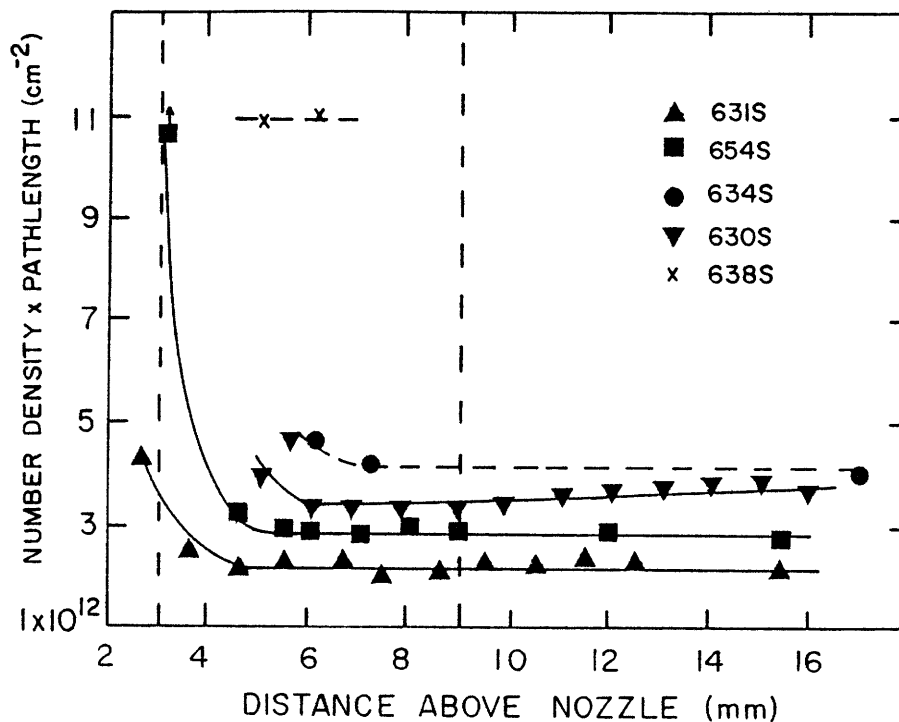


Figure IV.16. Product of the particle density and optical pathlength as a function of distance above the inlet nozzle for various synthesis runs.

rate and the time interval during which nucleation is occurring. These nuclei then grew to their final dimensions by depleting the available silane.

Comparison of the individual runs (631S, 654S, and 634S) depicted in Figures IV.15 and IV.16 reveals that as the SiH_4 gas stream was diluted the nuclei density increased. If the nuclei grew independently, the available volume of reactant gas per nuclei decreased with argon dilution. The density of silicon species within this volume also decreased with dilution. Therefore, the observed decrease in particle size with increasing Ar dilution is related to the combination of the increased nuclei density and the decreased SiH_4 concentration. The run synthesized with a high reactant gas velocity (630S) resulted in a significantly higher nuclei density than Run 631S synthesized with identical conditions but approximately three times slower reactant flow rate. Thus the decrease in particle size at the higher flow rate results from the decrease in reactant gas available for each growing nuclei.

A major limitation of the scatter/extinction technique is the inability to actually monitor the nucleation events. This is primarily a consequence of the minimum detectable particle radius being approximately 4 nm with the 632.8 nm wavelength HeNe laser as evidenced by Figure III.4. The radius of a critical sized nuclei is expected to be less than 1 nm. A shorter wavelength light source, perhaps ultraviolet, would permit smaller particle size determination as well as eliminate much of the uncertainty in the measurements since the indices for single crystalline, polycrystalline, and amorphous silicon converge in this region. In order to actually determine the nucleation kinetics, it may be necessary to improve the spatial resolution of the

scatter/extinction method. It is important to determine when the nucleation begins and the time elapsed between the onset and cessation of nucleation.

3. Gas Depletion and Possible Growth Mechanisms

The results of the previous section indicate that the maximum particle size was limited by the available silicon vapor species and not by the elapsed growth time at elevated temperatures. That is, particles are formed by homogeneous nucleation, the nucleation terminates, and the particles grow by the depletion of the reactant gas. The particle growth is limited by the impingement of the neighboring depletion volumes.

The change in the concentration of silicon atoms in the reactant gas stream can be determined from the scatter/extinction results. Mass balance measurements (see Section IVC) have shown that nearly all the SiH_4 gas was converted to solid silicon during the synthesis process. The amount of silicon in the gas phase was estimated by subtracting the amount of silicon in the solid particle (determined from the particle size and number density calculations) from the original silicon concentration. It was assumed that the SiH_4 was entirely depleted when the particles achieved their final dimensions.

Figure IV.17 shows the calculated concentration of silicon in the vapor phase as a function of position in the reaction zone for Run 654S in which a 2/1 Ar/ SiH_4 gas mixture was used. It is evident that the reaction occurred in a continuous manner and was essentially complete while the particles and gases are still in the laser beam. Similar

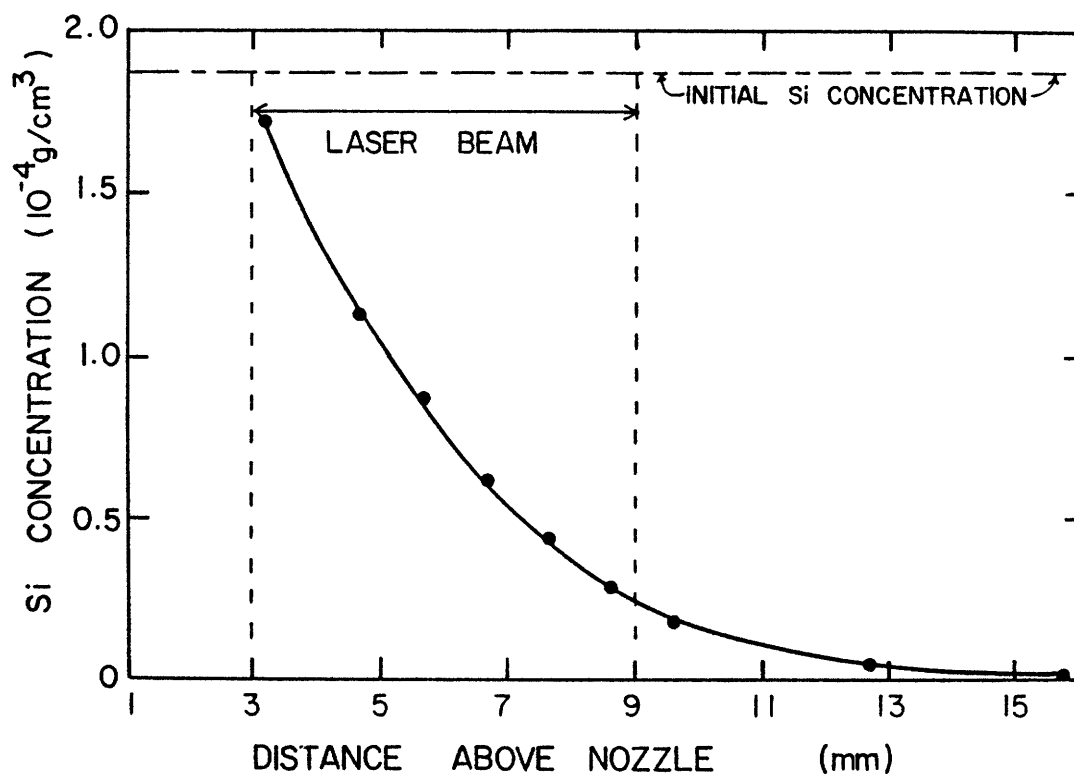


Figure IV.17. Calculated silicon concentration in the reaction zone as a function of distance above the inlet nozzle. (Run 654S)

plots have shown that for reaction zones consisting of pure silane, except at the highest flow rates, the reaction was entirely complete while the particles were in the laser beam.

As discussed in Section IIB, the growth rate is expected to vary with temperature, particle size, and reactant gas concentration. Since all of these variables are changing during the growth process, it is difficult to analyze the scatter/extinction results to determine the functional dependencies. At the temperatures encountered during growth, in all cases in excess of 900°C , the equilibrium constant for the decomposition of SiH_4 is very high.²⁶ Therefore, at least from a thermodynamic viewpoint, the particle growth is not expected to be reaction limited. For particles much smaller than the mean free path in the vapor phase, which is the situation for all the reaction conditions examined, the particle growth rate is typically limited by

molecular bombardment. That is, the particle growth rate is determined by the rate of which vapor molecules arrive at the surface of the particle. The radial growth rate is given by

$$\frac{dr}{dt} = \frac{\alpha v_{Si} (P_{Si(g)} - P_{\infty})}{(2\pi mkT)^{1/2}} \quad \text{IIB.20}$$

Thus the growth rate, dr/dt , is independent of the particle radius. If the reaction temperature remains constant, the growth rate will be directly proportional to the vapor concentration since P_{∞} is extremely low.

Figure IV.18 plots the natural logarithm of the growth rate versus the natural logarithm of the concentration of silicon within the reaction zone for Runs 630S and 654S. The run conditions are listed in Appendix 1. The growth rates were determined from the slope of the curves shown in Figure IV.15 with the assumption that the velocity remains constant in the spatial intervals examined. This assumption introduces little error since these intervals are small. For both runs, the reaction temperature is relatively constant in the regions plotted. Therefore, the change in the growth rate is expected to be directly related to the change in the vapor concentration. The slopes of these curves, for Run 654S and 630S, are in reasonable agreement with the value (1.0) predicted by Equation IIB.20.

For particles much larger than the mean free path in the vapor phase, the growth rate is typically limited by vapor diffusion and can be represented by

$$\frac{dr}{dt} = \frac{D v_{Si} (P_{Si(g)} - P_{\infty})}{r_p kT} \quad \text{IIB.14}$$

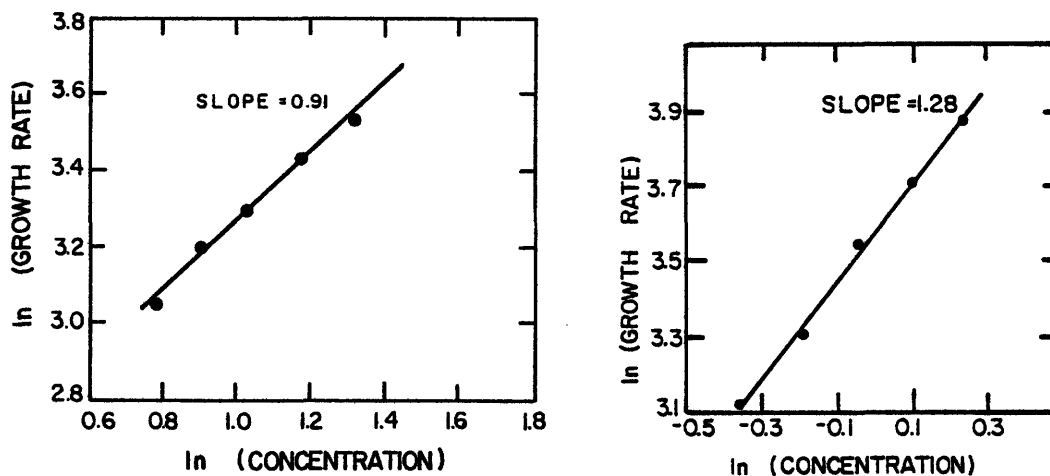


Figure IV.18. The logarithm of the growth rate calculated from the scattering/extinction results versus the logarithm of the silicon concentration in the reaction zone. a - Run 654S, b - Run 630S.

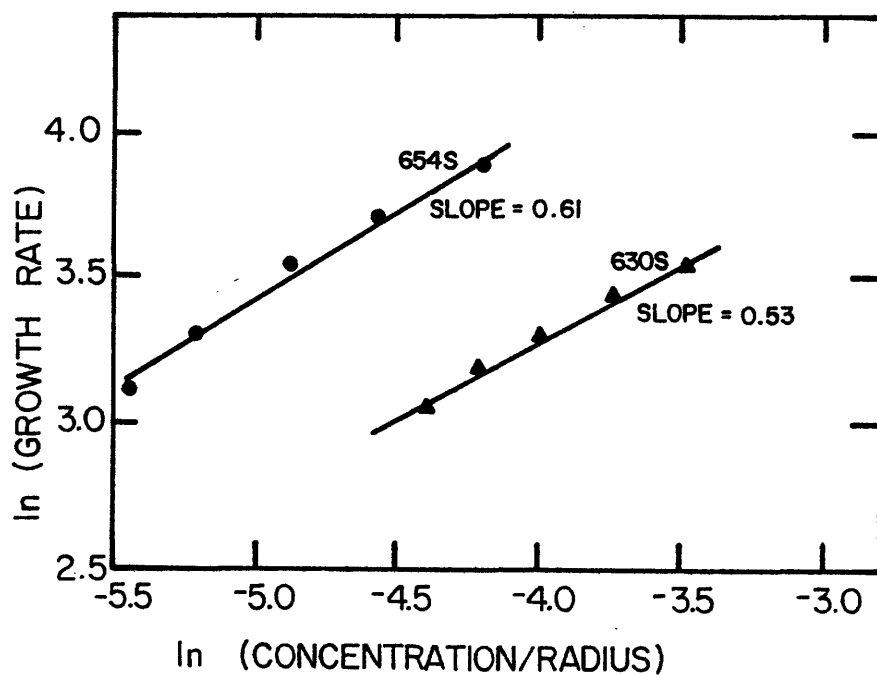


Figure IV.19. The logarithm of the growth rate calculated from the scattering/extinction results versus the logarithm of the quotient of the gas concentration and particle radius.

For particle growth exhibiting this behavior, the rate is dependent on the particle radius. Therefore, if the growth is diffusion limited, a plot of the logarithm of the growth rate versus the logarithm of the quotient of the concentration divided by the particle size will result in a straight line with a slope of unity if the reaction temperature is constant. Figure IV.19 shows such a plot for Runs 654S and 630S. The slopes of the least square lines were significantly smaller than unity. It was therefore concluded from the agreement of Figure IV.18 with that predicted by theory (Equation IIB.20), the growth process was determined by molecular bombardment, that is by the rate at which vapor molecules arrive at the particle surface. This conclusion is discussed more fully in Section IVD.

C. Effect of Process Variables on the Powder Characteristics

1. General Characteristics

In general, the silicon powders are all similar in character. From the standpoint of ceramic processing, they fulfill many of the attributes of an ideal powder. They are fine, with an average particle size from 20 to 160 nm, depending on the process conditions, are nearly monodispersed, are compositionally pure, have low oxygen content, and possess spherical shapes. The particles exhibit chain-like agglomeration; dispersion results have shown that the silicon agglomerates can be broken up by ultrasonic agitation in organic liquids such as n-propoanl.⁹⁸

A bright field TEM photomicrograph of a typical silicon powder is shown in Figure IV.20. This powder was taken from Lot 634S and the run conditions are given in Appendix 1. The powder is small with an average diameter of 27.5 nm, and nearly uniform in size, ranging from 19 to 35 nm. The particles are spherical in shape. A dark field TEM photomicrograph of the same powder is shown in Figure IV.21. It is evident that the powders are polycrystalline with a crystallite size significantly less than the particle diameter. Both Figures IV.20 and IV.21 indicate the powders generally exhibit chain-like agglomeration. Under some conditions, there appears to be neck formation between particles. The agglomeration and possible mechanisms for neck formation are discussed more fully in Section IVE.

The efficiency with which the SiH_4 gas is converted to powder ranged from 80-100%. The conversion efficiency exhibited no systematic dependence on the process variables within the range examined.

The chemistry of the powders is important in subsequent processing. Spectrographic analysis (Table IV.1) showed they typically have total cation impurity contents of less than 200 ppm. The oxygen content is generally less than 1.0% by weight and from some runs, the powders produced have O_2 concentrations as low as 0.05 weight %. The purity of the resulting powder varies somewhat from run to run, but it does not appear dependent on the synthesis conditions. Rather, it is related to specific experimental procedures such as outgassing time, vacuum tightness of the cell, and post-production handling of the powder.

Most powders are crystalline to both X-ray and electron diffraction. An X-ray diffraction pattern utilizing $\text{Cu-K}\alpha$ radiation

Table IV.1. Chemical Analyses of Silicon Powders

Sample Number	Summary of Spectrographic Analyses (ppm)												Other Analyses (wt %)				
	Al	Ag	Ba	Ca	B	Cu	Fe	Mg	Ni	Pb	Sn	Ti	O ₂	C	Cl	S	F
622S	-	-	-	-	-	-	-	-	-	-	-	-	0.64	-	-	-	-
625S	30	0	0	20	30	7	30	5	5	0	10	0	0.28	-	-	-	-
628S	20	0	0	30	0	10	10	3	3	0	10	0	-	-	-	-	-
631S	3	0	0	1	0	0	1	0	0	0	0	0	0.70	0.10	0.10	0	0
632S	3	0	0	1	0	0	1	0	0	0	0	0	0.68	0.03	0.14	0	0

($\lambda = 0.1542$ nm) from a typical powder is shown in Figure IV.22. The pattern was indexed to silicon (no extra peaks). For each powder lot, the crystallite size was determined from X-ray diffraction line broadening using Cu-K $_{\alpha}$ radiation. The procedure is discussed in detail in Appendix 3, where it is shown that the effects of lattice distortion and stacking faults can be ignored. The broadening of a single peak at 47.34° was used to determine the crystallite size. In all cases, the crystallite size was substantially smaller than the BET equivalent diameter which indicates that the individual particles are polycrystalline. The crystal microstructure was confirmed by bright and dark field transmission electron microscopy and scanning transmission electron microscopy. It was found that the particle size to grain size ratio depended on the process conditions.

The BET equivalent spherical diameter and the diameter measured from TEM micrographs have always been nearly equivalent as illustrated

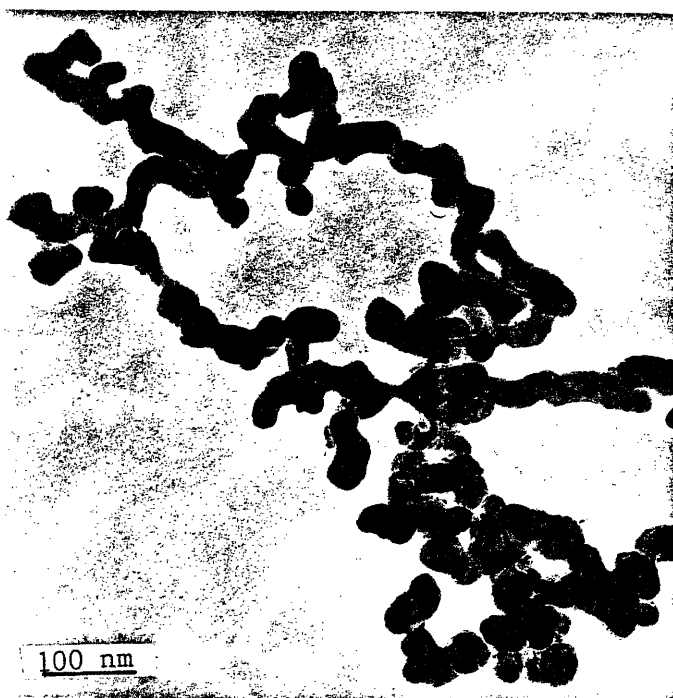


Figure IV.20. Bright field TEM micrograph of a typical laser synthesized silicon powder. (Run 634S)

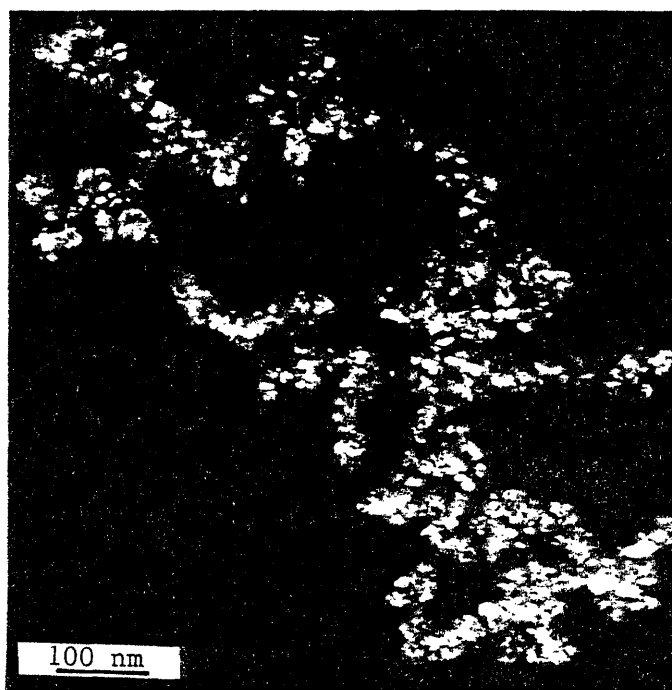


Figure IV.21. Dark field TEM micrograph of powder shown in Figure IV.20.

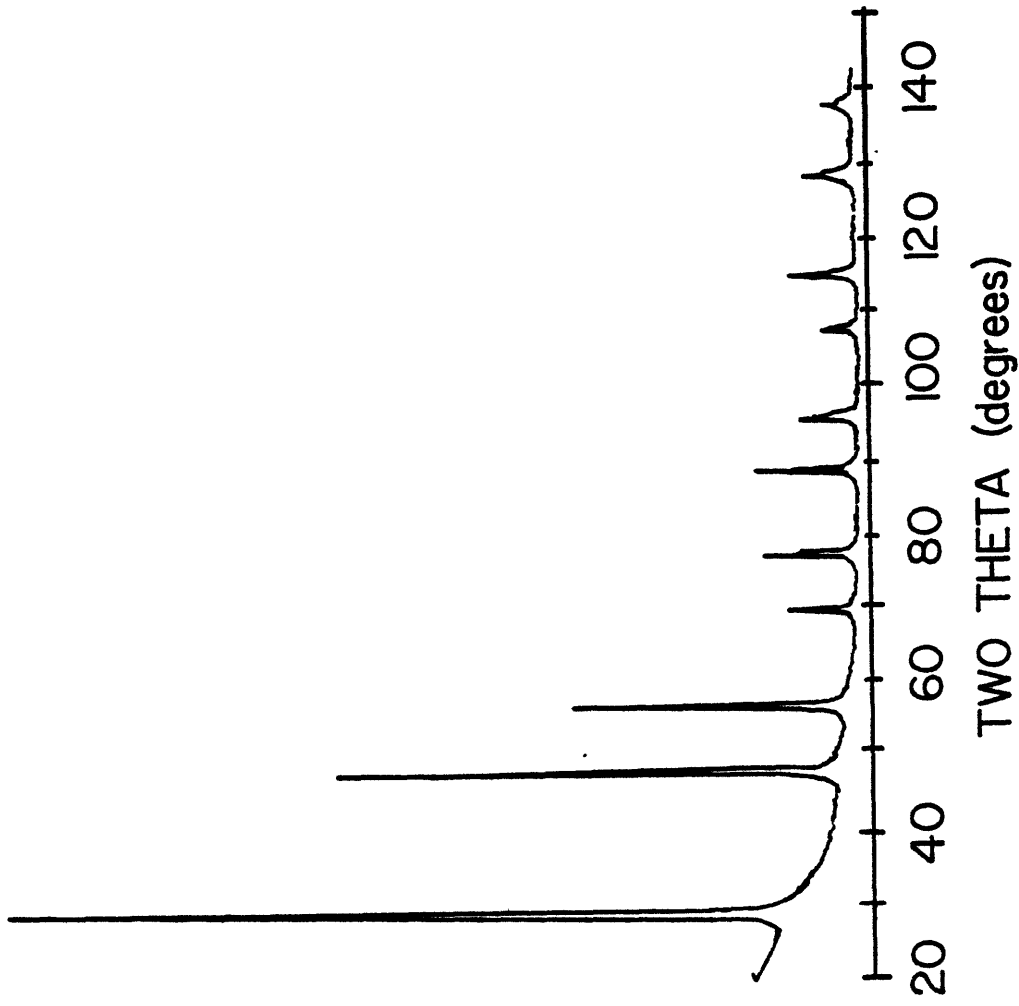


Figure IV.22. X-ray diffraction pattern of a typical laser synthesized silicon powder. ($\text{Cu}_{\text{K}\alpha}$ radiation)

in Figure IV.23. Also included in this figure are some results⁵ for Si_3N_4 powder synthesized from SiH_4/NH_3 gas mixtures and SiC powders synthesized from $\text{SiH}_4/\text{C}_2\text{H}_4$ mixtures. The BET surface area was measured by both single and multipoint methods. The results of the multipoint method, which is more accurate, showed that in all cases the value of the BET constant C was greater than 50. Therefore, the single point method can be used with less than 5% error. The results of the multipoint measurements are presented and discussed in Appendix 3. The accordance of the BET equivalent diameter and the diameter measured from TEM suggests the particles have a narrow size distribution, spherical shape, no porosity accessible to the surface, and smooth surfaces.

Powder densities of selected runs were determined from helium pycnometric measurements. The measured densities are summarized in Table IV.2. There was no appreciable difference in the density for large and small particle sized polycrystalline, amorphous, or boron doped silicon powders. All the measured densities ranged from 2.22 to 2.25 g/cm^2 . These values are slightly smaller than the generally accepted density for single crystalline silicon at 2.33 g/cm^2 .⁹⁹ There are several sources of error that may result in a low value for the powder density. If the surface contains open porosity or surface roughness with dimensions on the order of 0.1 nm, then the helium gas molecules cannot completely penetrate the crevices and a sample volume larger than actual is measured. A similar result occurs if any surface contaminants fill the fine pores. For large surface area powder, the annulus volume between the powder surface and the center of mass of the gas molecules at the interface may be significant. This

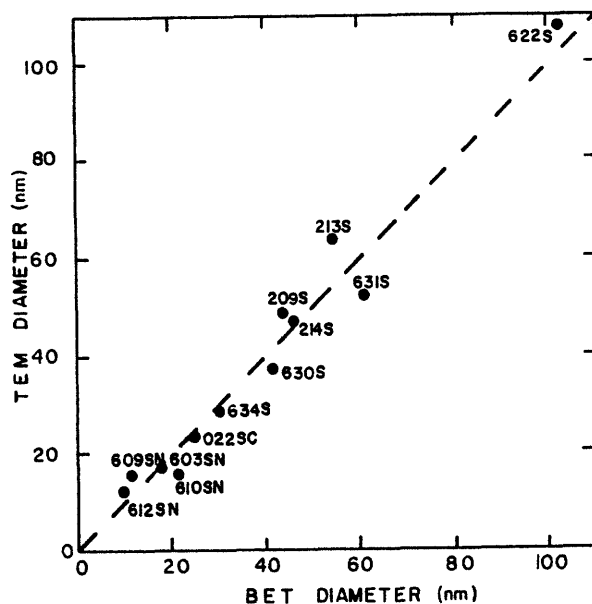


Figure IV.23. Comparison of particle diameter measured by transmission electron microscopy and BET surface area.

Table IV.2. Density of Silicon Powder Measured by He Pycnometry

Powder	Sample Weight (g)	Volume (cm ³)	Density (g/cm ³)
660S	0.48	0.216 ± 0.003	2.22 ± 0.028
623S	7.23	3.25 ± 0.130	2.23 ± 0.083
657S	3.33	1.48 ± 0.006	2.26 ± 0.006
SB4*	1.09	0.493 ± 0.005	2.21 ± 0.020

* Powder SB4 synthesized with a reactant gas comprised of 2/1 SiH₄ to 1.0% B₂H₆ + 99.0% Ar mixture.

will again lead to a measured sample volume larger than actual. It is also possible that the particles have a lower density oxide coating which results in a true density lower than crystalline silicon. Taking into account the above considerations, it was concluded that the silicon powders had no internal porosity.

2. Effect of Process Variables

a. Gas Velocity

Three sets of experimental runs were performed with pure SiH_4 (Ar was used as the annular and window gases) to examine the effect of reactant gas velocity. The powders were synthesized at either 2×10^4 Pa, 3.5×10^4 Pa, or 6×10^4 Pa. The velocity was altered by changing the volumetric flow rate of SiH_4 . Both the series of runs at 2×10^4 Pa and 6×10^4 Pa were produced with a 150 W unfocused laser beam, while the powders produced at 3.5×10^4 Pa utilized a 170 W unfocused beam. These runs are summarized in Appendices 1 and 2.

The effect of velocity on the reaction zone temperature was discussed in Section IVA. Figures IV.24, IV.25, and IV.26 show the effect of gas velocity on the equivalent spherical diameter calculated from single point BET surface area measurements. Each data point represents the average of two surface area determinations. All three curves exhibit an ascending-descending behavior with the largest sized particles resulting from reaction zones having the highest maximum temperatures. Flow velocity had no noticeable effect on the powder chemistry, agglomeration, or conversion efficiency.

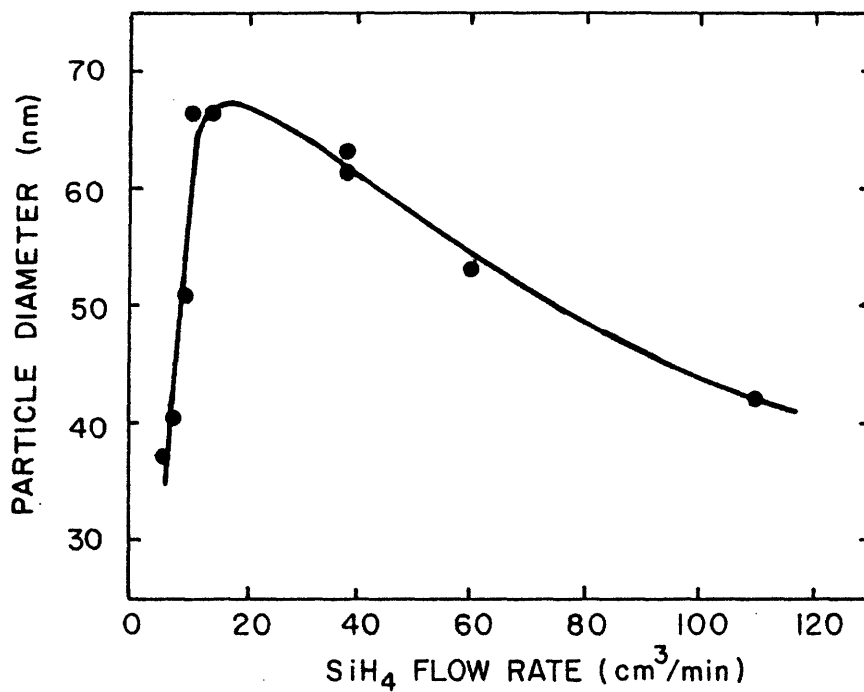


Figure IV.24. Effect of flow rate on the particle diameter calculated from the BET surface area measurements. (Pressure = 2×10^4 Pa, Laser intensity = 531 W/cm^2)

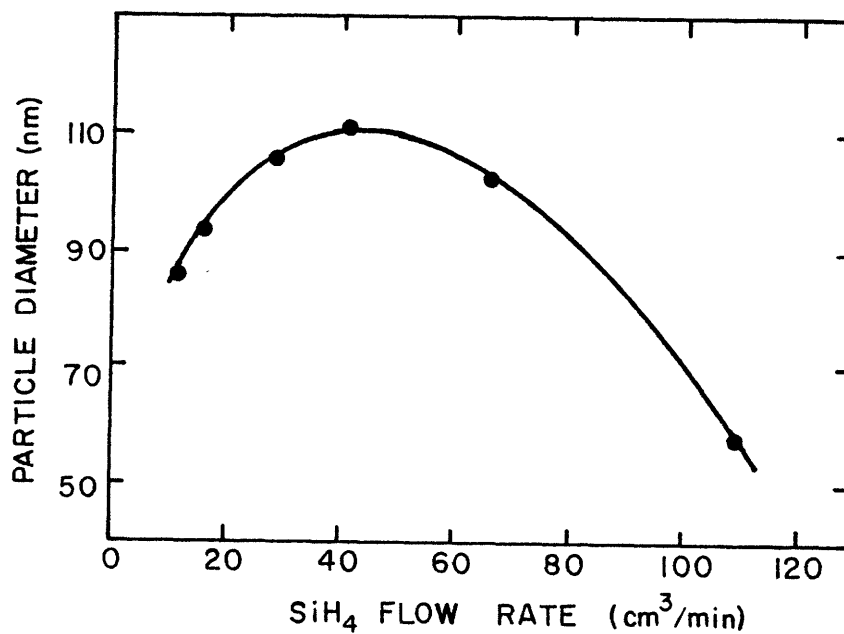


Figure IV.25. Effect of flow rate on the particle diameter calculated from the BET surface area measurements. (Pressure = 3.5×10^4 Pa, Laser intensity = 601 W/cm^2)

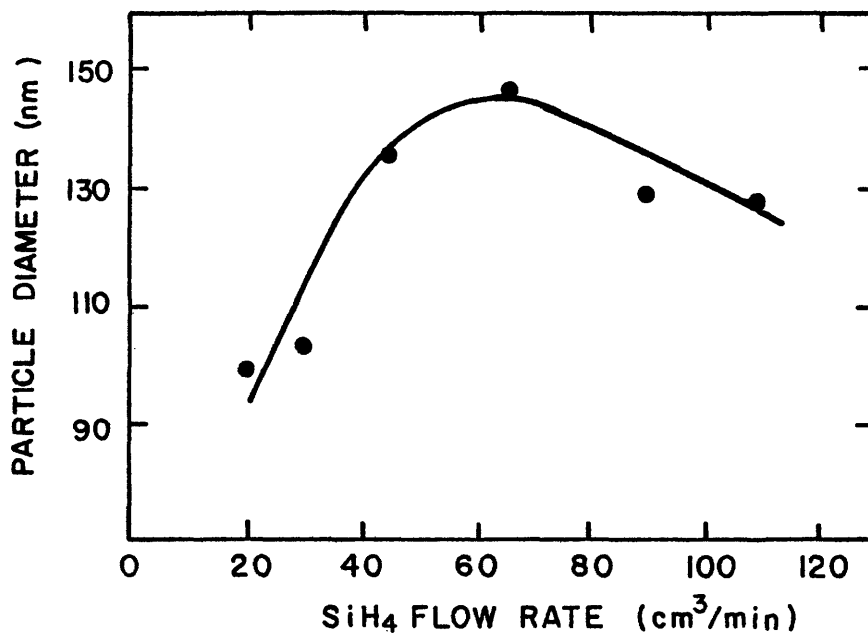


Figure IV.26. Effect of flow rate on the particle diameter calculated from the BET surface area measurements. (Pressure = 6×10^4 Pa, Laser intensity = 531 W/cm^2)

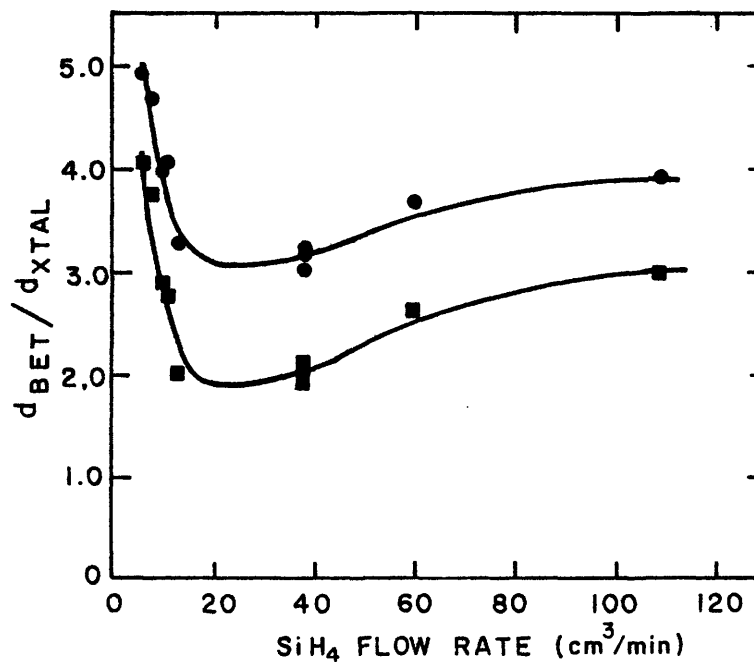


Figure IV.27. Effect of flow rate on the ratio of particle to crystallite size. ● assumes Gaussian shaped X-ray peaks. ■ assumes Cauchy shaped X-ray peaks. (Pressure = 2×10^4 Pa, Laser intensity = 531 W/cm^2)

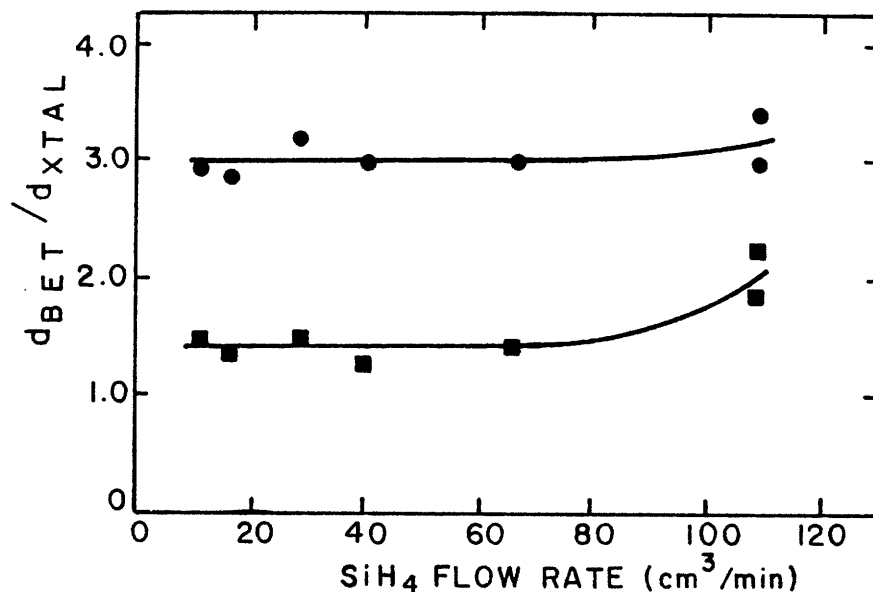


Figure IV.28. Effect of flow rate on the ratio of particle to crystallite size. ● assume Gaussian shaped X-ray peaks. ■ assumes Cauchy shaped X-ray peaks. (Pressure = 3.5×10^4 Pa, Laser intensity = 601 W/cm^2)

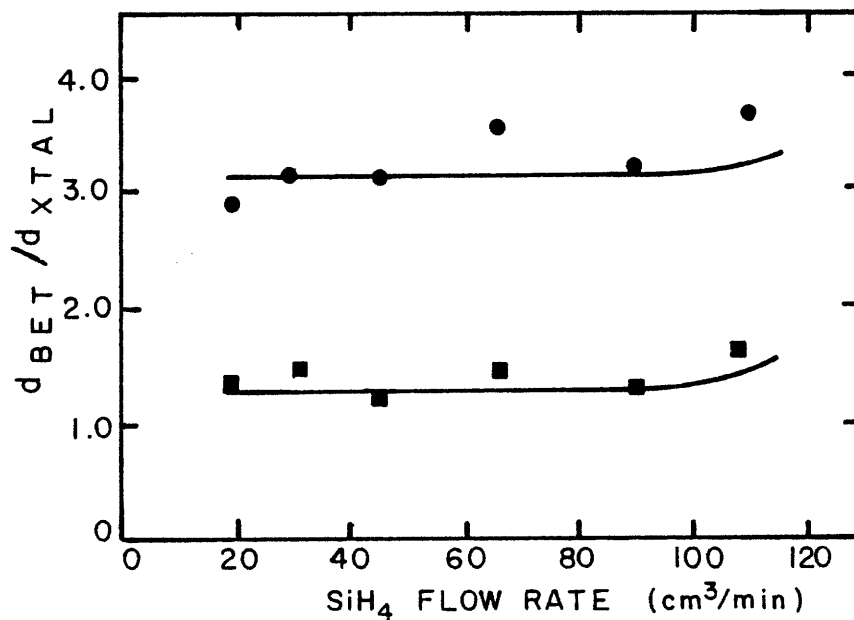


Figure IV.29. Effect of flow rate on the ratio of particle to crystallite size. ● assumes Gaussian shaped X-ray peaks. ■ assumes Cauchy shaped X-ray peaks. (Pressure = 6×10^4 Pa, Laser intensity = 531 W/cm^2)

The X-ray line broadening results are summarized in Appendix 2 and shown graphically in Figures IV.27, IV.28, and IV.29 for powders produced at 2×10^4 Pa, 3.5×10^4 Pa and 6×10^4 Pa respectively. The results are plotted as the ratio of BET equivalent diameter to crystallite diameter versus the flow rate. Examination of Figures IV.27 and IV.4, shows that at 2×10^4 Pa, the largest relative crystallite size [the smallest ratio of $d(\text{BET})/d(\text{X-ray})$] occurred for powder produced at the highest maximum reaction zone temperature. For powders produced at 3.5×10^4 Pa, the relative crystallite size remained essentially constant ($[d(\text{BET})/d(\text{X-ray, gaussian})] = 3.0$) and independent of both the flow rate and the reaction zone temperature except at the highest flow rate where the ratio $d(\text{BET})/d(\text{X-ray})$ appeared to increase slightly. At 6×10^4 Pa, the ratio $d(\text{BET})/d(\text{X-ray})$ was constant over the entire flow range. These results will be discussed further in Section IVF.

b. Laser Intensity

Several runs in which all process variables were held constant except laser intensity are summarized in Appendices 1 and 2. All these runs used an unfocused beam with a beam diameter of 0.6 cm except Run 645S where the 170 W laser beam was focused to a spot size of 0.2 cm producing an average intensity of 5400 W/cm^2 . The average intensity for the unfocused beam runs ranged from 134 W/cm^2 (658S) to 601 W/cm^2 (622S). The effect of intensity on the reaction zone temperature was summarized in Section IVA. The particle size increased significantly as the intensity was increased, as shown graphically in Figure IV.30.

Comparison of Run 622S (170 W unfocused beam) with Run 645S (170 W beam focused to 0.2 cm) showed that an approximate tenfold increase in laser intensity resulted in only a 7% increase in the particle diameter. This suggests that the maximum particle size achievable by the laser synthesis technique is limited. This is primarily a result of the large number of nuclei produced per unit volume by homogeneous nucleation. Various suggestions for the synthesis of larger particles are discussed in Section VI.

Occasionally, an experimental perplexity was encountered with low laser intensity synthesis runs. The Coherent Model 150 CO₂ laser was found to switch emission lines from P(20) to P(18) or combinations of these lines when operated at low laser intensities. It was particularly noticeable for Run 638S at 75 W (intensity = 264 W/cm²). Since the absorption coefficient of SiH₄ is higher for the P(20) emission line than the P(18) line,⁵ it is expected that the reaction zone and powder characteristics would be noticeably different for P(20) and P(18) absorption. By monitoring the emitted intensity at 632.8 nm with a photomultiplier, it was found that for Run 638S the reaction flame exhibited two types of behavior. During certain time intervals, the flame was relatively stable and the emitted intensity was constant. At other times, the flame flickered continuously and the emitted intensity was highly erratic with a much lower average value. This second type of behavior is consistent with the emission of a combination of P(18) and P(20) radiation. The particle size for this run (see Figure IV.30) was smaller than expected, probably a result of the emission line switching.

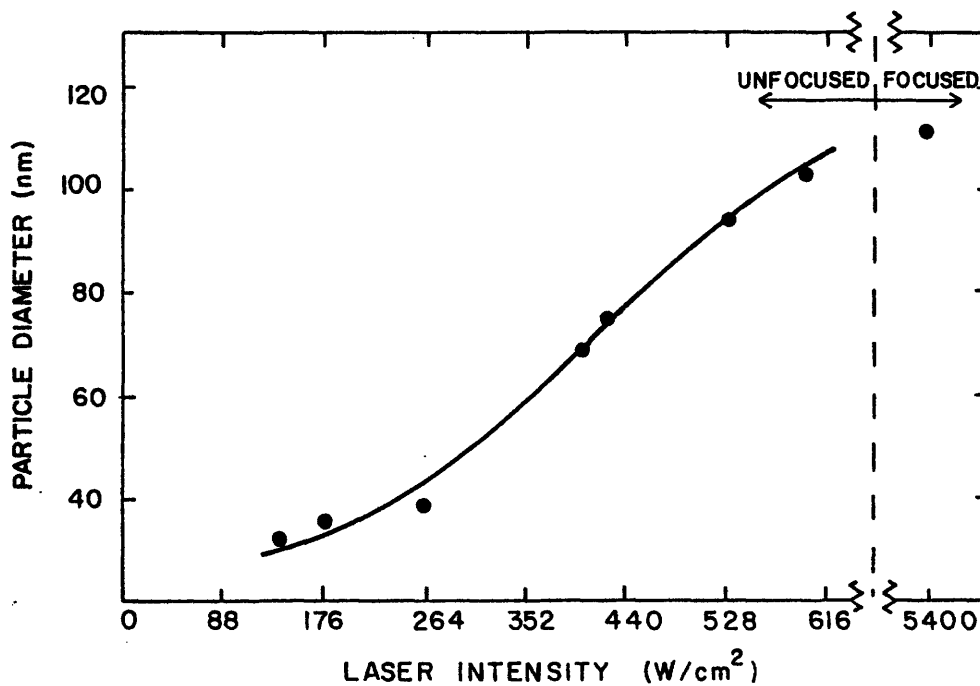


Figure IV.30. Effect of laser intensity on the particle diameter calculated from the BET surface area measurements. (Pressure = 3.5×10^4 Pa, Silane flow rate = $66 \text{ cm}^3/\text{min}$)

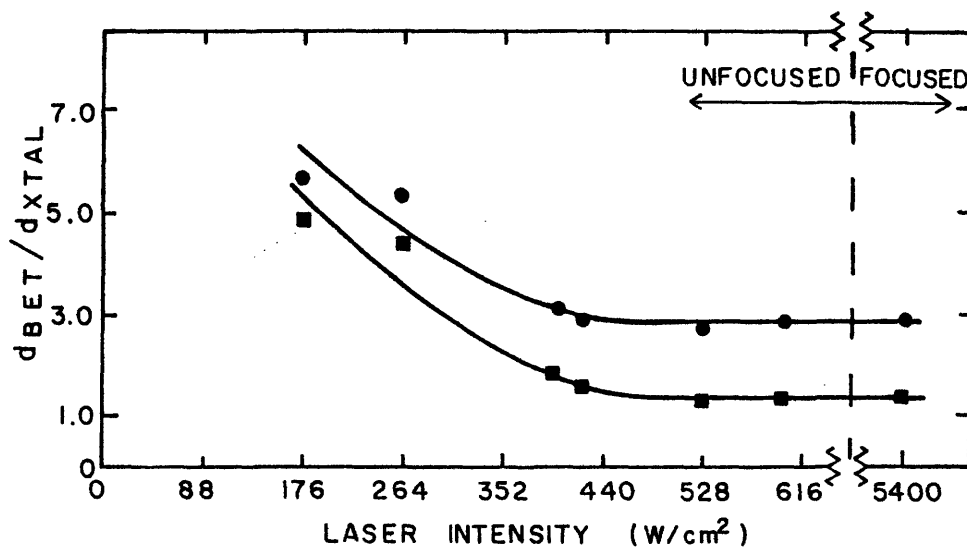


Figure IV.31. Effect of laser intensity on the ratio of particle to crystallite size. ● assumes Gaussian shaped X-ray peaks, ■ assumes Cauchy shaped X-ray peaks. (Pressure = 6×10^4 Pa, Silane flow rate = $66 \text{ cm}^3/\text{min}$)

The results of X-ray diffraction line broadening are shown in Figure IV.31. The $d_{\text{(BET)}}/d_{\text{(X-ray)}}$ ratio was approximately constant and equal to 3.0 for powders produced with intensities greater than 400 W/cm^2 . The powder produced with the focused laser beam (Run 645S) had a similar crystal structure. As the laser intensity was decreased, the $d_{\text{(BET)}}/d_{\text{(X-ray)}}$ ratio increased suggesting a temperature dependence similar to that observed for powders synthesized at 0.2 atm and a 150 W unfocused beam (see previous section). The X-ray diffraction pattern of the powder produced at 38 W (658S) showed a very broad peak suggesting an amorphous structure. This powder was observed by STEM to determine whether the particles were actually amorphous or comprised of small crystallites. The results, described in Section IVF, showed the powder to be amorphous within the resolution of the STEM.

Even for the lowest intensity run (658S, 38 W unfocused beam) the conversion efficiency was greater than 95%. Therefore, very little power is required to fully convert the SiH_4 gas to solid silicon.

c. Ar Dilution

A series of runs was made to examine the effect of diluting the reactant gas stream with argon. Runs 631S, 632S, and 653S were made under identical conditions with the reactant gas stream comprised of pure SiH_4 to serve as a benchmark from which the effect of dilution could be compared. In the other runs, the argon dilution ranged from a 1/5 Ar/ SiH_4 mixture (Run 662S) to a 5/1 mixture (634S). The process conditions for these runs as well as the resulting reaction zone and powder characteristics are summarized in Appendices 1 and 2.

The effect of dilution on the reaction zone temperature was discussed in Section IVA. Figure IV.32 shows the equivalent spherical diameter determined from the BET surface area measurements as a function of the Ar dilution. The particle size appeared to be fairly constant below 50 mole % Ar dilution. Further dilution of the reactant gas stream resulted in a decrease in the BET equivalent particle size.

All these powders were crystalline to X-ray diffraction. The ratio of $d_{\text{BET}}/d_{\text{X-ray}}$ versus the mole fraction Ar is plotted in Figure IV.33. This ratio was constant up to 50 mole % dilution and then increased as the reactant gas stream was further diluted. Once again the larger ratio of $d_{\text{BET}}/d_{\text{X-ray}}$ appears to be related to a decrease in the reaction zone temperature. The crystallinity of these powders is discussed more fully in Section IVF.

Figure IV.20 shows a TEM micrograph of powder 634S (5/1 Ar/SiH₄ ratio). The average particle size measured from this micrograph is 27.5 nm, which is in close agreement with BET equivalent diameter of 29 nm. The particle size appears to be quite uniform, ranging from 19 nm to 35 nm. It was anticipated that diluting the gas stream with Ar would decrease the probability of collision between particles and thus reduce the particle agglomeration. Figure IV.20 shows that the powder produced with this dilution still exhibits the typical two-dimensional chain-like agglomerates. The agglomeration is discussed more fully in Section IVE.

Two additional runs (655S and 660S) were made in which the reaction zone was diluted with Ar. In addition these runs were produced at lower laser intensities than the runs described above. It was anticipated that the combined effects of lowering the laser

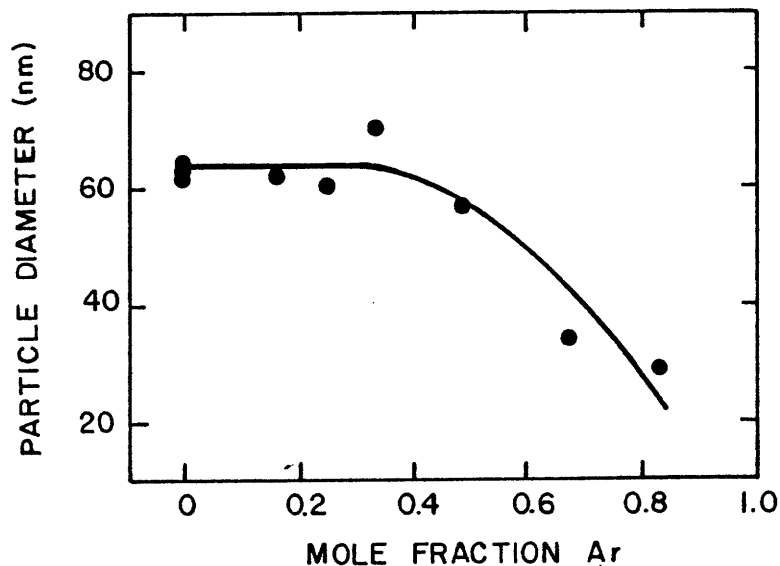


Figure IV.32. Effect of argon dilution on the particle diameter calculated from the BET surface area measurements. (Pressure = 2×10^4 Pa, Total flow rate = $38 \text{ cm}^3/\text{min}$, Laser intensity = $531 \text{ W}/\text{cm}^2$)

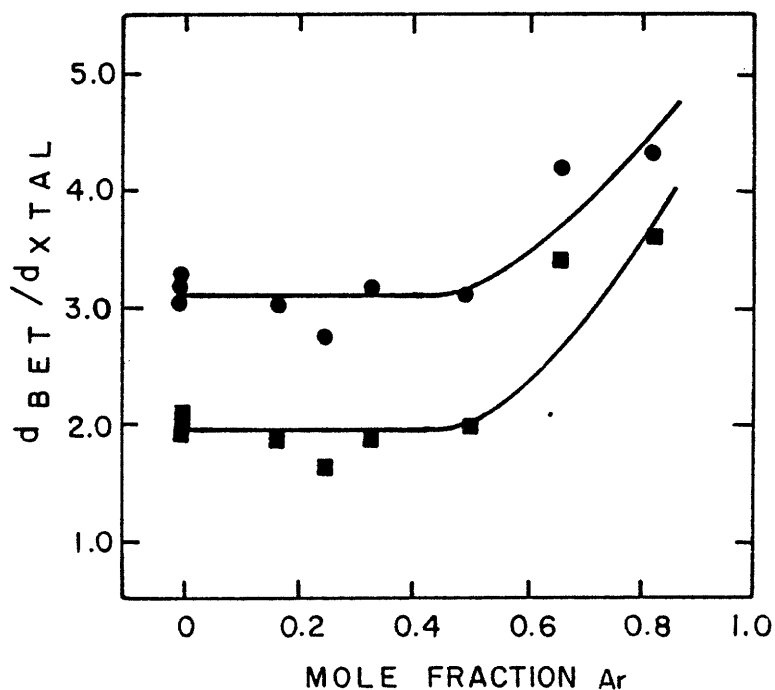


Figure IV.33. Effect of argon dilution on the ratio of particle to crystallite size. ● assumes Gaussian shaped X-ray peaks, ■ assumes Cauchy shaped X-ray peaks. (Pressure = 2×10^4 Pa, Total flow rate = $38 \text{ cm}^3/\text{min}$, Laser intensity = $531 \text{ W}/\text{cm}^2$)

intensity and diluting the reactant gas with Ar would result in a low reaction zone temperature thereby producing an amorphous Si powder. These runs are also summarized in Appendices 1 and 2. The powder produced with a 75 W unfocused beam and a 1/1 Ar/SiH₄ gas mixture did not appear totally amorphous but had a particle diameter of 29 nm (from BET surface area measurements) with small crystallites (5.8 nm). Run 660S, with a 50 W unfocused beam and a 2/1 Ar/SiH₄ gas mixture, produced powder with a very large BET surface area, 136 m²/g (equivalent spherical diameter of 19 nm). X-ray diffraction revealed only very broad peaks suggesting an amorphous structure. The reaction flame was too dim for a temperature to be measured. Bright field - dark field TEM or STEM will have to be done to determine conclusively whether the structure is truly amorphous or comprised of very fine crystallites.

d. Cell Pressure

The effect of pressure on the reaction zone and powder characteristics was examined by comparing the two series of runs produced at 2×10^4 Pa and 6×10^4 Pa. It is difficult to make a run to run comparison because of the difficulty of maintaining constant flow conditions while changing the total cell pressure. An increase in cell pressure resulted in an increase in the maximum reaction zone temperature as was described in Section IVA. Comparison of Figures IV.24 and IV.26 show that increased pressure produced a larger particle diameter. The same trend was observed for the powders produced at 3.5×10^4 Pa, however, since these powders were synthesized with a

170 W power instead of 150 W, a direct comparison with the runs synthesized at 2×10^4 Pa and 6×10^4 Pa is not valid.

Examination of Figures IV.27, IV.28 and IV.29 suggest that changes in total reaction cell pressures effected the crystallinity of the powders. For powders produced at 6×10^4 Pa, the ratio of the BET equivalent diameter to the crystallite size measured by X-ray line broadening was constant, while this ratio was dependent on reaction temperature for powders produced at 2×10^4 Pa. The difference in the crystallinity may be solely a consequence of the increased maximum reaction temperature at the higher cell pressure. The ratio of the BET diameter to the crystallite diameter as related to the crystal structure of the individual particles is discussed more fully in Section IVF. The increase in pressure had no noticeable effect on the conversion efficiency, particle chemistry, or agglomeration.

e. Boron Doping and Powder Synthesis Reproducibility

Various sets of runs were performed using identical process conditions to produce sufficient quantities of powder for sintering and nitriding studies and to examine the reproducibility of the laser synthesis process. These runs consisted of three runs produced with pure SiH_4 (631S, 632S, and 653S), 10 runs synthesized with a 1/2 Ar/ SiH_4 gas mixture and 9 runs having the identical conditions as the 1/2 Ar/ SiH_4 runs except a 1% B_2H_6 + 99% Ar gas mixture was used instead of pure Ar. The reaction zone and powder characteristics are summarized in Appendices 1 and 2 and Table IV.3.

Table IV.3. Comparison of B_2H_6/SiH_4 and Undoped SiH_4 Runs*

Run Type	BET Equivalent Size (nm)	Uncorrected Pyrometer Temperature ($^{\circ}C$)
SiH_4/Ar	55.1 ± 4.5	980 ± 6
$SiH_4/Ar + 1\%B_2H_6$	54.9 ± 2.3	1012 ± 10

*For all runs: Pressure = 2×10^4 Pa, Laser Intensity = 531 W/cm^2 ,
 SiH_4 Flow Rate = $50 \text{ cm}^3/\text{min}$, Ar or $Ar+B_2H_6$ = $25 \text{ cm}^3/\text{min}$

For these runs utilizing pure SiH_4 (631S, 632S, and 653S), the reaction temperature, conversion efficiencies, equivalent size calculated from the BET surface area, and the crystallite size measured by X-ray line broadening are nearly identical. These results show the process is easily controllable and can produce powders with similar characteristics from run to run. It should be noted that many of the earlier silicon powders were made with SiH_4 flow rates of about $10 \text{ cm}^3/\text{min}$ and a cell pressure of 2×10^4 Pa.⁸⁵ It is evident from Figures IV.4, IV.24 and IV.27 that in this regime, the reaction zone and particle characteristics exhibit large variation with small changes in flow rate. The differences previously reported⁸⁵ between powders synthesized with these lower, nominally identical SiH_4 flow rates are probably attributable to minor variations in the reactant gas flow rates.

The results of the runs synthesized with Ar/SiH_4 and $(1\% B_2H_6 + 99\% Ar)/SiH_4$ gas mixtures can be used to both verify the

reproducibility and determine the effects, if any, of B_2H_6 on the reaction zone and particle characteristics. For each set of runs, the results summarized in Table IV.3 indicate that the particle size and reaction temperatures were reproducible. Introducing B_2H_6 had little effect on the particle or crystallite size. It appears that the reaction temperature, measured by uncorrected optical pyrometry, increased slightly for the B-doped runs. For all runs, the conversion efficiency was greater than 85% and was not related to the addition of B_2H_6 . If the SiH_4 is completely reacted and the B_2H_4 is 100% incorporated in the particles, the powder should contain 0.38 wt. % boron. Chemical analyses indicated that 0.47 wt. % boron was incorporated into the powders. Within the precision of the analyses, the results indicate that all the B_2H_6 was incorporated.

D. Discussion of Particle Nucleation and Growth

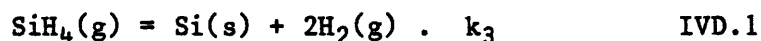
1. Nucleation

The formation of silicon particles via vapor phase reactions occurs by homogeneous nucleation and growth processes. Four stages of the phase transformation are the development of a supersaturated state, generation of nuclei of the new phase, growth of nuclei to form larger particles, and relaxation processes, such as coarsening and agglomeration.

A thermodynamic analysis of the nucleation of solid particles from the vapor phase is important for determining to what extent reactions will occur in the absence of any kinetic limitations. The

difficulty of carrying out the desired thermodynamic analysis depends upon the complexity and number of chemical reactions and species which must be considered. For a simple process involving only a single reaction and a few chemical species, the analysis is straight forward requiring only the knowledge of the equilibrium constant at the temperature of interest. For more complicated processes, it is necessary to calculate the type and amount of each chemical species which produces the minimum free energy configuration of the system. This requires knowledge of all pertinent equilibrium constants and computer calculating capabilities.

Both unimolecular and chain mechanisms have been reported for monosilane decomposition. The unimolecular decomposition leads to the formation of silicon and hydrogen by a simple chemical reaction.



The chain reaction occurs with the participation of radicals (SiH_2 , SiH_3 , Si_2H_5 , etc.) and usually results in the formation of higher silanes (Si_2H_6 , Si_3H_8 , etc.).

An early study of the laser induced silane decomposition by Oraevskii et al.⁷⁵ showed the only gaseous product was hydrogen suggesting that the decomposition occurred by a unimolecular mechanism. In a detailed study of the infrared laser photochemistry of silane, using mass spectroscopy Deutsch⁴⁹ detected SiH_2 and a number of unidentified peaks with masses between 32 and 44, however there was no evidence of the higher silanes. Bilenchi and Musci⁷⁶ found SiH_2 , SiH_3 and molecular hydrogen in the gas phase during the CO_2 laser enhanced CVD of amorphous silicon. Again there was no evidence of the higher silanes. These results are not sufficient to determine the actual

mechanism for decomposition, although the absence of the higher silanes suggests the laser induced pyrolysis occurs by a simple decomposition reaction.

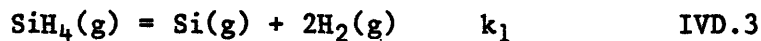
The maximum amount of solid produced can be calculated by assuming a unimolecular reaction occurs, that is only reaction IVD.1 is of importance. Since the equilibrium constant for this reaction is large, the conversion of silane to solid silicon is greater than 99.9% at all temperatures. Therefore, if the reaction was thermodynamically limited, the rate of synthesis would be essentially equal to the rate of silane input. In actuality, kinetic factors generally prevent achieving equilibrium and the rates are less than would be predicted by thermodynamics.

The thermodynamic analysis predicts that at temperatures as low as 300K, the rate of synthesis of solid silicon should be essentially equal to the input of silane gas. This is obviously not valid. It is necessary to examine the nucleation behavior in order to fully understand the reaction kinetics. In order for nucleation to occur at a significant rate, the vapor phase must be sufficiently supersaturated to overcome the free energy barrier imposed by creating a solid surface. Kinetically, there must be a sufficient number of silicon atoms in the vapor phase since nucleation occurs by an accretion process limited by the rate at which monomeric silicon collides with other monomers or existing clusters to create a nuclei of super critical size. It is therefore necessary to determine the concentration of silicon vapor molecules, the supersaturation ratio, and the nucleation rate from the existing theories.

Assuming the decomposition reaction occurs by a unimolecular mechanism, the supersaturation ratio within the reactant gas stream can be calculated as a function of temperature and gas composition from classical thermodynamics. The supersaturation ratio SS is determined by the quotient of the partial pressure of Si(g) in the reactant gas stream divided by the equilibrium vapor pressure of Si

$$SS = \frac{P_{\text{Si(reacting)}}}{P_{\text{Si(equilibrium)}}} \quad \text{IVD.2}$$

The equilibrium concentration of silicon vapor in the reactant gas stream is determined from the reaction:



with an equilibrium constant

$$k_1 = \frac{P_{\text{Si(g)}} P_{\text{H}_2}^2}{P_{\text{SiH}_4}} \quad \text{IVD.4}$$

Defining ξ as the extent of reaction:

$$\xi = \frac{n_j - n_j^i}{\nu_j} \quad \text{IVD.5}$$

where n_j is the number of moles of species j at equilibrium, n_j^i is the initial amount of species j and $\nu_{\text{SiH}_4} = +1$, $\nu_{\text{H}_2} = -2$ and $\nu_{\text{Si}} = -1$, the following relations can be written:

$$n_{\text{SiH}_4} = n_{\text{SiH}_4}^i - \xi \quad \text{IVD.6}$$

$$n_{\text{Si}} = n_{\text{Si}}^i + \xi \quad \text{IVD.7}$$

$$n_{\text{H}_2} = n_{\text{H}_2}^i + 2\xi \quad \text{IVD.8}$$

$$n_{\text{total}} = n_{\text{SiH}_4}^i + n_{\text{Si}}^i + n_{\text{H}_2}^i + 2\xi \quad \text{IVD.9}$$

Assuming ideal gas behavior, the partial pressure of each gas species is related to the total pressure by:

$$P_j = X_j P_{\text{tot}} \quad \text{IVD.10}$$

where the mole fraction $X_j = \frac{n_j}{n_{\text{total}}}$. For simplicity, the initial gas mixture is assumed to comprise of 1 mole of pure SiH_4 at a pressure P . Thus the equilibrium partial pressure of each species is

$$P_{\text{SiH}_4} = \left(\frac{1 - \xi}{1 + 2\xi} \right) P \quad \text{IVD.11}$$

$$P_{\text{Si}} = \left(\frac{\xi}{1 + 2\xi} \right) P \quad \text{IVD.12}$$

$$P_{\text{H}_2} = \left(\frac{2\xi}{1 + 2\xi} \right) P \quad \text{IVD.13}$$

and the equilibrium constant is

$$k_1 = \frac{4\xi^3 P^2}{(1 + 2\xi^2)(1 - \xi)} \quad \text{IVD.14}$$

With a known value for the equilibrium constant and a given total pressure P , the extent of reaction can be calculated from Equation IVD.14 and the equilibrium partial pressures of $P_{\text{SiH}_4(\text{g})}$, $P_{\text{H}_2(\text{g})}$ and $P_{\text{Si}(\text{g})}$ can be determined from Equations IVD.11, IVD.12, and IVD.13. Table IV.4a shows the equilibrium concentration of the gas species for a reactant gas stream comprised of pure SiH_4 at 0.2 atm as a function of reaction temperature. It is evident that at a low reaction temperature, the equilibrium concentrations of $\text{Si}(\text{g})$ and $\text{H}_2(\text{g})$ are very small. Even with a reaction temperature at 1300K, the extent of reaction ξ is less than 10%.

Table IV.4a. Extent of Gas Phase Decomposition and Equilibrium Pressures of Gaseous Species ($P_{\text{SiH}_4, \text{int}} = 0.2 \text{ atm}$)

Temp (°K)	$\log k_3$	Extent of Reaction, ξ	$P(\text{SiH}_4)$ (atm)	$P(\text{Si})$ (atm)	$P(\text{H}_2)$ (atm)
300	-61.046	8.25×10^{-21}	~ 0.20	1.65×10^{-21}	3.30×10^{-21}
400	-42.781	1.01×10^{-14}	~ 0.20	2.02×10^{-15}	4.04×10^{-15}
500	-31.746	4.82×10^{-11}	~ 0.20	9.64×10^{-12}	1.92×10^{-11}
600	-24.351	1.41×10^{-8}	~ 0.20	2.82×10^{-9}	5.64×10^{-9}
700	-19.052	8.22×10^{-7}	~ 0.20	1.64×10^{-7}	3.29×10^{-7}
800	-15.069	1.75×10^{-5}	~ 0.20	3.50×10^{-6}	7.00×10^{-6}
900	-11.969	1.89×10^{-4}	~ 0.20	3.78×10^{-5}	7.56×10^{-5}
1000	-9.489	1.27×10^{-3}	0.199	2.53×10^{-4}	5.07×10^{-4}
1100	-7.461	6.33×10^{-3}	0.196	1.25×10^{-3}	2.50×10^{-3}
1200	-5.772	2.24×10^{-2}	0.187	4.29×10^{-3}	8.58×10^{-3}
1300	-4.347	6.98×10^{-2}	0.163	1.22×10^{-2}	2.44×10^{-2}
1400	-3.128	1.93×10^{-1}	0.117	2.78×10^{-2}	5.57×10^{-2}
1500	-2.074	4.72×10^{-1}	0.054	4.85×10^{-2}	9.71×10^{-2}
1600	-1.154	8.20×10^{-1}	0.014	6.21×10^{-2}	1.24×10^{-1}

Table IV.4b. Nucleation Calculations for a Reaction Zone Initially Comprised of 0.2 atm. of Pure Silane

Temp (°K)	P_{Si} (atm)	P_{Si} (atm)	ln SS	r^* (nm)	ΔG_r^* (J)	J (#/cm ³ ·s)
300	1.65×10^{-21}	2.12×10^{-71}	114.9	0.075	2.15×10^{-20}	7.4×10^{-17}
400	2.02×10^{-15}	8.77×10^{-55}	90.6	0.072	1.94×10^{-20}	3.5×10^{-4}
500	9.64×10^{-12}	5.16×10^{-40}	65.1	0.080	2.40×10^{-20}	7.4×10^3
600	2.82×10^{-9}	3.59×10^{-32}	52.7	0.082	2.55×10^{-20}	7.6×10^8
700	1.64×10^{-7}	1.43×10^{-26}	43.9	0.085	2.70×10^{-20}	2.4×10^{12}
800	3.50×10^{-6}	2.24×10^{-22}	37.3	0.087	2.70×10^{-20}	1.4×10^{15}
900	3.78×10^{-5}	4.06×10^{-19}	32.2	0.090	3.03×10^{-20}	1.7×10^{17}
1000	2.53×10^{-4}	1.63×10^{-16}	28.1	0.093	3.23×10^{-20}	7.5×10^{18}
1100	1.25×10^{-3}	2.20×10^{-14}	24.8	0.095	3.43×10^{-20}	1.8×10^{20}
1200	4.29×10^{-3}	1.30×10^{-12}	21.9	0.099	3.70×10^{-20}	2.1×10^{21}
1300	1.22×10^{-2}	4.09×10^{-11}	19.5	0.103	3.97×10^{-20}	1.6×10^{22}
1400	2.78×10^{-2}	7.81×10^{-10}	17.4	0.107	4.30×10^{-20}	8.3×10^{22}
1500	4.85×10^{-2}	1.00×10^{-8}	15.4	0.113	4.78×10^{-20}	2.3×10^{23}
1600	6.21×10^{-2}	9.35×10^{-8}	13.4	0.121	5.55×10^{-20}	3.2×10^{23}



The Libraries
Massachusetts Institute of Technology
Cambridge, Massachusetts 02139

Institute Archives and Special Collections
Room 14N-118
(617) 253-5688

There is no text material missing here.
Pages have been incorrectly numbered.

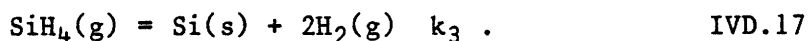
P. 146

Table IV.5. Extent of Gas Phase Decomposition and Equilibrium Pressures of Gaseous Species ($P_{\text{SiH}_4, \text{int}} = 0.2 \text{ atm}$)

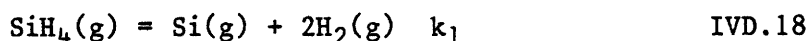
Temp (°K)	$\log k_3$	Extent of Reaction, ξ	$P(\text{SiH}_4)$ (atm)	$P(\text{Si})$ (atm)	$P(\text{H}_2)$ (atm)
300	-61.046	3.97×10^{-21}	~ 0.6	2.38×10^{-21}	4.76×10^{-21}
400	-42.781	4.86×10^{-15}	~ 0.6	2.92×10^{-15}	5.89×10^{-15}
500	-31.746	2.32×10^{-11}	~ 0.6	1.39×10^{-11}	2.78×10^{-11}
600	-24.351	6.75×10^{-9}	~ 0.6	4.06×10^{-9}	8.12×10^{-9}
700	-19.052	3.95×10^{-7}	~ 0.6	2.37×10^{-7}	4.74×10^{-7}
800	-15.069	8.41×10^{-6}	~ 0.6	5.04×10^{-6}	1.01×10^{-5}
900	-11.969	9.07×10^{-5}	~ 0.6	5.44×10^{-5}	1.08×10^{-4}
1000	-9.489	6.09×10^{-4}	0.599	3.65×10^{-4}	7.30×10^{-4}
1100	-7.461	2.89×10^{-3}	0.595	1.74×10^{-3}	3.48×10^{-3}
1200	-5.772	1.07×10^{-2}	0.581	6.29×10^{-3}	1.26×10^{-2}
1300	-4.347	3.25×10^{-2}	0.545	1.83×10^{-2}	3.66×10^{-2}
1400	-3.128	8.66×10^{-2}	0.467	4.43×10^{-2}	8.86×10^{-2}
1500	-2.074	2.11×10^{-1}	0.333	8.90×10^{-2}	1.78×10^{-1}
1600	-1.154	4.59×10^{-1}	0.168	1.44×10^{-1}	2.88×10^{-1}

reacting vapor pressure of Si(g) increased slightly as the pressure was raised from 0.2 to 0.6 atm. This results in a slight increase in the supersaturation ratio at any temperature.

The overall driving force for nucleation is the reduction in free energy accompanying the formation of solid silicon:



This reaction is the sum of the reactions:



and



Therefore:

$$k_3 = k_1 \cdot k_2 \quad \text{IVD.20}$$

The supersaturation ratio can be defined in terms of the equilibrium vapor pressure of the reacting gases:

$$SS = \frac{P_{\text{Si}}}{P_{\text{Si}}} = \frac{k_1 k_2 P_{\text{SiH}_4}}{P_{\text{H}_2}^2} = \frac{k_3 P_{\text{SiH}_4}}{P_{\text{H}_2}^2} \quad \text{IVD.22}$$

As stated above, Equation IVD.22 shows the driving force for nucleation is controlled by the overall reaction given by Equation IVD.1. Using an analysis similar to that described above, the supersaturation ratio for a reaction zone containing pure SiH₄ vapor at a pressure P can be related to the extent of reaction ξ by the following expression:

$$SS = k_3 \frac{(1 - \xi)}{4P\xi^2} \quad \text{IVD.23}$$

Figure IV.34 shows the effect of temperature and percent reaction on the supersaturation ratio assuming a reaction zone comprised of pure silane at 0.2 atm. The supersaturation decreases with increasing

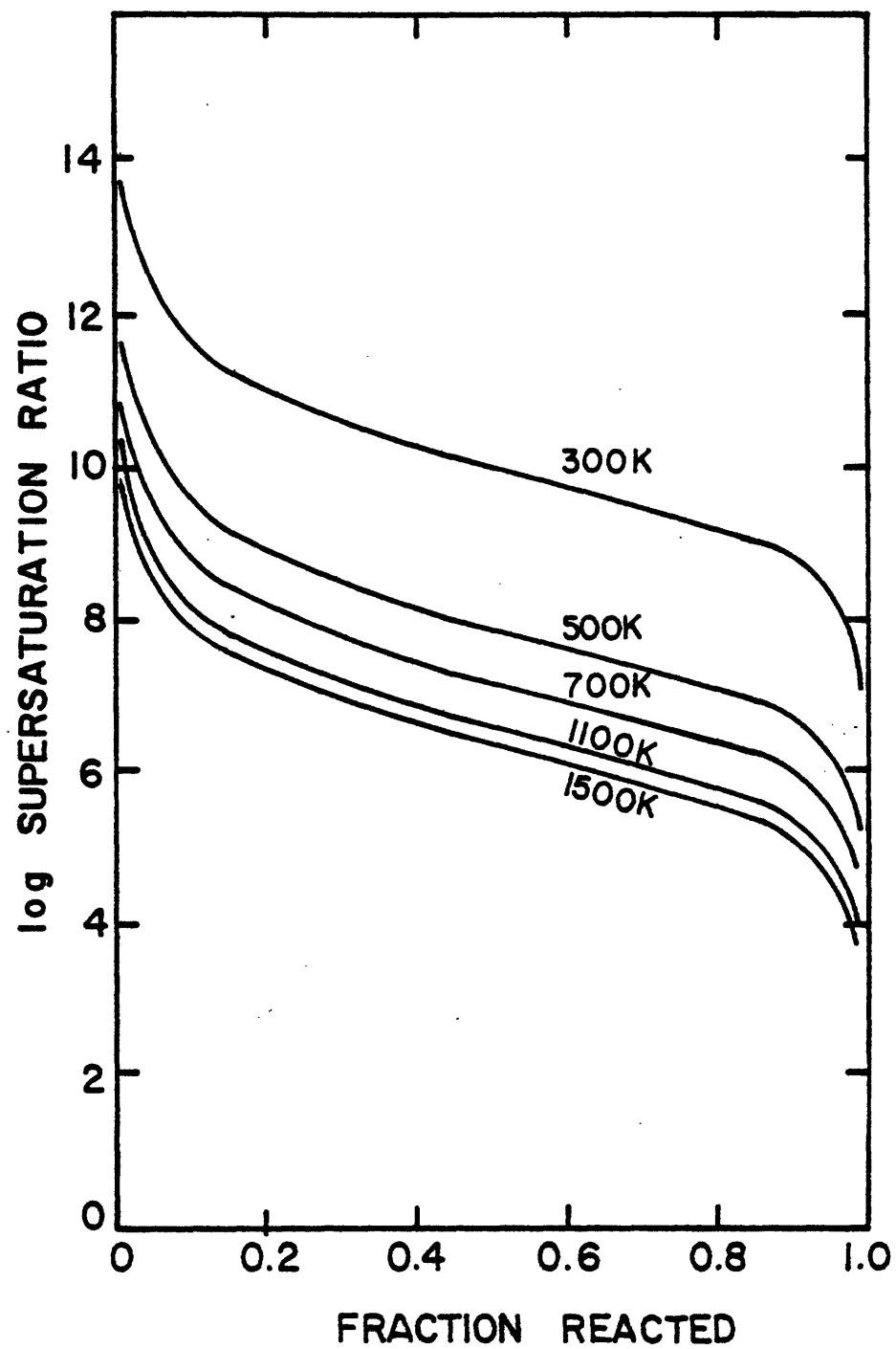
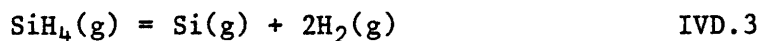


Figure IV.34. The effect of temperature and percent reaction on the supersaturation ratio for silane pyrolysis. Initial silane pressure equals 2×10^4 Pa.

temperature. The overall driving force for nucleation increases with temperature since the free energy change associated with reaction IVD.1 increases with increasing temperature.²⁶ Since $\Delta G_V = \frac{-RT}{V_{Si}} \ln(SS)$, where ΔG_V is the free energy change per unit volume of Si(s) formed and V_{Si} is the molecular volume of Si(s), the increase in ΔG_V with temperature indicates that $\ln(SS)$ decreases at less than a linear rate with increasing temperature.

At any particular temperature, the supersaturation ratio decreases sharply as the reaction initially proceeds. It is the equilibrium partial pressure of reacting silicon $P_{Si(g)}$ which defines the supersaturation ratio at a particular temperature. Table IV.4 showed the extent of the reaction:



was extremely small for temperatures up to approximately 1100K. For example at 1000K, the extent of reaction was 1.27×10^{-3} resulting in an equilibrium pressure of silicon in the gas stream of 2.53×10^{-4} atm. From Equation IVD.23 it was found that this resulted in a supersaturation ratio of 1.55×10^{12} . Therefore, once any silicon gas is produced even at the low equilibrium pressures defined by Equation IVD.12, there is a large driving force to nucleate solid silicon particles.

Both the nucleation rate J and the critical radius size r^* can be approximated by the application of homogeneous nucleation theory in a supersaturated vapor. The critical size nucleus is related to the supersaturation ratio by the Gibbs-Kelvin equation:

$$r^* = \frac{2\sigma v_{Si}}{kT \ln SS} \quad \text{IVD.24}$$

where σ is the interfacial energy between the solid and vapor and v_{Si} is the molecular volume of silicon. The free energy of formation of the critical size nucleus is given by:

$$\Delta F^* = \frac{16 \pi \sigma^3 v_{Si}^2}{3 (kT \ln SS)^2} \quad \text{IVD.25}$$

and using the Volmer-Weber¹⁰ formulism, the equation describing the homogeneous nucleation rate is:

$$J = \alpha_c \frac{P_{Si}}{(2\pi mkT)^{1/2}} 4\pi r^{*2} \frac{P_{Si}}{kT} \exp\left[\frac{-\Delta F^*}{kT}\right] \quad \text{IVD.26}$$

The nucleation rate is therefore dependent on both the thermodynamic driving force for the phase transformation and the kinetic requirement involving the collisions of vapor phase silicon atoms with a critical size silicon nucleus.

Table IV.4b summarizes the nucleation calculations for a reaction gas stream initially comprised of pure silane gas at 0.2 atm. In all cases, the critical size nucleus is very small. Based on the density and molecular weight of solid silicon, the atomic volume of silicon is $2.0 \times 10^{-2} \text{ nm}^3$. Therefore, the critical nuclei calculated from equilibrium thermodynamics will have a volume less than the atomic volume of silicon indicating that there is essentially no thermodynamic barrier toward nucleation. The nucleation rate is then primarily controlled by the kinetic factors involving the collisions between silicon atoms and the equilibrium concentration of silicon vapor. Even though the vapor is highly supersaturated at low temperatures, for

example, $SS = 7.8 \times 10^{49}$ at 300K, the nucleation rate is extremely small since the density of silicon vapor and consequently the number of molecular collisions is very low.

The scatter-extinction measurements discussed in Section IVB suggested that after the nucleation ceases, the particles grow to their final dimensions. The particle number density calculated from the scatter-extinction measurements ranged from 2.2×10^{12} to 1.1×10^{11} nuclei/cm³. Under all flow conditions, the reactant gas travelled from the inlet nozzle to the position where the particles were first observed in less than 10^{-2} sec. This time may be significantly longer than the time during which nucleation is actually occurring, since nucleation is not expected to occur precisely at the nozzle tip and the minimum diameter of the particles first observed by light scattering is greater than 8 nm which is much larger than the critical size nuclei. Therefore, the observed nucleation rate must be in excess of 10^{14} nuclei/cm³·sec.

It is difficult to measure the actual nucleation events with the scatter-extinction technique described in Section IIIB. This is primarily a consequence of the minimum detectable particle diameter being approximately 8 nm with a HeNe light source. The temperature at which nucleation begins cannot be measured with optical pyrometry. This is a consequence of the low radiance for small particles (~1.0 nm) having true temperatures below 900°C. It is possible to measure this temperature with an infrared pyrometer, but it will still be necessary to determine where the particles are actually forming.

The measurements of both the reaction temperature at the hottest region in the reaction zone and at the position where the reaction was first observed were reported in Sections IVA and IVB. The lowest temperature at which particles were first observed ranged from approximately 900°C to 1100°C. It is believed the actual nucleation occurred at temperatures significantly below these measured temperatures.

The nucleation rate calculated from the Volmer-Weber theory can be compared to the nucleation rate determined from the scatter-extinction results. It is assumed that nucleation occurs at temperatures in the range of 900K (627°C) to 1200K (927°C). For a reaction zone comprised of pure SiH₄ of 0.2 atm, the calculated nucleation rate varied from 1.7×10^{17} nuclei/cm³·sec at 900K to 2.1×10^{21} nuclei/cm³·sec at 1200K (Table IV.4). As stated above the minimum observed nucleation rate determined from the scatter-extinction measurements was greater than 10^{14} nuclei/cm³·sec. Depending upon the nucleation temperature chosen, the observed nucleation rate is approximately 3 to 7 orders of magnitude below the calculated nucleation rate. The following discussion addresses some of the possible causes of this discrepancy.

In the calculation of the nucleation rate from the Volmer-Weber formulism, it was assumed that the condensation coefficient α was equal to 1.0. This assumes that all molecules which strike the cluster surface will be incorporated. In actuality, the condensation coefficient is always less than unity. It is expected that the coefficient for small clusters will be less than that of the bulk coefficient since these clusters are unable to absorb the heat of

condensation to the extent that the large clusters can. For metals with a monatomic vapor phase, the energy of desorption is very high and at normal deposition temperature the condensation coefficient is expected to approach unity.¹⁰⁰ For non-metals or materials with polymeric vapor species, activation enthalpies and entropies for condensation may be appreciable so that the condensation coefficient is significantly smaller than unity.

It is possible that the time interval during which nucleation is occurring is much shorter than that estimated from the initial gas flow rate and the observed onset of nucleation. If the temperature at which nucleation occurs is 1000K, then the calculated nucleation rate is approximately 7×10^{18} nuclei/cm³·sec. For the observed particle density to conform with the calculated nucleation rate, the time interval for nucleation would have to be approximately 3×10^{-7} sec. With the present experimental techniques, it is not possible to determine if this is a realistic time frame for nucleation. It is also possible that the temperature at which nucleation actually occurs is somewhat lower than 900K. As shown in Table IV.4b, the nucleation rate is a strong function of temperature below 1000K. If nucleation occurred at approximately 800K, the calculated nucleation rate would be 1.4×10^{15} nuclei/cm³·sec. This is in good agreement with the nucleation rate determined from the scatter-extinction measurements.

The classical theory may be correct but the calculation of the nucleation rate may have utilized an incorrect value for one of the parameters. The effect of temperature has already been discussed. One of the major uncertainties of the classical homogeneous nucleation theory lies in the assumption that clusters containing only a few atoms

can be described in terms of bulk properties. For small clusters, the interfacial energy σ may be significantly different than the bulk value. Several workers have proposed that for single component systems the interfacial energy increases as the cluster radius decreases. ^{101 102} If the nucleating temperature is assumed to be 1000K, an increase in the interfacial energy from 0.9 J/m² to 1.5 J/m² would result in approximately a 10⁴ decrease in the calculated nucleation rate bringing the calculated value into good agreement with the measured nucleation rate.

The final possibility for explaining the discrepancy is that the classical theory of Volmer and Weber is incorrect and alternative approaches must be considered. As discussed in Section IIA, the actual steady-state nucleation rate is lower than the equilibrium rate approximation formulated by Volmer and Weber. This steady-state solution generally involves introducing a nonequilibrium or Zeldovich correction factor into Equation IVD.30. This factor is given by Equation IIA.30. For pure silicon at 0.2 atm and nucleation temperatures of 900K and 1200K, the Zeldovich factor was calculated to be 0.51 and 0.49 respectively. Therefore, the nonequilibrium correction cannot account for the discrepancy between the measured and calculated nucleation rates.

Another major alternative to the classical theory is the Lothe and Pound formalism in which the statistical mechanical contributions to the free energy of formation of the critical nuclei are considered. Lothe and Pound determined that the nucleation rate given by Equation IVD.26 should be adjusted by a pre-exponential correction factor Γ

$$\Gamma = (IkT)^{3/2} \frac{kT}{P} \frac{i^*}{\pi^2} (2mkT)^{3/2} \exp\left(\frac{-S}{K}\right) \bar{h}^{-6} \quad \text{IVD.27}$$

where I is the moment of inertia of a spherical cluster, i^* is the number of atoms in the critical nucleus, S is the molecular entropy, and $\bar{h} = h/2\pi$ where h is Plank's constant. At $T = 1000^\circ\text{K}$, with $i^* = 1$, $S = 7.85 \times 10^{-23} \text{ J/}^\circ\text{K} \cdot \text{molecule}$, $p = 25.3 \text{ Nt/m}^2$, $\bar{h} = 1.06 \times 10^{-34} \text{ J}\cdot\text{sec}$ and $I = 4.7 \times 10^{-43} \text{ g} \cdot \text{m}^2$, the Lothe-Pound correction factor is the order of 10^{23} . Thus the Lothe-Pound theory predicts an even larger value for the nucleation rate. Since the bulk value for the interfacial energy is also used in the Lothe-Pound formulism, the interfacial energy could be increased by an additional factor to force the agreement between the measured and calculated nucleation rates.

It is interesting to consider a totally different approach to the homogeneous nucleation from a supersaturated vapor. Bauer and Frurip¹⁰³ have postulated a kinetic theory which does not use bulk properties to explain the nucleation of the small clusters. The major difference between this model and the classical theory is that the critical supersaturation required for condensation to occur is determined by the rate at which the total free energy of transformation attains substantially large negative values and not the thermodynamic maximum in the free energy function. For the condensation of iron droplets from supersaturated vapor in an inert argon atmosphere, this kinetic theory resulted in a steady state nucleation rate which was approximately ten orders of magnitude lower than that predicted by the Becker-Doering formulism. Their experimental results and the comparison of other investigators results with the proposed kinetic

model were not sufficient to confirm or eliminate any of the proposed theories.

It is evident that the calculated nucleation rates are in reasonable agreement with the rate predicted by classical theory. The agreement can be improved by assuming nucleation occurred at lower temperatures or in shorter times than those determined from first order estimates. It is also possible to force better agreement by varying the value of the interfacial energy. There is still considerable disagreement over the most appropriate theory to describe homogeneous nucleation. The kinetic model proposed by Bauer and Fruip predicts a reduced nucleation rate which would better resolve the discrepancy between the measured and calculated rates. The uncertainties in the measured nucleation rates and the disparity among the existing nucleation theories limits the validity of any quantitative conclusion regarding the agreement or disagreement of the experimental results and the theoretical predictions.

2. Cessation of Nucleation

The number density calculated from the scatter-extinction measurements suggested that nucleation was initiated and ceased prior to the formation of a large fraction of solid material. As stated, it was not possible to determine the actual nucleation events using a HeNe light source. Figures IV.15 and IV.16 indicated that no nucleation was occurring at the position where particles were first observed. Table IV.6 gives the percent of silane converted to solid silicon at this position. For Run 654S with a 2/1 Ar/SiH⁴ gas mixture there was

Table IV.6. Percent of Silane Converted to Solid Silicon at Position Particles were First Observed by Light Scattering

Run Number	Distance Above Nozzle (mm)	Percent Converted to Solid Silicon
630S	5.0	7.1
654S	3.0	2.2
631S	2.5	8.7
638S	5.0	6.5
634S	6.1	12.0

only 2.2 percent of the SiH_4 converted to solid silicon at the base of the reaction "flame". For this run, careful experimental procedures were used to measure the minimum detectable scattering. It is likely that if the same care was taken to measure the scattering in the other runs, no significant nucleation would be detected after approximately 2-3 percent of the overall reaction had occurred.

The relative time intervals during which nucleation and growth are occurring is very important in determining the final particle size and the particle size distributions. Simultaneous nucleation and growth will result in a wide particle size distribution since new particles are always being created. Table IV.6 suggests that very little growth occurred during the time interval prior to the cessation of nucleation. Since the light scattering results indicated that no agglomeration occurred during the particle growth, it can be assumed that the

nucleated particles grow independently of each other. Thus, a large number of nuclei are formed in the early stages of the reaction; these nuclei then grow independently by depleting the available silane gas. The distribution of particle sizes is then dependent upon the statistical variations inherent in the growth process, and more importantly upon the nonuniformity in reaction temperature and the corresponding vapor pressures within the reaction zone. These nonuniformities, a consequence of the Gaussian power intensity profile, the parabolic distribution of gas velocities, and the dilution of the reactant gas stream by the annular and window argon, result in variations in the nucleation and growth rates and a distribution of particle sizes. The development of the final particle size and the particle size distribution is discussed more fully in Section IVD.4

The possible mechanisms by which the nucleation rate ceases is addressed in the following discussion. Similar behavior was observed by Murthy et al.⁶⁰ for the thermal decomposition of silane in a resistance heated reaction tube furnace. They found that particles formed at the beginning of the hot zone in the reactor (approximately 700°C) and that very little nucleation occurred once the particles achieved macroscopic sizes. These results were qualitatively explained by the depletion of silicon in the vapor phase, thus reducing the supersaturation to an extent that could no longer support nucleation. Hecht¹⁰⁴ found that the formation of sodium particles from gas evaporation techniques resulted from homogeneous gas phase nucleation, initial growth by single atom accretion, and the growth to final dimensions by particle-particle coagulation. He observed a monodispersed particle distribution in the initial growth stage,

and suggested that nucleation occurred only in the early stages of the growth process. The mechanisms for the cessation of nucleation were not discussed.

The classical approach to the prediction of the rate of formation of new particles by homogeneous nucleation neglects the effect of the existing particles on the nucleation rate. It is expected that particles present during the continuing nucleation process will influence the rate of formation of new nuclei by the accretion of vapor molecules that might otherwise be available for nucleation. Pesthy, Fagan, and Seinfeld¹⁴ considered the effect of a growing particle on the nucleation by determining the changes in the vapor concentration and gas temperatures near the particle. The simplified result was that the nucleation rate in the presence of growing particles \bar{J} could be related to the intrinsic nucleation rate J_{∞} (the rate based on the monomer concentration and temperature in the absence of particles) and the fraction of the reaction volume occupied by the solid particles Φ :

$$\bar{J} = J_{\infty} (1 - \rho^3 \Phi) \quad \text{IVD.28}$$

where ρ^3 , the dimensionless clearance volume, is a function of temperature, concentration of monomer in the gas phase, equilibrium vapor pressure over the solid, the thermal diffusivity of the gas, vapor atom mobility, and the heat of vaporization of the monomer. Sample calculations done for the condensation of dibutyl phthalate showed that for a wide range of conditions, the nucleation rate was found to quench when the fraction of available vapor condensed in an aerosol particle approached 5-9%. The critical fraction of condensed phase was essentially independent of the initial supersaturation and

the temperature achieved at the time when nucleation first occurred. The analysis cannot be directly applied to the present study since it is based on the continuum transport theory, that is the rate at which monomers arrive at the particle surface is based on the assumption that the particles are much larger than the mean free path in the surrounding gas phase.

If it is assumed that nucleation begins at approximately 900K for an initial reaction zone comprised of 2×10^4 Pa (0.2 atm) of SiH_4 gas, the equilibrium pressure of silicon vapor is approximately 3 Pa (3×10^{-5} atm). This is equivalent to a silicon vapor concentration of 1×10^{-8} g/cm³. If 2×10^{12} silicon nuclei with a radius of 1.0 nm are produced per cubic centimeter, the silicon vapor concentration is reduced to 4×10^{-9} g/cm³ or a pressure of 1 Pa (1×10^{-5} atm). This results in decrease in the nucleation rate from 2×10^{17} nuclei/cm³·sec to 1×10^{16} nuclei/cm³·sec.

As the growing nuclei deplete the available Si(g), the SiH_4 decomposition reaction will proceed to restore thermodynamic equilibrium. Thus, the concentration of silicon vapor will increase resulting in an increased nucleation rate. It is now necessary to compare the time required for further nucleation to that of particle growth to determine whether the growth process becomes dominant. In the following section, it will be shown that the growth is limited by the transport of vapor species to the particle surface. The observed growth rate was found to range from 10^2 to 10^3 nm/sec whereas the theoretical growth rate was approximately 2 to 3 orders of magnitude higher. For 2×10^{12} particles/cm³ of a diameter of approximately 2.0 nm, a growth rate of 10^5 nm/sec would require the utilization of

5×10^{20} Si molecules/cm³·sec. As described above the observed nucleation rate is on the order of 10^{14} nuclei/cm³·sec and the calculated rate at 1000K is approximately 7×10^{18} nuclei/cm³·sec. Since the critical nucleus is small, containing at most 5 silicon atoms, less than 4×10^{19} Si molecules/cm³·sec (based on theoretical calculations) and approximately 5×10^{14} Si molecules/cm³·sec (based on the observed nucleation) are used during the nucleation process. Therefore, once the particles are nucleated, the particle growth is kinetically favored over further nucleation thus explaining the sudden ceasure of nucleation.

3. Growth of the Particles

Once nucleation ceases, the particles grow to their final dimensions. The light scattering results suggested that the particle growth occured via the accretion of vapor phase molecules and not by coagulation. The final particle size is limited by the depletion of the available silane and not by the elapsed growth time at elevated temperatures. Since the particles appear to grow independently, the rate of particle growth is not particularly important in determining the final particle size. Rather, the size is dependent on the number of nuclei formed and the concentration of silicon atoms available to the growing nuclei. Nevertheless, the analysis of the growth process is of academic interest.

As described in Section IIB, the particle growth process occurs by the transport of vapor species to the particle surface, adsorption and

reaction at the surface, and the desorption and transport of any reaction products from the surface. The overall growth rate is determined by the slowest step in the growth process. In this section, the effect of reaction parameters on the growth rate will be discussed briefly, and the experimental results compared to the theory to determine the most plausible growth limiting step.

a. Transport Limited Growth

The equations governing growth limited by vapor transport were discussed in detail in Section IIB. Ignoring the effects of plurality of particles and the moving boundary on the growth rate, the growth law for particles much larger than the mean free path in the vapor phase is

$$\frac{dV}{dt} = \frac{4\pi D r_p v_{Si} (P_{Si(g)} - P_{\infty})}{kT} \quad \text{IVD.29}$$

and for small particles is

$$\frac{dV}{dt} = \frac{4\alpha\pi r_p^2 v_{Si} (P_{Si(g)} - P_{\infty})}{(2\pi m k T)^{1/2}} \quad \text{IVD.30}$$

The mean free path can be calculated from

$$\lambda = v \left(\frac{\pi m}{2kT} \right)^{1/2} \quad \text{IVD.31}$$

where m is the mass of the molecule, k is Boltzmann's constant, T is absolute temperature, and v is the kinematic viscosity which is defined as η/ρ where η is the gas viscosity and ρ is the gas density. At 1200°C and 0.2 atm, $\rho = 6 \times 10^{-5}$ g/cm³, $\eta = 3.5 \times 10^{-4}$ cm/cm²·sec and

$m = 4.7 \times 10^{-23}$ g, so $\lambda = 1.2 \times 10^{-4}$ cm = 1.2 μ m. The mean free path is significantly longer than the particle size; thus, it is anticipated, that if the growth is limited by vapor transport, the particle growth rate will be represented by Equation IVD.30. The radial growth rate $dr/dt = (1/4\pi r_p^2) dV/dt$ is therefore expected to be independent of the particle radius.

The temperature will effect the growth rate by altering the rate at which molecules collide with the particles, the probability that a colliding molecule will be incorporated into the particle, and the concentration of the particular vapor species being adsorbed onto the particle. For the present case, it is necessary to determine what chemical species are being adsorbed. Silicon atoms may form in the vapor phase through reaction IVD.3; particle growth could proceed simply by the adsorption of the silicon atoms. It is also possible that silane atoms are adsorbed and the particle growth occurs through a surface or bulk reaction, or that the adsorption of both silane and silicon molecules contribute to the particle growth.

The effect of temperature on the condensation coefficient is discussed in detail by Hirth and Pound.¹⁰⁰ For metals with a monatomic vapor phase, the energy of desorption is on the order of 80 to 300 kJ/mole; therefore, all the incident atoms will be adsorbed unless the temperature of the colliding atoms is in excess of 10^6 degrees, a condition that is not attainable with the laser synthesis process. For nonmetals or metals with polymeric vapor species, the activational enthalpies and entropies for condensation may be appreciable which may result in condensation coefficients considerably less than unity. In general, it can be concluded that variable temperature, in the range

achievable by this synthesis process, will have little effect on the condensation coefficient.

The effect of temperature on the number of collisions is easily determined from the kinetic theory of gases. The rate at which vapor molecules collide with a particle of surface area πr_p^2 is

$$\text{Rate} = N^* \left(\frac{kT}{2\pi m} \right)^{1/2} \pi r_p^2 \quad \text{IVD.32}$$

where N^* is the number of molecules per unit volume. Therefore, an increase in temperature will increase the collision frequency; but if constant pressure is maintained and the reactant gas is allowed to expand freely, an increase in temperature will result in a linear decrease in the concentration N^* and thus a decrease proportional to $T^{1/2}$ in the rate at which molecules arrive at the surface.

Depending on the molecular species which adsorbs at the particle surface, an increase in reaction temperature can result in either an increase or decrease in the rate of particle growth. This is a result of the changes in the equilibrium vapor concentrations with temperature as was discussed in Section IVD.1 and exemplified by Table IV.4. If silane vapor is adsorbed and a reaction to form silicon and hydrogen occurs at the surface or in the bulk, an increase in temperature will result in a decrease in the growth rate since the equilibrium concentration of silane decreases. It is unlikely that only SiH_4 will be adsorbed; any silicon vapor formed by the gas phase decomposition will also be adsorbed. If both $\text{SiH}_4(\text{g})$ and $\text{Si}(\text{g})$ are adsorbed on the surface, the concentration of adsorbing gas species will be essentially temperature independent. If particle growth occurs only by the adsorption of silicon vapor atoms, the growth rate will increase with increasing temperature since the concentration of silicon vapor atoms

Table IV.7. Comparison of Experimental Growth Rate and Calculated Growth Rate (Transport Limited)

Distance From Nozzle (mm)	P_{SiH_4} (Nt/m^2)	P_{Si}	Growth Rate (nm/sec)			α_{Si}	$\alpha_{\text{Si+SiH}_4}$
			Measured	Calc.A	Calc.B		
Run 654S							
3.5	4.1×10^3	6.7×10^2	4.5×10^3	1.9×10^5	1.1×10^6	0.02	0.004
4.5	1.2×10^3	9.1×10^2	2.4×10^3	2.4×10^5	5.7×10^5	0.01	0.004
5.5	6.1×10^2	8.0×10^2	1.6×10^3	2.2×10^5	3.8×10^5	0.008	0.004
6.5	4.9×10^2	4.8×10^2	7.0×10^2	2.5×10^5	2.6×10^5	0.005	0.003
7.5	7.0×10^2	2.6×10^2	4.8×10^2	7.4×10^4	2.7×10^5	0.007	0.002
8.5	4.6×10^2	1.0×10^2	2.0×10^2	2.9×10^4	1.4×10^5	0.007	0.002
Run 630S							
5.5	1.1×10^4	2.2×10^3	1.2×10^4	6.1×10^5	3.8×10^6	0.02	0.003
6.5	7.4×10^3	2.2×10^3	8.2×10^3	6.1×10^5	2.6×10^6	0.01	0.003
7.5	5.2×10^3	2.1×10^3	4.2×10^3	5.7×10^5	1.9×10^6	0.008	0.002
8.5	4.7×10^3	1.2×10^3	3.6×10^3	3.4×10^5	1.7×10^6	0.01	0.002

A calculates growth assuming only Si(g) atoms are adsorbed.

B calculates growth assuming Si(g) and SiH₄(g) are adsorbed.

increases. Therefore, the overall effect of temperature is to decrease the growth rate if both $\text{SiH}_4(\text{g})$ and $\text{Si}(\text{g})$ are adsorbed and to increase the growth rate if only $\text{Si}(\text{g})$ is adsorbed.

From Equation IVD.30, it is obvious that an increase in the concentration of the adsorbing species will result in an increase in the growth rate. Since equilibrium is assumed to exist at the particle surface, the rate will not be dependent on the nature of the surface such as whether the particle is amorphous or crystalline or the crystallographic orientation. Therefore, the particle will tend to grow isotropically resulting in a spherical shape.

By comparing the growth rate measured from light scattering with that predicted by Equation IVD.30, it should be possible to determine if transport limited growth is dominant. If the growth is transport limited, the comparison of the theoretical growth with the experimental results may enable estimation of the condensation coefficient α . Table IV.7 shows the calculated growth rate using Equation IVD.30 for Runs 630S and 654S (see Appendix 1 for reaction conditions). The temperature was determined by the corrected pyrometric technique described in Section IIIB. The partial pressure of $\text{SiH}_4(\text{g})$ and $\text{Si}(\text{g})$ was determined from the amount of silicon in the vapor phase (estimated from Figure IV.17 and a similar curve for Run 630S) and equilibrium thermodynamics. The growth was calculated by assuming: 1) only the adsorption of silicon vapor leads to particle growth and 2) both silicon and silane vapor molecules are adsorbed during growth. In both cases a condensation coefficient of unity was assumed.

It is evident that the experimentally observed growth rate is 2 to 3 orders of magnitude lower than theoretically calculated growth rate.

From Equation IIB.27, it was determined that the effect of plurality of particles could not account for this discrepancy since the correction term $\exp\left[-\frac{m}{c_0} \int_0^t F_0(\tau) d\tau\right]$ is approximately equal to the $\exp(-3 \times 10^{-4})$ which is negligibly different from unity. In the following section, it will be shown that the surface growth kinetics are extremely rapid in comparison with the vapor transport. Therefore, it is assumed the growth is limited by the bombardment of vapor molecules with a condensation coefficient significantly less than unity; the condensation coefficient required to bring the experimental and calculated results into agreement is shown in Table IV.7. If it is assumed that both $\text{SiH}_4(\text{g})$ and $\text{Si}(\text{g})$ species are adsorbed on the particle surface, the condensation coefficient is essentially constant (from 0.002 to 0.004). For silicon adsorption, the calculated condensation coefficient is larger and exhibits a larger range. The possible existence of the vapor species SiH_2 and SiH_3 has been ignored. If they are present in the vapor phase and also contribute to the particle growth, the theoretical growth rate will be approximately equal to that calculated above for $\text{SiH}_4(\text{g})$ and $\text{Si}(\text{g})$ adsorption since the total concentration of silicon species in the vapor phase will be equivalent.

b. Surface Controlled Growth

If the vapor transport is rapid, the particle growth will be controlled by processes that occur at the surface. The surface limited

growth kinetics for adsorption and simple decomposition of a hypothetical AB gas molecule were presented in Section II.B. In the following discussion, the calculated growth rate is compared with the measured growth to determine whether surface reactions can limit particle growth in the laser synthesis process.

Although the experimental rate data for silane decomposition is insufficient to verify the absolute mechanism, the species present at the silicon-vapor interface can be assumed thereby allowing speculation of the growth mechanism. In Section II.D, it was assumed $\text{SiH}_4(\text{g})$ and $\text{Si}(\text{g})$ were the predominant vapor species. If $\text{Si}(\text{g})$ is adsorbed on the surface, the reaction rate can be calculated from the rate of $\text{Si}(\text{g})$ chemisorption. When $\text{SiH}_4(\text{g})$ is adsorbed, the hypothetical analysis described in Section II.B is valid with a slight adaption to account for each mole of $\text{SiH}_4(\text{g})$ decomposition resulting in two moles of adsorbed $\text{H}_2(\text{g})$.

It was shown in Section IV.B that the measured growth rate was directly proportional to the partial pressure of the reactant gas. If only atomic silicon is being adsorbed, the measured dependence would be consistent with the theoretical aspects of surface controlled growth since the growth by simple adsorption is directly proportional to the vapor pressure. Following the analysis for adsorption and decomposition on the surface, presented in Section II.B, the observed growth rate is consistent with the surface rate limited theory only if the adsorption of $\text{SiH}_4(\text{g})$ on the surface is rate-limiting or the reaction at the surface is rate limiting and the concentration of $\text{SiH}_4(\text{g})$ is sufficiently low.

Values of β_{SiH_4} , the Langmuir adsorption coefficient, and k_R are required to calculate the theoretical growth rates. Seto¹⁰⁵ studied the growth rate of polycrystalline silicon from the pyrolysis of silane at temperatures in the regime where the growth behavior is surface limited. A reaction mechanism involving the chemisorption of silane onto the silicon surface, the decomposition of silane into silicon and hydrogen, and the desorption of hydrogen was found to satisfactorily explain the experimental results. Seto found that the hydrogen gas produced by the decomposition reaction did not effect the rate of decomposition and therefore the desorption step could be assumed fast in comparison with adsorption and decomposition. The values for the Langmuir adsorption coefficient β_{SiH_4} and the reaction rate constant k_R were determined to follow the relations:

$$\beta_{\text{SiH}_4} = 2.0 \times 10^{13} \exp - \frac{15200}{T} \quad \text{IVD.33}$$

and

$$k_R = 9.4 \times 10^{-4} \exp - \frac{5900}{T} \quad \text{IVD.34}$$

For silane concentrations ranging from 5×10^{-7} mole/cm³ to 4×10^{-8} mole/cm³ and temperatures from 650 to 800°C, Seto found the deposition to be surface reaction rate-limited; the overall growth could be represented by:

$$\frac{dV}{dt} = \frac{v_{\text{Si}} K_R \beta_{\text{SiH}_4} [\text{SiH}_4]}{1 + \beta_{\text{SiH}_4} [\text{SiH}_4]} \quad \text{IVD.35}$$

Using the equilibrium constants given by Equations IVD.33 and IVD.34, the growth rate at typical laser synthesis conditions

($[\text{SiH}_4] = 1.9 \times 10^{-6}$ mole/cm³ and a reaction temperature of 1000°C)

calculated from Equation IVD.35 was $dV/dt = 1.0 \times 10^{-4} \text{ cm}^3/\text{sec}$. From Section IVB, the measured radial growth rate was found to be on the order of 10^3 - 10^4 nm/sec and since $dV/dt = 4\pi r^2 dr/dt$, the measured growth rate assuming a particle diameter of 60 nm was approximately 10^{-13} to $10^{-14} \text{ cm}^3/\text{sec}$. This is much smaller than the calculated growth rate when a surface reaction¹⁵ rate limiting. It can therefore be concluded that the growth of particles in the laser powder synthesis process is limited by the transport of the silicon vapor species to the particle surface. This conclusion is in agreement with Bloem⁷⁸ who determined in the chemical vapor deposition of silicon from silane at temperatures above 900°C, the growth rate was dependent on vapor transport; at lower temperatures, the kinetics of the surface reaction determined the overall growth behavior. Everstyn et al.¹⁰⁶ also found the deposition from silane at 1050°C to be a transport limited process.

4. Control of Particle Size and Size Distribution

The control of particle size and particle size distribution is a prime concern in the production of powder from the vapor phase. As discussed above, the rapid cessation of homogeneous nucleation results in the production of a large number of independent nuclei; these nuclei grow to their final dimensions by the depletion of the available silane gas. During the short period of time in which nucleation and growth are occurring simultaneously, there will be a distribution of particle sizes generated. It is necessary to ascertain whether the difference in the particle sizes becomes accentuated or whether the system tends toward monodispersivity with growth.

If all the nuclei are exposed to approximately the same temperature and concentration profiles, the differences in the particle growth rate will result only from the initial differences in particle size. Frisch and Collins³⁵ showed the growth rates of particles of different radii are related by the following expression if the growth is limited by vapor transport:

$$\frac{dr/dt}{dr'/dt} = \frac{\gamma + r'}{\gamma + r} \quad \text{IVD.36}$$

where r and r' are the radii of particles which had radii equal to r and r' at the time at which nucleation was quenched and $\gamma = \rho/\alpha$ where ρ is on the order of the mean free path and α is the probability that impinging molecules will be adsorbed. The relative growth rate will be inversely proportional to the ratio of the radii in the region where $\gamma \ll r$, thus tending to suppress the initial differences in the relative particle radii. If $\gamma \gg r$, then the particles will grow at equal rates. Even if γ is greater than r throughout the entire growth period, since the nucleation is quenched early in the growth process, the initial differences in the particle sizes will become insignificant as the droplets approach their final sizes. Therefore, it may be concluded that homogeneous nucleation and growth with rapid cessation will result in a particle size distribution that tends towards monodispersity. Under all synthesis conditions, the final particle size distribution is always somewhat polydispersed, a consequence of the inherent temperature and gas concentration gradients within the reaction zone.

As described in Section IVD, the large thermodynamic driving force for the production of solid silicon from silane gas leads to the

complete utilization of the silane. If the particle growth is insignificant during the time period between the inception and cessation of nucleation, it can be assumed that a large number of nuclei are formed which then grow under similar conditions. The final particle size is determined by the amount of silane available for each growing nuclei. Assuming 100% conversion, a material balance gives the following relation for the final particle size:

$$d = \left(\frac{6}{\pi} \frac{C \cdot M}{N \rho} \right)^{1/3} \quad \text{IVD.37}$$

where d is the average diameter of the particles formed, C is the initial concentration of silane in the reaction zone, N is the number of nuclei formed per unit volume of reacting gas, M is the molecular weight of silicon, and ρ is the density of the product. The particle size can be controlled by manipulating the concentration of the reactant gas and the number density of nuclei.

The final particle size was measured for a wide variety of synthesis conditions, and the results were presented in Section IVC. Since the concentration of reactant gas is known from the initial conditions, the average number of nuclei per unit volume of reactant gas can be calculated using Equation IVD.37. Based on the He pycnometric measurements, the density of the particles was assumed to be the theoretical density of silicon. Appendix 2 lists the calculated number density for the various reaction conditions.

The particle number density calculated from Equation IVD.37 is in good agreement with the number density determined from the light scattering/extinction measurements (Section IVB). The small

discrepancies may result from errors in the assumed particle index of refraction and the extinction path length.

It is evident that as the maximum reaction zone temperature increases, the nucleus density decreases. This is anomalous because, as shown in Section IVD.1 the nucleation rate is expected to increase with temperature. The nucleus density is determined by the product of the nucleation rate and the time interval during the onset and cessation of nucleation. This can be represented by the integral:

$$N = \int_{t_1}^{t_2} R_N(t) dt \quad \text{IVD.38}$$

where $R_N(t)$ is the nucleation rate at time t and t_1 and t_2 are the times corresponding to the onset and cessation of nucleation.

Therefore, the smaller number of nuclei produced per unit volume for reaction zones with higher maximum temperatures implies that the time between the onset and termination of nucleation is shorter for the hotter reaction zones.

Figure IV.35 presents a plot of the natural logarithm of the nucleus density versus the reciprocal of the maximum reaction zone temperature for a large number of synthesis runs. Although this plot has little physical significance, it is useful in exploring the nucleation behavior. Despite a significant amount of scatter, the general trend of an increased nucleus density with a decreased reaction zone temperature is readily apparent. The fact that a single line can be satisfactorily drawn through all the points suggests that the partial pressure of silane within the reaction zone has little effect on the nucleation behavior. This is consistent with the theoretical

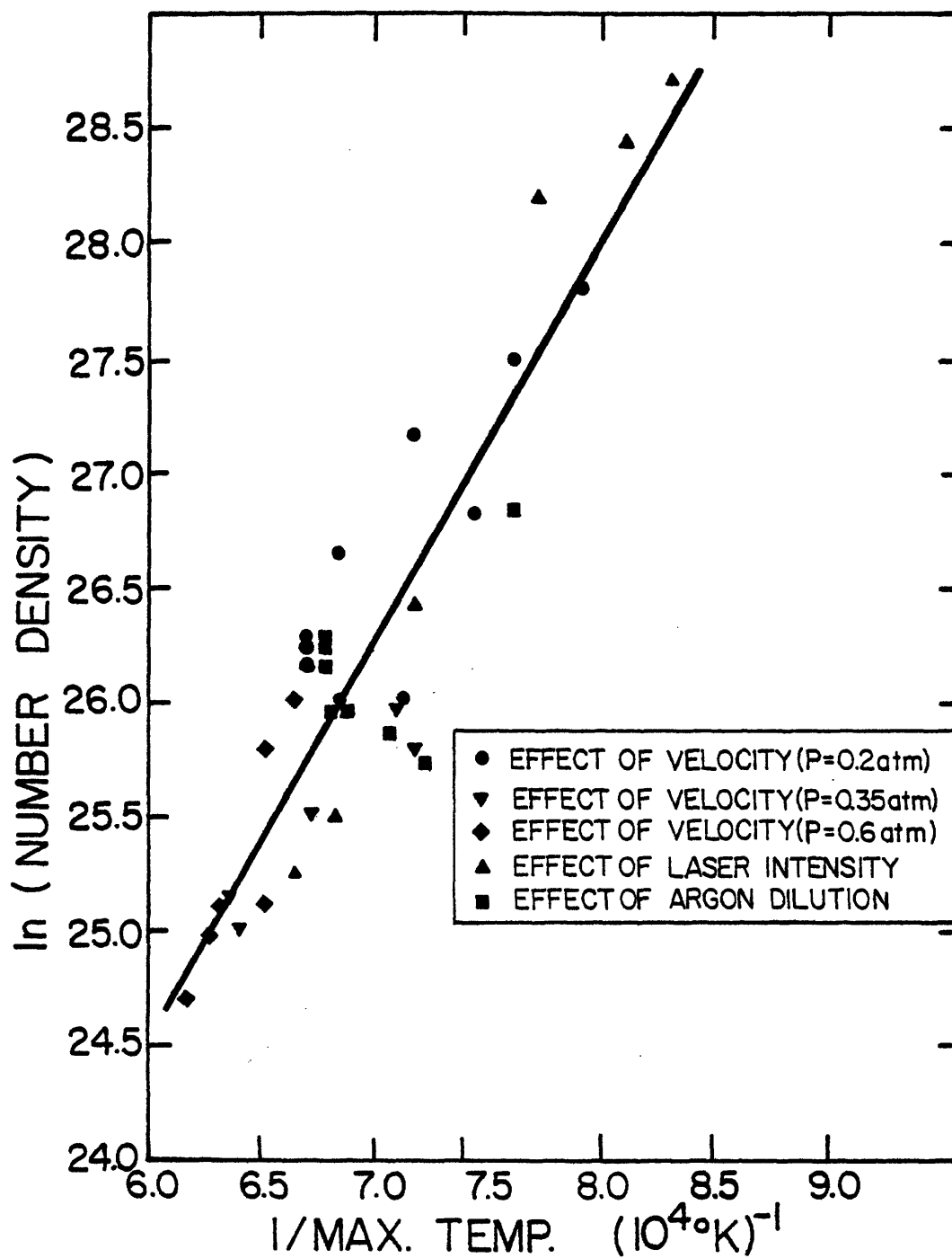


Figure IV.35. The logarithm of the calculated particle number density versus the reciprocal of the maximum reaction zone temperature for various synthesis runs.

calculations presented in Section IVD.1 which showed that at high silane partial pressure, the extent of reaction required to establish equilibrium is reduced; therefore, the equilibrium partial pressure of silicon vapor, the nucleating vapor species, is relatively insensitive to changes in the silane pressure. This results in a nucleation rate which is essentially independent of the initial silane concentration within the range of conditions examined.

Figures IV.24, IV.25, and IV.26 showed that the particle size exhibited an ascending then descending trend as the flow rate was increased while maintaining a constant laser intensity and total cell pressure. Comparison of these results with the maximum temperature within the reaction zone (Section IVA) indicated that the largest particles resulted from the hottest reaction zones. As previously discussed the particle number density decreased with increased reaction zone temperature. At a constant pressure, the silane flow rate has little effect on the concentration within the reaction zone but effects the velocity at which the reactant gas flows through the laser beam. Within the range of conditions investigated, it was found that the growth was limited by the amount of available silane and not the elapsed time at elevated temperatures. Therefore, the change in flow velocity has little effect on the growth behavior. The change in particle size was primarily a consequence of the change in the number of nuclei competing for growth by the depletion of the available silane.

An increase in the laser intensity resulted in an increased reaction zone temperature and a corresponding decrease in the particle number density (Appendices 1 and 2). Since the initial concentration

of silane was held constant for all these runs, the decreased number density resulted in an increased final particle size. Since it was determined both theoretically (Section IVD.1) and experimentally (Figure IV.35) that the concentration of silane has little effect on the nucleation behavior, larger particles can be synthesized by increasing the concentration of silane within the reaction zone. This was verified experimentally by the consistent increase in particle size as the silane pressure was increased from 0.20 to 0.35 to 0.60 atm.

E. Particle Agglomeration

1. General

The final stage of the growth process usually involves the collisions between particles. When fine particles collide, van der Waals forces will act to form agglomerates. The presence of agglomerates in the starting powder will result in inhomogeneities in green compacts formed by dispersion settling, casting, and compacting. These inhomogeneities will persist and may intensify during subsequent processing. Therefore, it is necessary to eliminate agglomerate formation in the early stages of processing preferably in the powder synthesis.

Particles entrained in a gas stream are unstable with respect to coagulation since particle contact results in a reduction in surface area and a corresponding decrease in the free energy. The two principal mechanisms by which particle collisions can occur are Brownian motion and fluid shear. In each, the collision rate can be

influenced by particle interactions such as van der Waals and Coulombic forces.

For particles much larger than the mean free path of the gas molecules, the collision frequency due to Brownian motion can be calculated from diffusion theory. At steady state, the collision frequency between particles of radii r_i and r_j is¹⁰⁷

$$F(t) = 4\pi D(r_i + r_j)N \quad \text{IVE.1}$$

where D is the particle diffusivity and N is the particle number density. Assuming the Stokes-Einstein relation holds, $D = \frac{kT}{3\pi\mu d}$, and the particles are of equal size, Equation IVE.1 becomes

$$F(t) = \frac{8kT}{3\mu} N \quad \text{IVE.2}$$

where μ is the viscosity of the gas phase, and $F(t)$ is collision frequency of a single particle.

For particles much smaller than the mean free path of the gas molecules, the collision frequency due to Brownian motion is obtained from the kinetic theory of gases. If the particle radii are equal, the collision frequency is

$$F(t) = \frac{192}{\rho} \frac{kTr}{\rho} N^{1/2} \quad \text{IVE.3}$$

where ρ is the particle density. It should be noted that for small particles ($d \ll \lambda$, mean free path), the collision frequency is a function of the particle characteristics while for large particle ($d \gg \lambda$), the properties of the fluid determine the collision behavior.

In the orthokinetic case,¹⁰⁸ particles flowing in a fluid stream collide because of their relative motion. Assuming the flow is laminar

with straight streamlines, the collision frequency is

$$F(t) = \frac{32}{3} r^3 \frac{du}{dx} N \quad \text{IVE.4}$$

where $\frac{du}{dx}$ is the velocity gradient across the gas stream.

Equations IVE.2, IVE.3, and IVE.4 are all similar in that the collision frequency per particle is directly proportional to the particle number density with the proportionality constant containing a measure of the relative speed of the colliding particles.

The collision frequency will be altered when the particles exert forces on one another. This effect can be represented by¹⁰⁷

$$F'(t) = \frac{F(t)}{W} \quad \text{IVE.5}$$

where $F'(t)$ is the collision frequency with particle interactions, $F(t)$ is the collision frequency for non-interacting spheres, and W is a correction factor to account for the particle interactions. For two particles of equal diameter, the correction factor is related to the potential energy of the particles $\phi(y)$ by

$$W = 2r \int_{2r}^{\infty} (\exp(\phi(y)/kT)/y^2) dy \quad \text{IVE.6}$$

where y is the distance between the centers of the particles. The potential energy term may be positive or negative and has different functional dependencies on the separation distance for different types of forces. When ϕ is negative, that is for an attractive force, W is less than unity leading to an increase in the collision frequency. For repulsive forces, ϕ is positive and W is greater than unity resulting in a reduced collision frequency.

Van der Waals forces will always result in an increase in the collision rate. The energy of attraction between two spherical particles with radii r and separated by a distance y was calculated by Hamaker:¹⁰⁹

$$\phi = \frac{-A}{6} \frac{2r^2}{y^2 - 4r^2} + \frac{2r^2}{y^2} + \ln \frac{y^2 - 4r^2}{y^2} \quad \text{IVE.7}$$

where A is the Hamaker constant. Substitution of this attractive energy term into Equation IVE.6 results in an integral for the correction factor that has been numerically evaluated and found to be independent of particle size and only dependent on A/kT . Figure IV.36 shows the reciprocal of the correction factor W as a function of A/kT .¹¹⁰

Numerous papers have dealt with the coagulation of fine particles dispersed in gaseous fluids. Of particular interest is the work of Onaka, Nakada, and Kimijor¹¹¹ on the clustering of fine silicon particles prepared in an argon gas atmosphere by gas evaporation techniques at a constant temperature of 1400°C and pressures up to approximately 40 torr. Since the particle size was much smaller than the mean free path of the gas molecules, the collision frequency was expected to follow Equation IVE.3. No significant coagulation was observed until the particles had traveled approximately 3 cm from the evaporation source. The results fit the perikinetic model if the agglomeration was assumed to occur in two dimensions. The cause of the two-dimensional necklace structure is not known although it is commonly observed in the clustering of fine particles. Most investigators have assumed the coagulation occurs in three dimensions and the two-

dimensional chainlike structure typically observed in microscopy is an artifact of the sample preparation.

When two particles are brought together attractive junctions are formed due to interatomic forces acting across the interface. There is always a thermodynamic driving force to reduce the surface area and curvature between the particles. The radius of the neck between the particle resulting only from plastic deformation can be related in a simple way to the surface tension and modulus of elasticity:¹¹²

$$x = \left(\frac{\gamma_{\text{eff}} r^2}{0.16 E} \right)^{1/3} \quad \text{IVE.8}$$

with γ_{eff} , the effective interfacial energy, given by:

$$\gamma_{\text{eff}} = 2\gamma_{\text{sv}} - \gamma_{\text{gb}} \quad \text{IVE.9}$$

where γ_{sv} is the interfacial energy between the solid and the vapor phase, γ_{gb} is the grain boundary energy, E is Young's modulus, r is the particle radius, and x is the radius of the neck. Numerous investigators¹¹³ have studied the effect of surface forces on the adhesion of metal contacts and Tabor and Winterton¹¹⁴ give an excellent review of the work. If no bonding occurs between the particles, it is presumed the necks can be broken by dispersion in appropriate organic liquids with suitable surfactants. If mass is transported to the neck region by sintering mechanisms such as evaporation/condensation, surface diffusion, lattice diffusion, or grain boundary diffusion, the separation of the particles will be difficult and may require mechanical techniques.

Table IV.8. Calculated Collision Frequency
Resulting from Brownian Motion

Run Number	Ar Dilution (mole %)	Temp* (°K)	Radius (nm)	Number Density ($\frac{\text{particle}}{\text{cm}^3}$)	Collision Rate ($\frac{\text{collisions}}{\text{particle}\cdot\text{sec}}$)
631S	0	1473	30	2.6×10^{11}	1800
637S	66.7	1303	18	4.5×10^{11}	2300
634S	83.3	1253	15	3.8×10^{11}	1800

* Corrected pyrometer temperature of hottest region assuming $C_S/C_E = 0.0$.

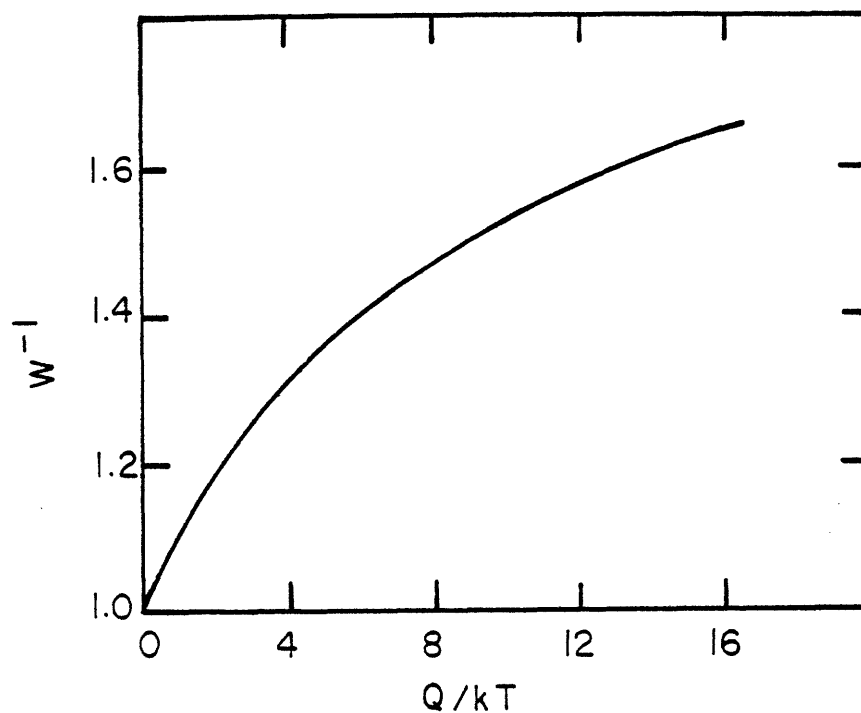


Figure IV.36. The particle collision correction factor $1/W$ versus A/kT for van der Waals attraction.

2. Experimental Results

TEM analysis has shown that most of the laser synthesized powders exhibit agglomeration characterized by two-dimensional networks of particles. The majority of the silicon powder appeared to have neck formation between the particles. Run 650S synthesized at 6×10^4 MPa (0.6 atm) was an exception to this generalization. This powder had an average particle size of 147 nm with many single particles and small clusters containing 2 to 4 particles.

The light scattering/extinction calculations showed that little agglomeration occurred as the particles passed through the laser beam. Therefore, the chainlike agglomeration may result from collisions in the upper region of the "flame", or during the powder collection method, or is an artifact of the TEM specimen preparation.

Since the particles are much smaller than the mean free path in the vapor phase, the collision frequency due to Brownian motion is given by Equation IVE.3. For a typical synthesis run (for example Run 631S), the particle radius is 3×10^{-6} cm, ρ is 2.33 g/cm^3 , N is $2.6 \times 10^{11} \text{ particle/cm}^3$, and T is 1473K. Thus, the calculated collision frequency is 1840 collisions/particle \cdot sec. Under these run conditions, the average velocity is estimated to be approximately 100 cm/sec and the dwell time of the particles in the beam is 6×10^{-3} /sec. Thus an average particle will undergo approximately 10 collisions within the beam. Using equations IVE.6 and IVE.7, van der Waals forces are estimated to increase the collision frequency by a factor of 1.15.

If fluid shear is predominant, the collision frequency is given by Equation IVE.4. For silicon synthesis conditions used in Run 631S,

dU/dx is estimated from the computer results to be 1×10^3 cm/sec \cdot cm. Using the same value for N and r as given above, Equation IVE.9 predicts a collision frequency of 4.9×10^{-2} collision/particle \cdot sec. Thus, Brownian coagulation is expected to be dominant.

Equation IVE.3 predicted that an average particle will experience 10 collisions within the laser beam region. When two particles collide, they may stick or rebound. Thus the lack of agglomeration as observed by light scattering is consistent with the calculated results if the sticking coefficient is significantly less than unity.

As shown by Equation IVE.3, the particle number density is the parameter which dominates the collision frequency. Reaction temperature and particle size have less of an effect since the collision frequency has a square root dependence on these parameters. Increased gas velocity should reduce the total number of collisions because the residence time is reduced proportionally.

It was anticipated that diluting the reactant gas stream with argon would decrease the collision frequency by the combined effects of reducing the reaction temperature and the particle number density. In Runs 631S, 634S and 637S this effect was investigated. Table IV.8 gives the calculated collision frequency for these runs.

Table IV.8 shows that the collision frequency did not change significantly as the gas stream was diluted. Even though the reaction zone temperature decreased, an effect which by itself would reduce the collision frequency, the density of particles within the gas stream increased because the average particle size decreased.

From Equation IVE.8, the neck diameter arising from elastic deformation was calculated using the following values:⁹⁹

$\gamma_{sv} = 900 \text{ ergs/cm}^2$, $E = 1.63 \times 10^{12} \text{ dynes/cm}^2$ and $r = 3 \times 10^{-6} \text{ cm}$.

This results in a neck diameter of approximately 7 nm for a 60 nm particle. This is in qualitative agreement with the TEM observations. It is possible to break these necks by dispersion as was shown by Mizuta et al.⁹⁸ If additional neck formation occurs through mass transport by diffusional mechanisms, it will be more difficult to break these bonds.

F. Particle Crystallinity

1. General

As discussed previously, under most synthesis conditions, the resulting powders were polycrystalline with the measured crystallite size significantly smaller than the overall particle size; that is, each individual particle contained numerous crystallites. This structure has been confirmed by BET surface area measurements, X-ray line broadening, and both bright and dark field TEM. The surface area and line broadening results were presented in Section IV.C. This discussion examines the particle crystal structure in more detail and describes briefly the possible formation processes which could result in polycrystalline particles.

It was found that the ratio of the overall particle size, determined by BET surface area measurements, to the crystallite size, determined from X-ray line broadening, was dependent on the synthesis conditions. This was presented graphically in Figures IV.27, IV.28, IV.29, IV.31, and IV.33. Comparison of these plots with Figures IV.4,

IV.5, IV.6, IV.7, and IV.8 (showing the effect of the process variables on the maximum reaction zone temperature) suggests that the ratio of the crystallite size to the particle size is related to maximum reaction zone temperature with the largest ratio occurring for reaction zones having the lowest reaction temperature. Above a particular reaction temperature, the ratio was constant, indicating that the particles contained an equal number of crystallites.

There are two possible structures consistent with the results from the surface area and line broadening measurements. First, under all reaction conditions the particles may be fully crystalline with a smaller relative crystallite size produced in particles synthesized at low reaction temperatures. Alternatively, when formed at low temperatures, the larger ratio of particle to crystallite size may result from a particle which is not fully crystalline; that is, the particles consist of individual crystallites surrounded by an amorphous matrix.

2. Annealing Results

To elucidate the observed temperature effect, a set of annealing studies were performed on the powders synthesized with varied laser intensities. These powders were annealed in argon at 550°C for 6 hours. At 550°C, there should be no nucleation of any crystalline material in the amorphous regions but the growth of existing crystalline silicon into the neighboring amorphous region will be rapid.¹¹⁵ Since the densities of crystalline and amorphous silicon are approximately equivalent, the change in volume with crystallization is

negligible. Thus, if the particles are fully crystalline, the anneal should have little effect on either the crystallite or particle size, but if the powders are partially crystalline, the crystallite size should increase while the overall particle size remains unchanged.

The extended anneal should eliminate any strain, if present, and thereby confirm the X-ray results in which it was determined that lattice strain contributed little to the peak broadening.

After annealing, the powders were analyzed using X-ray line broadening, BET surface area measurements, and He pycnometry. The results are presented in Table IV.9. Figure IV.37 shows the effect of the anneal on the X-ray diffraction peak shapes for powder which had a large ratio of the particle size to the crystallite size. This powder was synthesized with a 50 W unfocused beam. The X-ray peaks resulting from the (220) plane using Cu $K\alpha$ radiation are shown for the as-synthesized and annealed powders. The Rachinger correction was applied to both peaks to separate the $K\alpha_1$, and $K\alpha_2$ contributions to the diffraction peaks (Appendix 3). The crystallite size increased by approximately a factor of two while the anneal had little effect on the overall particle size.

Figure IV.38 shows a similar plot for powder which was synthesized with a higher laser intensity (125 W unfocused). This powder was in the regime where the ratio of the particle to crystallite size was independent of the reaction temperature. The anneal had little effect on either the overall particle or crystallite size. In all cases, annealing the powders did not effect the powder density as measured by He pycnometry.

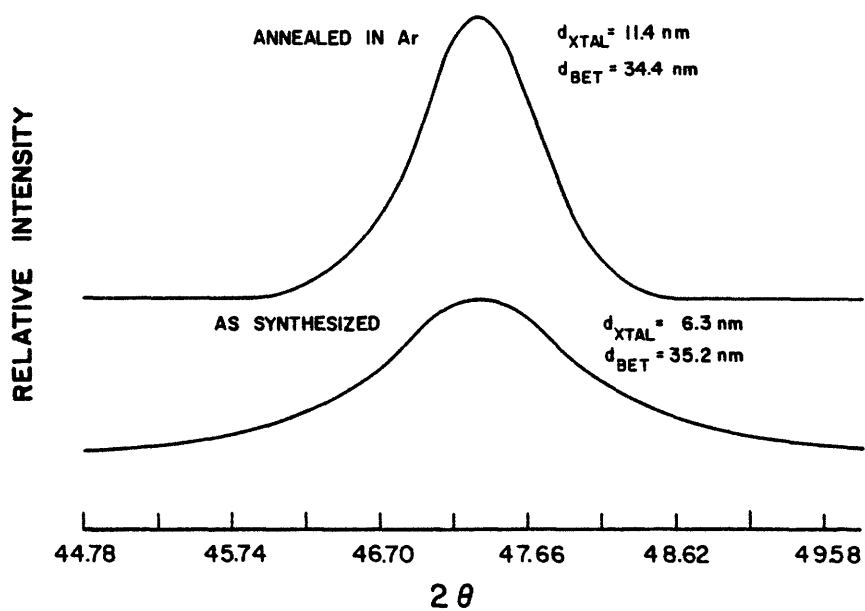


Figure IV.37. The effect of a 550°C, 6 hour anneal on the powder crystallinity for Run 640S. Shown are the X-ray ($Cu_{k-\alpha_1}$) diffraction peaks after application of the Rachinger correction.

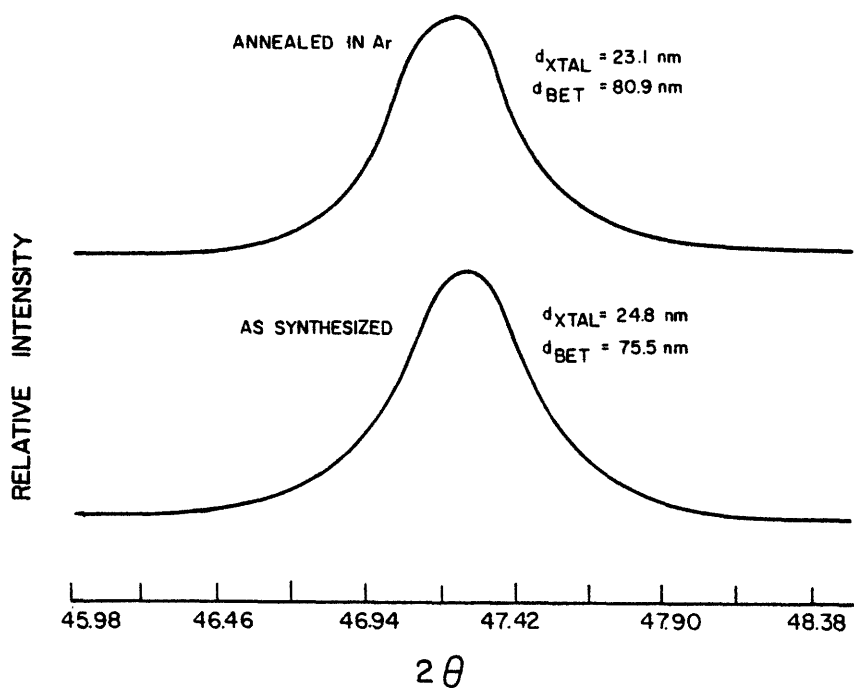


Figure IV.38. The effect of 550°C, 6 hour anneal on the powder crystallinity for Run 646S. Shown are the X-ray ($Cu_{k-\alpha_1}$) diffraction peaks after application of the Rachinger correction.

Table IV.9. Summary of Annealing Results[#]

Run Number	Intensity (W/cm ²)	Max. Temp. (°C)	As Synthesized		Annealed	
			d _{BET} (nm)	d _{XRAY} [*]	d _{BET} (nm)	d _{XRAY} [*]
658S ^{**}	134	930	32.1	4.0	31.6	8.2
640S	176	960	35.2	6.2	34.4	11.4
638S	265	1020	38.0	7.1	38.7	11.2
648S	407	1120	68.9	21.7	65.1	24.2
646S	424	--	75.5	25.4	80.9	23.1
635S	531	1190	93.2	33.8	88.6	30.3

[#] Annealing Temperature 550°C, 6 hours

^{*} Assumes Gaussian Peak Shapes

^{**} STEM analysis showed powder 658S to be amorphous.

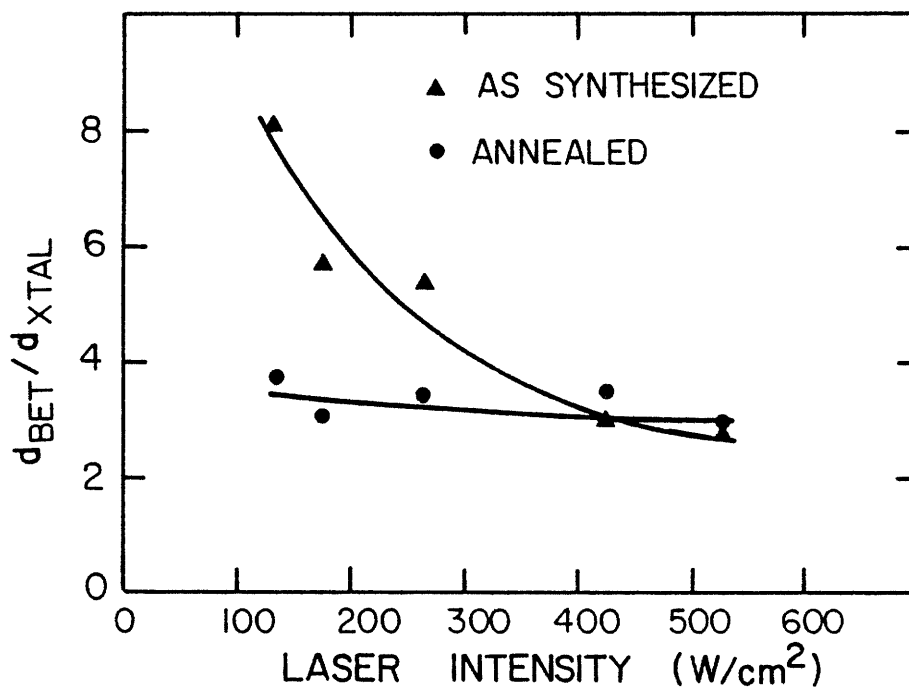


Figure IV.39. Effect of a 550°C, 6 hour anneal on the ratio of the particle to crystallite size for powders synthesized at different laser intensities.

The annealing results are summarized graphically in Figure IV.39. For the as-synthesized powders, the ratio of the particle to crystallite size increased sharply as the laser intensity, ie. the reaction zone temperature, was decreased. Above approximately 400 W/cm², the particle crystal structure was essentially independent of the reaction temperature. Annealing the powders synthesized at low temperatures increased the crystallite size but had little effect on the overall particles size or powder density. For powders synthesized at higher laser intensities, there was no noticeable change in either the crystallite or particle size. The results suggest that the powder synthesized with low reaction zone temperatures are not fully crystalline but consist of small particles embedded in an amorphous matrix. For powders that were fully crystalline as synthesized, ie. at high laser intensities, the fact that the anneal had little effect on the X-ray peak shapes verifies the line broadening experiments in which the broadening was found to result from small crystallite size and not from lattice strain.

3. STEM Analysis

Both the as synthesized and annealed powder were examined with scanning transmission electron microscopy (STEM). Bright field micrographs of powders synthesized at 38 W (run 658S), 50 W (640S) and 150 W (635S) are shown in Figures IV.40, IV.41, and IV.42. The bright field images of the annealed powders are shown in Figures IV.43, IV.44, and IV.45. As expected, the low temperature annealed had little effect on the overall particle size.

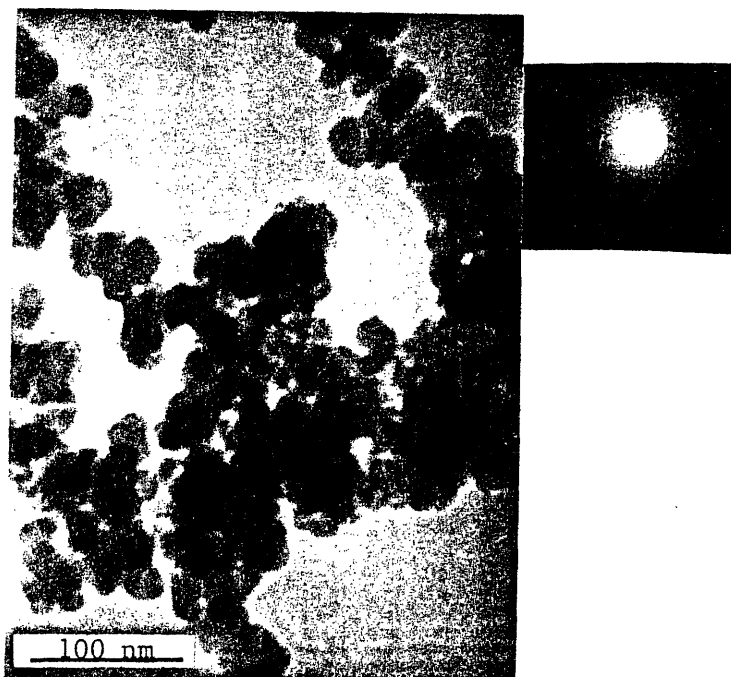


Figure IV.40. Bright field STEM micrograph and electron diffraction pattern of as synthesized powder from Run 658S.

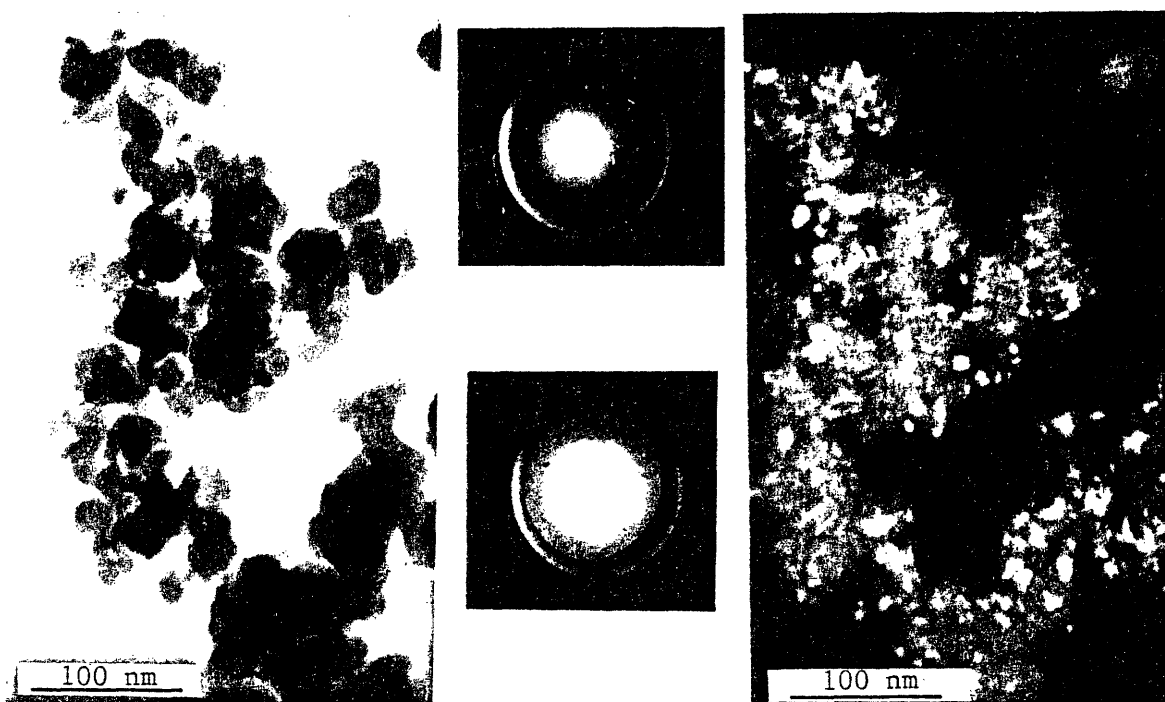


Figure IV.41. Bright and dark field STEM micrographs of as synthesized powder from Run 640S and microdiffraction patterns from different regions of the same particles.



Figure IV.42. Bright and dark field STEM micrographs of as synthesized powder from Run 635S and microdiffraction pattern from a single particle.

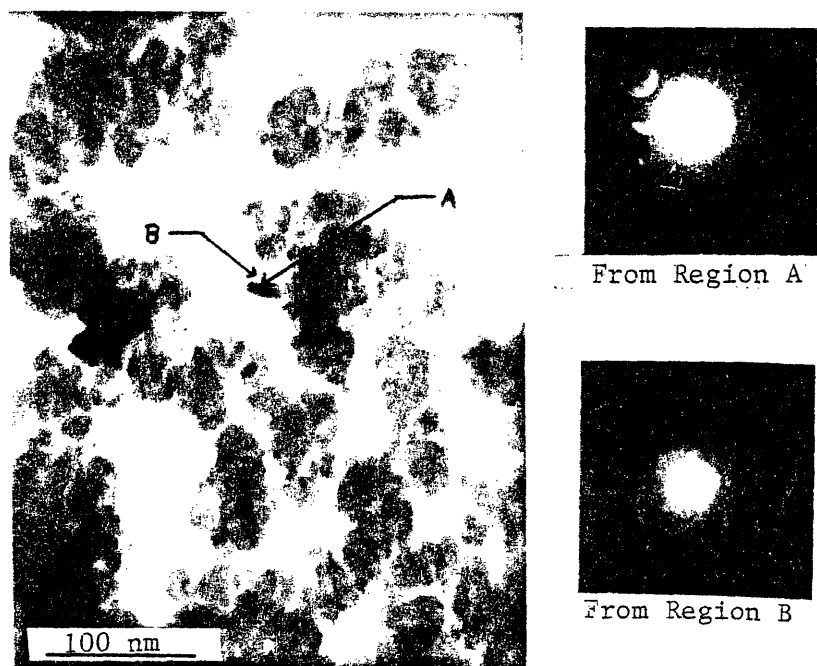


Figure IV.43. Bright field STEM micrograph of annealed powder from Run 658S.

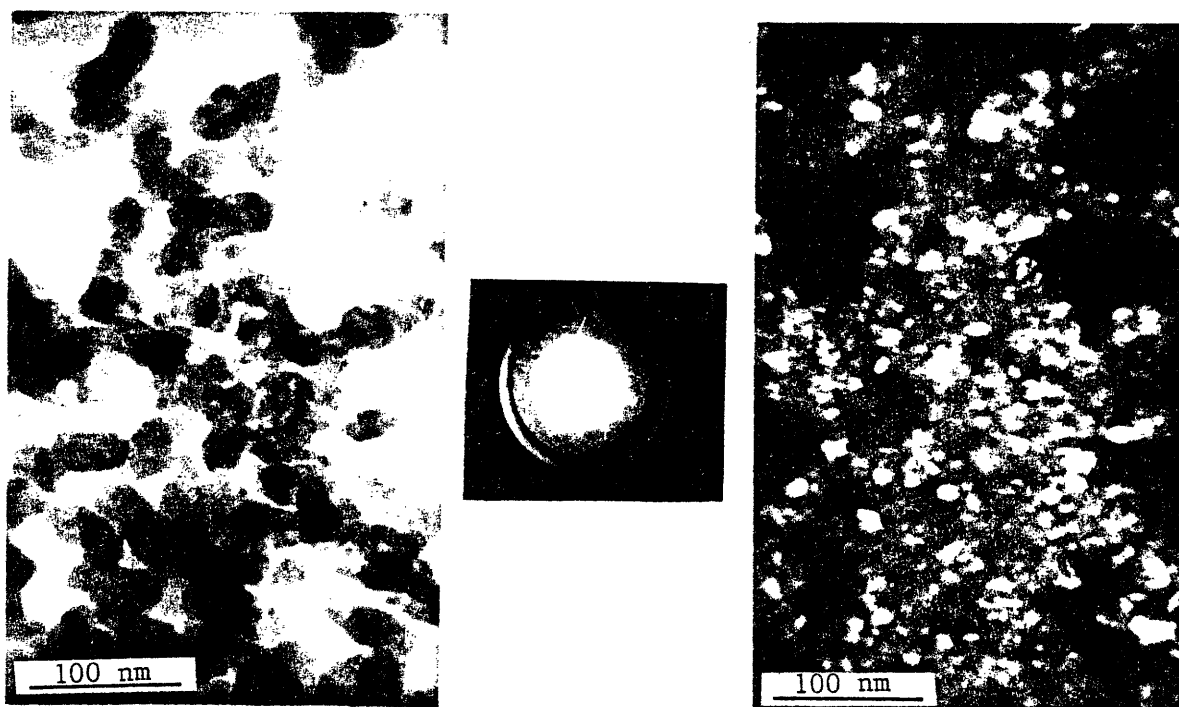


Figure IV.44. Bright and dark field STEM micrographs of annealed powder from Run 640S and diffraction pattern from a cluster of particles.

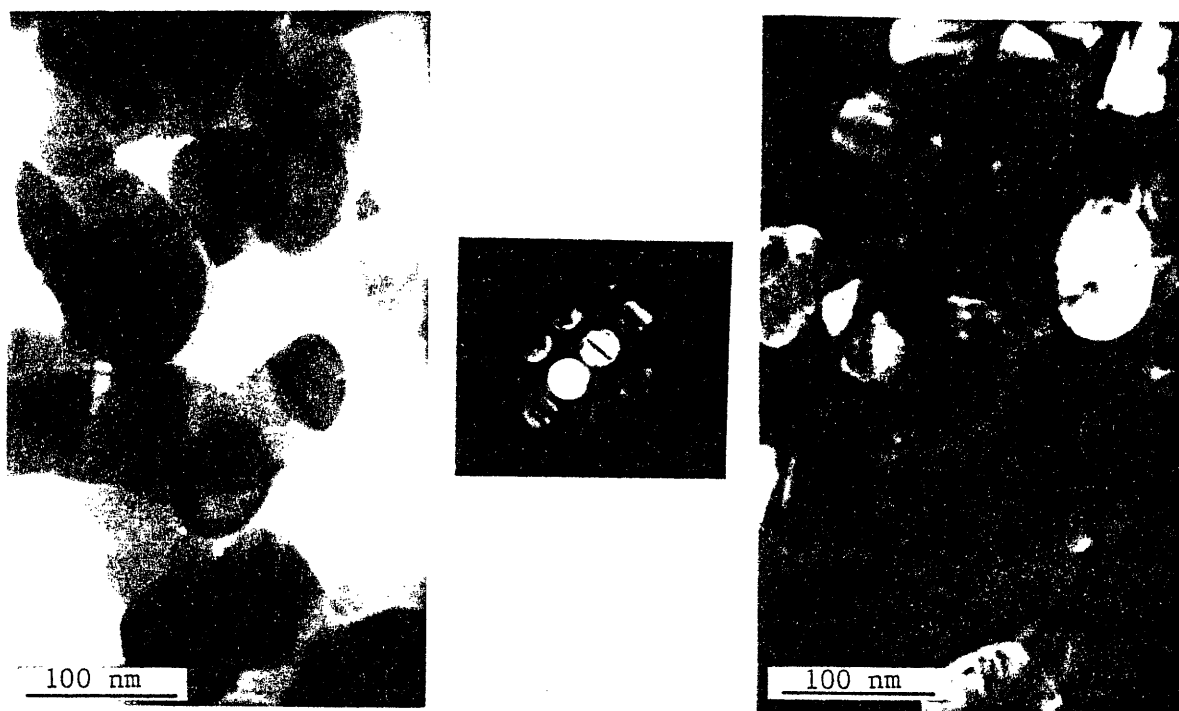


Figure IV.45. Bright and dark field STEM micrographs of annealed powder from Run 635S and microdiffraction pattern from a single particle.

Since the STEM utilizes an annular detector, it is possible to simultaneously image all the regions within the field of view which are diffracting the electron beam. By positioning a diffraction aperture around a single spot in the diffraction pattern only the crystallites which are oriented such that the diffracted electrons pass through this aperture appear bright. The resulting dark field image is similar to that obtained in conventional TEM by tilting the electron beam off the optic axis. These dark field images were used to investigate the particle crystallinity. If a diffraction aperture is not used, all regions which diffract the beam contribute to produce an annular dark field image. This image is not very informative in investigating particle microstructure because all regions including amorphous areas appear bright.

In the STEM, the electron beam can be focused to a small spot (1 nm). This enables both microdiffraction and microchemical analyses since the electron beam can be positioned to pass through only a small region of the specimen. It is therefore possible to examine the crystal structure within individual particles. By scanning the electron beam over the entire cross section of a particle and simultaneously observing the resulting diffraction pattern, it can be determined whether the particle consists of a single crystal, multiple crystallites, or a combination of amorphous and crystalline regions.

For run 658S (38 W beam power), the as-synthesized powder was totally amorphous. A diffraction pattern of a typical cluster of particles is shown in Figure IV.38. The annealed powder (Figure IV.43) was primarily amorphous confirming that a low temperature anneal (550°C) is insufficient to result in crystalline nucleation. There was a small number of regions within certain particles which were

determined to be crystalline. A microdiffraction pattern of one such region, labeled A, is shown in Figure IV.43. The region surrounding this crystallite was amorphous as evidenced by the microdiffraction of area B. It is unlikely that the region corresponding to this crystallite was amorphous in the as-synthesized powder. There were probably microcrystallites present too small to be imaged by STEM. X-ray line broadening, assuming Gaussian shaped peaks, of the annealed powder gave an estimated crystallite size of approximately 8.0 nm, which is consistent with high magnification STEM images of the crystalline regions.

The as-synthesized powder from run 640S (50 W beam power) consisted of particles that contained both amorphous and crystalline regions. A dark field image is shown in Figure IV.41. A diffraction aperture was positioned so that only those crystallites having their (111) plane in a particular orientation appear bright. The amorphous/crystalline nature of the particles is shown by the diffraction patterns in Figure IV.41. The patterns arise from different regions in the same particle. These diffraction patterns are different from those in Figure IV.43 because a 2x lens used to photograph the patterns in Figure IV. 41 was not used. A dark field image of the annealed powder is shown in Figure IV.44 along with a diffraction pattern from a group of particles. No amorphous areas were apparent in any of the particles observed. Comparison of the dark field images of the as synthesized and annealed powders showed that the fraction of crystalline material increased with annealing.

Powder 635S (150 W beam power) was entirely crystalline in both the as synthesized and annealed states. The dark field images and

diffraction patterns were very similar (Figure IV.42 and IV.45). Using microdiffraction and scanning across a single particle, it was determined that the particles were polycrystalline.

The STEM observations are consistent with the line broadening and BET surface area results. At sufficiently low synthesis temperatures, the as formed powders are completely amorphous. Annealing at 550°C for 6 hours is insufficient to initiate crystallization. At somewhat higher temperatures, the as-synthesized particles contain both amorphous and crystalline regions. Annealing the powder allows the growth of the crystalline phase into the surrounding regions and results in a fully crystalline powder. At higher reaction temperatures, the as-synthesized powder is fully crystalline and a low temperature anneal has little effect on the microstructural characteristics.

4. Temperature Dependence

For fully crystallized powder, the ratio of the particle to crystallite size was relatively constant regardless of the reaction conditions. Possible mechanisms to explain this behavior are discussed later in this section. Assuming that the powders synthesized at lower temperatures have the same number of crystallites per particle as the fully crystalline powders, the volume fraction of crystalline material can be estimated from the following relation:

$$X_{\text{XTAL}} = \left(\frac{d_{\text{XTAL}}}{d_{\text{BET}}} \right)^3_{\text{SAM}} \left(\frac{d_{\text{XTAL}}}{d_{\text{BET}}} \right)^3_{\text{FC}} \quad \text{IVF.1}$$

where $(d_{\text{XTAL}}/d_{\text{BET}})_{\text{FC}}$ is the ratio of the crystallite to particle size

for a fully crystalline powder and $(d_{XTAL}/d_{BET})_{SAM}$ is the ratio for the powder of interest. The results of this calculation are shown in Appendix 2. It was assumed that the X-ray peaks are Gaussian-shaped and the ratio of particle size to crystallite size for a fully crystalline powder equaled 3.0.

When crystallization is induced in the bulk of the material, Zellama et al.¹¹⁵ have shown that the fraction crystallized obeys the equation

$$\ln \left(\frac{1}{1-x} \right) = \frac{\pi}{3} n_0 R_G^3 t^3 \quad \text{IVF.2}$$

where n_0 is the number of crystallites per particle, R_G is the radial growth rate, and t is the crystallization time. Equation IVF.2 is valid only if the volume occupied by the initial crystallites at the time nucleation stops is insignificant compared to the final crystalline volume. Both nucleation and growth are activated processes; therefore the fraction crystallized will be a strong function of the reaction temperature.

Since it is not possible to control the reaction temperature and crystallization time independently and the particle formation mechanisms are not known conclusively, a plot of $\ln[\ln 1/(1-x)]$ versus $1/T_{MAX}$ (although having a slope related to the activation energy for crystalline growth if Equation IVF.2 holds) will have little physical significance. Nevertheless, examination of the crystalline fraction as a function of the maximum reaction zone temperature provides insight into the crystallization behavior. In general, if the maximum reaction zone temperature was sufficiently high, the resulting particles were fully crystalline. For the runs conducted with a 150 W unfocused beam

and a total cell pressure of 6×10^4 Pa (Figure IV.29) or with a 170 W unfocused beam at 3.5×10^4 Pa (Figure IV.28), the resulting powder was fully crystalline regardless of the flow conditions. Reducing the laser intensity, total cell pressure or diluting the reactant gas stream with argon resulted in partially crystalline powders. Since the temperature-time history of the reactant gases and resulting products is largely dependent on the particular run conditions, it is not appropriate to compare the calculated crystallinity results from run-to-run.

In Figure IV.46, which shows the effect of varying the laser intensity on the fraction of crystalline silicon; two curves are plotted. The solid line was calculated from the assumption that for high reaction zone temperatures the powders are fully crystalline. The fraction crystallized was calculated from Equation IVF.1. The dashed line is based on the annealing studies. By assuming that the six hour anneal at 550°C resulted in a fully crystalline powder while the initial crystallite density remained unchanged, the fraction of crystalline silicon in the as-synthesized powder can be estimated by comparing the initial crystallite size to the crystallite size after annealing:

$$X_{\text{XTAL}} = \frac{(d_{\text{XTAL}})^3_{\text{INITIAL}}}{(d_{\text{XTAL}})^3_{\text{ANNEALED}}} \quad \text{IVF.3}$$

Both curves exhibit the same general trends and are in excellent agreement. Above 1150°C the powder was fully crystalline. Decreasing the laser intensity reduced the reaction zone temperature and resulted in partially crystalline powder.

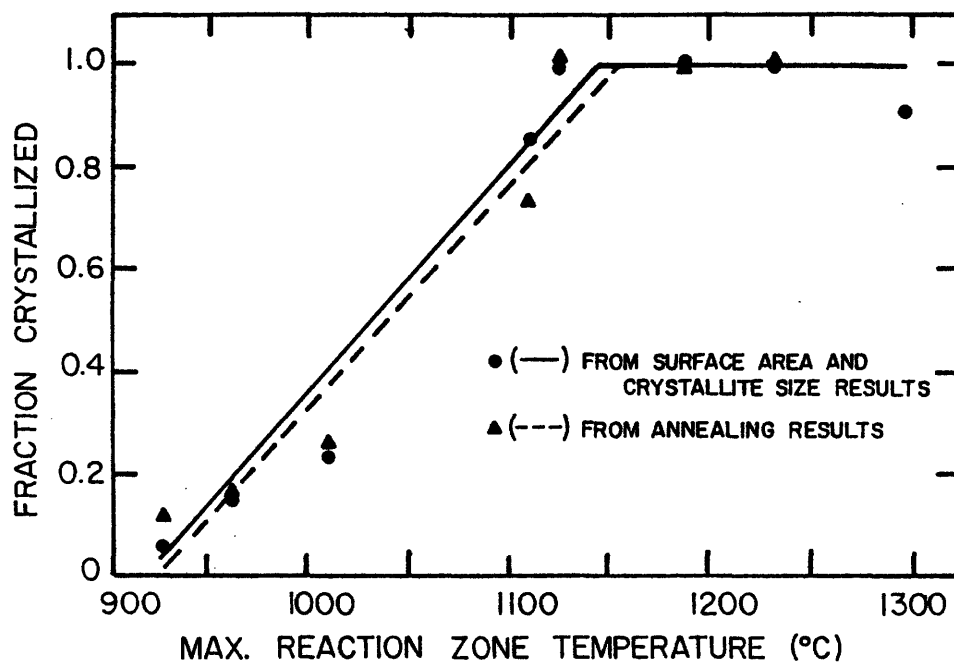


Figure IV.46. The effect of reaction zone temperature on the fraction of crystalline silicon in the final particles. (Varied laser intensity, Pressure = 3.5×10^4 Pa, SiH_4 flow rate = $66 \text{ cm}^3/\text{min}$)

5. Mechanisms for Particle Formation

There are numerous mechanisms in which solid particles may form from the vapor phase. The actual silicon powder synthesis mechanism must be consistent with the resulting powder crystallinity and the general powder characteristics. The remainder of this section discusses possible formation mechanisms based on the resulting powder characteristics and postulates the most plausible synthesis mechanism leading to polycrystalline/amorphous particles.

Individual particles may be formed from the vapor phase; these particles may coalesce and sinter to form the final powder. To be consistent with the observed particle characteristics, it is necessary that at low reaction zone temperatures some of the individual particles formed in the vapor phase must be amorphous. Therefore, coalescence of these individual particles will result in final particles that are polycrystalline; depending upon the process conditions, they may contain a mixture of amorphous and crystalline material. There are various observations which suggest that this is not a viable formation process. The close agreement between the particle diameter determined from BET surface area and electron microscopy indicate that there is no void space between the crystallites which are accessible to the nitrogen adsorbate gas and the particles have smooth surfaces. Also He gas pycnometry has shown that there is no internal porosity. If the final particle size distribution arises from the coalescence of smaller particles, it is expected to fit a log-normal distribution with a fairly large standard deviation¹¹⁶. In general, this was not observed,

and it was concluded that the variation in particle size was primarily a consequence of the inherent concentration and temperature variations within the reaction zone. Finally, the light scattering and extinction measurements showed that the particle number density remained essentially constant as the particles travelled from the minimum detectable distance to the highest position measured. Based on the observations, it is unlikely that the polycrystalline particles formed by the coalescence of individual crystallites.

The nucleation and growth process could involve the formation of liquid silicon droplets which then solidify upon cooling. If the cooling rate is very rapid, it is possible that the liquid will solidify as an amorphous material. It is more likely that the silicon will crystallize upon cooling. Depending upon the kinetics of the transformation process, the droplets might crystallize as single or polycrystalline particles. The temperature results discussed in Section IV.A showed that under all conditions the maximum reaction zone temperature never exceeded the silicon melting point. The refractive index of liquid silicon is significantly different from the solid indices; therefore, if liquid droplets were present in the reaction zone, the light scattering and extinction results would predict particle size much larger than actually observed. It is therefore concluded that particle formation from cooling liquid droplets is a highly improbable synthesis mechanism.

Particles may form from the vapor phase as amorphous material and crystallize as they pass through the hottest regions of the reaction zone. If the reaction temperature remains below the crystallization temperature of amorphous silicon, the particles will remain amorphous.

Since the particles are only in the reaction zone for a short period of time (10's of milliseconds), it is possible that even at temperatures above the crystallization temperature, amorphous particles may persist. Under certain conditions, particles appeared amorphous within the sensitivity limits of X-ray diffraction (see Section IV.C) although it is possible that these powders contained crystallites with sizes below the limit of detection. If the temperature at which particle nucleation commences is sufficiently high, the particles may be crystalline as they form. Subsequent growth on these particles should be epitaxial in nature.

The formation of solid particles, either amorphous or crystalline, directly from the vapor phase, subsequent growth by accretion of vapor molecules, and crystallization of the amorphous particles in the hotter regions of the reaction zone appears to be a plausible particle formation mechanism. Various aspects of this formation mechanism will now be qualitatively discussed.

The formation of amorphous particles that crystallize as they travel further into the laser beam is consistent with the light scattering results discussed in Section IV.B. It was found that the number density of particles remained essentially constant if the particles were assumed to have indices suitable for amorphous silicon at the base of the "flame" and polycrystalline or a mixture of polycrystalline and amorphous silicon at positions higher in the reaction zone. It is likely that this behavior would have been observed for more experimental runs if careful measurements of the scattering at the extreme base of the reaction zone were performed.

The crystalline nucleation rate can be estimated from the light scattering results and the final particle characteristics. From the BET surface area and X-ray line broadening results, it was determined that on average a particle contained approximately 10-30 crystallites depending on whether the X-ray peaks were assumed to be Gaussian or Cauchy shaped. All of the crystallites may not have been formed during the initial crystallization; as the particles grew, new crystallites may have formed at the particle surface.

Referring to Figure IV.15, the amorphous/crystalline transition occurred at approximately 1000°C, although it was not possible to actually measure the particle temperature at the base of the reaction zone because the emissivity of the particle cloud was extremely small. Since the particles were growing during crystallization, the particle size used to calculate the nucleation rate ranged from 4 nm to 12 nm. The particles travelled a distance of 1.5 mm during the time of crystallization. Assuming the gas velocity range of 180 cm/sec, the average gas velocity at the nozzle tip, to 10 cm/sec, the velocity of the annular gas flow, the crystallization time was on the order of 0.8 msec to 15 msec. The estimate for the maximum nucleation rate is obtained by assuming the largest possible number of nuclei formed within the smallest measured particle in the shortest time period; this nucleation rate was calculated to be approximately 10^{24} nuclei/cm³·sec. The minimum nucleation rate, determined by assuming one nuclei formed in a particle with a diameter of 12 nm in 15 msec, was on the order of 10^{20} nuclei/cm³·sec.

Assuming their results can be extrapolated to 1000°C, Zellema et al.¹¹⁷ predicted the nucleation rate in electron beam evaporated amorphous silicon film deposited at substrate temperatures of 300°C to

be approximately 10^{16} nuclei/cm³·sec while Koster's results⁸² predicted a nucleation rate of 10^{11} nuclei/cm³·sec for E-beam evaporated amorphous silicon films deposited at 25°C. Thus the estimated nucleation rate was 4 to 13 orders of magnitude faster than that reported in the literature.

A final growth mechanism is that the nuclei are initially formed as amorphous or crystalline silicon. Particles then grow by the accretion of gaseous molecules at the surface. If the particle temperature is sufficiently high, the addition of molecules on the surface may result in crystalline nucleation. Additional growth may proceed as epitaxial or involve further crystalline nucleation. The crystalline regions may propagate (grow) into the original amorphous particle resulting in a final particle which is entirely crystalline. Under certain reaction conditions, it is possible that the temperature and growth times are insufficient to produce fully crystalline particles thus resulting in totally amorphous particles or particles containing both amorphous and polycrystalline regions. This mechanism is consistent with the light scattering results in describing the amorphous to polycrystalline transition. It is also consistent with the physical characteristics, i.e. narrow size distribution, spherical shape, and lack of open or closed porosity. This mechanism does not require the extremely high crystallite nucleation rates calculated if the particles crystallize in the reaction zone.

The fact that in fully crystalline powders the ratio of the particle to crystallite size is constant, i.e., the particles appear to contain the same number of crystallites regardless of size, is somewhat puzzling. There are several mechanisms by which a totally amorphous

particle can crystallize; the final microstructure can be vastly different for different mechanisms. Nucleation of the crystalline region can occur homogeneously within the volume of the particle or heterogeneously at the particle surface. The growth process is of particular importance in determining the particle microstructure. The growth kinetics are either interface or diffusion controlled. Since no composition change accompanies crystallization, diffusion is expected to be unimportant and interface controlled growth kinetics can be assumed dominant.

If growth is limited solely by the impingement of a growing crystallite with other crystallites¹¹⁷ and the product of the growth rate and the time period between nucleation and impingement is less than the particle dimension, then the number of crystallites per particle is expected to be proportional to the particle volume if nucleation occurs homogeneously within the bulk of the sample or proportional to the surface area if nucleation occurs on the particle surface.

If the growth rate - growth time product is large compared to the physical dimensions of the particle, then a single crystalline particle is expected. Turnbull¹¹⁸ examined this case by following the solidification of mercury droplets in a methyl cyclopentane solution. The lack of single crystalline particles in the laser synthesized silicon makes this mechanism improbable.

Therefore, none of the existing theories involving the crystallization of an amorphous particle adequately explains the constant number of crystallites in a fully crystallized particle. This is not surprising since the microstructural development in the laser

synthesis process is far more complex than the simple crystallization of an amorphous particle.

Any proposed mechanisms to explain the observed particle microstructure are purely speculative. The two mechanisms described involving the initial formation of amorphous particles and either the crystallization in the amorphous material or crystalline nucleation on the surface may be consistent with the constant number of nuclei per particle. If under all run conditions, the particles begin to crystallize or crystalline nucleation occurs on the particle surface when the particles reach approximately the same diameter and reaction temperature, then the number of initial nuclei is expected to be the same for all particles. If ensuing growth occurs epitaxially, then the number of crystallites in the final particle will be independent of the final particle diameter. Kirkorian and Sneed⁷⁷ reported similar behavior in the formation of solid germanium on various substrates by evaporation and sputtering techniques. Depending on the reaction conditions, the final films were either amorphous, amorphous with randomly oriented crystallites, polycrystalline, or single crystal. In a study on the chemical vapor deposition of silicon from silane on a silicon single crystal, Bloem⁷⁸ found that the crystalline nature of the deposit was highly dependent on the temperature and growth rate. To validate any of the proposed mechanisms, more careful study of the initial nucleation and the transition between amorphous and crystalline behavior is required. This would necessitate a higher resolution light scattering apparatus, to measure the scattering from smaller particles and accurate determination of the reaction temperature at the onset of nucleation and during the amorphous to crystalline transition.

V. CONCLUSIONS

1. The laser synthesis process produces powder with nearly ideal characteristics. The particle characteristics can be systematically and reproducibly varied by manipulation of the laser intensity, reaction pressure, dilution of the reactant gas, and reactant gas flow rates. The conversion efficiency to solid particles is nearly 100%.
2. The silane decomposition reaction is thermal in nature with the temperature of the reactant gas determined by the laser intensity, the effective absorption coefficient at the particular emission line, the heat capacity of the the reactant gas mixture, and the residence time in the laser beam.
3. Thermal analyses showed that at low flow rates, conduction of heat to the inlet nozzle is sufficient to preheat the reactant gas. The heat generated by the exothermic decomposition is insufficient to sustain the reaction without further laser energy input.
4. Gas phase nucleation is initiated at the beginning of the reaction zone and ceases after little growth has occurred. The cessation is largely a result of the particle growth by the accretion of vapor molecules being favored over further nuc-

leation. The observed nucleation rate, $>10^{14}$ nuclei/cm³·sec, is in good agreement with the calculated rate using the Volmer and Weber theoretical formulism.

5. The growth was determined to be limited by the transport of vapor species to the particle surface, but the experimentally observed growth rate is 2 to 3 orders of magnitude lower than the growth rate calculated from the vapor transport model. A condensation coefficient of 0.002 to 0.02 is needed to bring the theoretical growth rate into agreement with the observed growth rate. The nature of the growth process results in a narrow distribution of particle sizes.
6. Particle agglomeration did not occur within the reaction zone but occurred as the particles travelled to the collection filter or as they were collected.
7. Depending on the reaction conditions, in particular the temperature, the as-synthesized particles can be amorphous, polycrystalline, or contain a mixture of amorphous and crystalline silicon. The percentage of crystalline silicon within the amorphous/polycrystalline particles was found to increase with the maximum reaction zone temperature.

VI. FUTURE WORK

Suggestions for future work include:

1. A survey study of a wide variety of chemical reactions with various dopants should be performed. If the reactant molecules do not sufficiently absorb the P(20) radiation emitted from high powered commercial lasers, a frequency tunable laser may be required. The economic viability of each process should be examined by considering the reactant costs, processing costs, value of the final powders, and value of any reusable products.
2. To quantitatively model the laser synthesis process more accurate absorption measurements are required. The following aspects should be examined: a) the effect of temperature and pressure on the silane absorption coefficient, b) the absorption behavior of the reaction intermediates and products, and c) the effect of laser intensity and the extent to which saturation causes the strong observed intensity dependence.
3. A more detailed growth model requires a better understanding of the gas flow characteristics. The effects of heating the gas and the expansion of the gas stream due to the pyrolysis reaction should be examined. It was shown that with certain reaction conditions, conduction of heat to the gas inlet

nozzle was important. The gas flow model should take this into account. This may result in computation problems since the typical computer models utilize a marching finite difference integration technique where it is assumed the gas volume elements are unaffected by the upstream conditions. This is not a valid assumption when the conduction of heat through the incoming gas is significant. By using interferometry or Schlieren photography, it is possible to determine the boundary between the reactant gas stream and the annular argon flow.

4. Higher resolution light scattering/extinction measurements are required to further understand the actual nucleation and growth behavior. Focusing the probe laser and using a short wavelength source should permit the detection of smaller particles. The effects of particle size, temperature, impurities, crystallinity and wavelength of incident light on the silicon index of refraction need to be investigated. The analysis of the scattering/extinction results might be simplified if a blue or ultraviolet light source is used since the refractive index for single crystalline, polycrystalline, and amorphous silicon converge at these wavelengths.¹²⁴ An infrared pyrometer should be used to determine the flame temperature in regions which are not luminous. The scattering/extinction in the upper region of the flame should be examined to determine if agglomeration is occurring.

5. A fundamental short coming of the present thesis is the uncertainty in the reaction sequence. To quantitatively compare the theoretically calculated nucleation and growth rates to the experimentally measured results, it is necessary to know the gas species which are involved in the nucleation process and which are absorbed onto the particle surface during growth. Mass spectrometry may provide insight into the species present within the reaction zone although the short lifetime of the intermediate molecules and radicals may prevent accurate measurement. Flame emission spectroscopy is probably not a viable measurement technique since the black body emission from the reaction zone will mask the fine emitted spectra.
6. Because it is extremely difficult to handle particles with average sizes less than 100 nm, various methods to increase the particle size should be examined. Since particle formation occurs via homogeneous nucleation and growth processes, the maximum particle size is limited by the number of particles produced during nucleation. Increasing the reaction pressure should increase the overall particle size since the nucleation rate is relatively insensitive to pressure changes but the increase in pressure will increase the silicon available to each growing particle. It was shown that soon after nucleation was initiated particle growth became dominant over further nucleation. Therefore, it may be

possible to inject additional silane into the reaction zone enabling growth to larger sizes. By using a second light source with a wavelength that silicon strongly absorbs, it should be possible to heat the particles with little effect on the unreacted silane gas molecules. Growth will occur rapidly on the heated particles by the adsorption and thermal decomposition of the silane.

7. By altering the laser intensity and reactant gas pressure, it is possible to cause heterogeneous nucleation on a substrate, rather than homogeneous nucleation within the vapor phase. The feasibility of this process has been demonstrated by Gattuso et al.¹²⁵ This process can be adapted to include the coating of the laser synthesized particles with other materials. For instance, a sintering aid may be deposited directly into the particle's surface providing maximum effectiveness. Also polymeric dispersants may be deposited onto the particles prior to agglomeration.

8. The feasibility of an industrial process utilizing the laser powder synthesis technique should be investigated. Different system geometries are required to permit full utilization of the laser energy and still maintain uniform gas heating rates. To be economically feasible, the powder production rate should be increased by at least a thousand times. A continuous powder collection technique must be designed.

Appendix K. Synthesis Process Conditions and Maximum Reaction Zone Temperature

Effect of Flow Rate*

Pressure = 2×10^4 Pa

Run Number	SiH ₄ Flow Rate ($\frac{\text{cm}^3}{\text{min}}$)	Average Velocity ($\frac{\text{cm}}{\text{sec}}$)	Max. Temp. $\frac{C(S)}{C(E)} = 0.3$ (°C)	Max. Temp. $\frac{C(S)}{C(E)} = 0.0$ (°C)
629S	5.5	26	1010	970
627S	7.5	35	1060	1020
628S	8.8	41	1090	1050
625S	11	52	1050	1110
626S	13	61	1210	1170
631S	38	179	1230	1200
632S	38	179	1230	1200
653S	38	179	1230	1200
633S	60	283	1200	1170
630S	104	490	1130	1100

* Laser Intensity = 531 W/cm² $\frac{C(S)}{C(E)}$ is the assumed ratio of the $\frac{C(S)}{C(E)}$ is the assumed ratio of the scattering to extinction cross sections.

Effect of Flow Rate*

Pressure = 3.5×10^4 Pa

Run Number	SiH ₄ Flow Rate ($\frac{\text{cm}^3}{\text{min}}$)	Average Velocity ($\frac{\text{cm}}{\text{sec}}$)	Max. Temp. $\frac{C(S)}{C(E)} = 0.3$ (°C)	Max. Temp. $\frac{C(S)}{C(E)} = 0.0$ (°C)
643S	11	30	1140	1100
636S	16	43	1230	1200
644S	28	75	1320	1280
624S	40	108	1310	1270
622S	66	178	1250	1220
623S	109	294	1150	1120
649S	109	294	1150	1120

* Laser Intensity = 601 W/cm²

Effect of Flow Rate*Pressure = 6×10^4 Pa

Run Number	SiH ₄ Flow Rate ($\frac{\text{cm}^3}{\text{min}}$)	Average Velocity ($\frac{\text{cm}}{\text{sec}}$)	Max. Temp. $\frac{C(S)}{C(E)} = 0.3$ (°C)	Max. Temp. $\frac{C(S)}{C(E)} = 0.0$ (°C)
659S	19.5	31	1250	1210
652S	30	47	1280	1240
656S	45	71	1330	1290
650S	66	104	1370	1330
651S	90	141	1330	1300
657S	110	173	1270	1240

Laser Intensity = 531 W/cm²Effect of Argon Dilution

Run Number	Ar/SiH ₄ Ratio	Max. Temp. $\frac{C(S)}{C(E)} = 0.3$ (°C)	Max. Temp. $\frac{C(S)}{C(E)} = 0.0$ (°C)
631S	0/1	1220	1180
632S	0/1	1220	1180
653S	0/1	1220	1180
662S	1/5	1210	1170
661S	1/3	1190	1160
639S	1/2	1150	1120
642S	1/1	1150	1120
637S/654S	2/1	1060	1030
634S	5/1	1010	980

* Total Pressure = 2×10^4 Pa; Total Flow Rate (Ar + SiH₄) = $38 \frac{\text{cm}^3}{\text{min}}$
Laser Intensity = 601 W/cm²

Effect of Laser Intensity*

Run Number	Power (W)	Intensity (W/cm ²)	Max. Temp. $\frac{C(S)}{C(E)} = 0.3$ (°C)	Max. Temp. $\frac{C(S)}{C(E)} = 0.0$ (°C)
658S	38	134	940	920
640S	50	176	970	950
638S	75	265	1030	1000
648S	115	407	1130	1100
646S	120	424	1090**	--
635S	150	531	1205	1170
622S	170	601	1250	1210
645S	170 focus	5401	1230**	--

* Pressure = 3.5×10^4 Pa; Silane Flow Rate = 66 cm³/min

** Uncorrected Pyrometric Temperature

Other Synthesis Runs*

Run Number	Intensity (W/cm ²)	SiH ₄ Flow Rate ($\frac{\text{cm}^3}{\text{min}}$)	Ar Dilution ($\frac{\text{cm}^3}{\text{min}}$)	Temperature*** (°C)
655S	265	30	30	~800
660S	176	20	40	****
SiH ₄ +B ₂ H ₆	531	50	25**	~1010
SiH ₄ +Ar	531	50	25	~980

* Pressure = 2×10^4 Pa

** 1.0% B₂H₆ + 99.0% Ar Gas Mixture Used as Dilutant

*** Uncorrected Pyrometric Temperature

**** Flame Temperature Too Low to Measure

Appendix 2. Powder Characteristics

Effect of Flow Rate

Pressure = 2×10^4 Pa

Run Number	Efficiency (%)	d_{BET} (nm)	$d_{\text{XRAY,G}}$ (nm)	$d_{\text{XRAY,C}}$ (nm)	Number Density (#/cm ³)	Fraction Crystalline
629S	>85	36.8	7.5	9.1	1.2×10^{12}	0.28
627S	90	40.2	8.6	10.7	8.8×10^{11}	0.32
628S	100	50.5	12.7	17.5	4.5×10^{11}	0.43
625S	92	66.4	16.2	24.2	2.0×10^{11}	0.48
626S	92	66.1	20.2	33.1	2.0×10^{11}	0.94
631S	87	60.5	20.0	32.4	2.6×10^{11}	1.18
632S	88	63.3	19.1	30.5	2.3×10^{11}	0.90
653S	--	61.2	19.1	30.5	2.5×10^{11}	1.00
633S	90	53.1	14.4	20.6	3.8×10^{11}	0.65
630S	98	41.9	10.7	14.0	7.8×10^{11}	0.55

* Assumes Gaussian X-ray peak shapes.

** Assumes Cauchy X-ray peak shapes.

Effect of Flow Rate

Pressure = 3.5×10^4 Pa

Run Number	Efficiency (%)	d_{BET} (nm)	$d_{\text{XRAY,G}}$ (nm)	$d_{\text{XRAY,C}}$ (nm)	Number Density (#/cm ³)	Fraction Crystalline
643S	89	85.9	29.3	58.3	1.6×10^{11}	1.07
636S	86	93.0	32.6	69.7	1.2×10^{11}	1.16
644S	90	105.9	33.5	72.3	8.4×10^{10}	0.85
624S	100	110.7	37.2	86.7	7.4×10^{10}	1.02
622S	90	102.7	34.8	72.1	9.3×10^{10}	1.05
623S	100	58.3	17.1	26.1	5.1×10^{11}	0.68
649S	97	58.3	19.7	31.7	5.1×10^{11}	1.04

Effect of Flow Rate

Pressure = 6×10^4 Pa

Run Number	Efficiency (%)	d_{BET} (nm)	$d_{\text{XRAY,G}}$ (nm)	$d_{\text{XRAY,C}}$ (nm)	Number Density (#/cm ³)	Fraction Crystalline
659S	96	94.5	33.3	69.8	2.0×10^{11}	1.40
652S	95	103.3	32.9	71.2	1.6×10^{11}	1.06
656S	87	135.1	43.3	112.4	7.0×10^{10}	1.08
650S	91	146.9	41.4	103.9	5.4×10^{10}	0.78
651S	95	129.0	46.5	100.5	8.0×10^{10}	1.01
657S	89	128.4	35.3	79.4	8.1×10^{10}	0.74

Effect of Dilution

Run Number	Efficiency (%)	d_{BET} (nm)	$d_{\text{XRAY,G}}$ (nm)	$d_{\text{XRAY,C}}$ (nm)	Number Density (#/cm ³)	Fraction Crystalline
631S	87	60.5	20.0	32.4	2.6×10^{11}	1.08
632S	88	63.3	19.1	30.5	2.3×10^{11}	0.82
653S	--	61.2	19.1	30.5	2.5×10^{11}	0.91
662S	90	62.5	20.4	33.0	1.9×10^{11}	1.04
661S	--	60.9	22.2	37.2	1.9×10^{11}	1.40
639S	88	70.9	22.4	38.7	1.7×10^{11}	0.94
642S	88	58.6	18.9	29.7	1.5×10^{11}	0.98
637S/654S	81	34.9	8.3	10.2	4.5×10^{11}	0.44
634S	80	29.4	6.8	8.2	3.8×10^{11}	0.33

Effect of Laser Intensity

Run Number	Efficiency (%)	d_{BET} (nm)	$d_{\text{XRAY,G}}$ (nm)	$d_{\text{XRAY,C}}$ (nm)	Number Density (#/cm ³)	Fraction Crystalline
658S	97	32.1	4.0	5.0	3.0×10^{12}	0.05
640S	92	35.2	6.2	7.2	2.3×10^{12}	0.15
638S	98	38.6	7.1	8.6	1.8×10^{12}	0.22
648S	92	68.9	21.7	36.8	3.0×10^{11}	0.84
646S	94	75.5	25.4	46.8	2.3×10^{11}	1.03
635S	89	93.2	33.8	74.1	1.2×10^{11}	1.20
622S	90	102.7	34.8	78.1	9.3×10^{10}	1.05
645S	91	110.6	35.3	78.9	7.4×10^{10}	0.89

Other Runs

Run Number	Efficiency (%)	d_{BET} (nm)	$d_{\text{XRAY,G}}$ (nm)	$d_{\text{XRAY,C}}$ (nm)
655S	85	28.9	5.6	6.7
660S	96	18.9	**	**
SiH ₄ + B ₂ H ₆	90-100	54.9		
SiH ₄ + Ar	90-100	55.1		

** Amorphous

APPENDIX 3: PARTICLE SIZE ANALYSIS

BET SURFACE AREA

The surface area was determined by measuring the amount of nitrogen adsorbed onto the sample and utilizing the Brunauer-Emmett-Teller (BET) equation¹¹⁹

$$\frac{P}{V(P_0 - P)} = \frac{1}{V_m C} + \frac{C - 1}{V_m C} \frac{P}{P_0} \quad \text{A3.1}$$

where P is the equilibrium pressure of nitrogen, P_0 is the saturation pressure of the nitrogen gas at liquid N_2 temperature, V is the volume of gas adsorbed at equilibrium pressure P , V_m is the volume of gas required to form a monolayer, and C a constant related to a special value of the heat adsorption,

$$C = \exp \left[\frac{(H_1 - H_2)}{RT} \right] \quad \text{A3.2}$$

where H_1 is the heat of adsorption at the monolayer point and H_2 is the heat of condensation.

The amount of adsorbed gas was determined by a continuous flow method* in which a thermal conductivity detector is used to determine changes in a flowing gas concentration. A line having intercept $I = 1/V_m C$ and slope $S = (C - 1)/V_m C$ is obtained when $P/V(P_0 - P)$ is plotted against P/P_0 . V_m is then calculated from

$$V_m = 1/(S + I) \quad \text{A3.3}$$

and the specific surface area is

* Quantachrome Corporation, Quantasorb.

$$S_W = \frac{N A_{CS} V_m}{M_W} \quad A3.4$$

where S_W is the specific surface area (m^2/g). A_{CS} is the area occupied by one adsorbate ($cm^3/mole$) and W is the sample mass (g).

If the particles are spherical with smooth surfaces and no open porosity, the particle diameter is

$$d = 6/\rho S_W \quad A3.5$$

where d is the diameter (μm), ρ is the powder density (g/cm^3) and S_W is the surface area (m^2/g).

To accurately determine the slope and intercept of the line represented by Equation A3.1, it is necessary to measure the volume of gas adsorbed at a minimum of 3 to 4 values of P/P_0 . If the value of C is large, the analysis time can be considerably shortened by measuring only the adsorption at a single point assuming a value of infinity for C . Therefore Equation A3.1 reduces to:

$$P/V(P_0 - P) = P/P_0 \cdot V_m \quad A3.6$$

or

$$V_m = V(1 - P/P_0) \quad A3.7$$

The amount of relative error is determined from Equations A3.1 and A3.7:

$$\frac{V_m - V_m'}{V_m} = \frac{1 - P/P_0}{1 + P(C - 1)/P_0} \quad A3.8$$

where V_m is the actual volume at monolayer coverage and V_m' is the volume at monolayer coverage calculated from a single measurement at a relative pressure P/P_0 . For an adsorbate/adsorbent system having a C

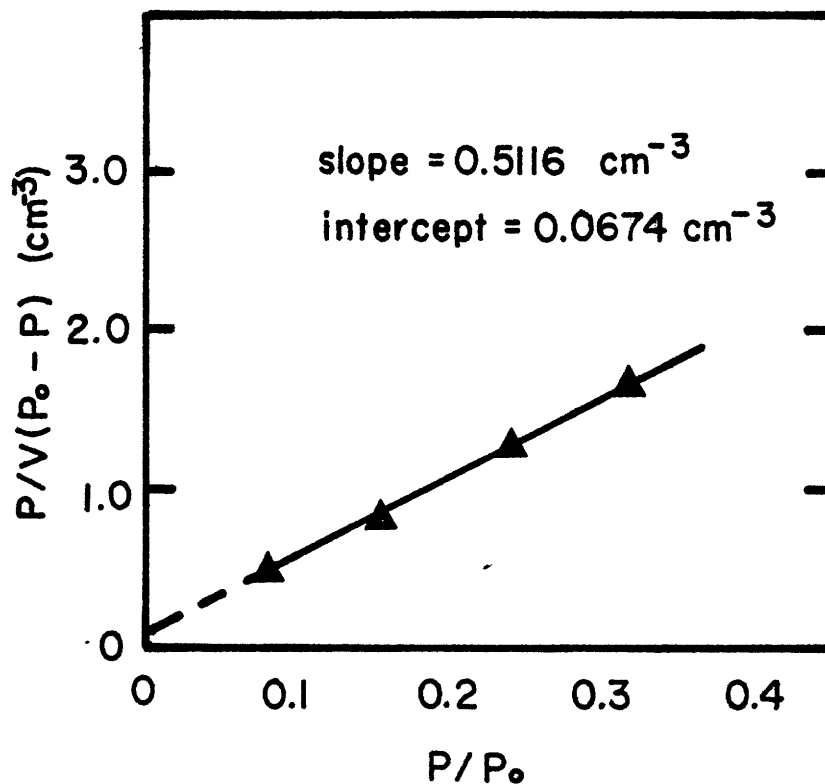


Figure A3.1. Plot of $P/V(P_0 - P)$ versus P/P_0 from BET multipoint surface area measurement. (Run 630S)

Table A3.1. Comparison of Multipoint and Single Point BET Surface Area Measurements

Run Number	Surface Area (m^2/g)		BET Constant, C	Relative* Error (%)
	Multipoint	Single Point		
630S	62.9	61.4	80	2.5
	62.6		81	2.5
631S	44.3	42.6	66	3.4
660S	137	136	53	3.8

* Relative error introduced with single point measurement and assumption that $C = \infty$.

value of 50, a single point measurement at $P/P_0 = 0.3$ will result in less than 5% error.

Figure A3.1 shows a plot of $P/V(P_0 - P)$ versus P/P_0 for surface area measurements on a typical silicon powder (630S). From the slope and intercept, the volume occupied by monolayer coverage V_m was calculated to be 0.193 cm^3 . With a sample weight of 0.0122 g this corresponds to a specific surface area of $61.2 \text{ m}^2/\text{g}$ or an equivalent diameter of 42.1 nm. The C value was calculated to be 77, corresponding about 2.5% if only a single point measurement was performed at $P/P_0 = 0.3$

Table A3.1 shows numerous runs in which both multipoint and single point adsorption measurements were performed. In general, the agreement between the two techniques was very good as anticipated from the high value of C. It was therefore concluded that single point measurements could be used with less than 5% error which is approximately equivalent to the systematic error expected from random sampling of a powder batch.

X-RAY LINE BROADENING

The crystallite size was determined by measuring the broadening of an X-ray diffraction line. The procedure is based on the principal that X-ray interference lines undergo broadening when the crystallite size is below about 100 nm. Broadening will also result if the lattice parameters show scatter around the mean value, that is there is significant lattice distortion or if stacking faults are present.

Heckel and Youngblood¹²⁰ have shown the effect of stacking faults in nonmetals is negligible.

It is necessary to separate the contributions of small crystallite size and lattice distortions. Since the broadening effects have different angular dependencies, the separation is straightforward if at least two diffraction peaks are measured. Ziegler¹²¹ describes the techniques used and the application in measuring the crystallite size in ceramic powders and compacts.

The first step is to separate the $K\alpha_1/K\alpha_2$ doublet. If the peaks are assumed symmetrical with the $K\alpha_1$ intensity two times that of the $K\alpha_2$ intensity, the Rachinger correction¹²² can be used to resolve the doublet. Next, it is necessary to separate the instrument broadening from the machine broadening. A large grained 10 μm polycrystalline silicon sample was used to determine the instrument broadening. After the Rachinger correction was applied, the peak breadths were determined by measuring the full width at half maximum intensity. Determination of the integral breadth will give more accurate results, but since the qualitative difference from run to run was the prime interest, it was decided that the simpler full width at half maximum intensity was sufficient. To actually separate the machine broadening from the crystallite and strain broadening requires a complete Fourier analysis. If the peak shapes are assumed to be either Gaussian or Cauchy, the following relations can be used:

$$\beta = B - b \quad \text{Cauchy Shaped Peaks} \quad \text{A3.9}$$

or

$$\beta^2 = B^2 - b^2 \quad \text{Gaussian Shaped Peaks} \quad \text{A3.10}$$

Table A3.2. Diffraction Line Broadening from Typical Laser Synthesized Silicon (Run 631S)

Bragg Diffraction Angle θ (degrees)	(hkl)	$\frac{\sin\theta}{\lambda}$ (nm^{-1})	Broadening β (radians)	$\frac{\beta\cos\theta}{0.9\lambda}$ (nm^{-1})
14.24	(100)	1.58	0.00702	0.0490
23.68	(220)	2.60	0.00751	0.0500
28.10	(311)	3.05	0.00769	0.0488
34.62	(400)	3.68	0.00890	0.0528

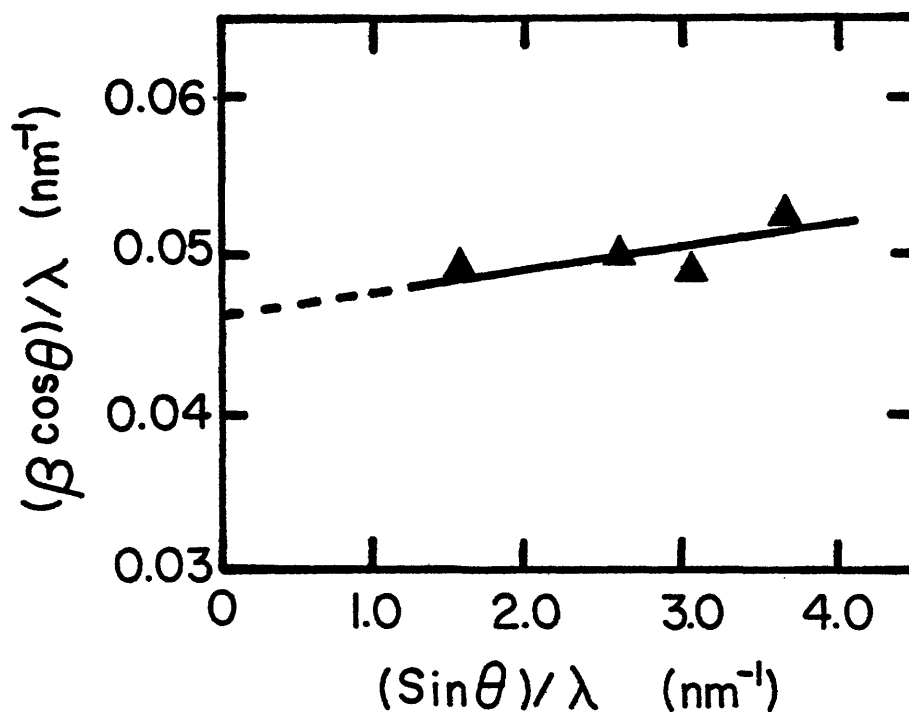


Figure A3.2. Plot of $(\beta\cos\theta)/\lambda$ versus $(\sin\theta)/\lambda$ from line broadening results for powder from Run 631S. Slope is related to the percent of lattice distortion. Intercept is related to the crystallite size.

where β is the broadening due to strain and small crystallite effects, B is the sample broadening, and b is the standard peak broadening.

The line broadening resulting from small crystallite size and lattice distortion are related by

$$\frac{\beta \cos\theta}{k\lambda} = \frac{1}{\Lambda} + 4 \frac{\Delta a}{a} \frac{\sin\theta}{k\lambda} \quad \text{A3.11}$$

where Λ is the mean crystallite size normal to the diffraction plane, λ is the X-ray wavelength, $\frac{\Delta a}{a}$ is the average lattice distortion normal to the diffraction plane, k is a shape factor equal to approximately 0.9 and θ is the Bragg diffraction angle. A plot of $\sin\theta/k\lambda$ versus $\beta\cos\theta/k\lambda$ will have a slope and intercept related to the lattice distortion and crystallite size.

Table A3.2 summarizes the broadening from four different diffraction peaks of sample 631S. There is some uncertainty in the broadening of the peak corresponding to the (400) diffraction since this intensity was quite low. Figure A3.2 shows a plot of $\sin\theta/\lambda$ versus $\beta\cos\theta/k\lambda$. The intercept of 0.0462 nm^{-1} gives a crystallite size of 21.6 nm and the slope of 0.0014 indicates a lattice distortion of less than 0.04%. It can therefore be concluded that the majority of the broadening is a consequence of the small crystallite size and not lattice distortion.

APPENDIX 4: GAS FLOW CHARACTERISTICS

To characterize the reaction zone, it is essential to understand the reactant gas flow characteristics. Under all synthesis conditions the flow can be assumed laminar in nature. For fully developed laminar flow, the velocity distribution will have a parabolic shape with the maximum velocity at the center of the stream equal to twice the average velocity. If the reactant gas stream has a much larger velocity than the annular flow, it can be assumed that the gas is flowing into a stagnant atmosphere. As the gas travels into the reaction cell, the stream will expand in a conical fashion, the axial velocity will decrease approximately linearly with distance, and there will be diffusive transport between the reactant gas stream and the outer argon flow. The rate of transfer across the argon/reactant gas interface will be constant regardless of the initial velocity and nozzle radius.⁹³

The minimum gas velocity can be assumed equal to the annular argon flow. Therefore, the actual velocity at any position within the reactant gas stream is bounded by the maximum velocity at the nozzle inlet and the velocity of the outer argon flow.

A computer model was used to characterize the laminar streamlined gas flow behavior⁹⁴. The model treats the gas flow as an axi-symmetric jet emerging from a circular nozzle which enters a coaxial stream. The values of the dependent variables, ie. flow velocity in the direction of flow, mass fraction of a chemical species, etc., are calculated by a finite difference numerical integration of the differential equations describing the heat, mass, and momentum transfer.

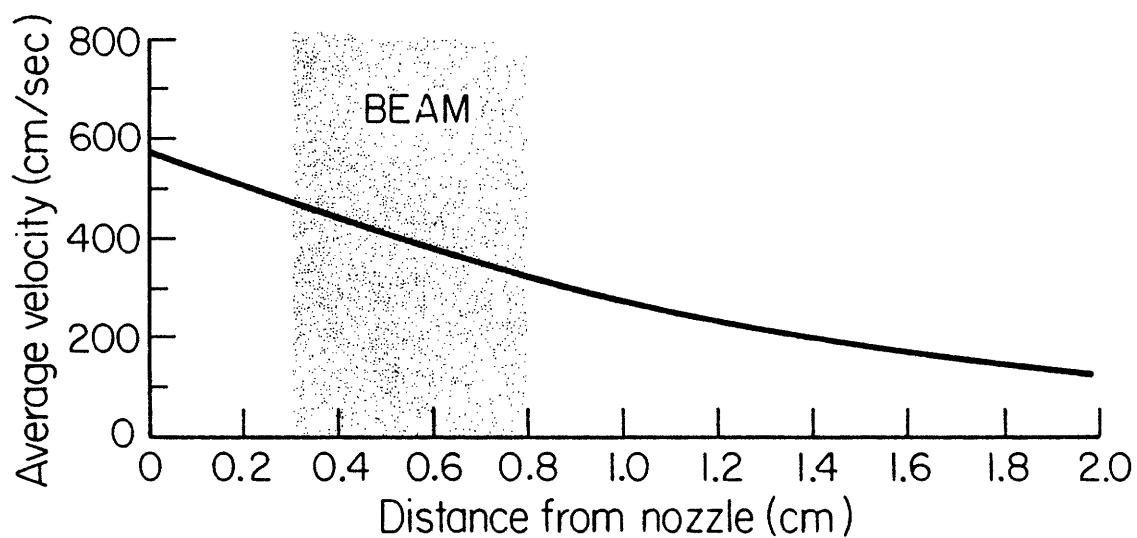


Figure A4.1. Average velocity of gas stream as a function of distance from the inlet nozzle. (Run condition similar to Run 630S)

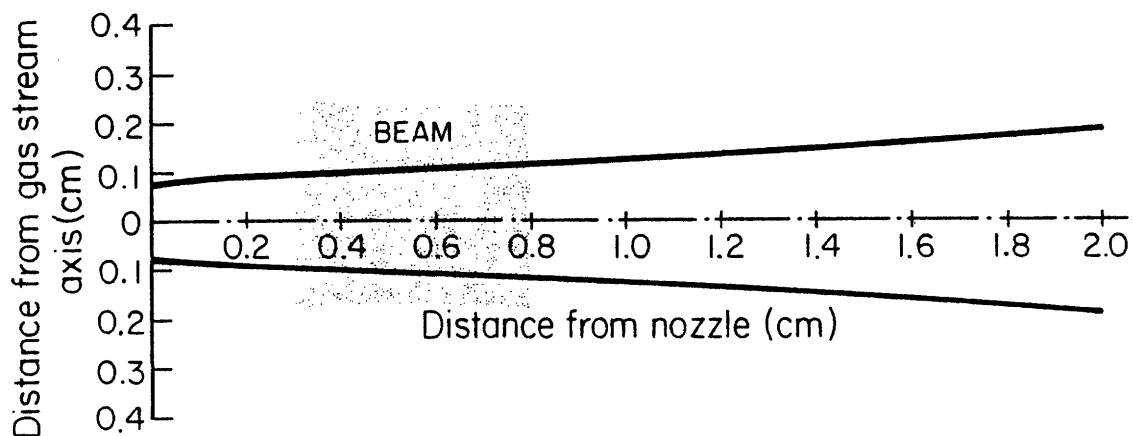


Figure A4.2. The computed width of the gas stream as a function of distance from the inlet nozzle. (Run conditions similar to Run 630S)

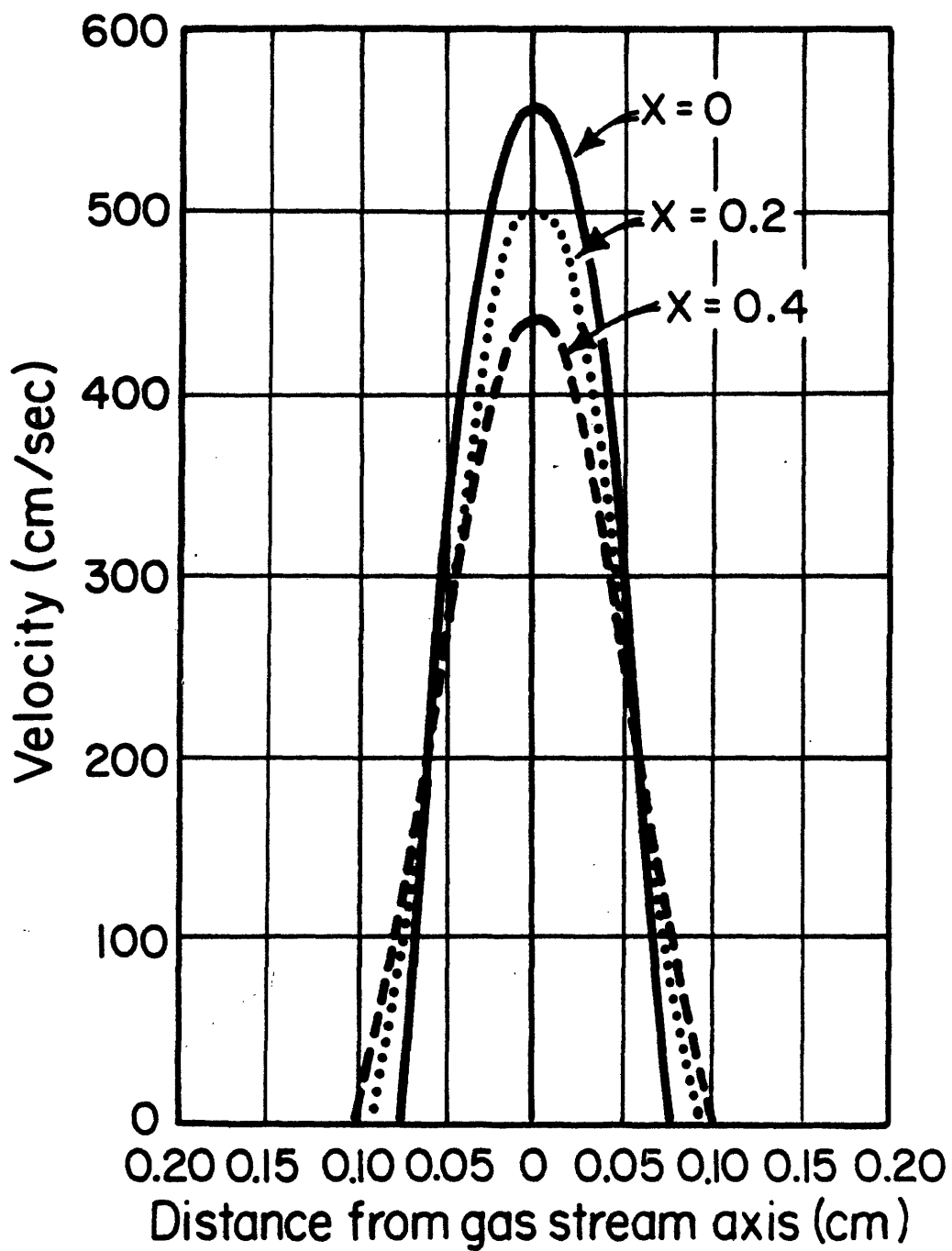


Figure A4.3. The computed velocity profile of reactant gases at several distances ($x = _ \text{ cm}$) from the inlet nozzle. (Run condition similar to Run 630S)

In the form utilized, the computer model only considers the velocity distribution and mass within the gas jet. The fluid is treated as a single phase containing only one chemical species with a constant density and viscosity. The annular gas flow is assumed to have the same fluid properties as those of the inner jet. Gradients in temperature and pressure as well as the effect of an exothermic reaction are ignored. Although highly simplified, this model provides at least qualitative insight into the fluid flow.

Figures A4.1, A4.2, and A4.3 show typical computer results describing: 1. the change in average velocity with distance from the inlet nozzle, 2. the boundary between the inner stream of reacting gas and the outer argon flow, and 3. a typical velocity profile at a particular distance from the inlet nozzle.

Comparison of the calculated gas flow behavior with the observed flame shape showed that at the base of the flame the reactant gas stream diameter is approximately 3x larger than the calculated diameter. Since the computer model does not consider the volumetric increase in the gas due to heating and the decomposition reaction, these effects should be added to the calculated stream width. A temperature increase from 300K to 1100K will produce a volume increase of 3.6x while the increase due to the silane decomposition reaction will result in a volume increase of 2x. Combined these effects result in a radial increase of about 1.9x if Δr is proportional to $(\Delta V)^{1/3}$ or 2.6x if Δr is proportional to $(\Delta V)^{1/2}$, which assumes only radial expansion. The combination of these effects substantially resolves the difference between the observed and calculated gas stream diameters.

REFERENCES

1. P. Popper, "Introductory Lecture," in Proceedings of the NATO Advanced Study Institute on Nitrogen Ceramics, Ed. F.L. Riley, Canterbury, U.K., 1976.
2. C. Greskovich and J.H. Roslowski, "Sintering of Covalent Solids," J. Am. Ceram. Soc., 59, 336-43 (1976).
3. A. Kato, et al., "Formation of Ultrafine Powder of Refractory Nitrides and Carbides by Vapor Phase Reaction," Memoirs of the Faculty of Eng., Kyushu Univ., 41, 319-34 (1981).
4. A. Kaldor and R.L. Woodin, "Applications of Lasers to Chemical Processing" to be published in IEEE, Special Issue on Laser Applications.
5. J.S. Haggerty, Sinterable Powders from Laser Driven Reactions, Under Contract N00014-77-C0581, Final Report, M.I.T., Cambridge, MA, 1981.
6. W.R. Cannon, et al., "Sinterable Ceramic Powders from Laser Driven Reactions, Part I: Process Description and Modelling," J. Am. Ceram. Soc., 65, 324-30 (1982).
7. Y. Suyama, et al., "Synthesis of Ultrafine SiC Powders by Laser Driven Gas Phase Reactions," to be published.
8. C.M. Golino, Unpublished research.
9. T.R. Gattuso, Unpublished research.
10. M. Volmer and A. Weber, "Keimbildung in übersättigten Gebilden," Z. Phys. Chem., 119, 277 (1926).
11. R. Becker and W. Doring, "Kinetische Behandlung der Keimbildung in übersättigten Dämpfen," Ann. physik, 24, 719-52 (1935).
12. R.A. Swalin, Thermodynamics of Solids, John Wiley & Sons, New York, 1972, p. 182.
13. J.C. Fisher, et al., "Nucleation," J. Appl. Phys., 19, 775-84, (1948).
14. A.J. Pesthy, et al., "The Effect of a Growing Aerosol on the Rate of Homogeneous Nucleation of a Vapor," J. Colloid Interface Sci., 82, 465-79 (1981).
15. E.H. Kennard, Kinetic Theory of Gases, McGraw Hill, New York, 1938.
16. J. Zeldovich, Soviet Phys. JETP, 12, 525 (1942).

17. F.F. Abraham, *Homogeneous Nucleation Theory*, Academic Press, New York, 1974, pp. 184-91.
18. J.C. Kirkwood and F.B. Buff, "Statistical Mechanical Theory of Surface Tension," *J. Chem. Phys.*, 17, 338-43 (1949).
19. F.C. Buff, "The Spherical Interface: I. Thermodynamics," *ibid.*, 19, 1591-4 (1951).
20. J. Lothe and G.M. Pound, "Reconsideration of Nucleation Theory," *ibid.*, 36, 2080-5 (1962).
21. A. Kantrowitz, "Nucleation in Very Rapid Vapor Expansions," *ibid.*, 19, 1097-100 (1951).
22. R.F. Probst, "Time Lag in Self Nucleation of a Supersaturated Vapor," *ibid.*, 19, 619-26 (1951).
23. F.C. Collins, *Z. Elektrochem.*, 59, 404 (1955).
24. H. Wakeshima, "Time Delay in Homogeneous Nucleation," *J. Chem. Phys.*, 22, 1614 (1954).
25. H. Reiss, et al., "Translation-Rotation Paradox in the Theory of Nucleation," *ibid.*, 48, 5553-60 (1968).
26. JANAF, *Thermodynamic Tables*, NSRDS-NBS, 37, 1971.
27. F. Smoluchowski, "Über Brownsche Molekularbewegung unter Einwirkung äußerer Kräfte und deren Zusammenhang mit der verallgemeinerten Diffusionsgleichung," *Ann. Physik*, 48, 1103 (1915).
28. F.C. Collins and G.E. Kimball, "Diffusion Controlled Reactions in Liquid Solutions," *Ind. Eng. Chem.*, 41, 2251-3 (1949).
29. L.M. Skinner and J.R. Sambles, *Aerosol Sci.*, 3, 199 (1972).
30. S.K. Friedlander, *Smoke, Dust, and Haze*, Chap. 7, John Wiley and Sons, New York, 1977.
31. H.L. Frisch and F. Collins, "Diffusional Processes in the Growth of Aerosol Particles," *J. Chem. Phys.*, 20, 1797-803 (1952).
32. N.A. Fuchs and A.G. Sutagin, "Highly Dispersed Aerosols" in *Topics in Current Aerosol Research*, Vol. II, Eds. G.M. Hidy and J.R. Brock, Pergamon Press, Oxford, 1972.
33. N.A. Fuchs, *Evaporation and Droplet Growth in Gaseous Media*, Pergamon Press, Oxford, 1959.
34. H. Reiss and V.K. LaMer, "Diffusional Boundary Value Problem Involving Moving Boundaries Connected with the Growth of Colloidal Particles," *J. Chem. Phys.*, 18, 1-12 (1950).

35. H.L. Frisch and F.C. Collins, "Diffusional Processes in the Growth of Aerosol Particles, II," *ibid.*, 21, 2158-65 (1953).
36. H.L. Frisch, *Z Elektrochem.*, 56, 324 (1952).
37. N.G. Basov, et al., "Stimulation of Chemical Reactions by Laser Radiation," *Sov. Phys. JETP Letts.*, 14, 165 (1971).
38. S.W. Mayer, et al., "Isotope Separation with cw Hydrogen Fluoride Laser," *Appl. Phys. Letts.*, 17, 516-19 (1970).
39. G.W. Pratt, "Method of Altering Biological and Chemical Activity of Molecular Species," U.S. Patent 3,941,670 (1976).
40. R.V. Ambartzumian and V.S. Letokhov, "Infrared Laser Chemistry," in Chemical and Biological Applications of Lasers, Ed. C.B. Moore, Vol. III, Academic Press, New York (1977).
41. D. Welti, Infrared Vapor Spectra, Heyden and Sons LTD/Sadtler Research Laboratories Inc., Philadelphia, 1970.
42. a. R.N. Zare, "Laser Alchemy: The New Chemistry," *Opt. Commun.*, 18, 94 (1976).
b. A.N. Oraevskii and A.V. Pankratov, "Laser Chemistry," *Lect. Note Phys.*, 43, 304-23 (1975).
c. A.M. Ronn, "Laser Chemistry," *Sci. Am.*, 240, 114 (1979).
43. A. Mooradian, et al., "Continuous Stimulated Spin-Flip Raman Scattering in InSb," *Appl. Phys. Letts.*, 17, 481-3 (1970).
44. I.M.T. Davidson, in Reaction Kinetics, Vol. I, Specialist Periodical Report, The Chemical Soc., London, p. 253.
45. A.V. Nowak and J.L. Lyman, "The Temperature Dependent Absorption Spectrum of the ν_3 Band of SF₆ at 10.6 μm ," *J. Quant. Spectrosc. Radiat. Transfer*, 15, 945-6 (1975).
46. J.W.C. Johns and W.A. Kreiner, "Measurement and Analysis of the ν_4 Band of Silane," *J. Mol. Spectrosc.*, 60, 400-11 (1976).
47. A.C.G. Mitchell and M.N. Zemansky, Resonance Radiation and Excited Atoms, Cambridge Univ. Press, Cambridge, 1961, p.163.
48. N.G. Basov, et al., "Stimulation of Chemical Reactions with Laser Radiation," in Chemical and Biological Applications of Lasers, Vol. I, Ed. C.B. Moore, Academic Press, New York, 1974, pp. 203-29.
49. T.F. Deutsch, "Infrared Laser Photochemistry of Silane," *J. Chem. Phys.*, 70, 1187 (1979).
50. E.J. Mezey, "Pigments and Reinforcing Agents," in Vapor Deposition, Eds. C.F. Powell, J.H. Oxley, and J.M. Blocher, John Wiley and Sons, New York, 1966.

51. a. A.Kato, et al., *Yogyo Kyokai Shi*, 80, 114 (1972).
b. K.S. Mazdiyasni and C.M. Cooke, "Synthesis, Characterization, and Consolidation of Si_3N_4 Obtained from Ammonolysis of SiCl_4 ," *J. Am. Ceram. Soc.*, 56, 628-33 (1973).
c. S. Prochazka and C Greskovich, "Synthesis and Characterization of a Pure Silicon Nitride Powder," *Bull. Am. Ceram. Soc.*, 57, 579-81,86 (1978).
d. A. Kato, et al., see Ref. 3.
52. R. Uyeda, "Growth of Polyhedral Metal Crystallites in an Inactive Gas," *J. Cryst. Growth*, 45, 485-489 (1978).
53. C.G. Granqvist and R.A. Buhrman, "Ultrafine Metal Particles," *J. Appl. Phys.*, 47, 2200-19 (1976).
54. a. S. Yatsuya, et al., "Formation of Ultrafine Metal Particles by Gas Evaporation Technique, I. Aluminum in Helium," *Jap. J. Appl. Phys.*, 12, 1675-84 (1973).
b. J. Hecht, "Formation and Growth of Na Smoke Particles," *J. Appl. Phys.*, 50, 7186-94 (1979).
55. A. Yokozeki and G.D. Stein, "A Metal Cluster Generator for Gas Phase Electron Diffraction and Its Application to Bismuth, Lead, and Indium: Variation in Microcrystal Structure with Size," *J. Appl. Phys.*, 49, 2224-32 (1978).
56. A. Kato, et al., "Preparation of Finely Divided Alumina by Vapor-Phase Reaction Between Aluminum Chloride and Oxidizing Gases and Its Properties," *Zairyo*, 21, 540-3 (1972).
57. H. Takeuchi, et al., "Preparation of Finely Divided Alumina by Vapor Phase Oxygenolysis of Aluminum Tribromide," *Yogyo Kyokai Shi*, 83, 23-7 (1975).
58. J. Tanaka and A. Kato, "Preparation of Finely Divided Silica by Vapor Phase Reaction Between Silicon Tetrachloride and Oxygen," *ibid.*, 81, 179-83 (1973).
59. Y. Suyama and A. Kato, " TiO_2 Produced by Vapor Phase Oxygenolysis of TiCl_4 ," *J. Am. Ceram. Soc.*, 59, 146-9 (1976).
60. T.U.M.S. Murthy, et al., "Gas Phase Nucleation During the Thermal Decomposition of Silane in Hydrogen," *J. Crystal Growth*, 33, 1-7, (1976).
61. L.P. Hunt and E. Sirtl, "A Thorough Thermodynamic Evaluation of the Silicon-Hydrogen-Chlorine System," *J. Electrochem. Soc.*, 119, 1741-5 (1972).
62. G.G. Deryatyk, et al. "Kinetics of the Thermal Decomposition of Monosilane, Arsine, and Monosilane with Arsine Impurity," *Russ. J. Inorg. Chem.*, 18, 1528 (1965).

63. T.R. Hogness, et al., "The Thermal Decomposition of Silane," *J. Am. Chem. Soc.*, 58, 108 (1936).
64. H. Niki and G.J. Mains, "Mercury-Photosensitized Decomposition of Monosilane," *J. Phys. Chem.*, 68, 304 (1964).
65. A. White and E.G. Rochow, "Reaction of Silane with Unsaturated Hydrocarbons," *J. Am. Chem. Soc.*, 76, 3897 (1954).
66. J.H. Purnell and R. Walsh, "Pyrolysis of Monosilane," *Proc. Royal Soc., Series A, London*, p. 545 (1966).
67. V.V. Dudorov and A.D. Zorin, "The Mechanism of the Pyrolysis of Silane," *Russ. J. Phys. Chem.*, 49, 1727-9 (1975).
68. C.G. Newman, et al., "Kinetics and Mechanisms of the Silane Decomposition," *Int. J. Chem. Kin.*, XI, 1167-82 (1979).
69. B.A. Scott et al., "Kinetics and Mechanism of Amorphous Hydrogenated Silicon Growth by Homogeneous Chemical Vapor Deposition," *Appl. Phys. Letts.*, 39, 73-5 (1981).
70. M. Hirose, "Physical Properties of a-CVD Silicon," in Proc. 9th Int. Conf. on Amorphous and Liquid Semiconductors, Eds. B.K. Chalanaverty and D. Kaplan, *J. de Physique*, C4, 705-14 (1981).
71. J.Y.W. Seto, "Deposition of Polycrystalline Silicon by the Pyrolysis of Silane in Argon," *J. Electrochem. Soc.*, 122, 701-6 (1975).
72. M.E. Jones and D.W. Shaw, "Growth from the Vapor," in Treatise on Solid State Chemistry, Vol. 5, N.B. Hannay, Plenum Press, New York, 1976.
73. D. White and E.G. Rochow, "Reaction of Silane with Unsaturated Hydrocarbons," *J. Am. Chem. Soc.*, 76, 3987-902 (1954).
74. G. Perkins, et al., "147 nm Photolysis of Monosilane," *J. Am. Chem. Soc.*, 10, 1109-15 (1979).
75. A.N. Oraevskii, et al., "Laser-Chemical Decomposition of Monosilane," *High Energy Chem.*, 12, 48 (1978).
76. R. Bilenchi and M. Musci, "Laser Enhanced Chemical Vapor Deposition of Silicon," in Proc. 8th Int. Conf. on Chemical Vapor Deposition, Eds. J.M. Blocher and G.E. Vulillard, *The Electrochemical Soc.*, Pennington, N.J., 1981 p.275-85.
77. E. Krikorian and R.J. Sneed, "Nucleation, Growth, and Transformation of Amorphous and Crystalline Solids Condensing from the Vapor," *Astrophysics Space Sci.*, 65, 129-54 (1979).

78. J. Bloem, "Gas Phase Diffusion and Surface Reactions in the Chemical Vapor Deposition of Silicon," *Pure Appl. Chem.*, 50, 435-47, (1978).
79. J. Bloem and W.A.P. Claassen, "Structure of CVD-Grown Silicon Layers," see Ref. 76, pp. 128-30.
80. L.I. Popova, et al., "Thin Polycrystalline Silicon Films from Low Temperature Pyrolysis of Silane," *Bulgarian J. Phys.*, 4, 178-84 (1977).
81. E. Bustarret, et al., "Hydrogen Profiles in Virgin and in situ Post Hydrogenated LPCVD a-Si:H Films," see Ref. 76, pp. 347-56.
82. U. Koster, "Crystallization of Amorphous Silicon Films," *Phys. Stat. Sol.*, 48, 313 (1978).
83. R. Drosd and J. Washburn, "Some Observations on the Amorphous to Crystalline Transformation in Silicon," *J. Appl. Phys.*, 53, 397-403 (1982).
84. W.S. Coblenz, "Physics of Sintering of Silicon," Ph.D. Thesis, M.I.T., Cambridge, MA 1981.
85. J.S. Haggerty and W.R. Cannon, Sinterable Powders from Laser Driven Reactions, under contract N00014-77-C0581, Annual Report, M.I.T., Cambridge, MA 1979.
86. G.A.W. Rutgers and J.C. DeVos, "Relation Between Brightness Temperature, True Temperature, and Colour Temperature of Tungsten," *Physica*, XX, 715-20 (1954).
87. H.G. Van de Hulst, Light Scattering by Small Particles, John Wiley and Sons, Inc., New York, 1957.
88. T.M. Lowes and A.J. Newall, "The Emissivities of Flame Soot Dispersions," *Combustion and Flame*, 16, 191-4 (1974).
89. J.H. Flint, "Powder Temperatures in Laser Driven Reactions," M.S. Thesis, M.I.T., Cambridge, MA 1982.
90. M. Kerker, The Scattering of Light and Other Electromagnetic Radiation, Academic Press, 1969.
91. K.G. Neoh, "Soot Burnout in Flames," S.D. Thesis, M.I.T., Cambridge, MA 1980.
92. M. Janai and B. Karlson, "Temperature Variation of the Absorption Edge of CVD Amorphous and Polycrystalline Silicon," *Solar Energy Materials*, 1, 387-95 (1979).
93. D.B. Spalding, Genmix- A General Computer Program for Two-Dimensional Parabolic Phenomena, Pergamon Press, New York, 1977.

94. S.V. Patantov and D.B. Spalding, Heat and Mass Transfer in Boundary Layers, Second Ed., Intertext Books, London, 1970.
95. Handbook of Chemistry and Physics, Ed. R.C. Weast, The Chemical Rubber Co., Cleveland, Ohio, 52nd Ed., 1972, p. E.2.
96. N.V. Tsederberg, Thermal Conductivity of Gases and Liquids, M.I.T. Press, Cambridge, MA.
97. H.K. Bowen, Physics and Chemistry of Packing Fine Ceramic Powders, Under Contract DE-ACO2-80ER10588, M.I.T., Cambridge, MA, 1980.
98. S. Mizuta, et al., "Wetting and Dispersion of Silicon Powder Without Defloculents," Bull. Am. Ceram. Soc., 61, 872-5 (1982).
99. See Ref. 95, p.B133.
100. J. Hirth and G.M. Pound, "Condensation and Evaporation: Nucleation and Growth Kinetics" in Progress in Materials Science, Vol. 11, MacMillan Co., New York, 1963, p. 5.
101. F.F. Abraham, Homogeneous Nucleation Theory, Academic Press, New York, 1974, pp. 184-91.
102. A.W. Castleman, Jr., et al., "The Properties of Ion Clusters and Their Relationship to Heteromolecular Nucleation," J. Chem. Phys., 68, 1760-7 (1978).
103. D.J. Frurip and S.H. Bauer, "Homogeneous Nucleation in Metal Vapors, 3. Temperature Dependence of the Critical Supersaturation Ratio for Iron, Lead, and Bismuth," J. Phys. Chem., 81, 1001-6 (1977).
104. J. Hecht, "Formation and Properties of Na Smoke Particles," J. Appl. Phys., 50, 7186-94 (1979)
105. J.Y.W. Seto, "Deposition of Polycrystalline Silicon by Pyrolysis of Silane in Argon," J. Electrochem. Soc.: Solid State Science and Technology, 122, 701-6 (1975).
106. F.C. Eversteyn, et al., "A Stagnant Layer Model for the Epitaxial Growth of Silicon from Silane in a Horizontal Reactor," ibid., 117, 925 (1970).
107. S.K. Friedlander, "Relating Particulate Pollution to Sources: Fundamental Principles," in Proc. of Ann. Meeting Gesselschaft fur Aerosol fur schung, 113-115 (1973).
108. S.G. Mason, "Orthokinetic Phenomena in Disperse Systems," J. Colloid Interface Sci., 58, 275-85 (1977).

109. H.C. Hamaker, "The London van der Waals Attraction Between Spherical Particles," *Physica*, 4, 1058 (1937).
110. M.V. Tikhomirov, et al., "On the Influence of van der Waals Forces on Coagulation of Aerosols," *Acta Phys-Chim., URSS*, 17, 185 (1942).
111. T. Onaka, et al., "Experiment on the Clustering of Fine Particles," *Astrophys. Space Sci.*, 65, 103-17 (1979).
112. K.E. Easterling and A.R. Tholen, "Surface Energy and Adhesion at Metal Contacts," *Acta Met.*, 20, 1001-8 (1972).
113. a. I. Hansson and A.R. Tholen, "Adhesion Between Fine Gold Particles," *Phil. Mag. A*, 37, 535-9 (1978).
b. See Ref. 114.
c. K.L. Johnson, et al., "Surface Energy and Contact of Elastic Solids," *Proc. R. Soc. Lond. A*, 324, 301-13 (1971).
114. D. Tabor and R.H.S. Winterton, "The Direct Measurement of Normal Retarded van der Waals Forces," *ibid.*, 312, 435-50 (1969).
115. K. Zellama, et al., "Crystallization in Amorphous Silicon," *J. Appl. Phys.*, 50, 6995-7000 (1979).
116. J.T.G. Overbeek, "Monodisperse Colloidal Systems, Fascinating and Useful," *Adv. Colloid Interface Sci.*, 15, 251-77 (1982).
117. M. Avrami, "Kinetics of Phase Change, II," *J. Chem. Phys.*, 8, 212-24 (1940).
118. D. Turnbull, "Isothermal Rate of Solidification of Small Droplets of Mercury and Tin," *J. Chem. Phys.*, 18, 768 (1950).
119. S. Brunauer, et al., "Absorption of Gases in Multimolecular Layers," *J. Am. Chem. Soc.*, 60, 309-19 (1938).
120. R.W. Heckel and J.L. Youngblood, "X-ray Line Broadening Study of Explosively Shocked MgO and Al₂O₃," *J. Am. Ceram. Soc.*, 51, 398-401 (1967).
121. G. Ziegler, "Structural and Morphological Investigations of Ceramic Powders and Compacts," *Powd. Met. Int.*, 10, 70-3 (1978).
122. W.A. Rachinger, "A Correction for the α_1, α_2 Doublet in the Measurement of the Width of X-ray Diffraction Lines," *J. Sci. Instrum.*, 25, 254-5 (1948).
123. G.K. Williamson and W.H. Hall, "X-ray Line Broadening from Filed Aluminum and Wolfrum," *Acta Met.*, 1, 22-31 (1953).

124. C. Kuhl, et al., "Optical Investigation of Different Silicon Films," J. Electrochem. Soc., 121, 1496-500 (1974).
125. T.R. Gattuso, M. Meunier, and J.S. Haggerty, "Laser Induced Deposition of Thin Films," Annual Report, MIT-EL82-022, M.I.T., Cambridge, MA, 1982.

BIOGRAPHICAL NOTE

Robert Allen Marra was born in Rockville Center, New York on April 27, 1956. His family moved to Jamestown, New York in 1971, where he attended Southwestern High School under the assumed name, "Moose". He graduated magna cum laude with a B.S. degree in Ceramic Science and a B.A. degree in Mathematics in 1978 from Alfred University. At Alfred, he also received the alias "Rock". In September of 1978, Bob, Moose, Rock, entered M.I.T. as a graduate student in ceramics under the guidance of Dr. John Haggerty and Professor Kent Bowen. The author is a member of Phi Kappa Phi and the American Ceramic Society. He has accepted a job at the Alcoa Technical Center in Alcoa Center, Pennsylvania.